AZƏRBAYCAN RESPUBLİKASI ELM VƏ TƏHSİL NAZİRLİYİ
AZƏRBAYCAN DÖVLƏT NEFT VƏ SƏNAYE UNİVERSİTETİ

MINISTRY OF SCIENCE AND EDUCATION
REPUBLIC OF AZERBAIJAN
AZERBAIJAN STATE UNIVERSITY OF OIL AND INDUSTRY

"NEFTİN, QAZIN GEOTEXNOLOJİ PROBLEMLƏRİ VƏ KİMYA" ELMİ-TƏDQİQAT İNSTİTUTUNUN

ELMİ ƏSƏRLƏRİ

SCIENTIFIC PROCEEDINGS

SCIENTIFIC-RESEARCH INSTITUTE "GEOTECHNOLOGICAL PROBLEMS OF OIL, GAS AND CHEMISTRY"

VOLUME 25 No. 2

BAKU-2025

AZƏRBAYCAN RESPUBLİKASI ELM VƏ TƏHSİL NAZİRLİYİ

AZƏRBAYCAN DÖVLƏT NEFT VƏ SƏNAYE UNİVERSİTETİ

MINISTRY OF SCIENCE AND EDUCATION

REPUBLIC OF AZERBAIJAN

AZERBAIJAN STATE UNIVERSITY OF OIL AND INDUSTRY

“NEFTİN, QAZIN GEOTEXNOLOJİ PROBLEMLƏRİ VƏ KİMYA” ELMİ-TƏDQİQAT İNSTİTUTUNUN

ELMİ ƏSƏRLƏRİ

SCIENTIFIC PROCEEDINGS

SCIENTIFIC RESEARCH INSTITUTE

“GEOTECHNOLOGICAL PROBLEMS OF OIL, GAS AND CHEMISTRY”

Sci. Proc. SRI GPOGC. Volume 25, Number 2, 2025

BAKU-2025

Scı. Proc. SRI GPOGC

Editor-in-Chief

Rauf Yu. Aliyarov

Scientific Research Institute of Geotechnological Problems of Oil, Gas and Chemistry, SRI GPOGC, Dilara Aliyeva Str. 227, AZ 1010, Baku, Azerbaijan Republic

Editorial Board

R.Yu. Aliyarov (Editor-in-Chief), **H.Kh. Malikov** (Deputy Chief Editor), **M.M. Asadov** (Deputy Chief Editor)

Phone: +994 12 4937957

E-mail: info@gpogc.az

Journal of SRI "Geotechnological Problems of Oil, Gas and Chemistry" of ASOIU,Issue 2, 2025, pp. 05-175
https://doi.org/10.65294/gpogc.2025.00

ISSN 2218-5054

Scientific Proceedings. Scientific Research Institute of "Geotechnological Problems of Oil, Gas and Chemistry". Ministry of Science and Education of Azerbaijan. Dilara Aliyeva Street 227, AZ1010 Baku, Azerbaijan. Sci. Proc. SRI GPOGC. 2025. Volume 25. Number 2

Contents

1	A.E. Abetov, Sh.B. Yesirkepova, M.Kh. Iskandarov, Sh.A. Umarov, R.Yu. Aliyarov, B.S. Aslanov **Regional evaluation of hydrocarbon potential in the south Ustyurt region based on integrated geological and geophysical data**	**5**
2	B.S. Aslanov, I.E. Safarli **Prospects for exploration of the non-anticlinal traps of Hovsan shallow water area by geophysical methods**	**44**
3	G.I. Guseinova, G.S. Guseinov, R.N. Ahmedova, A.R. Babaev, V. Kh. Hamzayev **Geological and geochemical characteristics of the Qosha gold deposit and the role of rare elements in ore genesis**	**62**
4	A.M. Mamed-zade, E.N. Aliyev, E.F. Alizade, T.Kh. Malikov, N.S. Bayramova, A.M. Salimli **Pore-scale evaluation of oil samples with distinct physicochemical properties for enhanced oil recovery efficiency**	**68**
5	Sh. Ismayilov, I. Karimov **Real-time acoustic detection of sand production and its impact on oil and gas well productivity**	**80**
6	E.N. Aliyev, T.S. Babayeva **Choice of method for determining pressure losses during multiphase flow in vertical wells**	**89**
7	I. Karimov, Sh. Ismayilov **Assessment of sand control strategies and their impact on well productivity and lifetime**	**97**
8	H.Kh. Malikov, T.E. Abdulmutalibov, G.V. Jabbarova, R.R. Tashmenov **Forecasting the risk of formation damage (colmatation) with a 14-day horizon using calibrated probabilistic models**	**106**
9	V.A. Iskandarov, G.V. Jabbarova, Y.Y. Shmoncheva, R.R. Tashmenov **Python-based modelling improves torque and drag modelling in horizontal extended reach well**	**121**
10	A.I. Babaev **Study of the possibility of the phenomenon of fugitive emissions in current petrochemical productions**	**130**

11 A.I. Babayev [1], Q.S. Hasanov [2], K.M. Ismailova [1], Z.O. Gahramanova [1], N.A. Sadigova [1], N.A. Yusubova [1] **138**
IR spectroscopy in the analysis of hydrocarbons isolated from oil-contaminated soils

12 A.I. Babayev, V.Kh. Hamzayev, G.I. Guseinova, R.N. Ahmedova, A.R. Babaev, F.Z. Madatova, K.Kh. Agayeva, D.G. Ismayilova **142**
Investigation of the distribution of rare elements in ores of the Gedabek deposit

13 M.Y. Agamammadova, Kh.E. Aliyarova, S.B. Mammadova **149**
Types of natural bitumens, composite properties and their classification

14 F. Madatova, K. Agayeva, D. Ismailova, A. Babayev **156**
Hydrogen storage with carbon nanotubes

15 N.I. Salmanova, A.B. Huseynov, E.B. Zeynalov, E.N. Aliyev, Z.E. Bayramova, A.Y. Guliyeva, E.B. Huseynova, K.V. Amirmatova, E.A. Ismailova, T.A. Isgandarova **162**
CVD synthesis of multi-walled carbon nanotubes with integrated by-product recycling

16 M.M. Asadov, E.N. Aliyev, A.M. Salimli
Janus interfacial catalysts and nanoparticles for enhanced oil recovery: synthesis, mechanisms, and novel conceptual approaches **169**

Journal of SRI "Geotechnological Problems of Oil, Gas and Chemistry" of ASOIU,
Issue 2, 2025, pp. 05-43
https://doi.org/10.65294/gpogc.2025.01

Regional evaluation of hydrocarbon potential in the south Ustyurt region based on integrated geological and geophysical data

A.E. Abetov[1], Sh.B. Yesirkepova[2], M.Kh. Iskandarov[2], Sh.A. Umarov [3], R.Yu. Aliyarov[4], B.S. Aslanov[4]

[1]Satbayev University, Almaty,
[2]JSC "O'ZLITINEFTGAZ", Tashkent,
[2]Uzbek Institute of Standards, Tashkent,
[4]Scientific Research Institute "Geotechnological Problems of Oil, Gas and Chemistry", Ministry of Science and Education of Azerbaijan, Dilara Aliyeva Street 227, AZ1010 Baku, Azerbaijan

Abstract. A methodology for regional hydrocarbon prospectivity assessment in the South Ustyurt Region (SUR) has been developed through the integration of drilling, seismic exploration, gravimetry, magnetometry, geothermal studies, and airborne gamma-ray spectrometry data. The hydrocarbon potential of the SUR was evaluated using advanced software tools, including IP Seismic, ArcGIS, and others.

The research methodology based on machine learning techniques, specifically Self-Organizing Map (SOM) clustering, to identify correlations between geophysical anomalies, regional and local structures, and predicted hydrocarbon accumulations.

Structural mapping analysis confirmed the block heterogeneity of the sedimentary cover. Airborne gamma-ray spectrometry identified 15 anomalous zones characterized by reduced concentrations of thorium, potassium, and uranium, suggesting potential hydrocarbon presence. Most of these anomalies are concentrated in the Shakhpakhty Steppe. The correlation between airborne gamma-ray spectrometry and seismic data further confirmed the association of radioactive anomalies with fault tectonics.

In the Shakhpakhty Step and Assakeaudan Depression, the Kazgurly, Utezhan, Kozhantay, Western Kozhantay, Otynshy, and Southern Tabyn areas show high probabilities of hydrocarbon accumulation. Exploratory drilling and additional 3D seismic surveys are recommended for these locations.

Furthermore, the research findings require further validation through the integration of remote sensing and well data within a unified 3D model.

The integration of modern digital technologies and artificial intelligence to improve forecasting accuracy and exploration efficiency is recommended for similar studies in Kazakhstan and other regions with comparable geological condition.

Key words: Interpretation, IP seismic, airborne gamma-ray spectrometry, geodensity, geomagnetic and geothermal models, reflecting horizons, geospatial analysis, digital technologies, artificial intelligence.

*Corresponding author +994 12 4937957
e-mail: r.aliyarov@asoiu.edu.az, beyler@inbox.ru

Introduction. In the past decade, a clear trend of depletion has emerged in a number of producing hydrocarbon fields in the energy sector of the Republic of Kazakhstan. Therefore, replenishing the country's hydrocarbon resource base is one of the key economic priorities and is reflected in strategic programs approved at the state level, including the *Geological Exploration Development Program for 2021–2025*.

These program documents outline two main directions for geological exploration: (a) further study of underexplored hydrocarbon fields; (b) the discovery of new oil and gas fields.

The first direction focuses on refining the structural, formational, and reservoir characteristics of productive formations in already explored and developed hydrocarbon fields.

However, the potential for replenishing, expanding, or maintaining a competitive hydrocarbon resource base in Kazakhstan is nearly exhausted.

The primary driver for stabilizing and subsequently expanding this resource base lies in the second direction—exploration and development of new oil and gas fields. Key objectives include:

- Advancing and implementing digital technologies, artificial intelligence, and machine learning;

• Developing new theories and concepts of hydrocarbon formation while strengthening the scientific and methodological framework for geological exploration;

• Applying innovative approaches in predictive exploration and acquiring new subsurface data to enhance the reliability of hydrocarbon accumulation forecasts;

• Expanding the role of project management methodologies aligned with international standards.

Implementing regional geological exploration programs in a phased approach is both advisable and justified. Initially, cost-effective large-scale regional methods should be applied, followed by the selection of promising areas for more detailed and resource-intensive geological and geophysical studies.

The choice of exploration and development methods depends on geological specifics, the level of previous studies, and set objectives. A rational complex of geological exploration activities is selected based on prior work analysis, geological science advancements, and technology to ensure reliable geological information at minimal cost.

The choice of exploration and development methods depends on geological characteristics, the extent of previous studies, and specific objectives. A rational combination of geological exploration activities is determined based on the analysis of prior research, advancements in geological science, and technological innovations to ensure the acquisition of reliable geological information at minimal cost.

In regional geological exploration, remote geophysical methods play a key role, forming a basis for “heavy” and expensive seismic surveys and exploratory drilling aimed at localizing hydrocarbon deposits.

Remote geophysical methods offer a cost-effective approach while enabling the exploration of vast areas. These methods include airborne gamma-ray spectrometry (AGSS), geothermal surveys, gravity and magnetic prospecting, as well as integrated data interpretation and modeling within a unified computational platform using advanced software. Our research utilized the innovative IP Seismic software.

1. Study area and geological setting. The South Ustyurt Region (SUR) is located in the southeastern part of the South Mangyshlak Sedimentary Basin, within the same-named oil and gas-bearing region (OGR) of the Turan Epig Hercynian Platform [1].

Tectonically, the South Mangyshlak Sedimentary Basin is situated within a large zone of Mesozoic intracratonic subsidence, known as the South Mangyshlak-Assakeaudan Depression System. It is bounded to the north by the Mangyshlak-Central Ustyurt Dislocation System and to the south by the northern slopes of the Karabogaz Arch and the Tuarkyr Uplift Zone. To the west, the basin extends toward the Caspian Sea, i.e. it covers oil and gas bearing regions and areas of 3 countries: the Republic of Kazakhstan, the Republic of Uzbekistan and the Republic of Azerbaijan.

The axial zone of the South Mangyshlak-Assakeaudan Depression System is characterized by a linear series of basin-like Depressions and depressions, separated by structural saddles. These depressions and synclines vary in size and exhibit irregular, often sub-isometric shapes in plain view [1, 2].

From west to east along the axis of this system, the major Jazgurly and Assakeaudan depressions, as well as the Uchkuduk Depression, can be distinguished. Within these structures, smaller Depressions and subordinate local uplifts have been identified (Fig. 1).

A key characteristic of the tectonic structure of the South Mangyshlak–Assakeaudan Depression System is the stepwise subsidence of rock sequences of different ages from the zone’s margins toward its axial part [2]. On the northern flank, these steps are arranged either parallel to each other or in a staggered pattern, aligning with the general strike of the Mangyshlak–Central Ustyurt Dislocation System (Fig. 1).

These steps are associated with chains of local anticlinal uplifts that act as hydrocarbon traps. The identified local anticlines in the South Mangyshlak petroleum-bearing region exhibit asymmetric

structures, characterized by a steep southern wing, a more gently dipping northern limb, and minor faulting [1].

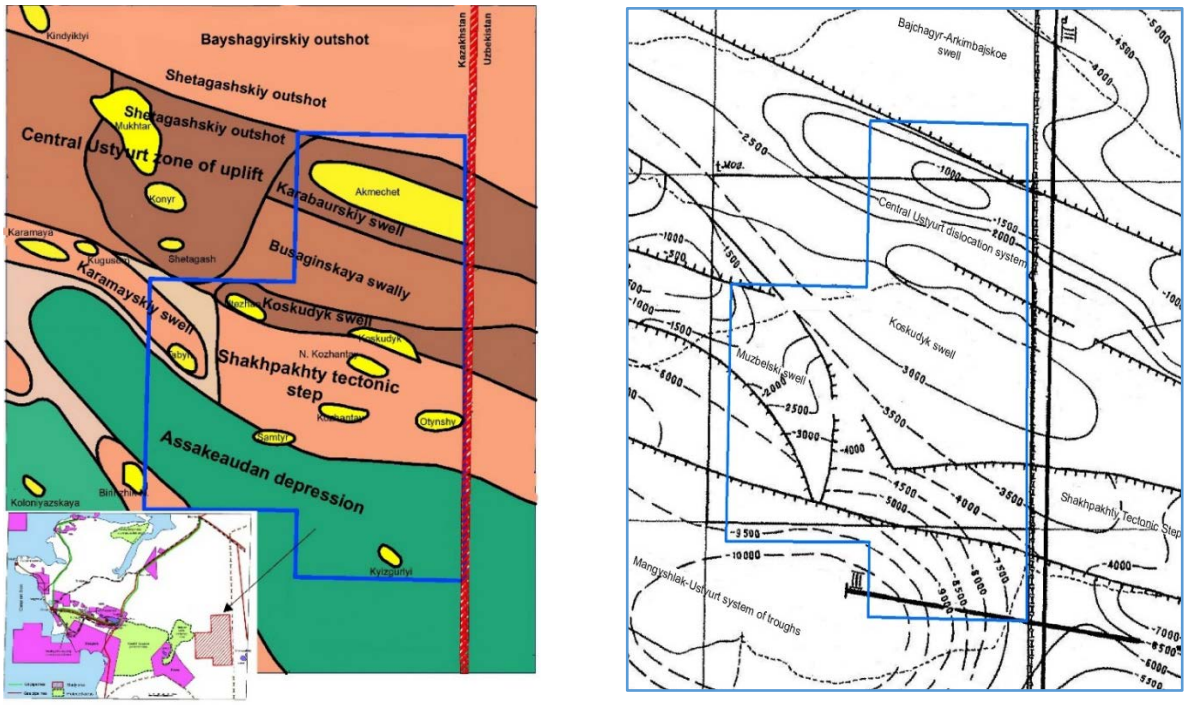

Fig. 1. Scheme of tectonic elements of the study region

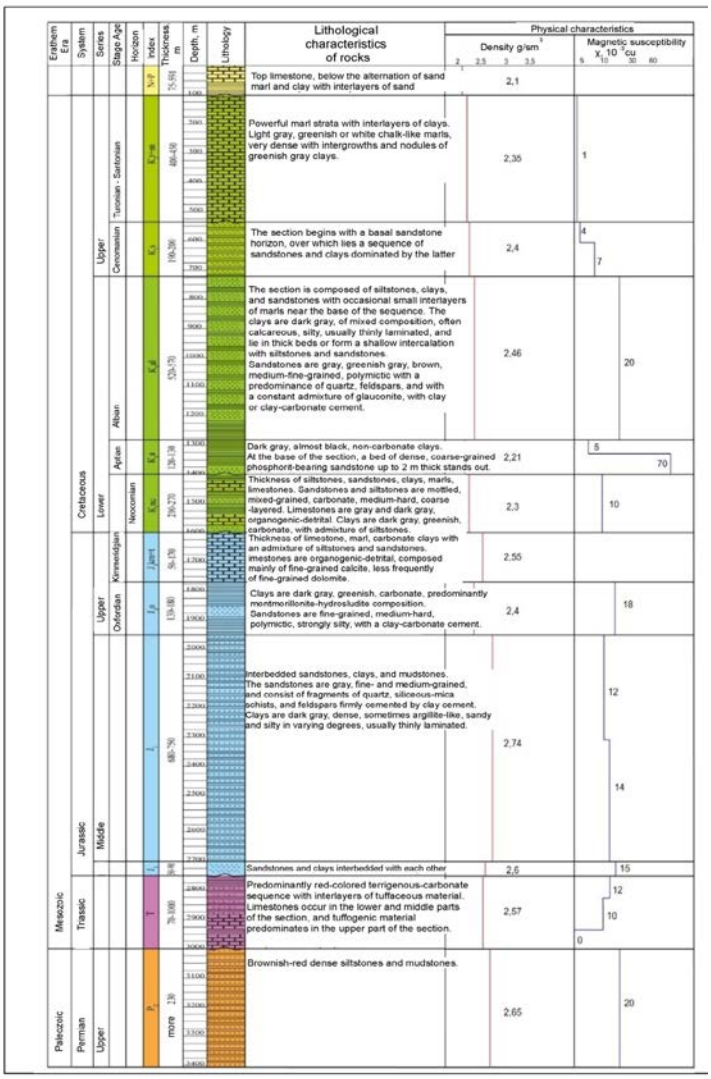

Fig. 2. Consolidated lithological-stratigraphic section of South Ustyurt

The geological section of the study region can be divided into three main structural-formational levels:

- Platform cover of Jurassic-Cenozoic age.
- Transitional complex (intermediate structural level), characterized by more intense, predominantly block-related dislocations. This level includes two subunits: the Permian-Triassic terrigenous-carbonate sequence and the pre-Upper Permian sequence, with a total thickness ranging from 3,500 to 6,000 meters.
- Folded basement, composed of rigid massifs and Paleozoic folded systems

The oldest deposits, represented by thick Upper Permian and Triassic rock sequences, are exposed in the Mountainous Mangyshlak region. These rocks are highly deformed and partially metamorphosed (Fig. 2).

In the central, most subsided part of the South Mangyshlak–Assakeaudan Depression System, these deposits occur at depths exceeding 4 km. Here, they exhibit minimal deformation and a subhorizontal bedding orientation [1].

Above these deposits, a sharp angular unconformity marks the transition to thick Jurassic sediments, which include all three Jurassic series. The Jurassic sequence, in turn, is overlain by Cretaceous deposits with evidence of erosion and angular unconformity. The eroded surface of the Cretaceous is further covered by Paleogene sediments (Fig. 2).

Neogene deposits, which form the uppermost layer of the sedimentary cover, rest unconformably on Paleogene sediments and, in some cases, on older formations, also with signs of erosion and angular discordance.

Mesozoic–Cenozoic sediments are predominantly terrigenous, except for the Upper Turonian–Danian carbonate sequence and interbedded shell limestones within the sand-clay Neogene section (Fig. 2).

The South Mangyshlak-Assakeaudan Depression System represents a typical Mesozoic-Cenozoic basin, characterized by a platform-type, weakly deformed Jurassic–Neogene sedimentary cover overlying a more deformed pre-Jurassic section. The uppermost stratigraphic unit consists of Miocene sediments of the Sarmatian stage. Beyond the study area, along the western escarpment of the Ustyurt Plateau, Jurassic and Triassic deposits are exposed [2].

In the South Mangyshlak petroleum region, Triassic, Jurassic, and Cretaceous formations host commercial oil and gas reserves. The primary productive interval consists of Middle Jurassic terrigenous sediments, which contain the majority of the discovered hydrocarbon reserves.

Eight oil, gas, and gas-condensate fields have been explored within this complex. Hydrocarbon-bearing horizons with minor reserves have also been identified in Upper and Lower Jurassic sediments. Commercial Triassic petroleum potential has been confirmed at fields such as Northen-Rakushechnoye and Southern-Zhetybai. Gas accumulations in Cretaceous sediments have been explored at the Uzen and Kansu fields, while oil fields have been identified at Dunga, Zhozaskan, Spemesai, and others [1].

The pay horizons of the discovered **South Mangyshlak** petroleum region are mainly composed of terrigenous rocks, including sandstones, clayey sandstones, and siltstones. **Cretaceous hydrocarbon-bearing horizons** exhibit effective thicknesses ranging from a few meters to 25 meters, with well flow rates reaching up to **25,000 m³/day.** In contrast, **Jurassic reservoirs** can attain effective thicknesses of up to **65 meters,** with gas well flow rates reaching **800,000 m³/day** [1,3].

The South Ustyurt potentially gas-bearing area is located between the Kansu (in the west) and Shakhpakhy (in the east) gas-bearing areas [1, 24]. Structural-tectonic, lithofacial, geochemical factors, and direct signs of hydrocarbon saturation in the adjacent gas-bearing areas suggest a high probability of gas and gas - condensate fields discovery in the SUR.

2. Vintage data

2.1. Seismic and drilling. In 2019, Tat-Arka LLP conducted MOGT-2D field seismic surveys in the SUR, covering the Central Ustyurt Dislocation System (CUSD), the Shakhpakhy Step, and the northern flank of the Assakeaudan Graben. The objective was to enhance the understanding of the geological structure and assess the oil and gas potential of Cretaceous, Jurassic, Triassic, and Paleozoic sediments.

The processing of MOGT-2D seismic data, along with structural and dynamic interpretation, was carried out by Professional Geo Solutions (PGS) Kazakhstan LLP using Spark (PGS), HoloSeis, GeoGraphix Discovery, DUG Insight, and Petrel software. As a result, final migrated profiles in the time domain were obtained, covering 1,200 full-fold linear kilometers.

Structural and dynamic interpretation of these profiles was conducted in conjunction with digitized “old” MOGT data from 1984-1991, amounting to 2,000 linear kilometers, and was complemented by well log data from 12 wells drilled ш the SUR.

As a result of the conducted work, isochron maps and structural maps were compiled, for ten reflective horizons: I, II, III, IV, IVbt, V, TV1, TV2, TV3, and “b”. These maps served as the basis for identifying and confirming seven gas- and oil-prospective local structures: Kyzgyrly, Samtyr South, Samtyr West, Tabyn South, Kozhantay West, Otynshi, and Kazgyrly South. AVO anomalies were detected at three areas in the SUR—Kazgyrly, Kozhantay West, and Kazgyrly South - which may indicate the presence of gas within these local structures.

Exploration drilling in the SUR was conducted on seven structures - Birinzhik, Birinzhik South, Kozhantai, Utezhan, Samtyr, Mukhtar, and Koskudyk. A total of 15 wells were drilled on the crests and periclines of these structures, penetrating Cretaceous, Jurassic, and pre-Jurassic formations.

The Birinzhik South and Birinzhik structures were identified within the Assakeaudan Depression (Fig.1), while the Kozhantai, Utezhan, and Samtyr structures are located on the

Shakhpakhty Step. The Mukhtar and Koskudyk structures are situated within the Central Ustyurt Dislocation System (CUSD).

A standard well logging (of that time) was conducted in all drilled wells. In addition to various methods used to assess the hydrocarbon potential of the section, it also included uncompensated neutron-gamma logging, which is highly sensitive to gas saturation, typically indicated by abnormally high readings. However, no abnormally high spikes in neutron-gamma log readings were recorded in any of the wells.

The likely cause of this is the heavy drilling mud invasion, with penetration into the reservoir ranging from 2 to 16 wellbore diameters, as well as suboptimal well placement and an underestimation of the structure of the oil and gas-bearing system (see below). Given these factors, the definitive classification of the drilled structures as unpromising remains questionable.

2.2. Gravimetric study. In the 1950s, VNIGRI and the Karakalpak Oil and Gas Exploration Trust conducted a regional gravimetric survey in Ustyurt Region at a 1:200,000 scale. Based on the interpretation of the acquired data: a) The first insights into the structure of the pre-Jurassic rock complex were obtained; b) Structural maps of the Permo-Triassic and pre-Early Permian rock complexes were compiled. The latter was identified by many researchers (V.A.Lapshov, 1963) with the top of the basement.

Gravity survey in the SUR has been conducted since 1954, aiming to provide a detailed analysis of the gravity field characteristics and to identify local anomalies associated with structures in the Permo-Triassic and older sediments. The survey scale ranged from 1:200,000 to 1:50,000.

2.3. Geomagnetic study. Magnetic survey in the Ustyurt region has been conducted since the late 1950s to obtain information on the regional structure of the basement and to support geological and mineral exploration. The survey scale ranged from 1:25,000 to 1:1,000,000.

Based on the results of the aeromagnetic survey conducted in 1954, ΔTa maps at a scale of 1:200,000 were compiled. The potential of magnetic surveying for mapping the top of the crystalline basement was demonstrated, followed by the solution of structural and tectonic zoning objectives.

As a result, new insights into the geological structure of the Ustyurt Region were obtained, magnetic field zoning was conducted, and recommendations for regional prospecting were provided. Promising areas for identifying local structural uplifts favorable for oil and gas exploration were delineated [8,9].

The aeromagnetic survey of the Ustyurt region was conducted by KazAGGE between 1974 and 1976. As a result, anomalous field ΔTa map at a scale of 1:50,000 were compiled. According to some researchers (14, Seifulin et al.), the observed anomalies are associated with magnetically disturbing masses of basement rocks. However, the depths of these formations were systematically underestimated, particularly in areas of deep subsidence. No clear correlation between the magnetic field and structures within the sedimentary cover has been established, which is attributed to the low magnetic susceptibility and lithological differentiation of sedimentary rocks.

Ground magnetic surveys were also conducted in the SUR to develop regional tectonic zoning maps and assess its structural connections with adjacent areas. The results revealed no distinct correlation between the magnetic field and the structures within the sedimentary cover.

Therefore, the results of the magnetic survey were further utilized for structural and tectonic zoning of the region along the crystalline basement surface. In this context, the authors of the article incorporated the results of aeromagnetic surveys at a scale of 1:200,000 (Spirin E.A., Makarova Z.A., 1952; Purgalin A.I. et al., 1958; Dzabaev A.A. et al., 1963) to construct composite digital datasets of the anomalous magnetic field.

2.4. Thermal field study. In the SUR, infrared (IR) survey in the long-wave spectrum (8–14 μm), conducted in 2009, was used to assess oil and gas prospective areas. This wavelength range corresponds to the intrinsic thermal radiation of surface objects, and the acquired data are widely applied in solving various geological targets.

IR survey was carried out in summer, in the pre-morning hours and in cloudless time, when the solar-thermal inertia component, as well as the temperature influence of moistened soil and green vegetation is practically excluded.

Additionally, the influence of terrain is reduced, while the intrinsic radiation of geological objects is enhanced due to the release of internal heat from the Earth's interior through weakened (fractured) zones, creating in thermal anomalies. For thermal field processing, seven spectral channels within the wavelength range of 9.58 to 14.385 µm were selected.

2.5. Aerogamma spectrometry coverage. An aerogamma spectrometric survey (hereinafter referred to as AGSS) was conducted in the South Ustyurt region (SUR) for the first time. However, to the west, on the North Bozashy uplift, a similar survey (experimental-methodological studies) at a scale of 1:200,000 was carried out by the NPO "Neftegeofizika" in 1981–1983 (Gauer Z.E., Tsytovich B.L.). Based on the survey results, the regional gamma field was zoned, and areas promising for further detailed studies were identified.

In 1982–1984, a comprehensive AGSS at a scale of 1:25,000 was conducted over a 4,000 km² area in the western part of the South Mangyshlak Depression. However, the survey results did not yield positive outcomes in the search for hydrocarbon fields.

3. Materials and methods

3.1. General approaches to interpretation and modelling. A comprehensive interpretation of geological and geophysical data, along with a regional prediction of the oil and gas potential of the South Ustyurt region (SUR), was conducted using the inversion-forecasting software package IP Seismic [5,6].

For an in-depth qualitative and quantitative analysis of multi-scale data, the authors utilized drilling, seismic, gravity, and magnetic survey data, as well as AGSS and geothermal data, applying innovative machine learning algorithms and artificial intelligence [8, 14].

The **SOM_Clustering Seis plug-in** was used, developed based on Kohonen’s algorithm to classify geophysical potential field maps within a moving window.

Kohonen's Self-Organising Map (SOM) 1D, 2D or 3D, is a computer modelling technique designed primarily for clustering, visualisation and data analysis of multivariate data. The main purpose of applying SOM is to identify hidden patterns in the data by reducing the dimensionality of the original space. In practice, a two-dimensional space is often used due to its convenience for visualization while preserving the topology of the original data space [8, 10].

As a result of machine learning, the model generates a grid of trained neurons, referred to as a "map" of the original data space [11, 12, 14].

The IP_Prediction 2D module (version 2019.1.0.1) is used for profile modeling of geophysical potential field parameter distributions. This is based on structural maps of key sedimentary cover interface surfaces, well intersection points with these surfaces, and various machine learning algorithms [5, 6]. To enhance the correlation of complex data, an inversion technique was applied to calculate the contrast of geophysical parameters in the vicinity of the target layer.

In the **IP Seismic** software, the prediction process is carried out in two stages:

1. Training – This stage involves the self-learning of neural networks to determine cluster centers (clusters of points representing classification objects in a multidimensional feature space). It uses paired input data: an attribute of potential geophysical fields and a set of map values within sliding windows for forecasting. During this phase, the optimal neural network coefficients are computed by minimizing the objective function.

2. Calculation – At this stage, the attribute of potential geophysical fields is computed across a given set of maps. The distance of current points (objects) to the nearest cluster centers is determined, and each point is assigned to the corresponding cluster.

The output is the values of standard deviation of maps P10, P50, P90 (pessimistic, probable and optimistic forecasts).

The main advantages of using a nonlinear operator based on a neural network include: 1. Modelling complex nonlinear relationships between different types of data, which facilitates more accurate analysis and prediction. 2. Automatically adapting the model to a variety of input data types and conditions, which improves its efficiency. 3. Automatic tuning of model parameters, which helps in achieving optimal results in inversion and prediction objectives [5, 13].

Thus, the combination of a neural network-based nonlinear operator and an evolutionary algorithm provided an effective tool for simultaneously analyzing multiple variables, interpreting complex geological systems, and optimizing forecasting.

In the computations, Surface and Optional Points attributes were utilized. The Surface attribute specifies the surface with classification attributes, the sliding window size, and the number of classes. The Optional Points attribute defines the points used to identify similar locations based on the features applied to the map [7, 11, 12].

In addition, the study of gravity and magnetic fields was performed in the **GraviMag Modeling Inversion** module integrated into IP Seismic software and designed for solving problems of inversion of gravity and magnetic survey data, combining them with seismic data. Geodensity and geomagnetic models were built in the depth range from 100 to 20 000 metres. The input data for modelling were a digital model of gravity field anomalies in Bouguer reduction and a digital model of magnetic field anomalies [5, 6].

The application of the GraviMag Modeling Inversion module enabled the following: 1. Modeling and interpretation of gravity and magnetic data. 2. Construction of mathematical models for calculating gravity and magnetic fields based on predefined geological structures. 3. Inversion processing using observed data, enhancing the accuracy of determining the depth, shape, and composition of gravity- and magnetically anomalous objects.

3.2. Classification of airborne gamma-ray spectrometry data. In oil and gas exploration, the presence of microscopic hydrocarbon microseepages is considered a direct indicator of hydrocarbon accumulations. According to several studies [15, 16, 19, 21], areas above potentially productive structures are often characterized by a decrease in background gamma radiation, accompanied by the formation of halos with relatively elevated radioactivity. These radiogeochemical anomalies can serve as diagnostic markers for identifying prospective hydrocarbon-bearing zones.

Taking this indicator into account, an integration of GIS technologies [7] with statistical and spatial analysis methods was implemented in the ArcGIS environment (Model Builder), utilizing the IP Seismic platform (SOM_Clustering Seis plug-in module). This approach enabled correlation analysis of AGSS datasets, identification of hidden patterns through clustering, visualization of results in 1D and 2D formats, and substantiation of decisions regarding the localization of prospective hydrocarbon targets.

To account for geomorphological, landscape, and soil factors affecting the distribution of surface radioelement concentrations, the study of the South Ustyurt Region (SUR) employed satellite imagery with a spatial resolution of 25×25 meters, along with topographic maps. The primary source was a 2019 GeoEye satellite image from the Esri database, provided in GeoTIFF format and referenced in the WGS coordinate system

The study utilized digital models of potassium, thorium, and uranium concentrations. A self-organizing map (SOM) was subsequently generated using a neural network-based approach to visualize spatial variations in gamma activity. These results substantially augmented conventional geological and geophysical datasets, significantly improving the depth and accuracy of their interpretation [9, 18, 21].

At the initial stage, the airborne gamma spectrometry survey (AGSS) data were interpreted using thorium normalization in the COSCAD software [4]. Subsequently, digital models of radioelement concentrations were integrated into Model Builder, where cell values were extracted at 500-meter intervals and converted into point features.

Subsequently, a classification map was generated based on cluster analysis, dividing the South Ustyurt Region (SUR) into eight statistically homogeneous classes characterized by distinct combinations of radioactive potassium, uranium, and thorium concentrations (Fig. 3). All classes (0–8) were identified within the studied structural units, with sharp boundaries observed along tectonic faults. These boundaries reflect the block-type heterogeneity of the facies composition of the rocks and variations in radioelement enrichment along tectonic contacts.

The analysis of the spatial distribution of gamma activity classes based on AGSS data (Fig. 3) enabled the differentiation of hydrocarbon prospectivity across key structures of the SUR.

The Central Ustyurt System Dislocation (CUSD), which includes the Karabaur Ridge, the Busagin Depression, the Akmechet structure, and others, is predominantly characterized by the development of Class 1 (57%) and Class 2 (33%) (Table 1), together accounting for 90% of its region. This indicates a generally homogeneous and background level of radioelement enrichment (Table 1). Combined with the intense deformation and tectonic disruption of the Paleozoic and Permo-Triassic formations, the classification

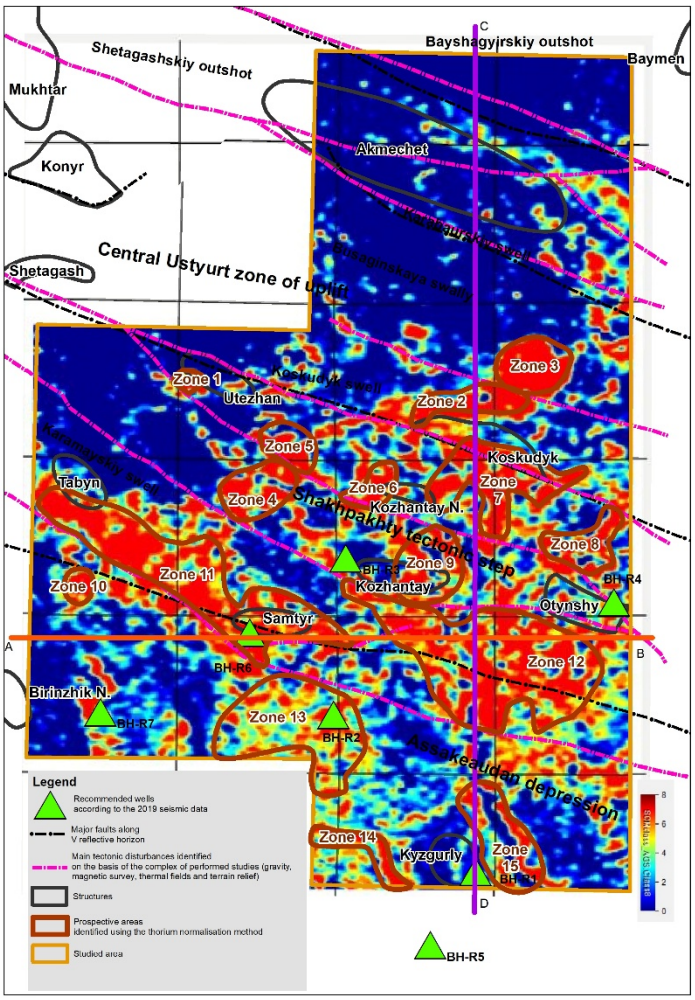

Fig. 3. Distribution of classes based on the content of radioactive elements in the SUR, calculated using the SOM_Clustering module from AGSS data results based on radioactive potassium, uranium, and thorium content suggest that the structures of the CUSD are of low or no hydrocarbon potential.

In the Assakeaudan Depression, classes 5 (32%) and 6 (44%) predominate, reflecting greater spatial differentiation and lower concentrations of radioactive potassium, uranium, and thorium (Table 1). These features, combined with favorable lithofacies, geochemical, and structural characteristics, support the forecast of increased hydrocarbon potential in the Assakeaudan Depression.

In the Shakhpakhty Step, classes 6–7 (35%) and class 8 (47%) dominate, collectively covering 81% of its area (Table 1). The highest-ranking classes were identified in the areas of local structures such as Kozhantay, Otynshy, Koskuduk, and others, indicating their elevated prospectivity for hydrocarbon accumulation (Fig. 3).

The wide range of differentiation of the Shakhpakhty Step in terms of classes of radioactive potassium, uranium, and thorium content reflects the presence of zones with both minimal and maximal concentrations of these elements. The spatial distribution of these classes, taking into account deep-seated faults and the structural-formational composition of the sedimentary cover and

intermediate structural tier, indicates the development of microseepage, migration, and accumulation processes of hydrocarbons within the gas- and oil-prospective local structures of this step [16, 18, 20].

Thus, the integration of AGSS data with spatial analysis and statistical classification techniques has enabled the identification of consistent patterns in the distribution of radioactive elements and their correlation with potentially hydrocarbon-bearing structures situated along inferred migration pathways. Among the studied areas, the Shakhpakhty Step demonstrates the highest exploration potential, whereas the Assakeaudan Depression exhibits less distinct geochemical and structural indicators of hydrocarbon accumulation.

3.3. Classification of Gravity and Magnetic Data. The integration of ArcGIS (Model Builder) with the inversion and predictive modeling software package IP Seismic (SOM_Clustering Seis plug-in) has facilitated the classification of gravity and magnetic datasets, their visualization in both 1D and 2D formats, and the subsequent analysis of their correlation with regional variations in the thickness of the sedimentary cover and the intermediate structural level. This approach enhances the interpretation of geophysical anomalies in relation to subsurface geological architecture.

The CUSD exhibits well-expressed heterogeneity in the vertical gradient of the anomalous gravity field, with classes 7-8 covering approximately 69% of its area. A similar pattern is observed in the distribution of the vertical gradient of the magnetic field, where classes 6-7 are identified across 67% of the domain's territory (see Table 1).

Table 1. Class Values Computed from 2D IP Prediction across Geophysical Survey Types *(percentage of area covered indicated in parentheses)*

Types of geophysical surveys	Airborne gamma spectrometry	Gravimetry	**Magnetometry**	Geothermics	Structural models
Assakeaudan Depression	5 class (32%) 6 class (44%)	1-2 classes (75%)	2 class (34%)	5 class (32%)	4-5 classes (25%)
Shakhpakhty Step	6-7 classes (35%) 8 class (47%)	2 -3 classes (82%)	3-4 classes (47%)	6-7 classes (52%)	5-6 classes – (34%)
Central Ustyurt System Dislocation (CUSD)	1 class (57%) 2 class (33%)	7 class (44%) 8 class (25%)	6-7 classes (67%)	7 class (25%)	7-8 classes – (62%)

The integrated analysis of gravity and magnetic anomalies indicates a well-expressed anisotropy in the section regarding density and geomagnetic properties, reflecting the saturation of the stratigraphic succession with bodies exhibiting gravity and magnetic disturbances [22, 23].

The results of cluster analysis, combined with the high degree of structural disruption and tectonic deformation of the rocks, suggest that the CUSD is a region with low or negligible hydrocarbon potential. This conclusion is further supported by the spatial distribution of radioactive elements, with the majority of the area characterized by minimal concentrations of potassium, uranium, and thorium - classes 1 and 2 account for 90% of the domain's surface.

In contrast to the CUSD, the local structures within the Shakhpakhty Step exhibit geophysical characteristics more conducive to hydrocarbon accumulation. The vertical gradient of the gravity field is dominated by classes 2–3, covering up to 82% of the area, while the magnetic field gradient is primarily represented by classes 3–4, occupying approximately 47% (Table 1). When considered alongside elevated concentrations of radioactive elements, these parameters collectively indicate more favorable geological conditions for the accumulation of hydrocarbons within both the sedimentary cover and the intermediate structural level.

The Assakeaudan Depression is characterized by minimal values of both the vertical gravity gradient (classes 1–2 covering 75% of the area) and the magnetic field gradient (class 2 covering 34% of the area). This is likely attributed to the orthoplatform nature of its thick sedimentary cover, which is marked by more homogeneous lithofacies and other geophysical properties. Additionally, the predominance of lower classes in the distribution of radioactive elements may further indicate the presence of effective reservoir sealing capacities and the absence of microseepage signals typically associated with hydrocarbon migration.

Overall, the analysis of the spatial localization of gravity and magnetic anomalies indicates a consistent decrease in gradients and their cluster classes from south to north - from the tectonically active and geologically and geophysically anomalous CUSD toward the more stable structures of the Shakhpakhty Step and further to the Assakeaudan Depression.

And furthermore, gravimetric and magnetic anomaly-generating features are most prominently expressed within the CUSD, become less contrasted in the Shakhpakhty Step, and are weakly developed in the Assakeaudan Depression. This gradation reflects the degree of structural, density, and other types of differentiation within the sedimentary cover, as well as its hydrocarbon prospectivity.

The identified geological phenomenon represents a transition from intensely deformed fold structures to an orthoplatform-type sedimentary cover characterized by decreasing levels of dislocation and structural contrast. This transition correlates clearly with the tectonic framework of the SUR. Similar cases have been discussed in [29, 31, 32], supporting the observations made in this study.

Analysis of classification data obtained from AGSS, gravimetric, and magnetic surveys reveals a stable inverse correlation: higher classes of vertical gradients in gravity and magnetic fields correspond to lower classes in the distribution of radioactive elements, and vice versa. This relationship may serve as an informative indicator of hydrocarbon potential - elevated concentrations of radioactive elements are associated with diminished gravimetric and magnetic anomalies, which may reflect the presence of sealing reservoirs and the absence of deep-seated density and magnetic contrasts.

3.4. Classification of Infrared Survey Data. The integration of neural networks with subsequent clustering of infrared data using the SOM_Clustering module in IP Seismic enabled the development of 1D and 2D classification models based on the local component of the thermal field, aimed at predicting hydrocarbon potential across the SUR. These results have substantially augmented the conventional set of geological and geophysical data, including the work of Petrovsky V.B. (2019).

In the CUSD, only 25% of the area could be confidently classified, primarily falling into Class 7. This classification indicates a high level of endogenous geodynamic activity, an unstable thermobaric regime, and intense tectonic deformation (see Table 1). Such conditions are typically unfavorable for the generation and accumulation of hydrocarbons. An additional risk factor is the increased rock density and magnetization, which are often indicative of crystalline and metamorphic basement lithologies.

In the Assakeaudan Depression, 32% of the area was classified as Class 5, while on the Shakhpakhty Step, 52% of the territory fell within Classes 6–7 (Table 1). These results point to comparatively more stable thermal conditions across both zones, which are conducive to the generation, migration, and long-term preservation of hydrocarbon systems. The higher classification percentages, particularly in the Shakhpakhty Step, suggest favorable geothermal regimes that enhance the prospectivity of these structures for hydrocarbon accumulation.

Significant correlation patterns have been established:

- In the Shakhpakhty Step and Assakeaudan Depression, direct correlations are observed between geothermal and radioactive anomalies, while inverse correlations are noted with gravity and magnetic anomalies.
- Conversely, within the CUSD, geothermal and radioactive anomalies exhibit inverse relationships, and positive correlations are observed with gravity and magnetic field anomalies.

Of particular importance are the localized geothermal anomalies identified within the Shakhpakhty Step, which extend into adjacent areas of Uzbekistan. In similar structural and geological settings, Jurassic-aged gas fields such as Shakhpakhty and Dzhel have been discovered and developed. This cross-border geothermal continuity strongly supports the hydrocarbon prospectivity of the Shakhpakhty Step and underscores its high potential for further exploration efforts within the SUR.

3.5. Classification of Structural Model Data. As part of the study of the SUR, structural models were classified using artificial intelligence techniques, followed by a comprehensive analysis of their correlations with gravimetric, magnetic, geothermal, and surface radioactive element distribution data. The results were visualized in both 1D and 2D formats and employed to assess the hydrocarbon prospectivity of local structural features.

Comparable cases have been examined in studies [6, 7], confirming the relevance and practical applicability of an integrated approach combining geophysical data with artificial intelligence methods.

The foundation for this analysis consisted of structural maps based on reflective seismic horizons compiled from the works of Ibragimov A.A. et al. (2019), Akchulakov A. et al. (2011), and Godin Yu.N. & Tal-Virsky B.B. (1969). These included:

– Horizon III: boundary between the Lower Cretaceous and the top of the Upper Jurassic;

– Horizon V: base of the Jurassic / top of the Permian or Triassic;

– Horizon "b": base of the Upper Permian / top of the Upper Paleozoic carbonate–terrigenous sequence.

These maps were digitized using Surfer and ArcGIS software [7, 13]. Loading the data into the *SOM_Clustering 2D* module enabled the construction of a multilayered structural model of the SUR, reflecting key tectonic and lithological features. This integrative model provides a valuable tool for forecasting hydrocarbon-bearing zones and significantly enhances the geoscientific basis for exploration targeting in the region.

Analysis of classifications derived from structural horizons maps using artificial intelligence techniques has revealed well-expressed differences in the geological architecture of the key tectonic units within the SUR.

The CUSD is dominated by high classification levels (Classes 7–8), covering up to 62% of its total area (Table 1). This predominance reflects a high degree of tectonic dislocation and fragmentation, strongly associated with metamorphic overprinting and a widespread presence of intrusive and effusive igneous bodies. These characteristics, when coupled with the unfavorable distribution of radioactive elements at the surface, indicate minimal or absent hydrocarbon accumulation potential in this domain.

In contrast, the Shakhpakhty Step exhibits a notable decrease in classification levels, primarily within Classes 5-6, which account for up to 34% of the area (Table 1). This suggests a moderate degree of deformation and a more coherent structural expression of the seismic reflectors. When considered alongside favorable lithofacies assemblages, geochemical signatures, paleogeographic evolution, and thermobaric conditions, the Shakhpakhty Step demonstrates a significantly enhanced potential for hydrocarbon entrapment. Prospective targets include both the sedimentary cover and the underlying Indermediate Structural Level, affirming the region’s importance for further exploration.

The Assakeaudan Depression is characterized by predominantly low prospectivity classes (4–5), occupying about 25% of its area, primarily along the northern flank. This structural configuration indicates limited development of local traps; however, the potential presence of hydrocarbon accumulations within the sedimentary cover cannot be excluded, especially if additional favorable geological conditions are present.

The analysis of structural model classification results (Table 1) reveals a direct correlation with geothermal anomalies and the distribution of radioactive elements, and an inverse correlation with gravity and magnetic anomalies for both the Assakeaudan Depression and the Shakhpakhty Step.

In contrast, the CUSD exhibits a strong correlation between high structural differentiation classes and gravity, magnetic, and geothermal anomalies, accompanied by an inverse relationship

with the distribution of radioactive elements. These patterns underscore the subdued tectonic expression of the Assakeaudan Depression, while highlighting the CUSD as the most structurally complex zone in the region.

The findings provide important predictive insights for refining the geological framework of the South Ustyurt Region and for evaluating the hydrocarbon potential of the studied structures.

4. Research finding

4.1. Airborne Gamma-Ray Spectrometry. Analysis of AGS data using thorium normalization enabled effective suppression of regional background levels and enhanced the identification of local variations in the distribution of radioactive elements. The normalized data revealed a marked decrease in potassium concentrations and a relative increase in uranium, which is attributed to lithological control and may serve as a diagnostic indicator in the interpretation of geophysical anomalies, as demonstrated in studies [16, 17, 20].

Using GIS technologies (ArcGIS) and the SOM_Clustering module of the IP_Seismic software suite, 15 areas with reduced radioactivity background were identified in the South Ustyurt Region. These areas are characterized by low concentrations of potassium, uranium, and thorium.

To assess the spatial distribution of radioactive elements, orthogonal profiles A–B and C–D were generated using the IP_Prediction 2D module (Figures 8 and 9). These profiles clearly delineate the Shakhpakhty Step by zones of decreased concentrations of radioactive elements. When integrated with geothermal and seismic data, this pattern indicates potentially favorable conditions for hydrocarbon accumulation.

In contrast, the CUSD is characterized by background concentrations of radioactive potassium, uranium, and thorium, which likely reflect its elevated tectonic activity and the advanced metamorphic grade of its basement rocks.

The Assakeaudan Depression is characterized by an elevated background of radiogeochemical anomalies, which show a correlation with the complex structural architecture of its northern board.

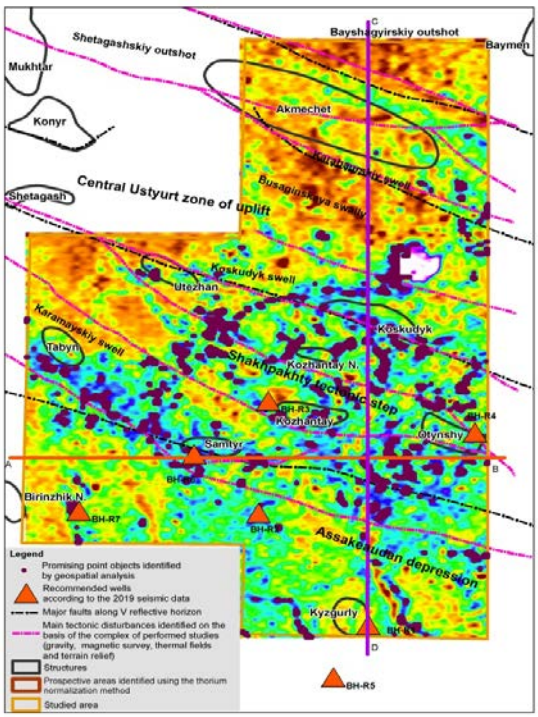

Fig. 6. Location of prospective point targets identified by airborne gamma spectrometry and layout of survey profiles (plan view).

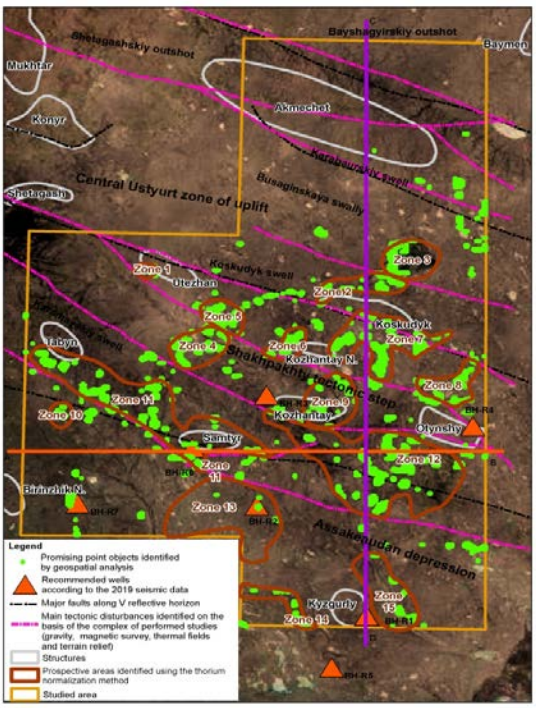

Fig. 7. Distribution of prospective point anomalies from airborne gamma spectrometry overlaid on satellite imagery.

Importantly, the identified radioactive anomalies generally do not coincide with local structural features interpreted from MOGT-2D seismic data and previously targeted by exploration drilling. This misalignment may point to the presence of non-structural hydrocarbon traps or suggest that the placement of certain exploration wells may have been suboptimal.

The analysis of the spatial distribution of radioactive elements (K, Th, U) revealed that zones of anomalously low concentrations are associated with deep fault systems as supported by the findings in [19, 21]. This observation suggests that these structures may have acted as conduits for vertical hydrocarbon migration, subsequently leading to the saturation of overlying reservoir formations. This interpretation is supported by the radiogeochemical data presented in Figures 8 and 9.

Figure 8. Graph illustrating the distribution of radioactive potassium (purple), thorium (red), and uranium (green) concentrations along profile A–B

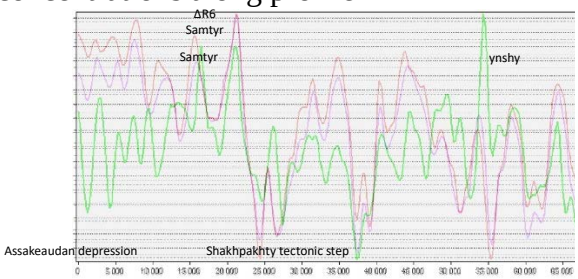

Figure 9. Graph illustrating the distribution of radioactive potassium (purple), thorium (red), and uranium (green) concentrations along profile C–D

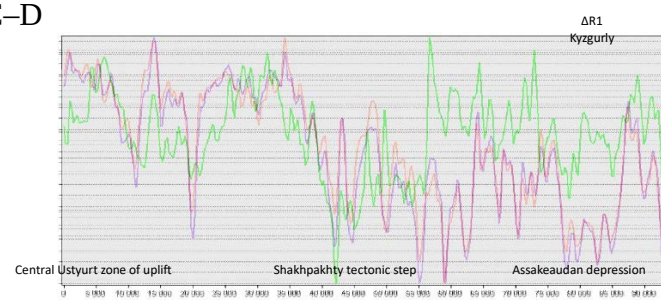

The observed pattern of radiogeochemical anomalies underscores the applicability of AGSS for direct hydrocarbon prospecting. Exploration efforts should prioritize areas exhibiting low background levels of total radioactivity, as well as localized anomalies spatially associated with tectonic faults.

These findings establish a reliable geophysical basis for defining and justifying targets for exploration and seismic surveys, thereby enhancing the focus, efficiency, and effectiveness of subsequent subsurface investigations.

4.2. Thermal Field. The processing of infrared survey data using thermal field separation methodologies [36, 39] facilitated the development of digital models representing the spatial distribution of heat flow density throughout the South Ustyurt Region (SUR).

Analysis of the regional thermal component identified linear anomalies interpreted as deep-seated fault systems. The local thermal component revealed a consistent spatial correlation between positive geothermal anomalies and Jurassic stratigraphic units, previously delineated based on MCDP-2D seismic data.

Geothermal modeling results obtained using the IP_Prediction 2D module along profiles A–B and C–D confirm that the major tectonic features of the region possess distinctive geothermal signatures. The Assakeaudan Depression is distinguished by an extensive zone of suppressed geothermal anomalies extending to depths of approximately 5 km, punctuated by localized maxima at shallower depths of up to 2 km [37] This distribution indicates the presence of a substantial sedimentary succession characterized by low thermal conductivity and a high proportion of potentially oil-prone source formations.

The fault systems transecting the depression likely serve as pathways for deep heat and mass transfer, as well as vertical hydrocarbon migration [33, 34, 35, 38]. The established correlation between geothermal lows, deep basement configurations, and thick sedimentary cover likely reflects the structural inheritance of elements from a Paleozoic rift system.

Figure 10. Plot of the thermal field (purple), extrapolated into the lower half-space. Cross-sections along profile A–B are

Figure 11. Plot of the thermal field (purple), extrapolated into the lower half-space. Cross-sections along profile A–B are shown at depths of 1,500 m (pink) and 2,500 m (blue).

ΔR6
Samtyr

ΔR1
Kyzgurly

shown at depths of 1,500 m (pink) and 2,500 m (blue).

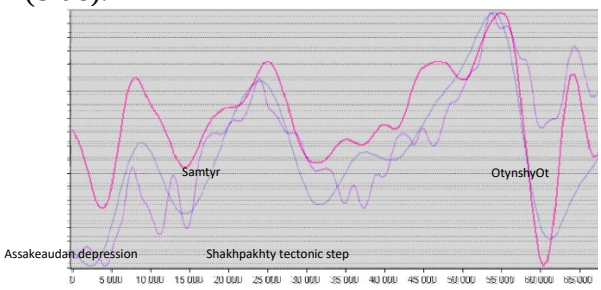

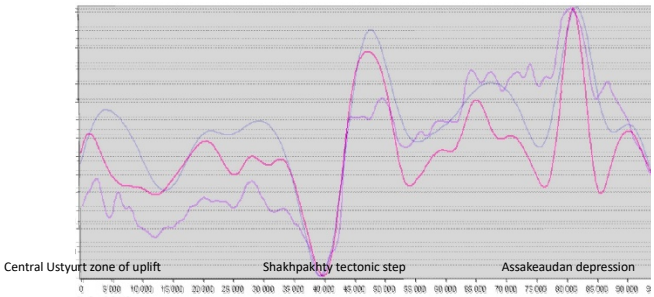

Interpretation of thermal field data at subsurface depths of 1,500 and 2,500 meters has identified the Shakhpakhty Step, distinguished by persistent positive geothermal anomalies. These anomalies indicate the presence of rocks with elevated thermophysical properties (Figures 10 and 11).

The step is morphologically confined by a system of deep-rooted faults, delineated based on gradient anomalies in regional geophysical fields. Three major fault zones extend in a northwestern direction. Along the southeastern flank of these structures are the discovered Shakhpakhty and Zhel gas fields [4, 33], while to the west, several prospective local structures have been identified, including Otynshy, Kozhantay, North Kozhantay, Utezhan, and others.

The identified local structures are regarded as potential traps for hydrocarbon accumulations, provided an effective seal is present. Based on these considerations, geothermal and structural criteria support prioritizing the Shakhpakhty Step for geological exploration.

Thermal field anomalies show a strong correlation with airborne gamma-ray spectrometry (AGRS) data interpreted using thorium normalization. The observed increase in heat flow amplitude with depth may indicate a block-faulted structural framework and contrasting thermophysical properties within deformed zones. A similar judgment can be found in the publication [35].

In the zones of deep faults, high vertical and horizontal gradients of the thermal field and local minima of heat flow are observed. This is interpreted as a result of the abrupt change in thermophysical properties and the functioning of these faults as channels for deep heat and mass transfer. The faults are predominantly oriented in a northwest direction, although submeridional elements are also identified.

A geothermal phenomenon has been identified on a cross-section through the Shakhpakhty gas field (Uzbekistan), manifested as a relative heat flow minimum at depths of up to 3,000 m, complicated by two positive anomalies at depths of 2,200–2,500 m [33]. According to the literature [36, 37], such geothermal signatures are characteristic of major gas accumulations and may be associated with the presence of compacted cap rocks. Nevertheless, the interpretation of these anomalies requires additional integrated analysis using high-resolution gravity surveys, seismic data, and drilling information.

The CUSD is characterized by distinct minima in heat flow density at depths of approximately 1,500 and 2,500 meters, as revealed by heat flow mapping and the results of regional and local geothermal transform analysis. These low heat flow areas likely reflect a combination of geological and thermophysical factors. In particular, they may indicate the presence of thick, low-conductivity rock sequences that inhibit upward heat transfer.

The spatial correlation of these heat flow minima with structural features such as deep-seated faults and flexural zones further suggests that they may represent areas of restricted vertical migration of fluids and heat. These features underscore the importance of the thermal field as a valuable exploration criterion for predicting hydrocarbon saturation in the SUR.

4.3. Gravitational and magnetic fields. The inversion of gravity and magnetic data was based on forward modeling equations in the frequency–wavenumber domain developed by R.L. Parker (1973), as well as an optimization technique introduced by A.I.Kobrunov (1981). These methodologies underpin the **GraviMag Modeling Inversion** module, which is integrated into the **IP_Prediction 2D** software package [5].

Using this module, profiles A–B and C–D were generated to model the distribution of gravity and magnetic anomalies across the SUR. The results clearly demonstrate a marked geophysical differentiation between the Shakhpakhty tectonic step, the Assakeaudan Depression, and the CUSD), as evidenced by the distinct patterns and intensities of gravity and magnetic anomalies (see Figures 10 and 11).

Analysis of deep slices at levels of 5, 10, and 20 km revealed a consistent trend of increasing size of gravity and magnetic anomalies with depth, accompanied by a decrease in their spatial concentration. This effect is interpreted as reflecting the consolidation and coalescence of anomalously dense and/or magnetized bodies within the deeper layers of the lithosphere [24].

Numerical values of density and geomagnetic parameters for the main tectonic elements of the SUR at various depths are presented in Table 2.

Table 2. Statistical summary of geodensity and geomagnetic models' parameters along profiles A-B and C-D

Potential fields data	Depth	Profile A-B		Profile C-D		
		Assakeaudan depression	Shakhpakhty step	Central Ustyurt System Dislocation	Shakhpakh-ty Step	Assakeaudan Depressi-on
Geodensity model, mGal	0-5 km	**Up to 1 km:** heterogeneous surface, values range from -25 to 60 **From 1 km to 3 km:** values range from -10 to 40 **Below 3 km:** values range from -10 to 30	from -30 to 50	from -70 to 70	from-30 to 30	from -40 до 40
	5-10 km	from -30 to 30	from -20 to 30	from -60 to 60	up to -20	from -20 to 10
	10-20 km	Down to a depth of -13 km: from -30 to 15 From -13 to -20 km depth: from 0 to -40	from -20 to 10	from -50 to 20	from -30 to 0	from -20 to 10
Geomagnetic model, nT	5 km	Down to a depth of -2.3 km: from -50 to 80 Below -2.3 km: up to -50	Down to a depth of -3.5 km: from -50 to 50 Below -3.5 km: from -50 to 100	from -200 to 200	from -80 to 80	from -80 to 100
	10 km	from -50 to 50	from 20 дто120	from -80 to 80	from -130 to -20	from -100 to 100

	20 km	Up to 120	from -100 to 100	from -120 to 100	from -200 to -80	from -20 to 100

To enhance the reliability of geological interpretation, the vertical distribution of geodensity and geomagnetic heterogeneities was correlated with the positions of key seismic reflecting horizons: III, V, and “b” (see Figures 10 and 11).

The Shakhpakhty tectonic step is distinguished by an alternation of local positive and negative Bouguer gravity anomalies of moderate to low intensity (reduced to an elevation of 2.5 km). In our previous studies, it was established that this zone is characterized by low values of horizontal gradient transforms and elevated values of the vertical gradient of the Bouguer gravity field, which indicates the presence of significant density contrasts at depth [23, 28].

The Assakeaudan Depression is characterized by a relatively homogeneous geological structure, as reflected in the low gradients of both gravity and magnetic fields. This uniformity likely indicates the predominance of sedimentary sequences with minimal density and magnetization contrasts. Accordingly, the region exhibits predominantly local negative gravity anomalies with low horizontal and vertical gradients.

In contrast, the CUSD exhibits elevated values of local gravity anomalies and intermediate values of horizontal and vertical gradient transforms [23], indicating a complex combination of structures with varying densities and tectonic origins.

The density heterogeneity of the subsurface down to depths of 8 km is supported by the distribution of Euler solutions derived from gravity data using Geosoft Oasis Montaj™ software [29].

In the CUSD, gravity-disturbing bodies predominantly exhibit a northwest trend; in the northern part of the Shakhpakhty Step, their orientation shifts to northeast, while in the southern part of the step and within the Assakeaudan Depression, they display northwest to submeridional trends. These structural patterns are corroborated by the distribution of anisotropic transform values [23].

The CUSD is marked by elevated local gravity anomalies combined with intermediate vertical gravity gradient values, reflecting the superposition of geologic structures with contrasting densities and tectonic origins, including both thrust-related and block-fault systems.

The density heterogeneity of rocks down to depths of 8 km is confirmed by the distribution of Euler’s special points in the gravitational field, calculated using **Geosoft Oasis Montaj™ software [41].** In the northern part of the Shakhpakhtinsky step, gravity-disturbing objects exhibit a northeastern trend; within the CUSD - a northwestern trend; and in the southern part of the step and the Assakeaudan Depression - both northwestern and sub-meridional orientations. **This is confirmed by the spatial distribution of anisotropic transformant values [23].**

In the CUSD, these objects are characterized by a northwestern orientation. In the southern part of this tectonic step and in the Assakeaudan Depression, they are oriented northwestward and sub-meridionally, **which is also supported by the distribution of anisotropic transformant values.**

The Assakeaudan trough is characterized by a relatively homogeneous geological structure, which is reflected in the reduced gradients of both the gravimetric and magnetic fields. Such homogeneity may indicate the predominance of sedimentary cover layers that are weakly differentiated in density and magnetization [22, 23].

In the Assakeaudan Depression, gravity anomaly interpretation has revealed zones of increased Euler solution concentration aligned with the stratigraphic boundary between Upper Jurassic and Lower Cretaceous sediments. This clustering is likely attributed to lithological contrasts between the weakly consolidated Cretaceous and the denser Jurassic formations, as well as the presence of concealed tectonic faults.

Interpretation of gravity anomalies revealed zones of increased concentration of Euler points, confined to the stratigraphic contact between Upper Jurassic and Lower Cretaceous deposits. The concentration of points in this area is probably due to both lithological contrasts between poorly consolidated Cretaceous and denser Jurassic rocks, and the presence of hidden tectonic faults.

The highest density of Euler solutions corresponding to the boundaries of gravity-anomalous bodies is observed at depths of 1000–2000 m. Within this interval, MCDP-2D seismic data delineate

the reflective horizon III, whose geophysical properties and spatial correlation with anomalies in potential fields suggest it may play a key role in controlling fluid migration and the formation of hydrocarbon traps [23].

It is noteworthy that at depths exceeding 8–10 km, the density structure of the Shakhpakhty Step exhibits characteristics similar to those of the Assakeaudan Depression: in both cases, gravity anomaly values range from –5 to –30 mGal (see Table 2).

The CUSD is characterized by increased values of local gravity anomalies in combination with intermediate values of gravity gradients, which reflects the superposition of geological structures of different densities and tectonic nature, including both thrust and block-fault elements.

In the Assakeaudan Depression, the upper boundary of magnetically anomalous bodies descends to depths of 8–10 km, corresponding to the top of basement as identified by MCDP-2D seismic data. This depth level likely reflects the occurrence of mafic and ultramafic rock assemblages within the basement composition [22].

In the Shakhpakhty Step, the upper boundary of magnetically anomalous bodies is traced at depths of 8–12 km, while gravity-anomalous masses are primarily concentrated within the 6–7 km range. This vertical separation reflects the presence of two structural levels — a fragmented crystalline basement and an intermediate structural level. Beyond depths of 12 km, a well-expressed decrease in the variability of Euler depth solutions is observed, suggesting a relatively homogeneous geological structure in the deeper horizons.

The magnetic field over the Shakhpakhty Step is characterized by reduced magnetization values at depths of 6–20 km, in marked contrast to the higher magnetic anomalies observed in the adjacent Assakeaudan Depression. This contrast likely reflects differences in the petrological composition and magnetic properties of the basement rocks, possibly due to a higher concentration of mafic and ultramafic lithologies within the depression [22].

Of particular scientific interest is the persistent deepening of the magnetically active layer beneath the Shakhpakhty Step, which highlights the distinct tectonic architecture of the region. This geophysical configuration - manifested by deep gravity and magnetic anomalies and a well-defined stratification of tectonic levels - suggests favorable geological conditions for the development of hydrocarbon traps, both within the sedimentary cover and the intermediate structural level. Together, these features underscore the elevated petroleum potential of the Shakhpakhty Step.

Against this background, an integrated analysis of gravity and magnetic anomalies has confirmed the consistency between basement depths interpreted from potential field data and the crystalline basement surface delineated by MCDP-2D seismic surveys. This correlation significantly enhances the reliability of the geological interpretation and indicates that the observed anomalies are tectonically controlled, associated with heterogeneities in the composition and structure of the basement rocks.

One of the most important geological phenomena is the contact zone of the CUSD and the Shakhpakhtinskaya step, revealed in the process of interpreting geophysical data. Here, along the meridional profile, a thrust of decompressed rocks of the Shakhpakhtinskaya step onto the compacted complexes of the CUSD with an angle of 50–70° and an established depth of up to 8–10 km is recorded, which indicates large-scale nappe-thrust processes [22, 23].

The results of the analysis of the transforms of gravity-magnetic fields confirm the presence of deep tectonic activity. Thus, in the area of the Karabaur swell, an area of concentration of Euler points was identified, interpreted as a manifestation of the effect of a "double" crust caused by its submersion under the South Ustyurt region. These findings are consistent with the results of our previous works (2022).

Within the CUSD, localized gravity anomalies with intermediate gradient values are observed, reflecting a combination of different structural types, including both thrust-related and fault-block features. Notably, there is a spatial correlation between the depths of gravity and magnetic anomaly sources, indicating their association with the surface of the crystalline basement. The position of this basement surface was determined based on data from MCDP-2D.

In the area of the Karabaur Ridge, a concentration zone of Euler solutions has been detected, interpreted as evidence of a "double crust" effect resulting from underthrusting beneath the South Ustyurt massif. This interpretation is consistent with the results of our earlier studies [5, 6, 8].

Furthermore, magnetic field transformant analysis within the CUSD revealed two distinct depth intervals of magnetically active bodies: 4,000-6,000 m and 10,000-12,000 m. These reflect vertical structural segmentation associated with thrust and overthrust deformation.

Fig. 10.1. Profile geodensity, geomagnetic and thermal models along A-B combined with the relief of OG up to 5 km	Figure 11.1. Profile geodensity, geomagnetic and thermal models along C-D combined with the OG plot up to 5 km
Geodensity model 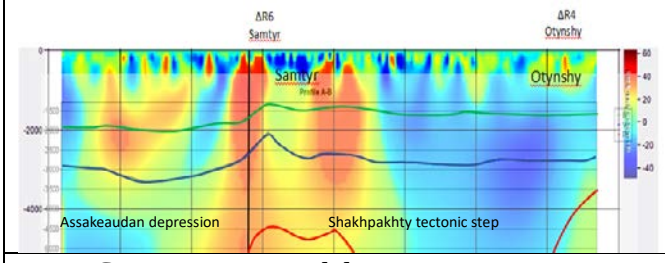	Geodensity model 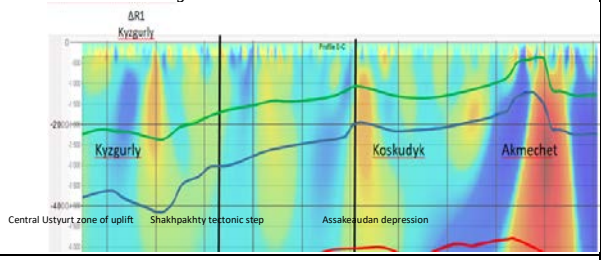
Geomagnetic model 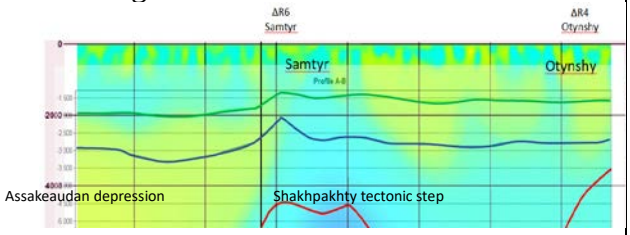	Geomagnetic model 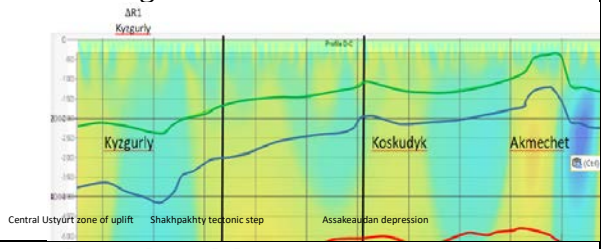
Thermal model 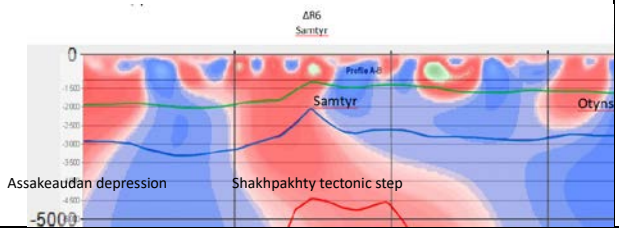	Thermal model 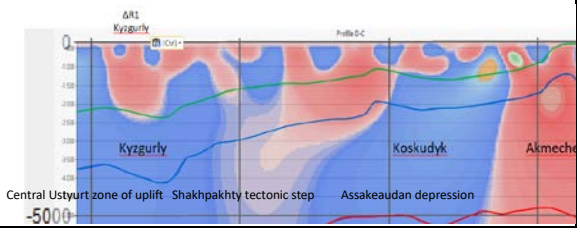

Fig. 10.2. Profile geodensity, geomagnetic and thermal models along A-B combined with the relief of OG up to 10 km	Figure 11.2. Profile geodensity, geomagnetic and thermal models along C-D combined with the OG plot up to 10 km	Fig. 10.3. Profile geodensity, geomagnetic and thermal models along A-B combined with the relief of OG up to 20 km

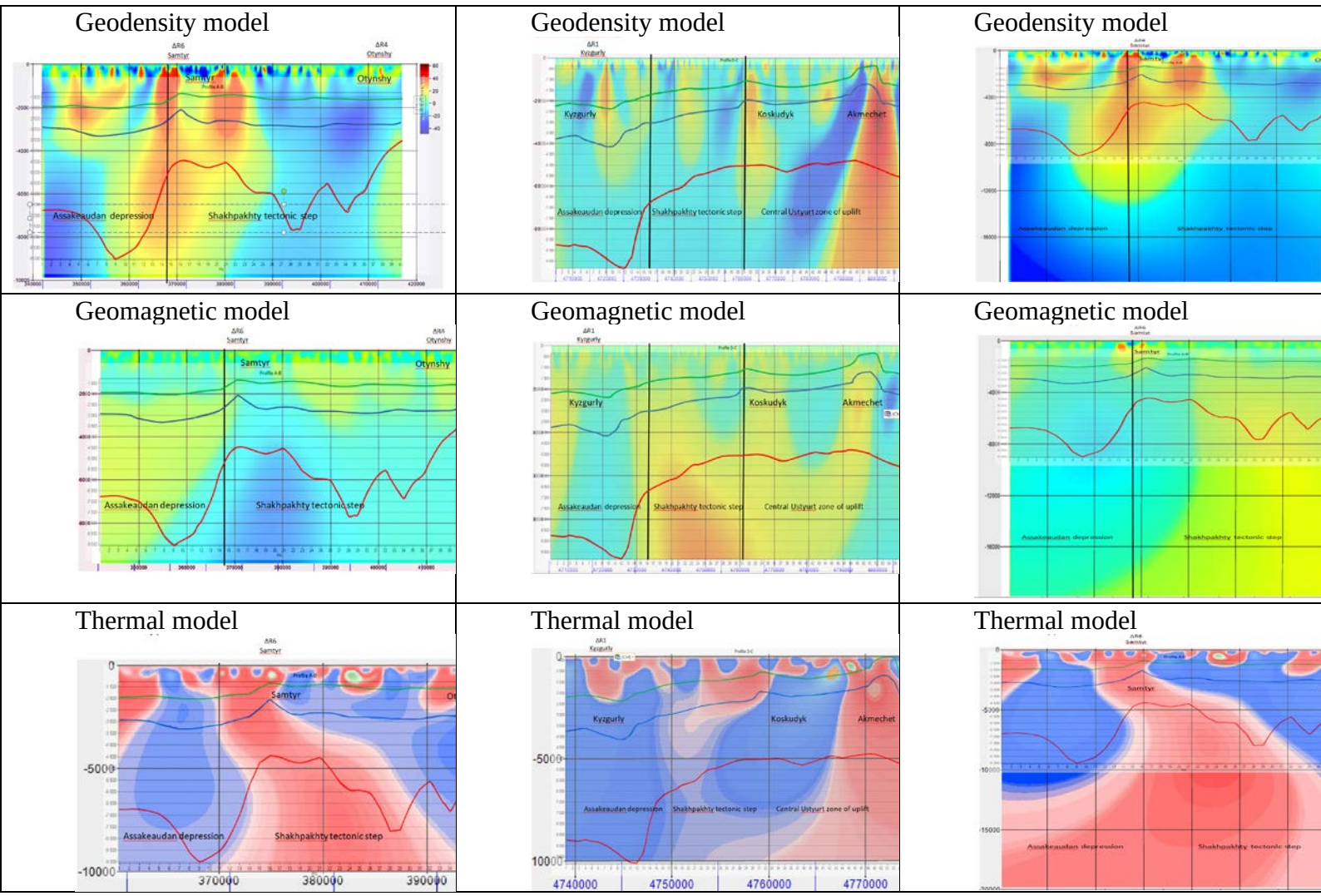

The spatial correlation between the sources of gravity and magnetic anomalies within the CUSD confirms their association with the crystalline basement top. The spatial coincidence of the depths of gravity and magnetically disturbing bodies in the CUSD confirms their confinement to the basement surface [22, 23].

The integrated interpretation of gravity, magnetic, and seismic data indicates that the Shakhpakhty Step holds high hydrocarbon potential. A key factor contributing to this prospectivity is the substantial cumulative thickness of the sedimentary cover and the intermediate structural tier. These geological conditions favor the development of high-capacity reservoirs and various types of traps, as well as the presence of effective seals with good insulating properties.

Consequently, the combination of critical factors - marked structural differentiation, deep subsidence of tectonic elements, the presence of a thick sedimentary succession, and the correlation of geophysical anomalies with seismic reflectors - justifies classifying the Shakhpakhty Step as a priority target for future hydrocarbon exploration and appraisal activities. The obtained data reveal additional opportunities for exploration and emphasize the necessity of continued investigation to refine the geological structure and improve the prediction of potential hydrocarbon accumulations.

This conclusion is supported by AGSS data, processed and interpreted using the thorium normalization method within the COSCAD software. The results substantiate the rationale for continuing integrated investigations in the Shakhpakhty Step. Similar conclusions were drawn based on the results of high-precision magnetic and radiometric surveys conducted in Western Canada [32].

An integrated interpretation of gravity and magnetic field transformants has significantly enhanced the understanding of the structural framework of the South Ustyurt region, enabling the identification of several local zones with high hydrocarbon potential. The effectiveness of

transformant analysis has been confirmed through the detection of previously unrecognized tectonic features and anomalies associated with potential hydrocarbon traps, thereby increasing the reliability of geophysical interpretation [31, 32].

A key result of the study is the recognition of a systematic deepening of the magnetically active layer within the Shakhpakhty Step, accompanied by reduced magnetization relative to the neighboring Assakeaudan Depression. This contrast highlights the differing geological compositions of these zones and points to favorable conditions for hydrocarbon accumulation within the Shakhpakhty Step.

In addition, the deep burial of the magnetically active layer, coupled with elevated thermal gradients, indicates the presence of deep thermal and fluid migration processes - favorable conditions often associated with hydrocarbon generation. These conclusions are further supported by thorium-normalized airborne gamma spectrometry data and thermogradient analysis.

Overall, the integration of geophysical and radiogeochemical patterns - together with the region's complex stratigraphic architecture, tectonic block segmentation, structural heterogeneity, and lithofacies variability - strongly supports the high hydrocarbon potential of the Shakhpakhty Step. These findings form a solid scientific foundation for the targeted planning of future geological exploration efforts in the South Ustyurt region.

4.4. Applied aspects of regional geophysical field modeling. Along profiles A-B and C-D (Figs. 10–11), constructed based on gravity, magnetic, and thermal data, a comprehensive interpretation of the deep structure of the SUR was carried out using the **GraviMag Modeling Inversion** module of the *IP_Seismic* software package. The obtained results were correlated with outputs from automatic classification and predictive modeling conducted using *IP_Prediction 2D*, which significantly enhanced the reliability of the geophysical interpretation and refined the assessment of hydrocarbon potential across the SUR.

The results confirm the presence of major tectonic elements in the region, including the Assakeaudan Depression, the Shakhpakhty Step, and the Central Ustyurt Structural Domain (CUSD). Within these zones, several local structures—such as Samtyr, Otynshy, Kyzgyrly, Koskudyk, and Akmechet - have been identified, showing the highest contrasts in geophysical anomalies within the upper 5 km of the sedimentary cover and intermediate structural level.

Along the sublatitudinal profile A–B, the Samtyr structure is characterized by prominent positive gravity (+60 mGal) and magnetic (+150 nT) anomalies, reflecting the presence of a high-density, magnetically susceptible block extending to depths exceeding 12 km. The combination of elevated rock densities, well-developed faulting, and increased magnetic susceptibility - affecting both the lower horizons of the sedimentary cover and the intermediate structural level-suggests the presence of compacted lithologies with poor reservoir potential. Consequently, despite the presence of a favorable structural high, the Samtyr high is considered to have low prospectivity for oil and gas exploration.

Along the meridional profile C–D, the local structural highs of Akmechet, Kyzgurlu, and Koskudyk are clearly delineated, along with a well-expressed boundary separating the Shakhpakhty Step from the Central Ustyurt Depression. This boundary is expressed as a regionally significant gravity step and is interpreted as a deep-seated fault zone or a major overthrust (sharyazh) structure.

Within the Shakhpakhty Step, consistently negative magnetic field values - reaching as low as –150 nT from depths of approximately 2.5 km - indicate the presence of lithologies with low magnetic susceptibility. This geophysical signature is characteristic of rock types depleted in ferromagnetic minerals, such as clay-rich, siliceous, and carbonate formations.

The observed magnetic attenuation may also reflect diagenetic or hydrothermal alteration processes, during which primary magnetically active minerals are replaced by non-magnetic phases. These petrophysical characteristics, although indirect, serve as important indicators of potential reservoir development and support a favorable assessment of the Shakhpakhty Step within the regional hydrocarbon prospectivity framework.

The results of thermal modeling indicate the presence of abnormally high geothermal activity at depths of 12–20 km within the Shakhpakhty Step and along the northern margin of the Assakeaudan

Depression. These thermal anomalies may reflect deep-seated heat-generating processes and/or zones of thermal fluid discharge, potentially contributing to the formation of conditions favorable for hydrocarbon generation and migration.

Localized anomalies of elevated heat flow have been identified within the CUSD, likely associated with the reactivation of deep-seated faults, including thrust zones. The spatial correspondence between these thermal anomalies and major tectonic features suggests the operation of heat and mass transfer channels facilitating the upward migration of deep-sourced thermal fluids.

The integration of gravity, magnetic, and geothermal models has revealed a block-type heterogeneity in the Earth's crust of the CUSD, alongside the relative tectonic stability of the Shakhpakhty Step and the Assakeaudan Depression.

Regional gravity and magnetic anomalies clearly define the boundaries of the Shakhpakhty Step, which extends southward into Uzbekistan, where analogous Jurassic formations host the Shakhpakhty and Djel gas fields.

Modeling using the **IP_Prediction 2D** technology has confirmed the prospectivity of several local structures within the Shakhpakhty Step, which are recommended as priority targets for further exploration and appraisal activities.

5. Discussion

5.1. Artificial Intelligence and Machine Learning. A comprehensive evaluation of the hydrocarbon potential of the SUR, based on the integration of drilling data, seismic surveys, gravity and magnetic exploration, airborne gamma spectrometry, and geothermal studies, combined with advanced digital techniques, enabled a refined understanding of the geological structure and the identification of prospective hydrocarbon accumulation zones.

The application of machine learning algorithms, including Kohonen self-organizing maps and neural network-based modules (SOM_Clustering Seis, IP_Prediction, IP Seismic), facilitated the detection of hidden geological patterns and provided spatial differentiation of potentially productive areas [5, 6, 12].

The application of advanced inversion technologies, including the specialized **GraviMag Modeling Inversion** module, played a crucial role in enhancing the integrative interpretation of heterogeneous geoscientific datasets - gravity, magnetic, seismic, and geothermal. These methods significantly improved the correlation between diverse data sources and enabled more accurate modeling of the deep structure of the sedimentary cover, including the reconstruction of the geometry and depth of potential hydrocarbon traps.

The use of neural network operators added further analytical depth by effectively handling high-dimensional, nonlinear relationships between geophysical parameters. This not only improved the reliability of the resulting models but also helped uncover hidden patterns in the distribution of anomalous features [8-10, 13, 14].

Of particular importance was the integrated analysis of inversion results, geothermal anomalies, and radiogeochemical data, which made it possible to localize zones of active fluid mobility. These zones are likely associated with deep-seated tectono-magmatic conduits that may serve as migration pathways for hydrocarbons. Altogether, this approach provides a robust basis for identifying high-potential targets for subsequent exploration and drilling.

The supplementary analysis of thermogeophysical and radiogeochemical anomalies uncovered robust indicators of active fluid migration linked to hydrocarbon transport [19, 35]. The integrated application of these methodologies enabled a precise and well-substantiated forecast of prospective hydrocarbon-bearing zones, thereby establishing a strong scientific framework to guide the optimization and improve the effectiveness of exploration efforts in the SUR.

5.2. Airborne Gamma Spectrometry. An analysis of normalized radioelement fields, conducted using ArcGIS and IP_Seismic (SOM_Clustering), revealed 15 areas with decreased concentrations of potassium (K), uranium (U), and thorium (Th), predominantly localized within the Shakhpakhty Step.

These anomalously low concentrations consistently correlate with zones of deep-seated faulting, likely reflecting the upward migration of deep fluids, including hydrocarbons, which facilitate the removal or redistribution of radionuclides. This interpretation aligns with the findings of previous studies [15, 18], which describe radiogeochemical transformation processes induced by the presence of hydrocarbon-bearing fluids.

Profile-based modeling has confirmed the regular spatial distribution of radioactive elements and the presence of well-expressed negative anomalies over the Shakhpakhty Step, supporting its interpretation as a territory with potential hydrocarbon accumulations. The diagnostic significance of such anomalies is emphasized in previous studies [19].

It is important to note that a significant portion of the identified radiogeochemical anomalies does not coincide with previously mapped local structures based on MCDP-2D data. This discrepancy may indicate the presence of non-structural hydrocarbon traps (such as lithological, stratigraphic, or fault-sealed types), or suggest that geochemical criteria were insufficiently considered during the planning of exploration wells.

Based on the above, the following scientific and practical conclusions can be drawn:

- The AGS (Airborne Gamma Spectrometry) method, particularly when normalized to thorium, has demonstrated high effectiveness in direct hydrocarbon prospecting, as corroborated by several regional studies [16, 20].
- Areas exhibiting reduced concentrations of K, U, and Th should be considered priority targets for further geological exploration.
- The spatial correlation between deep fault zones and radiogeochemical minima highlights their potential role in hydrocarbon migration pathways.
- Integrating radiogeochemical data provides a valuable tool for refining seismic survey models and optimizing the placement of exploration wells.
- The results obtained offer a reliable foundation for improving the design of seismic acquisition programs and for revising exploration drilling plans, incorporating both radiogeochemical and structural information in a comprehensive manner.

5.3. Geothermal Surveys. Geothermal study carried out in the SUR led to the development of thermal flux distribution models, the identification of geothermal anomalies, and the establishment of their correlation with major tectonic structures and the lithological composition of the subsurface. The analysis demonstrated that each principal structural element of the region is characterized by a distinct geothermal signature.

In particular, the Assakeaudan Depression exhibits consistently low heat flow values down to depths of 5 km, which is attributed to a thick sedimentary cover composed predominantly of low-thermal-conductivity, hydrocarbon-generating source rocks. Similar patterns have been previously documented in deep marine basins with organic-rich sediments [34, 38].

Conversely, the Shakhpakhty Step is marked by stable positive geothermal anomalies at depths of 1.5–2.5 km. These are associated with elevated thermophysical properties of the host rocks and an extensively developed system of disjunctive faults, which likely enhance vertical fluid migration. Such anomalies are considered potential indicators of hydrocarbon accumulation zones [42, 43], particularly within stepped uplifts and active fault networks.

A localized heat flow minimum observed in the area of the Shakhpakhty field **(Uzbekistan)**, combined with positive anomalies in the upper stratigraphic section, is of particular interest. This pattern likely reflects the presence of dense, low-permeability cap rocks that inhibit vertical heat transfer and help preserve hydrocarbon accumulations [36].

On the southeastern flank of the associated fault zones, the Shakhpakhty and Djel fields **(Uzbekistan)** have already been discovered. Meanwhile, the western flank hosts several promising structures - such as Otynshy, Kozhantay, and Utezhan **(Kazakhstan)** - which are recommended as priority targets for exploration, provided the presence of effective sealing formations is confirmed.

The integration of geothermal indicators with gravity-magnetic and seismic data significantly enhances regional hydrocarbon prospectivity assessments. This conclusion is strongly supported by the present study and corroborated by international research findings [33, 39].

5.4. Gravity and Magnetic Surveying. The application of gravity and magnetic field transformants - including horizontal and vertical gradients, TDR-type derivatives, ΔTa, and automated anomaly axis tracing - significantly enhanced the interpretive capacity of geophysical data for the SUR. This approach greatly improved the understanding of the geological framework and increased the efficiency of exploration targeting.

The use of these methods enabled the identification of previously undetected structural features, localized density and magnetic anomalies, and hydrocarbon-prospective zones, thereby confirming the high diagnostic value of such techniques. Notably, this methodology proved particularly effective for interpreting fault and fracture zones that control fluid migration and accumulation.

The results are consistent with international studies [26, 27], where transformant-based analysis is recognized as a sensitive and reliable tool for structural interpretation in petroleum geophysics.

Distinct geophysical signatures differentiate the CUSD, the Shakhpakhty Step, and the Assakeaudan Depression.

The Shakhpakhty Step is characterized by low remanent magnetization, alternating gravity anomalies of contrasting polarity, and the presence of a deep-seated magnetically active layer at depths reaching up to 12 km, accompanied by an elevated geothermal gradient. These features indicate favorable conditions for hydrocarbon accumulation both within the sedimentary cover and in underlying structural levels - comparable to inverted basin settings observed in regions with active tectonic inversion regimes [30].

In the Assakeaudan Depression, magnetically active bodies are found at depths of 8–10 km, which correlate with the crystalline basement top. Their geophysical expression suggests an association with ultramafic intrusions, indicating the possible presence of diapiric structures similar to those identified in the Precaspian Basin [45].

The contact zones between Upper Jurassic and Lower Cretaceous formations exhibit a high density of Euler solution clusters, reflecting well-expressed lithological contrasts and likely indicating the presence of concealed fault systems. These structures may have influenced sedimentation patterns and played a key role in the development of stratigraphic and structural hydrocarbon traps.

In the CUSD, deep-seated gravity and magnetic anomalies correlate closely with the basement surface delineated by MCDP-2D seismic data, thereby confirming the tectonic origin of the detected geophysical heterogeneities [30].

A notable anomaly identified over the Karabaur Ridge is interpreted as a manifestation of a "double crust" phenomenon, likely caused by the overthrusting of the South Ustyurt block onto the deformed complexes of the CUSD [30]. Magnetic data reveal the presence of two distinct magnetically active horizons at depths of 4-6 km and 10–12 km, which are interpreted as expressions of thrust-and-fold tectonics - analogous to structures previously described in the Turkestan orogenic belt [44].

These results demonstrate the diagnostic value of potential field transforms in resolving deep geological architecture and delineating prospective hydrocarbon-bearing structures that may remain undetected using conventional interpretation methods. The observed correlations among deep density heterogeneities, magnetically active bodies, fault zones, and potential hydrocarbon traps emphasize the applied relevance of this approach.

Taken together, the findings substantiate the need to systematically integrate transform-based potential field analysis into three-dimensional geological modeling and exploration planning, particularly in geologically complex and underexplored regions such as South Ustyurt.

5.5. Integration of Geophysical Methods. A comprehensive interpretation of gravity and magnetic field transformants has considerably refined the tectonic framework of the South Ustyurt Region (SUR) and allowed the identification of new areas with significant hydrocarbon prospectivity. The use of horizontal gradients, second-order derivatives, and Euler solutions has enabled detailed delineation of concealed fault-block structures and lateral boundaries of tectono-stratigraphic complexes.

The integration of gravity and magnetic data with airborne gamma-ray spectrometry and geothermal modeling has revealed strong and consistent spatial correlations among geophysical

parameters that capture both physical properties and tectono-thermal characteristics of the subsurface. These correlations underscore the high diagnostic value of the integrated dataset for elucidating the structural architecture of the South Ustyurt Region and affirm its critical role in developing geologically sound predictive models of hydrocarbon prospectivity.

Radiogeochemical anomalies - particularly the depletion of potassium and uranium - demonstrate spatial association with potential hydrocarbon traps, indicating their utility as supplementary indicators in petroleum system analysis. The combined use of these data through advanced machine learning algorithms (e.g., Self-Organizing Maps, SOM) and conventional geophysical techniques (gravity, magnetometry, seismic surveying) provides a scientifically robust platform for constructing high-resolution predictive models and prioritizing exploration targets at early stages of geological prospecting. Stable spatial connections between anomalies of geophysical fields and tectonic elements of various orders have been established, which made it possible to substantiate the high oil and gas potential of the Shakhpakhtinsky stage and, to a lesser extent, the Assakeaudan Depression.

The integrated interpretation of geophysical, geothermal, and radiogeochemical datasets - employing multiparametric analysis and advanced data processing techniques, including state-of-the-art machine learning algorithms - has substantially improved the accuracy and reliability of predicting potential hydrocarbon accumulation zones within the South Ustyurt Region.

This comprehensive approach has yielded a significantly refined understanding of the region's geological architecture, including the reconstruction of deep crustal structures, delineation of concealed fault-block systems, and characterization of geophysical heterogeneity across major geostructural domains.

A key outcome of the study was the identification of consistent spatial correlations between gravimagnetic, geothermal, and radiogeochemical anomalies and tectonic features of varying hierarchical levels. These correlations underpin a set of robust predictive criteria for hydrocarbon prospectivity and have enabled the delineation of the most favorable structural settings for trap formation. The Shakhpakhty Step stands out as the most prospective zone, exhibiting clear structural segmentation and strong evidence of deep fault control on hydrocarbon entrapment. The Assakeaudan Depression also demonstrates moderate exploration potential.

Conversely, the **CUSD** is characterized by well-expressed tectonic and geophysical heterogeneity, suggesting limited favorability for the development of significant hydrocarbon accumulations.

These findings form the basis for a scientifically grounded revision of the regional geological model and support the design of a strategically targeted exploration framework. This approach not only enhances the overall efficiency of exploration programs but also reduces geological uncertainty and economic risk at the early stages of hydrocarbon resource development.

The most promising targets for further investigation within the SUR are the Shakhpakhty Step and, to a lesser extent, the Assakeaudan Depression. These structural domains exhibit well-expressed radioactive heterogeneity, contrasting anomalies in gravity, magnetic, and geothermal fields, as well as indications of active deep fluid dynamics. The convergence of these geophysical and geochemical features is interpreted as a reliable indicator of enhanced hydrocarbon saturation.

Notably, the Shakhpakhty Step is distinctly manifested across gravity, magnetic, and thermal data, with localized geothermal anomalies interpreted as zones of deep fluid discharge. These zones are believed to promote the formation of hydrocarbon traps within the sedimentary succession. The southern continuation of the step into the territory of Uzbekistan shows spatial correlation with major Jurassic gas fields - Shakhpakhty and Dzhel **(Uzbekistan)** - underscoring the regional extent of the petroleum system and its strong structural control.

The integration of gravimagnetic modeling with thorium-normalized airborne gamma-ray spectrometry has facilitated the identification of several local structures with high exploration potential, including Utezhan, Kozhantay, North Kozhantay, and Otynshy **(Kazakhstan)**.

The exploration significance of these targets is further substantiated by a combination of geological criteria, including favorable lithofacies distributions and structurally controlled settings,

both of which increase the likelihood of hydrocarbon trap formation. Consequently, these structures are justifiably regarded as priority targets for the next phase of exploration, aimed at identifying and evaluating new hydrocarbon accumulation zones.

5.6. Gravimagnetic modeling and geostructural features of the South Ustyurt Region: Hydrocarbon potential assessment using the SIGMA DVOP software platform. To ensure the reliability of the interpretation and validate the outcomes, a comparative analysis was performed using our own data alongside geophysical models constructed in the **SIGMA DVOP** software platform. This system is based on the method of interpretational tomography and was applied in earlier studies of the SUR, including work conducted by P.N. Kovrizhny, who utilized this approach for deep structural modeling.

The analysis relied on an integrated dataset that included gravity and magnetic survey data, as well as seismic information from CDP and CMRW methods. For additional verification, these data were cross-referenced with borehole results, AGSS and geothermal measurements.

The resulting geodensity and geomagnetic models provided a more detailed representation of both vertical and lateral heterogeneities within the sedimentary cover and crystalline basement. These models enabled spatial interpretation of anomalies associated with major structural elements and potential hydrocarbon traps. A consistent increase in sediment density with depth was observed, reaching values of approximately 2.60 g/cm^3 near the basement surface - reflecting progressive compaction and porosity reduction in the deepening sedimentary succession.

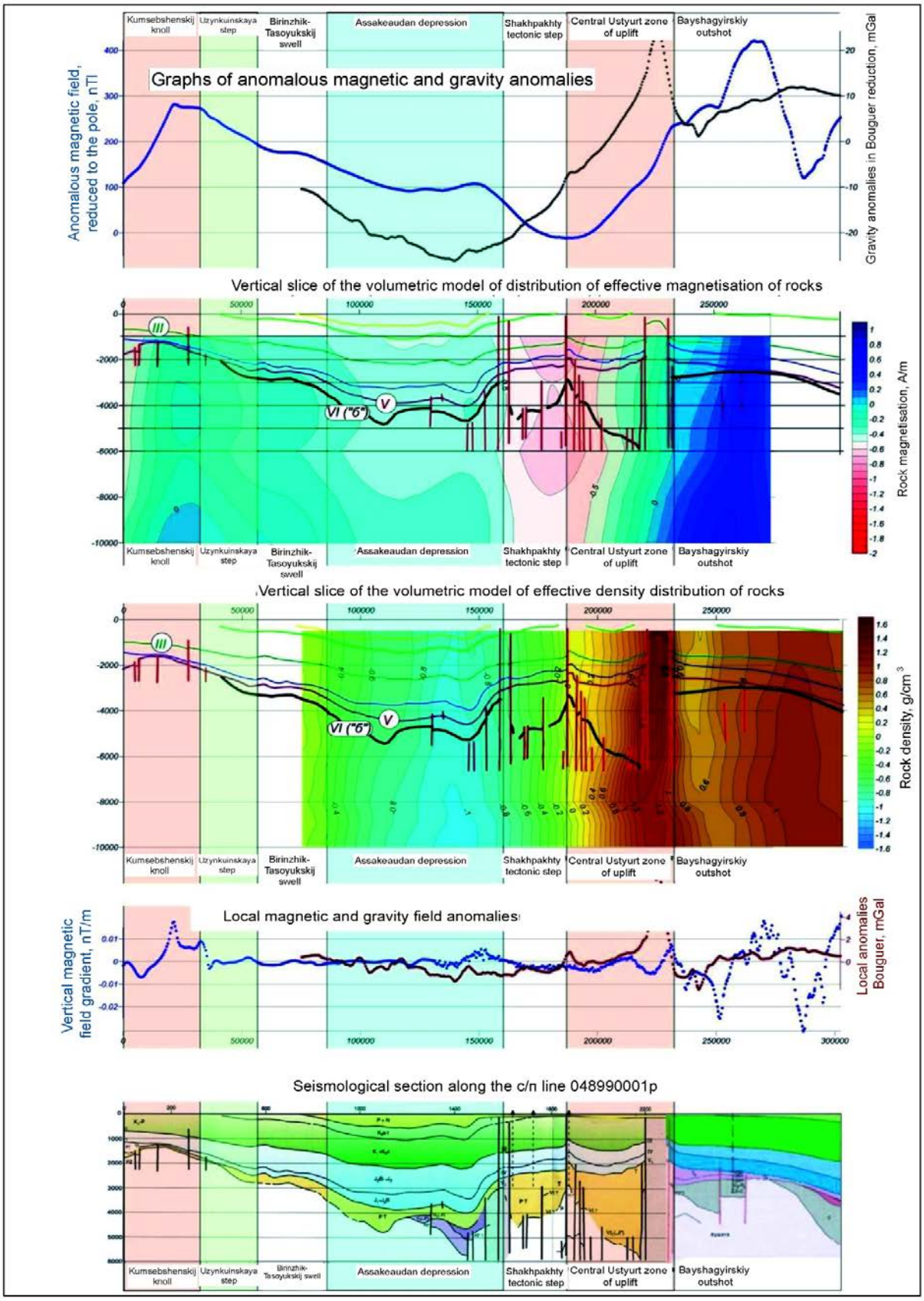

Fig. 12. Vertical section of volumetric models of density and magnetic induction along seismic profile line 048990001 (according to data from Kovriznyh P.N.)

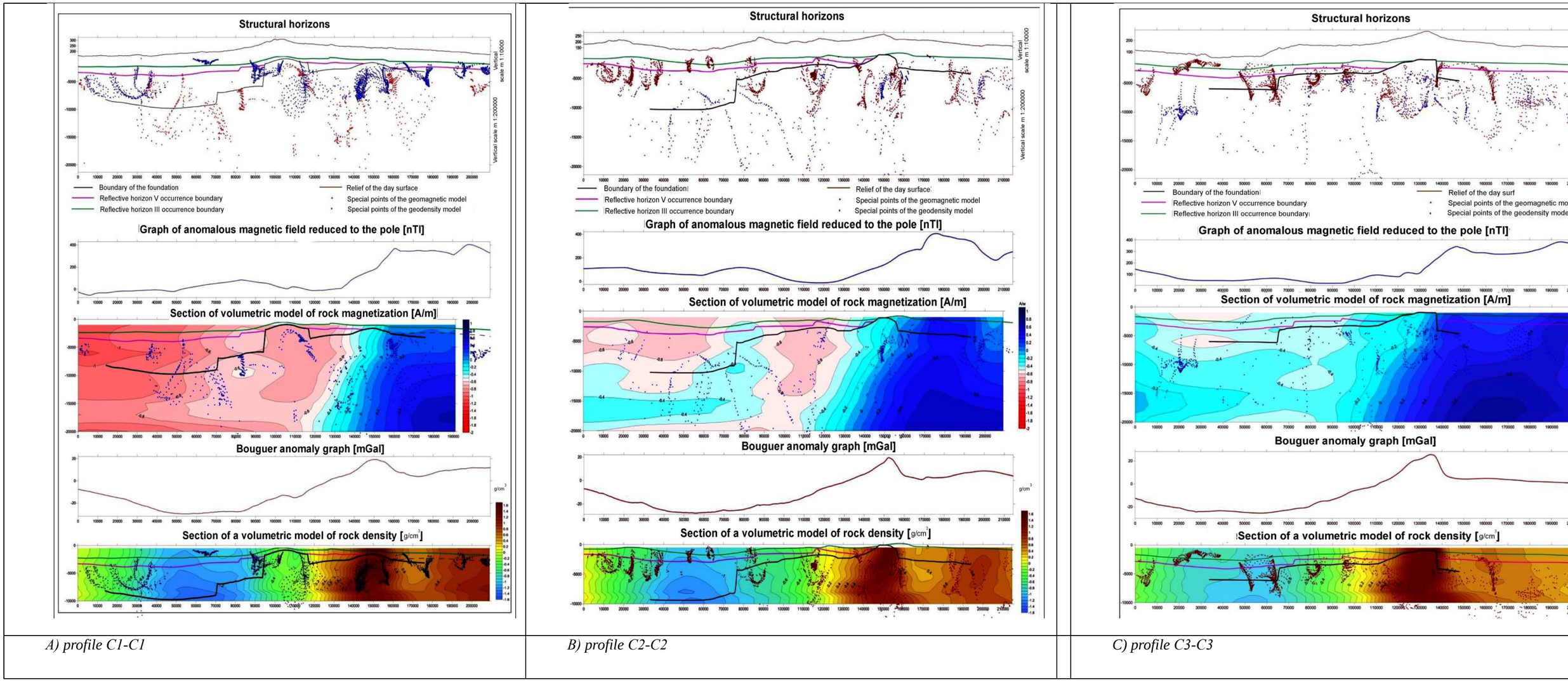

A) profile C1-C1 | *B) profile C2-C2* | *C) profile C3-C3*

Fig. 13. Display of geomagnetic and geodensity volume models in structural constructions along arbitrarily selected lines through the Samtyr area. SIGMA DVOP constructions (based on data from Kovriznyh P.N.)

Gravimagnetic modeling of the CUSD, the Shakhpakhty Step, and the Assakeaudan Depression revealed that the depth to the crystalline basement ranges between 7 and 10 km - significantly deeper than previous estimates of 5–6 km. This finding highlights a more well-expressed and complex gravitational expression of the basement and emphasizes its active geodynamic role in shaping the regional structural framework and influencing the localization of hydrocarbon accumulation zones.

The comparison of gravity (ΔGa) and magnetic (ΔTa) anomalies with seismic profile 048990001 revealed a stable spatial correlation between gravimagnetic expressions and the deep geological structure of the South Ustyurt Region. Elevated ΔGa values are observed over the Karabaur Uplift and the Baishagyr High, which are confirmed by seismic data and reflect the presence of dense crystalline basement rocks.

In the Assakeaudan Depression - the deepest part of the region - well-expressed ΔGa minima and reduced ΔTa values are recorded, indicating decreased rock density and significant basement depth (Figs. 12, 13).

Magnetic anomalies (ΔTa) show consistent correlation with tectonic boundaries and local structural features. The Baishagyr High and the Samtyr structure are characterized by elevated magnetic activity, likely associated with intrusive bodies or volcanic-sedimentary sequences. In contrast, the Shakhpakhty Step exhibits negative ΔTa anomalies (down to –150 nT), which may be attributed to lithological variations or zones of deep fluid discharge (Figs. 12, 13).

These observed patterns confirm the diagnostic value of gravimagnetic data in refining tectonic models and in predicting potential hydrocarbon accumulation zones.

Correlation analysis has identified nonlinear relationships between ΔGa, ΔTa, and the depth to the crystalline basement, as derived from MOGT-2D seismic survey data. These patterns are attributed to the block-faulted structure and petrological heterogeneity of the SUR. Deviations from expected statistical correlations are explained by both the inherent variability of the geological model and uncertainties in seismic data interpretation.

Further evidence supporting the hydrocarbon potential of the SUR was obtained through the correlation of ΔGa with the depth of Jurassic sediments along the top of Seismic Horizon III, revealing a consistent functional relationship (Figures 11 and 12). The development of thick quasi-platform sedimentary sequences within the Shakhpakhty Step and the Assakeaudan Depression suggests favorable geological conditions for the formation of traps and hydrocarbon accumulation.

A comprehensive geophysical analysis of the SUR, conducted using the SIGMA DVOP software suite and integrating gravity, magnetic, seismic, and well data, allowed for a more precise delineation of the morphology and spatial configuration of the crystalline basement. Additionally, several local structures with indicators of hydrocarbon potential were identified.

Particular attention is paid to the Shakhpakhtinsky step and the Assakeaudan Depression, where stable statistical relationships between gravity field anomalies and basement morphology have been established. These patterns formed the basis for geological and geophysical criteria for predicting zones of possible hydrocarbon accumulation.

The results of the study indicate strong potential for further exploration and appraisal activities, particularly in areas of localized positive gravity anomalies associated with zones of tectonic activation. While thick sedimentary cover typically corresponds to regional gravity lows due to lower rock densities, its combination with active tectonics may contribute to the formation of structural traps and favorable conditions for hydrocarbon accumulation. The identified zones exhibit stable geophysical indicators supporting their hydrocarbon prospectivity.

A comparative analysis of interpretational tomography data from SIGMA DVOP and classification-based modeling using the IP_Prediction 2D module revealed consistent geophysical and structural correlations, confirming the reliability of an integrated approach to hydrocarbon prospectivity assessment.

One of the key findings is the characterization of the deep block structure: tomographic modeling clearly delineates the block segmentation of the crystalline basement at depths of 7–10 km. The predictive model in IP_Prediction 2D identifies similar structural boundaries and further refines the interpretation by outlining sub-parallel horizons with high hydrocarbon accumulation potential.

Several key areas with contrasting prospectivity were identified:

1. Deep block structure: Tomography records the block discreteness of the basement at depths of 7–10 km. The IP_Prediction 2D prognostic model identifies similar structural boundaries, additionally specifying subparallel horizons with high hydrocarbon accumulation potential.

2. Prospective structures (Karabaur, Bayshagyr, Kyzgurlu): SIGMA DVOP tomography revealed positive gravimagnetic anomalies in the Karabaur, Bayshagyr, and Kyzgurlu areas, which are interpreted as potential targets for further explorationIn addition, the IP_Prediction 2D model highlights other targets, including local structures within the Shakhpakhty Step such as Otynchi, Utezhan, and others.

3. *Low-prospectivity zone (Samtyr):* Tomographic analysis using SIGMA DVOP reveals several unfavorable geological features in the Samtyr area, including an ineffective seal, well-expressed tectonic disruption, and thermal instability. These findings are consistent with the results of the IP_Prediction 2D model, which classifies the zone as having low hydrocarbon prospectivity.

4. High-Prospectivity zone - Shakhpakhty step: This area is confidently identified by both approaches as one of the key hydrocarbon-prospective regions. It is characterized by stable gravimagnetic and thermal anomalies, as well as the development of Jurassic sedimentary complexes. The IP_Prediction 2D model classifies it as a territory with a high probability of hydrocarbon accumulation.

5. Assakeaudan depression: Interpreted as a deep subsiding zone with well-expressed density and thermal contrasts, suggesting favorable conditions for the development of source rocks and trap formation in the upper parts of the sedimentary section (particularly in flank zones). These findings align closely with the IP_Prediction 2D model, which also highlights the hydrocarbon potential of this depression.

An integrated analysis of radiogeochemical, gravimetric, magnetic, geothermal, and seismic data, combined with advanced artificial intelligence and machine learning techniques, has significantly improved the geological understanding of the SUR and enabled the identification of priority targets for further exploration and appraisal **activities.**

The key outcomes of the study include:

- Detailed mapping of the crystalline basement morphology and the delineation of its deep block structure;
- Identification of zones with elevated hydrocarbon potential, primarily within the Shakpakhty Step and, to a lesser extent, along the northern margin of the Assakeaudan Depression;
- Development of geophysical and geochemical criteria for hydrocarbon trap prediction, based on the spatial integration of density, magnetic susceptibility, heat flow, and radiogeochemical anomalies;
- Validation of machine learning-based modeling results (IP_Prediction 2D), supported by geological interpretation and deep geophysical verification.

Overall, the results point to a high hydrocarbon prospectivity of the SUR, particularly in areas characterized by the intersection of deep faults, positive gravimagnetic anomalies, thick sedimentary sequences, well-developed reservoirs, and effective clay seals forming promising hydrocarbon traps.

5.7. Reliability and Verifiability of the Research Results. The reliability of the research findings is ensured through the deep integration of artificial intelligence (AI), machine learning (ML) techniques, and comprehensive interpretation of geological and geophysical data. This approach significantly enhances the objectivity of interpretations, minimizes human bias, and enables the identification of hidden patterns within complex, high-dimensional, and heterogeneous datasets.

According to studies [9, 10], the synergy between physically based geological models and adaptive machine learning algorithms results in markedly higher accuracy in predicting geological structures and fluid-bearing zones compared to conventional analytical methods.

Particularly effective has been the integration of diverse geodata types - seismic, gravity and magnetic, geothermal, and geochemical - using advanced algorithms such as self-organizing maps (SOM), artificial neural networks, principal component analysis (PCA), stochastic inversion modeling, and deep learning. Publications [11, 13] provide compelling examples of the successful

application of these approaches for constructing reliable geological models, identifying anomalous fluid accumulations, and increasing the efficiency of exploration programs.

Thus, the credibility of the dissertation's conclusions is determined not only by the comprehensiveness and representativeness of the geological data employed, but also by the application of modern analytical tools that enable their rigorous integration and interpretation. This aligns with global standards of reproducibility and the principles of data-driven science in geosciences [12].

5.8. Hydrocarbon Systems of South Mangyshlak and the South Ustyurt Regions: Geological framework and generative potential

South Mangyshlak region. A major outcome of our study was the refinement of the regional geological model for the Jurassic and Triassic petroleum systems of the Southern Mangyshlak Petroleum Province and the South Ustyurt Region. Central to this model is the stratigraphic positioning of the principal petroleum source rock formations (PSRFs), which plays a critical role in determining the generative potential of the basin.

The most favorable conditions for organic matter accumulation and sediment deposition were associated with the Mangyshlak and Karaaudan grabens and their flanking structural zones. Geological data indicate the presence of deep, anoxic palaeodepressions with restricted water circulation, which promoted the preservation of organic-rich sediments and the development of effective source rock facies.

Stratigraphic analysis, lithofacies reconstruction, and analog-based geological modeling indicate that the main PSRFs Petroleum Source Rock Formations in Southern Mangyshlak are confined to the basal facies of the Upper Olenekian to Middle Triassic carbonate–terrigenous complex. Of particular significance is the Karadzhatyk Formation, which displays high organic content and laterally persistent facies characteristics [46, 47].

This formation is composed of interbedded dark shales, carbonates (limestones and dolomites), and tuffs. Its thickness reaches up to 750 meters in the southern part of the Zhetybai Step and tapers to 250–300 meters in the Peschanymys Uplift [46], reflecting a structurally and sedimentologically heterogeneous depositional environment.

The stratigraphic position, composition, and lateral extent of the Karadzhatyk Formation support its role as a key generative unit within the regional petroleum system.

The black bituminous shales of the Karadzhatyk Formation are distinguished by a high content of dispersed organic matter, reaching up to 9.8% [47], and a predominance of Type II kerogen. These characteristics point to a strong generative potential, particularly for liquid hydrocarbons [48].

By contrast, the source rock formations of Lower Induan (T_1) and Upper Triassic (T_3) age exhibit significantly lower organic richness and thus a much more limited capacity for hydrocarbon generation [50, 51].

In the central part of the Mangyshlak palaeorift, the organic matter contained in the Middle Triassic strata has undergone advanced catagenesis, accompanied by structural deformation and partial denudation of the host sediments as a result of pre-Jurassic erosion. Despite these processes, petroleum source rocks have been preserved in the southern part of the Zhetybai Step and within the Karaaudan Rift [50].

It is noteworthy that during the Triassic period, the Karaaudan Rift likely represented a shallow marine platform with limited organic productivity and suboxic to anoxic conditions, which constrained the development of high-quality source rocks and reduced the overall generative potential of this zone.

An alternative model suggests that Middle Triassic petroleum source rock formations are extensively developed across the region, ranging from the Zhetybai Step to the Southern Mangyshlak depressions. However, hydrocarbon generation and subsequent migration into Jurassic reservoirs may have been significantly impeded by the presence of Upper Triassic seal rocks and the isolating properties of disjunctive fault systems, which acted as effective barriers to vertical migration.

In contrast, Lower and Middle Jurassic source rocks are generally considered to exhibit low generative potential. These intervals are dominated by Type III kerogen, and the total organic carbon (TOC) content in the shales ranges from 0.5% to 1%, with maximum values reaching 1.5% in the central part of the Segenydek Depression [52]. Despite these modest values, these formations may have contributed limited volumes of dry gas, which later mixed with liquid hydrocarbons migrating from older, Paleozoic source intervals.

Based on lithostratigraphic and tectonic similarities, a structural and genetic correlation has been proposed among the Jazgurlin, South Mangyshlak, and Assakeaudan depressions. These basins are thought to host petroleum source rocks that served as hydrocarbon contributors not only to the Uzen and Zhetybai fields **in Kazakhstan**, but also to the Shakhpakhty and Dzhel fields **in Uzbekistan.**

This interpretation is further supported by biostratigraphic subdivision of Jurassic deposits conducted in accordance with the International Stratigraphic Guide [54, 55], which allowed for the identification of potentially productive horizons and refinement of the regional assessment of hydrocarbon prospectivity

South Ustyurt Region. An integrated interpretation of stratigraphic, lithofacies, and tectonic data for the SUR has enabled the reconstruction of the principal elements of its petroleum systems.

Source rocks are primarily associated with Middle Triassic (T_2) deposits, with potential analogs inferred in the Lower and Middle Jurassic successions. Reservoir units have been identified within the Upper Paleozoic (PZ_3), Middle Triassic, Jurassic, and, locally, Cretaceous formations. Seals are predominantly composed of clay-rich Upper Triassic and Upper Jurassic sediments, which provide effective caprock integrity and trap preservation [47, 49, 52].

Hydrocarbon traps developed in multiple tectono-sedimentary phases, notably during the Late Triassic (T_3), Late Jurassic (J_3), and later during the Late Cretaceous and Pliocene (N_2) periods.

Hydrocarbon generation and accumulation occurred in discrete stages: the principal phase of generation is attributed to the Late Cretaceous–Paleogene interval, while major hydrocarbon accumulation likely took place during the Neogene. The preservation of hydrocarbon accumulations is supported by the presence of all critical elements of a working petroleum system - including mature source rocks, effective reservoirs, competent seals, structurally and stratigraphically defined traps, and viable migration pathways [46, 48].

From a regional perspective, sediments of the intermediate structural level are extensively developed throughout the area, with the notable exception of Triassic formations, which are predominantly confined to the Assakeaudan Depression. Lower Jurassic sequences are primarily associated with tectonic depressions, while Middle and Upper Jurassic, as well as Cretaceous strata, exhibit widespread stratigraphic and structural distribution across the region. The absence of Paleogene–Neogene formations on uplifted blocks is indicative of well-expressed tectonic reactivation during the Late Cenozoic [52].

The presence of a complete and geologically coherent set of essential petroleum system elements - including mature source rocks, high-capacity reservoir intervals, regionally effective seals, structurally and lithologically diverse traps, and well-established hydrocarbon migration conduits - provides compelling evidence for the existence of fully developed, operational petroleum systems. This integrated geodynamic and petroleum-geological framework substantiates the region's high oil and gas potential and provides a robust scientific rationale for prioritizing and intensifying prospecting and appraisal-stage exploration efforts.

Geological analogues. In the southeastern sector of the South Ustyurt Region (SUR), within the territory of ***Uzbekistan***, the Shakhpakhty Step and the Assakeaudan Depression continue their structural development, while the Koplankyr Step is distinctly delineated. Between 2006 and 2014, PJSC «Gazprom» carried out a substantial program of geophysical surveys, exploration and appraisal drilling, and thematic geological studies in this area, which led to a significant revision of the region's assessed hydrocarbon potential [4].

Within the Shakhpakhty Step, two gas fields have been discovered - Shakhpakhty (1964) and Djel (2009) - both associated with Lower, Middle, and Upper Jurassic formations. The accumulations

are confined to anticlinal traps at depths ranging from 1,700 to 2,400 meters, hosted in sandstones and siltstones with porosity values of 16–20% and permeability ranging from 0.109 to 0.312 μm². The Shakhpakhty gas field is classified as medium-sized [1], while Djel is categorized as a small gas field.

The portfolio of undrilled structures within the Uzbek sector of the Shakhpakhty Step includes seven identified prospects, among which the North Karaaudan and Ergazy structures are of particular note; the latter has already been prepared for exploratory drilling. Jurassic strata remain the principal focus of exploration, while Paleozoic formations and non-anticlinal trap types are also considered promising targets, though they require further geophysical delineation and evaluation [4].

In the southern sector of the Shakhpakhty Step and the Assakeaudan Depression, a series of local uplifts have been identified within the Permian–Triassic stratigraphic complex, including Kumoy I, Kumoy II, Ergazy Prirazlomnaya, Nikolaevskaya, and Assake-Audan. These structural uplifts, complicated by faulting, form anticlinal and drape-type hydrocarbon traps. Reservoir quality within these features is largely determined by the development of secondary porosity in Paleozoic formations, associated with processes of chemical and mechanical weathering. Effective regional seals are provided by dense, low-permeability rocks of the lower Permian-Triassic sequence.

Hydrocarbon entrapment in the Upper Paleozoic complex is controlled by the internal architecture of reservoir units, the presence of structural and lithofacies traps, the development of effective secondary reservoirs, and the integrity of overlying sealing formations. Among the most prospective targets for further exploration are the local structures of Karaaudan, Chuymak, Ergazy, Shakhty, Tamarly, and Zhaptyr.

Seismic interpretation suggests the possible presence of biohermal buildups within the Paleozoic section, which enhances the exploration potential of areas such as Kumoy II and Zhaptyr by indicating the likelihood of stratigraphically and lithologically controlled unconventional traps.

Recommendations for Exploration and Appraisal in the South Ustyurt Region. The South Ustyurt Region (SUR) contains several priority targets for hydrocarbon exploration, including the Utezhan, Kozhantay, North Kozhantay, and Otynshy structures within the Shakhpakhty Step, as well as the Kyzgyrly and South Kyzgyrly structures located in the Assake-Audan Depression. According to estimates by the Geoken Research Center [15], the combined prospective gas resources for these structures are approximately **96.9 billion cubic meters,** underscoring the region's significant resource potential.

Hydrocarbon generation in the area is thought to be primarily associated with Triassic source rocks, which may have produced hydrocarbons that subsequently migrated into traps formed within Jurassic and Paleozoic reservoirs. Despite encouraging geological settings, some previously drilled structures have not yielded commercial discoveries, highlighting the need for further investigation into source rock presence, maturity, and migration dynamics.

In this context, additional integrated geological studies are recommended, with a particular emphasis on basin modeling to better assess the petroleum systems. These studies should aim to:

- characterize the thickness, composition, and thermal maturity of potential source rock intervals in the Triassic, Jurassic, and Paleozoic strata;
- reconstruct hydrocarbon generation and migration pathways;
- identify the geological and structural factors that may explain the absence of accumulations in previously tested prospects.

The application of advanced basin modeling techniques, supported by integrated geological, geophysical, and geochemical data, will enhance the reliability of subsurface interpretations. A data-driven, multidisciplinary approach will be critical to improving the predictive accuracy of reservoir presence and quality, thereby increasing the efficiency and success rate of future exploration and appraisal activities across the South Ustyurt Region.

Based on the results of integrated geological and geophysical analysis, it is recommended to drill an exploratory well on the Kyzgyrly structure to test for potential gas accumulations within the Jurassic –Triassic interval. The planned total depth of the well is approximately 4,320 meters. The estimated geological resources are 42 billion cubic meters, distributed across nine prospective

reservoir horizons -eight within the Jurassic and one within the Triassic - with a projected probability of geological success of 22.6% [15].

In addition to Kyzgyrly, several other local structures have been identified as promising targets for further exploration, including West Kozhantay, Otynshy, South Samtyr, West Samtyr, South Tabyn, and South Kyzgyrly. Among these, Otynshy (estimated at 6.5 bcm) and Tabyn (5.7 bcm) are considered high-priority targets, with potential hydrocarbon accumulations expected in Middle Jurassic reservoirs.

To improve the efficiency and accuracy of drilling and subsurface evaluation, the implementation of advanced drilling and data acquisition technologies, as outlined in [56, 57], is recommended.

The structural geometry has been defined based on a sparse grid of CDP-2D seismic profiles (with line spacing exceeding 3 km), which necessitates refinement of trap parameters.

This limited resolution introduces uncertainty in the delineation of trap morphology and closure. Therefore, to enhance the reliability of structural interpretation and reduce exploration risk, additional high-density 3D seismic acquisition (CDP-3D) is strongly recommended.

At this stage, proposed well locations are preliminary and should be refined and validated based on the results of detailed geophysical surveys and updated seismic interpretation.

Conclusion

1. An integrated approach to regional hydrocarbon prospectivity assessment in the South Ustyurt Region (SUR) has been developed and successfully tested. This methodology is based on the comprehensive interpretation of drilling data, MOZT seismic surveys, gravimetry, magnetometry, airborne gamma spectrometry, and geothermal data.

2. The approach incorporates advanced digital technologies using specialized software platforms such as IP Seismic, ArcGIS, and others, alongside machine learning algorithms, including self-organizing maps (SOM clustering). This has enabled the identification of robust correlations between geophysical anomalies, tectonic structures, and potential hydrocarbon traps.

3. The analysis has revealed a stable correlation between geophysical anomalies, deep-seated faults, and zones of reduced natural radioactivity, which can be used as reliable indicators for early-stage hydrocarbon prediction.

4. The use of self-organizing maps (SOM) in combination with geospatial analysis has proven highly effective in detecting hidden patterns and improving the accuracy and automation of subsurface interpretation.

5. Key structural features influencing hydrocarbon prospectivity include: thrust and overthrust zones, subvertical basement faults, and thermal and radiogeochemical anomalies. These elements define a complex but promising tectonic framework in the South Ustyurt Region, providing a solid basis for targeted drilling, risk reduction, and exploration optimization.

6. Geophysical modeling has identified density, magnetic, and geothermal heterogeneities at depths of 5, 10, and 20 km, spatially aligned with mapped hydrocarbon traps. Additionally, airborne gamma spectrometry has detected 15 anomalous zones with low thorium, potassium, and uranium concentrations - primarily associated with the Shakhpakhty Tectonic Step, confirming its high exploration potential.

7. Integrated analysis of seismic and radiogeochemical data has revealed a stable spatial correlation between radioactive anomalies and deep-seated tectonic faults, supporting their use as reliable indicators in early-stage hydrocarbon exploration.

8. The most prospective structures include the Shakhpakhty Step and, to a lesser extent, the Assake-Audan Depression, where a deeply buried magnetically active layer has been identified. This is interpreted as a favorable geodynamic condition for the formation of petroleum systems within the sedimentary cover.

9. In the Shakhpakhty Step, localized thermal anomalies - associated with deep faults and potential traps - have been detected through geothermal surveys. These are interpreted as signs of vertical fluid migration, suggesting the presence of hydrocarbon accumulations. A geothermal-based

criterion for hydrocarbon prediction has been developed, improving the accuracy of prospect assessment at early exploration stages.

10. Additionally, the junction zone between the CUSD and the Shakhpakhty Step exhibits confirmed thrust-and-overthrust tectonics, with fault planes dipping at 50–70°. This is supported bythe presence of paired magnetically active bodies, and a high concentration of Euler solution points, indicating structural complexity. Together these features define a tectonically active and promising setting for trap formation and hydrocarbon accumulation.

11. Key tectonic and lithofacies factors controlling the formation of potential hydrocarbon accumulations have been identified. A genetic relationship has been established between the Assakeaudan, Zhazgurlin, and South Mangyshlak depressions, reflecting a common mechanism of petroleum system development. The primary productive horizons are associated with Triassic, Jurassic, and Cretaceous formations.

12. A comprehensive, multi-method approach - incorporating seismic surveys, drilling, gravimetry, magnetometry, airborne gamma spectrometry, and geothermal studies - has made it possible to refine the positioning of prospective structures and improve previously proposed models of hydrocarbon distribution.

13. Automated interpretation has significantly enhanced predictive accuracy, revealing block-faulted architecture within the sedimentary cover (an important indicator of possible hydrocarbon migration pathways) and supporting the delineation of targets for exploration and appraisal drilling.

14. As a result, several promising local structures have been identified - Kyzgyrly, Utezhan, Kozhantay, Otynshy, and South Tabyn - located within the Shakhpakhty Step and Assakeaudan Depression. Their hydrocarbon potential is supported by a consistent set of geophysical, lithological, and structural indicators.

15. The results obtained hold substantial practical significance and can inform the planning of subsequent phases of exploration and appraisal activities. While the integrated geological and geophysical analysis yielded promising insights, the findings require further validation. This necessitates exploratory drilling, acquisition of high-resolution 3D seismic data (CDP-3D), and refinement of key parameters such as fault architecture, source rock maturity, and fluid migration pathways.

16. Future investigations should incorporate a comprehensive analysis of deep-seated fault zones as potential vertical conduits for hydrocarbon migration, as well as fluid flow modeling and basin modeling. These methods will improve our understanding of the thermal maturity of Jurassic, Triassic, and Paleozoic source rocks, help reconstruct migration routes, elucidate trap formation mechanisms, and clarify the absence of accumulations in previously drilled structures.

17. A fully integrated approach will significantly improve the reliability of hydrocarbon prospectivity assessments, reduce geological uncertainty, and provide a robust foundation for optimized exploration planning.

18. It is also important to investigate the causes of hydrocarbon absence in previously drilled structures. A recommended approach involves the integration of remote sensing (RS), well logging, and drilling data into a unified 3D conceptual model, enabling a comprehensive evaluation of hydrocarbon prospectivity across the SUR. The adoption of digital technologies and artificial intelligence (AI) offers the potential to significantly improve forecast accuracy, reduce exploration costs, and minimize environmental risks.

19. The findings confirm that the integration of conventional geophysical methods with advanced digital tools - including potential field analysis, remote sensing, AI, machine learning (particularly self-organizing maps, SOM clustering), and well logging - substantially enhances the reliability of hydrocarbon prospecting, especially in underexplored areas with complex geological frameworks.

20. The developed methodology has demonstrated high efficiency and scalability, allowing it to be effectively applied to other regions of Kazakhstan with similar geological conditions. These results represent a meaningful contribution to the evolution of modern exploration strategies and may serve as a methodological foundation for both public-sector programs and private operators.

21. Looking ahead, further development of AI- and machine learning-based interpretation techniques, including nonlinear modeling of geoscientific data, should be prioritized. This will increase predictive confidence, reduce geological uncertainty, and optimize investment in exploration activities

Conflict of interest.

The authors declare that they have no conflict of interest in relation to this research.

References:

1. Priezzhev, I, Scollard, A. and Lu, Z. Regional production prediction technology based on gravity and magnetic data from the Eagle Ford formation. // Texas, USA. SEG Technical Program Expanded Abstracts: 1354-1358. https://doi.org/10.1190/segam2014-0289.1.
2. Priezzhev, II, PCH, Veeken, SV, Egorov, AN, Nikiforov. 2019. Seismic waveform classification based on Kohonen 3D neural networks with RGB visualization. First Break. Volume 37. Issue 2. Feb 2019. p. 37-43.
3. Grekusis, D. Methods and Practice of Spatial Analysis: With Solution Examples in ArcGIS, GeoDa and GeoDaSpace. // 2021.
4. Abetov, A.Ye., Essirkepova, Sh.B., Kozhamsugirov, D. Effectiveness of aerogamma-spectrometric research in solving applied problems of oil and gas geology. // Геология и охрана недр. 2021. Т. 78. № 1. С.55-62.
5. Abetov, A.E., Yessirkepova, Sh.B., Curto, Ma J. Geomagnetic field transforms and their interpretation at exploration for hydrocarbon field in the southern part of the Ustyurt region. // News of the National Academy of Sciences of the Republic of Kazakhstan. Series of Geology and Technical Sciences. 6(450). 2021. p.6-14. Almaty. NAS RK. ISSN 2518-170X (Online). ISSN 2224-5278 (Print). https://doi.org/10.32014/2021.2518-170X.113.
6. Abetov, A.E., Yessirkepova, Sh.B., Curto, MaJ. Gravity field transforms at the exploration for hydrocarbon field in the southern part of the Ustyurt Region. // News of the National Academy of Sciences of the Republic of Kazakhstan, Series of Geology and Technical Sciences. 3(453). 2022. 17-31. Almaty. NAS RK. ISSN 2518-170X (Online). ISSN 2224-5278 (Print). https://doi.org/10.32014/2022.2518-170X.177.
7. Abetov, A.E., Yessirkepova, Sh.B., Curto, Ma J. Remote sensing in the study of the thermal field of the South Ustyurt region in order to find hydrocarbon deposits. // News of the National Academy of Sciences of the Republic of Kazakhstan. Series of Geology and Technical Sciences. 2(458). 2023. p.6-16. Almaty. NAS RK. ISSN 2518-170X (Online). ISSN 2224-5278 (Print). https://doi.org/10.32014/2023.2518-170X.275.
8. Abetov, A.E., Yessirkepova, Sh.B., Curto, Ma J. The Geomagnetic Field Transformants and Their Complexing with Data of Gravitational. Thermal and Radioactive Fields: During the Exploration of Hydrocarbon Fields at the Southern Part of the Ustyurt Region. // DOI: http://dx.doi.org/10.5772/intechopen.111560.
9. Abetov, A., Niyazova, A., Saurikov, Z. 3d modeling of euler's points for geodensity and geomagnetic models of north ustyurt region in Geosoft Oasis Bontaj. // News of NAS RK. Series of geology and technical sciences. 2017. № 4.
10. Beznosov, N.V., Korchagin, V.I., Nikolaev, A.I. etc. al. Reference Book on the Stratigraphy of Oil and Gas Bearing Provinces of the USSR. // Nedra. Moscow. 1987. 335p.
11. Daukayev, S.Zh., Uzhkenov, B.S., Abdulin, A. A. etc. al. Deep Structure and Mineral Resources of Kazakhstan. // Oil and Gas. Volume 3. Almaty. 2002. 248p.
12. Votsalevsky, E.S., Bulekbaev, Z.E., Iskuzhiev, B.A. etc. al. Handbook of Oil and Gas Fields of Kazakhstan. // Almaty. 1999.
13. Krylov, N.A., Zabolotnaya, Yu.I., Grizik, A.Ya. Geological Exploration and Reassessment of Oil and Gas Prospects in the Uzbek Part of the Ustyurt Region. // Gazprom Bulletin. N.3. 2015. pp. 45-58.
14. Seifullin, Sh.M., Kalinin, M.I., Kryzhko, Yu.A. et al. Report on the high-precision aeromagnetic survey at a scale of 1:50,000 in South Buzachi, Mangyshlak and Ustyurt in 1982-84. // Aerogeological and geophysical expedition, Nikolaevka village. 1984.
15. Kovrizhnykh, P.N. Report on the results of works at a scale of 1:100,000 on the object: "Conducting airborne geophysical and ground-based gravimetric works on the Samtyr site, carried out in 2019 in the Mangistau region (Sheets K-40-16 (partial); K-40-27 (partial); K-40-28; K-40-39; K-40-40; K-40-51 (partial); K-40-52 (partial). // GEOKEN, book 1 198 pages, book 2 130 pages. Almaty. 2019.

16. Florensky, P.V., Mukhametkaliyev, N.Zh., Kuliyev, R.K. et al. Geochemical Features and Generation Potential of Source Rocks in Mangyshlak. // Nedra. Moscow. 1975. 184p.

17. Shablinskaya, T.G., Ginzburg, M.M., Kalugina, N.P. et al. Organic Matter of Triassic and Jurassic Deposits of Western Kazakhstan. // Geology of Oil and Gas. No. 6. 1990. pp.25-33.

18. Tverdova, N.I., Shcherbakov, A.A., Litvinova, N.V. Geochemistry and Source Rock Potential of Triassic Deposits in Mangyshlak. // Geochemistry. No.3. 1982. pp.45-55.

19. Tverdova, N.I., Litvinova, N.V., Baranova, T.A. Generation Properties of Organic Matter in the Jurassic and Triassic of the Mangyshlak Region. // Oil Industry. No.10. 1988. pp. 48-52.

20. Orudzheva, N.A., Isaev, I.A., Alipbekov, S.T. Middle Triassic Source Rocks of Mangyshlak and Their Hydrocarbon Potential. // Nauka. KazSSR. Almaty. 1985. 132p.

21. Polyakova, T.M. Geochemical Characteristics of Jurassic Shales in Southern Mangyshlak. // Reports of the Academy of Sciences of the Kazakh SSR. Geological Series. 1977. No.4. pp.66-71.

22. Milanovsky, E.E. Geodynamics of the lithosphere. // Moscow. Nedra. 1992.

23. Zagorodniy, A.M., Tyumenev, S.S. & Osipov, E.V. Geodynamic Model of Hydrocarbon Potential in the Pre-Caspian Syneclise. // Geology of Oil and Gas, No. 4, 2012. pp. 3-12.

24. Iskandarov, M.Kh., Umarov, Sh.A., Khabibullaev, S.S. Fundamentals of Hydrocarbon Localization Analysis in the Aral–Ustyurt Region. // LAP LAMBERT. Academic Publishing. Germany. 2024. 73p. www.lap-publishing.com.

25. Iskandarov, M.Kh., Tursunova, T.M., Umarov, Sh.A. How Oil and Gas were formed in the Aral–Ustyurt Region. // LAP LAMBERT. Academic Publishing. Germany. 2023. 111p. www.lap-publishing.com.

26. Iskandarov, M.Kh., Umarov, Sh.A. Geological-Geodynamic model and development of a new method for hydrocarbon prospecting in Jurassic and Paleozoic deposits of the Aral-Ustyurt Region. // LAP LAMBERT. Academic Publishing. Germany. 2023. 70p. www.lap-publishing.com.

27. Koroviaka, Ye.A., Mekshun, M.R., Ihnatov, A.O., Ratov, B.T., Tkachenko, Ya.S. & Stavychnyi, Ye.M. Determining technological properties of drilling muds. // Naukovyi Visnyk Natsionalnoho Hirnychoho Universytetu. (2). 2023. p.25-32. https://doi.org/10.33271/nvngu/2023-2/025.

28. Ratov, B.T., Bondarenko, N.A., Mechnik, V.A., Prikhna, T.A. & Kolodnitsky, V.M. A study of the structure and strength properties of the WC-Co drill insert with different CRB2 content sintered by Vacuum Hot Pressing. // SOCAR Proceedings. (1). 2022. p.037-046. https://doi.org/10.5510/ogp20220100626.

29. Montaj MAGMAP Filtering. Software module for two-dimensional processing of potential field data in the frequency domain for Oasis montaj v7.1. // January. 2013.

30. Čermák, V. & Rybach, L. Thermal conductivity and specific heat of minerals and rocks. // In G. Angenheister (Ed.). Landolt-Börnstein - Group V Geophysics: Physical Properties of Rocks. 1982. Vol.1. pp.305-343. Springer. https://doi.org/10.1007/10201924_7.

31. Jessop, A.M. Thermal Geophysics. Elsevier. // 1990. https://doi.org/10.1016/B978-0-444-88943-0.50004-6.

32. Gorny, V.I., Shilin, B.V., Yasinsky, G.I. Thermal Aerospace Imaging. // Nedra. Moscow. 1993. 128 p.

33. Shilin, B.V. Thermal Imaging in the Study of Natural Resources. // Gidrometeoizdat. Moscow. 1980.

34. Dalyan, I.B., Sydykov, Zh.S. Geothermal conditions of the eastern margin of the Pre-Caspian Basin. // Soviet Geology. No.6. 1972. pp. 126-131.

35. Kronberg, P. Remote sensing of the earth: Fundamentals and methods of remote Geological investigations. Translated from German. |// Moscow. MIR Publishers. 1988. 343 p.

36. Moiseenko, U.I. Temperature distribution map of the Earth's crust in the USSR at a depth of 10 km. // Leningrad. Ministry of Geology of the USSR. 1985.

37. Ozdoev, S.M. Prospects for hydrocarbon potential of Kazakhstan's sedimentary basins. // Proceedings of the National Academy of Sciences of the Republic of Kazakhstan. Series of Geology and technical sciences. No.1. 2012. pp.61-76.

38. Zhang, Y., Xiong, W., Zhao, Y., Li, D. & Wang, H. Machine learning-based integration of geophysical data for hydrocarbon reservoir characterization. // Geophysics. *85*(4). B229–B240. 2020. https://doi.org/10.1190/geo2019-0657.1.

39. Bergen, K.J., Johnson, P.A., de Hoop, M.V. & Beroza, G.C. Machine learning for data-driven discovery in solid Earth geoscience. // Science. 363(6433). eaau0323. 2019. https://doi.org/10.1126/science.aau0323.

40. Karpatne, A., Atluri, G., Faghmous, J.H., Steinbach, M., Banerjee, A., Ganguly, A. & Kumar, V. Theory-guided data science: A new paradigm for scientific discovery from data. // IEEE Transactions on Knowledge and Data Engineering. 29(10). 2017. p.2318–2331. https://doi.org/10.1109/TKDE.2017.2720168.

41. Leucci, G. & Chianese, D. Geophysical methods for cultural heritage management. Springer. 2020. https://doi.org/10.1007/978-3-030-49132-6.

42. Reichstein, M., Camps-Valls, G., Stevens, B., Jung, M., Denzler, J., Carvalhais, N. & Prabhat. Deep learning and process understanding for data-driven Earth system science. // Nature. 566(7743). 2019. p.195-204. https://doi.org/10.1038/s41586-019-0912-1.

43. Wu, X., Zhang, Y., Sun, H. & Liu, J. A deep learning method for seismic lithology prediction based on well-log data. // IEEE Access, 7. 136688–136698. 2019. https://doi.org/10.1109/ACCESS.2019.2942713.

44. Elsheikh, A.H., Wheeler, M.F., Hoteit, H. & Hossain, M.E. Integration of geostatistics, geophysics, and machine learning for robust reservoir characterization. // Journal of Petroleum Science and Engineering. 179. 2019. p.910-927. https://doi.org/10.1016/j.petrol.2019.04.036.

45. IAEA, 2003 International Atomic Energy Agency (IAEA). Guidelines for Radioelement Mapping Using Gamma Ray Spectrometry Data. // IAEA-TECDOC-1363. Vienna. Austria. 2003. https://www-pub.iaea.org/MTCD/publications/PDF/te_1363_web.pdf.

46. Sabanov, S.V., Semenova, T.N., Vasyutkin, V.I. Radiogeochemical Methods for Oil and Gas Exploration: Theory and Practice. // M. Наука. 2010. 248 с.

47. Smirnov, S.Z., Nikiforova, G.A., Tsvetkov, M.P. СПб. Недра. 2006. 210 с. Radiogeochemical fields of oil and gas bearing territories. // St. Petersburg. Subsoil. 2006. 210p.

48. El-Kaliouby, B.A., El-Naggar, M.M. & Salama, M.A., Integration of airborne gamma-ray spectrometric and magnetic data for exploration of hydrocarbon microseepage in the Western Desert of Egypt. // Journal of African Earth Sciences. 127. 2017. p.115–129. https://doi.org/10.1016/j.jafrearsci.2016.11.009.

49. Gregorauskas, A., Motiejūnas, S. & Dobilas, G. Application of gamma-ray spectrometry in hydrocarbon exploration in Lithuania. // Geologija. Geografija. 1(1). 2015. p.35-43. https://doi.org/10.6001/geol-geogr.v1i1.3101.

50.Saunders, D.F., Nielson, D.L. & Frank, G.E. Petroleum microseepage and related near-surface alteration in sedimentary basins. // AAPG Bulletin. 77(8). 1993. p.1338-1343. https://doi.org/10.1306/BDFF8D8E-1718-11D7-8645000102C1865D.

51. Donald, F. Saunders et al. Model for Hydrocarbon Microseepage and Related Near-Surface Alterations. // AAPG Bulletin. V.83. No.1. January 1999. P.170-175.

52.Blakely, R.J. Potential theory in gravity and magnetic applications. // Cambridge University Press. 1995.

53. Nabighian, M.N., Grauch, V.J.S., Hansen, R.O., La Fehr, T.R., Li, Y., Peirce, J.W. & Ruder, M.E. The historical development of the magnetic method in exploration. // Geophysics. 70(6). 2005. 33ND–61ND. https://doi.org/10.1190/1.2133784.

54. Hildenbrand, T.G., Gettings, M.E. & Morin, R.L. Constructing magnetic anomaly maps for geologic mapping and interpretation. // U.S. Geological Survey Open-File Report 01-223. 2001.

55. Fairhead, J.D., Green, C.M. & Odegard, M.E. Regional gravity anomaly mapping using wavelets and residual separation. // First Break. 31(1). 53-60. 2013.

56. Telford, W.M., Geldart, L.P. & Sheriff, R.E. Applied geophysics (2nd ed.). // Cambridge University Press. 1990.

57. Reeves, C., Macnab, R. & Finn, C. Airborne geophysics: Old physics, new applications. // The Leading Edge. 26(3). 2007. p.328-333. https://doi.org/10.1190/1.2715058.

58. Matusevich, A.V. The Structure of the Local Gravitational Field as a Basis for Zoning Salt Domes in the Pre-Caspian Basin. Proceedings of the National Academy of Sciences of the Republic of Kazakhstan. // Geological Series, No.5. 2006. pp. 65-76.

59. High-resolution ground-magnetic (HRGM) and radiometric surveys for hydrocarbon exploration: Six case histories in Western Canada. // Le Shack and Van Alstine. January. 2002.

Authors:

Abetov Auez Egemberdievich, professor, doctor of sciences in geology and mineralogy, academician of the National Academy of Sciences of the Republic of Kazakhstan, National Research Technical University named after K.I.Satpayev. Kazakhstan. Almaty. E-mail: abetov.auez@mail.ru.

Yessirkepova S.B., Deputy Chief of Department GIS&DB SPC GEOKEN, PhD student of the National Academy of Sciences of the Republic of Kazakhstan, National Research Technical University named after K.I. Satpayev. Kazakhstan, Almaty. E-mail: sh_yessirkepova@mail.ru.

Iskandarov M.Kh., senior researcher at the Integrated Laboratories for Petrophysical Research of JSC "O'ZLITINEFTGAZ". Uzbekistan. E-mail: manholiskandarov@ gmail.com.

Umarov Sh.A., Scientific secretary. Uzbek Institute of standards. Candidate of technical sciences. Uzbekistan. E-mail: shakhumarov@gmail.com.

Aliyarov R..Y., Director of the Research Institute «Geotechnological Problems of Oil, Gas and Chemistry». Doctor of geological and mineralogical sciences, associate professor. Azerbaijan. Baku. E-mail: r.aliyarov@asoiu.edu.az.

Aslanov B.S., associate professor, chief researcher of the research institute «Geotechnological Problems of Oil, Gas and Chemistry». Doctor of earth sciences. Azerbaijan. Baku. E-mail: beyler@inbox.ru.

Journal of SRI "Geotechnological Problems of Oil, Gas and Chemistry" of ASOIU,
Issue 2, 2025, pp. 44-61
https://doi.org/10.65294/gpogc.2025.02

Prospects for exploration of the non-anticlinal traps of Hovsan shallow water area by geophysical methods

Aslanov Beyler Suleyman [1], Ilkin Safarli Elshan[2]

[1]Institute, Azerbaijan AZ1010, Geotechnological problems of oil, gas and chemistry, Senior Researcher, dress Baku, Dilara Aliyeva Street 227

Abstract. The paper analyzes the complex geophysical (seismic, gravimetric) and downhole geophysical survey (DGS) of the SW part of the Hovsan Shallow Water area, specifying the lithofacies composition of Pliocene sediments, predicting oil and gas potential, identifying promising areas in the Turkan and Gala areas related to non-anticlinal traps, substantiating the directions of search and exploration work for these types of traps, predicting favorable conditions for hydrocarbon accumulation, and predicting oil and gas potential.

At the Hovsan oil and gas field, research work was carried out on the temporal sections of the seismic profile of two common depth points developed in 2004.

Based on the obtained amplitude and energy diagrams, a comparative analysis of anomalies in the zones of minimum values of dynamic parameters of tested and reflected waves at oil and gas facilities of profiles No. 030808 and 030908 was carried out.

As a result, as can be seen from scheme of the seismic profiles in the Hovsan shallow water field, it was assumed that during the migration of oil and gas, the border of this local change in lithology plays the role of local change in lithology, due to the fact that the borders of these local change in lithology diverged due to the approximate overlap with the borders of two small tectonic faults, which are observed at a sufficient distance, based on numerous downhole and seismic data.

Taking into account the complex topography of the area, we have chosen such an observation system, in which field on the Hovsan area is exposed to 2 directions (Shah dili and Gala field island). Here, it was possible to detect trap type anomalies in the same places by radiating the area from different directions. By choosing such a mutual observation system and radiating the same area from different directions, the location of trap type anomalies was determined.

The main purpose of the complex geophysical studies carried out on subjects No. 091-96 and 165-2000 was the predicting and analysis of oil and gas deposits at the Hovsan-Deniz field as a result of the combined use of the seismic exploration method with refracted and reflected waves with high-precision gravimetrical exploration, and determination of formation boundaries in plan and the depth of the section based on trap type anomalies obtained in geophysical areas. Comparative analysis of the trap type anomaly overlapping obtained in 1996 and 2000 on both subjects was conducted and issues related to the non anticlinal trap were examined. The following conclusions and recommendations were made based on the direct exploration of oil and gas fields using complex geophysical methods:

1. In seismic exploration works carried out in the Hovsan area, direct methods of searching for oil and gas fields due to changes in the amplitudes of refracted and reflected waves were used to determine a connection with a lithological fault-bounded non-anticlinal trap, corresponding to different depths (depths of 3600-4200 m) and sediments (related to horizons Lower Girmaki Suite 2 and Lower Girmaki Suite 3) and a formation anomaly was identified;

2. As a result of reservoir-type anomaly, discovered on the basis of a comparative analysis of complex geophysical works carried out in the area No. 165-2000 slightly west of Cape Hovsan, wells No. 1700, 1701, 1703, 1704, 1705, 1706, 1707, 1708, 1709 were drilled and from horizons Lower Girmaki Suite 1, Lower Girmaki Suite 2, Lower Girmaki Suite 3 industrially important oil was produced.

Keywords: Productive Series, oil and gas contour, sediment accumulation process, transgression, regression, konsedimentasion and postsedimentasion, diagenesis, katagenesis, gipergenesis and tektogenesis

Corresponding author. Tel.: +994 12 493 01 80.
E-mail address: E-mail: beyler@inbox.ru; ilkin.1999.99@gmail.com

Introduction. Since the 1930s, seismic, gravimetric, electrical exploration and magnetometric works have been carried out in the Hovsan shallow water area, located in the eastern part of the Absheron Peninsula, and as a result of the geophysical work carried out, it was found that there is a monocline uplift due to the surface of the productive series. In the 1950s and 1960s, in order to study the tectonics of the productive series and the sediments beneath it, a number of works were carried out using the reflection

method and refraction correlation method of seismic exploration, and the location of wells to be drilled for oil and gas was determined [1, p. 17].

In the Hovsan Shallow water area, exploration work was carried out in 1994-1995 to predict oil and gas reservoirs in the productive series sediments based on vertical seismic sounding with reflected waves and precise gravimetric methods, and additional promising areas for oil and gas exploration were identified [1, p. 17].

Considering the complex terrain of the area, we have chosen an observation system in which the field in the Hovsan area is irradiated from 2 directions (Shah Dili and Gala field island) (Figure 1). Here, it was possible to detect the trap type anomaly from the same places by irradiating the area from different directions. By choosing such a mutual observation system and irradiating the same area from different directions, the location of the trap type anomaly was determined (Figure 1).

Research was conducted on the time sections of 2 common depth point seismic profiles developed in 2004 for the Hovsan oil and gas field (Figure 2) [3, p. 17].

Observations were carried out in the WE direction of the field on seismic profile No. 030808 [3, p. 46]. Seismic exploration works were carried out in the field by "Azneftgeofizika" Trust, the top and bottom of the Girmaki suite, Lower Girmaki suite, Lower Girmaki suite Pont layer were monitored, the wave information was evaluated and specified based on well data (Figure 2) [3, p. 47].

As can be seen from the figure, the top and bottom of Girmaki suite are accompanied by high-amplitude intense waves and are well monitored (Figure 3). Here, the wave pattern of the Girmaki suite is observed to be chaotic, slightly transparent trace, which is associated with the clay formation. Intensive, fairly reliable monitoring of the wave landscape is also observed in the upper part of Lower Girmaki suite . Due to the rather complex design, it was possible to trace the top and the bottom of the Lower Girmaki suite by conducting additional studies and using borehole data (Figure 3). The figure shows that the main boundaries are represented by high-amplitude intense waves [3, p. 47].

In addition to the lithological composition of the sediments, other factors are also involved in changing the wave landscape of the Lower Girmaki suite (thickness 300 m), which is considered the main oil and gas facility in the Hovsan Shallow water area [3, p. 76]. These factors can be mainly due to the replacement of oil-saturated reservoirs with water bearing ones, minor tectonic faults, paleomorphological conditions, and other geological processes involved in the formation of Lower Girmaki suite. If we carefully consider the paleo-reconstructed sections, we can see that the roof of Lower Girmaki suite$_1$ and Lower Girmaki suite$_3$ in both sections was washed away (Figure 4). Here, the change in the thicknesses of Lower Girmaki suite$_1$ and Lower Girmaki suite$_3$ in area and cross-section is more clearly visible [3, p. 76]. For this reason, we see that the thickness indicated in section No. 030808 is less in the middle part of the section. The thickness of the Lower Girmaki suite$_2$ horizon varies less than Lower Girmaki suite$_1$ and Lower Girmaki suite$_3$ and is quite stable (Figure 5) [3, p. 80].

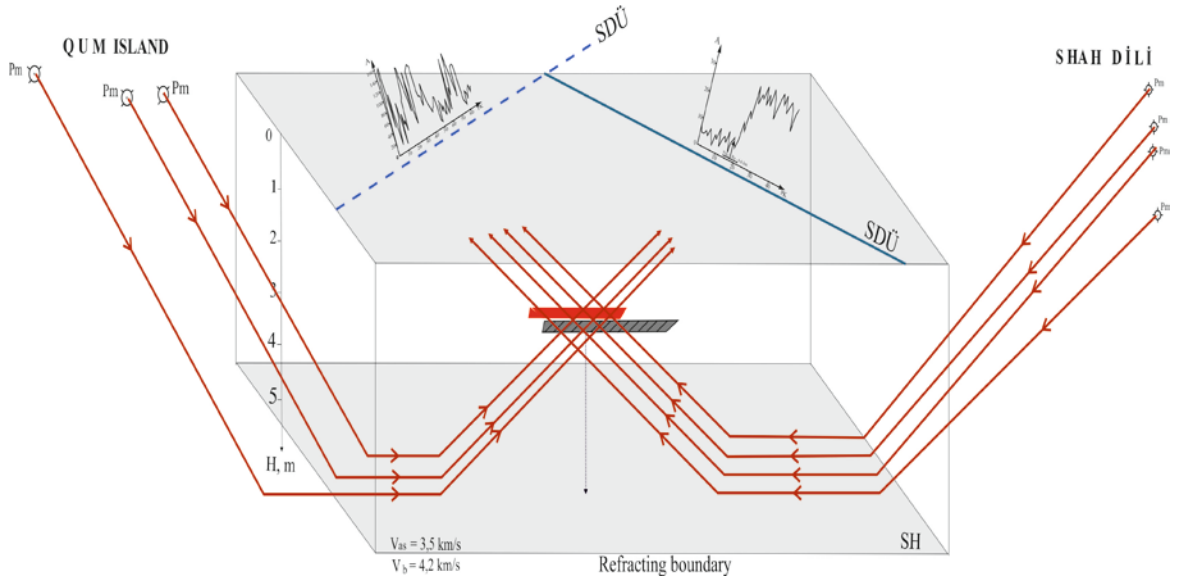

Figure 1. Forecasting of the oil and gas field in the Hovsan area from different directions
Legends:
1 – Amplitude curve; 2 – path of the refracted wave ray; 3 – refracting boundary; 4 – boundary velocity; 5 – profile (refracted waves method); 6 –trap type anomaly of 1996; 7 –trap type anomaly of 2000; 8 – Explosion point.

Seismic profile No. 030908 was developed intersecting seismic profile No. 030808 in the NE-SW direction of the field (see Figure 2). The wave pattern of both profiles is practically the same. As can be seen from the figure, the description of high-amplitude waves characterizes the complexities in the section (figure 6).

Oil and gas facilities have been predicted in the section based on seismic data. It can be assumed that the increase in the thickness of the lower Girmaki suite in the eastern direction of the section is related to the conditions of sedimentation and the exposure of some boundaries to washing [20, p. 54].In the seismic section, productive facilities are attributed to the lower Girmaki suite 1 and lower Girmaki suite 2 horizons. Here, oil and gas reservoirs (the first 170-460 trass) are observed at a 3100-3700 m depth interval, and their thickness is 40-100 m (Figure 6).

Oil and gas facilities were predicted in the seismic dynamic depth section [3, p. 73]. In the seismic section, productive facilities are attributed to the lower Girmaki suite 2 and lower Girmaki suite 3 horizons. Here, oil and gas reservoirs (the first 90-450 trass) are observed at a 3500-4000 m depth interval, and their thickness is 80-90 m (Figure 7).

Thus, formations with reservoir properties were separated on the dynamic depth sections of both profiles involved in the research, and their oil and gas content was predicted. As a result,

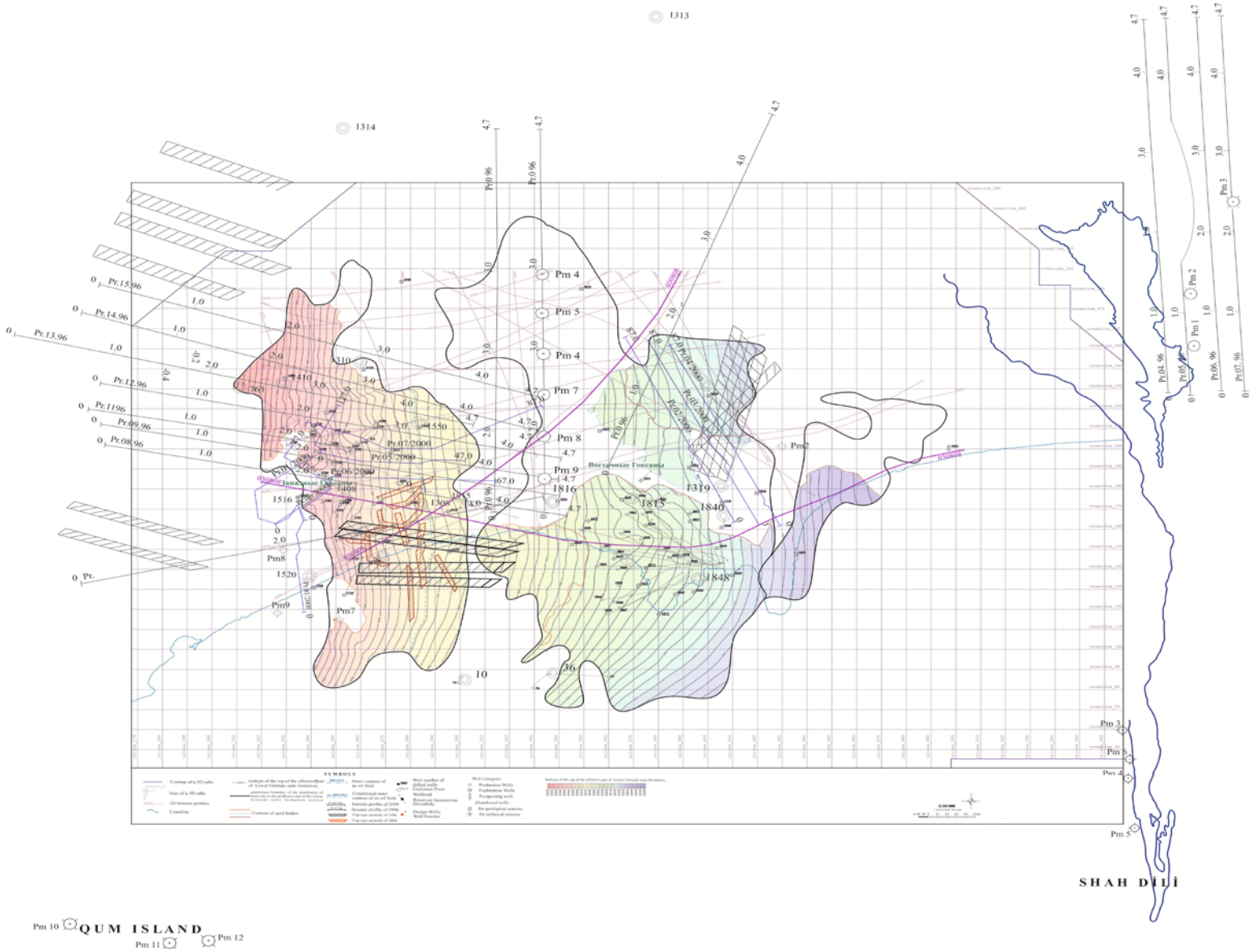

Figure 2. Location map of seismic profiles in the Hovsan Shallow water area [1; 2; 3; with addition by M. Huseynova].

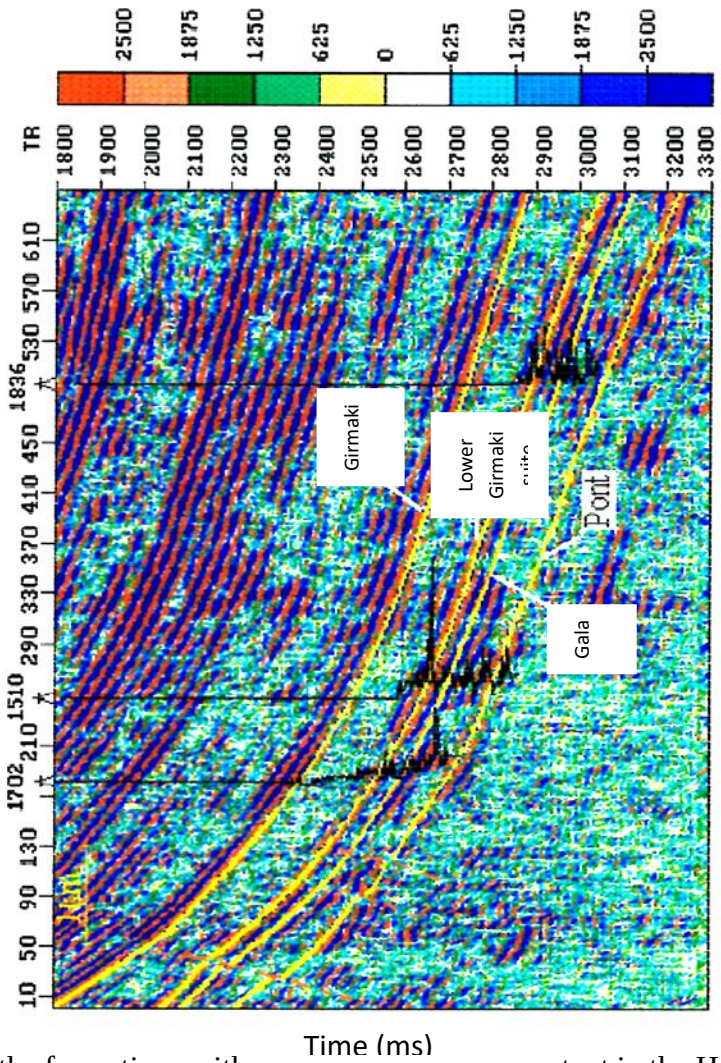

Figure 3. Selection of research facilities in seismic time-section.

the formations with negative oil and gas content in the Hovsan area are found in the section between two small tectonic faults that are traced over a long distance, intersecting the area in the SE-NE directions on the structural map based on well data. These faults can be one of the factors preventing the migration of oil and gas to the reservoirs located between them (see: fig. 2, 9) [3, p. 73].

As a result of the joint analysis of the sections, which reflect the amplitude and energy graphs, seismic dynamic cross sections, well data, and the distribution of petrophysical parameters, two oil-gas regions separated by a supposed "screen" were predicted [3, p.84]. It is predicted that the oil and gas reservoirs, which are attributed to non-anticlinal traps, located in the southwest of the area and the width of the assumed local change in lithology separating them is approximately 1200-1400 m (See: Figure 4, 8) [3, p. 84].

The depths and distribution areas of stratigraphic units in the lower productive series sediments were specified and traced along seismic sections by jointly processing and interpreting seismic profiles 030808 and 030908 and well data located close to them [3, p. 83]. In addition, the lithofacies characteristics of the formations were evaluated, amplitude and energy graphs were calculated, and on the basis of the joint analysis with the correlation scheme established by the well data, a local change in lithology preventing the migration of oil and gas was predicted, trap-type anomalies were identified, and log and seismic data were adapted. Another interesting pattern observed in the paleosections is that the existence of presumed lenticular structures is manifested in the form of local change in lithology and as a result of the sediment accumulation process, the formation of lithological non-anticlinal trap is observed (see: fig. 4, 8) The seismic wave pattern of these structures, separated by elliptic curve in the sections,

and the local change in lithology, which is observed to be related to small-amplitude tectonic faults, play an important role in the distribution of oil and gas reservoirs across the section and area [3, p. 80].

As a result, as can be seen from the layout of seismic profiles in Hovsan Shallow Water area (see: fig. 2, 9), due to the approximate overlapping of the borders of two small tectonic faults, which are traced at a sufficiently large distance by numerous wells and seismic data it is assumed that the borders of these separated local change in lithology act as local change in lithology during oil and gas migration (see: Figure 7, 8) [3, p. 80].

Thus, as can be seen from the paleoreconstructed section of seismic profile 030808 (see: Figure 4), it is assumed that there is a local change in lithology with a width of approximately 1370 m, attributed to lower Girmaki suite 1, lower Girmaki suite 2 and lower Girmaki suite 3 intersecting the SE direction of the area, in seismic profile 030908 (see: Figure 8), it is assumed that there is a local change in lithology with a width of approximately 1200 m, attributed to lower Girmaki suite 1, lower Girmaki suite 2 and lower Girmaki suite 3 intersecting the NE direction of the area [3, p. 80].

As a result, the seismic exploration data of the Hovsan area were evaluated, the wells drilled in the area and the seismic exploration data were comprehensively processed and interpreted in order to separate small thickness formations and predict their probable oil and gas content, the research interval was defined, the sections were traced and dynamic analyses (instantaneous amplitude, frequency, phase, etc.) were conducted on them [3], the geological structure was specified according to the lower productive series sediments, it was determined that the trap type anomaly was related to non-anticlinal traps (lithological and tectonic screened traps) discovered in the SE part of the area, and criteria were developed for separating the traps.

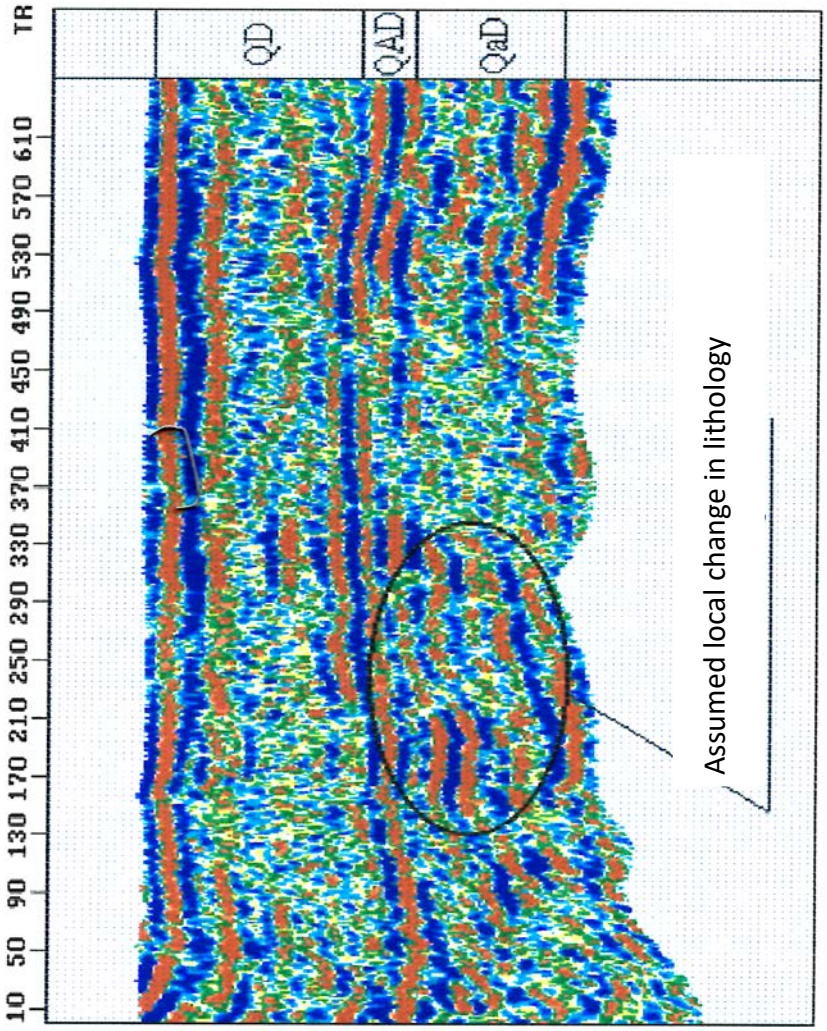

Figure 4. Paleoreconstructed section of seismic profile.

PR 03080813 n 781

Transverse seismic profiles 01.96 – 07.96 developed in the Hovsan Shallow Water area are located west of the Hovsan region and the exploration points are located 6-7 km east of the profiles. Processing and interpretation of the materials of transverse seismic profiles No. 01.96.-07.06 was predicted oil and gas content under the Hovsan region (See: Figure 9) [1, p. 26].

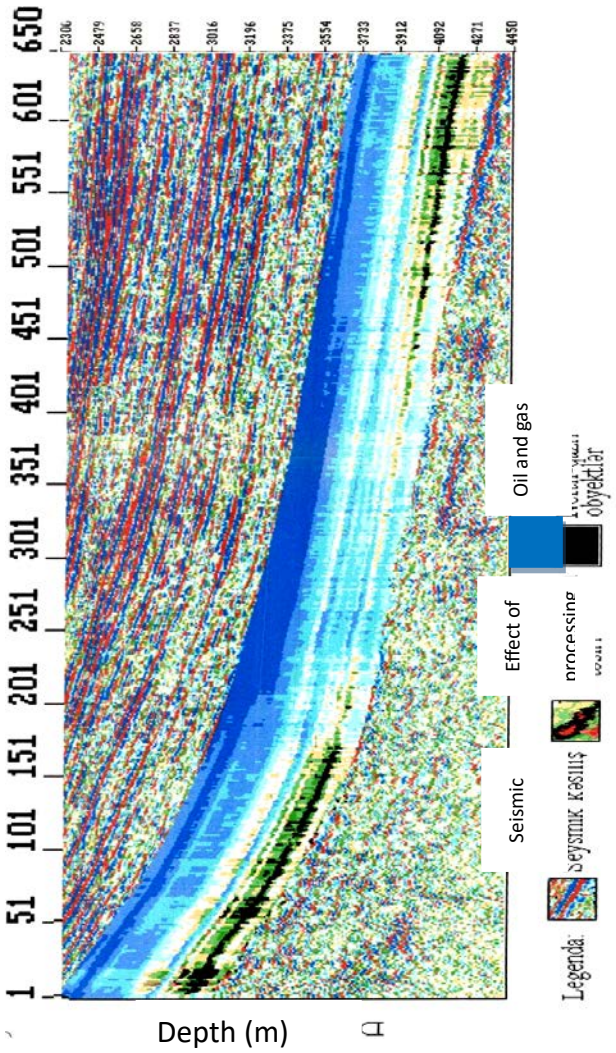

Figure 5. Distribution of assumed oil and gas facilities by depth section.

Exploration Point. 030808. [3, p. 61].

The results of the cross-sectional seismic profiles numbered 02.96 and 03.96 are shown in Figure 10. [1, p. 26]. At the beginning of both profiles, between stakes 0-20, a Trap Type Anomaly characteristic of an oil-gas field was observed, with the seismic boundary depth determined to be 4800 m, and the depth of the presumed oil-gas reservoir established at 4200 m. These depths correspond to the upper part of the Miocene deposits and the productive series deposits of Lower Girmaki Suite 1, Lower Girmaki Suite 2, and Lower Girmaki Suite 3. [1, p. 28].

Profiles numbered 09.96, 10.96, 12.96, and 14.96 are located in the northern part of the field. The distance from the profiles to the explosion points is 4.5 – 5.0 km, and the distance between the explosion points is 0.5 km. Amplitude anomalies characteristic of the oil-gas field have been observed in each profile (PK 0-12). Here, the seismic boundary depth is between 3700-4000 m, while the depth of the presumed oil-gas reservoir is estimated to be around 3250 m. (See: figure 9, 11) [1, p. 32].

The location of the Trap-Type Anomalies detected in the Hovsan Sea area has been specified on the plan. (See: figure 8). As can be seen, the presumed oil-gas reservoir beneath the Hovsan settlement extends towards the sea in the southwest direction. (figure 9) [1, p. 32].

Based on the structural map constructed according to the surface of the Miocene deposits, it can be inferred that the tectonic structure of the Miocene deposits may play a key role in the formation of the identified oil and gas reservoirs in the Hovsan Sea area. Thus, the observation of a buried volcano at the Miocene surface in the Zıgh and Qum island- offshore areas (Figure 9) could be a key factor in the formation of oil and gas reservoirs. "The structures formed by the buried volcanoes, such as the Bibi-

Heybat and Qum island-offshore fields, are large oil and gas reservoirs of significant industrial importance." [1, p. 47].

Field seismic exploration in Hovsan shallow sea area was carried out by recording waves refracted and reflected in transverse profiles by direct search method. The profiles were located on the shore, while the explosion points (EP) were used on Qum Island, the Turkan field, and cape of Shah dili (figure 9, 12, 13) [1, p. 18].

In the seismic records obtained along the transverse seismic profiles processed from wave sources No. 3, 4, 5, 6 in the areas of Gum island, Turkan and Shah dili several correlated seismic waves were observed, amplitude and energy plots of their dynamic and kinematic parameters were plotted along the profile, as a result of which local anomalies were identified and it was analyzed that these oil and gas zones belong to non-anticlinal traps (see Fig. 9, 12, 13).

Based on the obtained amplitude and energy plots on the profiles, the zones of maximum and minimum values of dynamic parameters of tested and reflected waves were selected. The characteristic minima were compared, and oil and gas objects were forecasted based on the technique of direct search in the graphs (see: Figs. 10, 12, 13) [1, p.19].

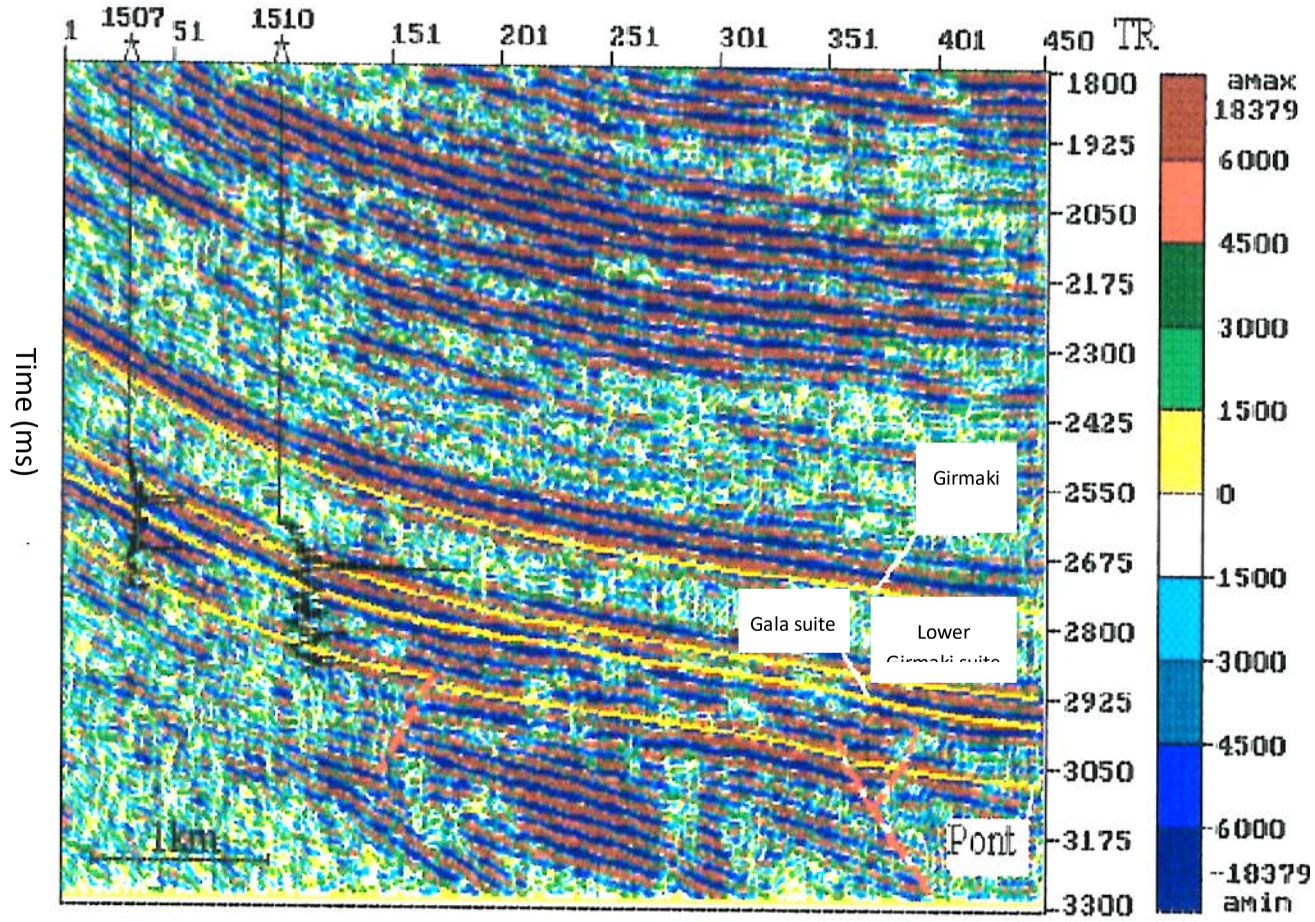

Figure 6. Selection of research facilities in seismic time-section.

Exploration Point, 030908 [3, p. 63]

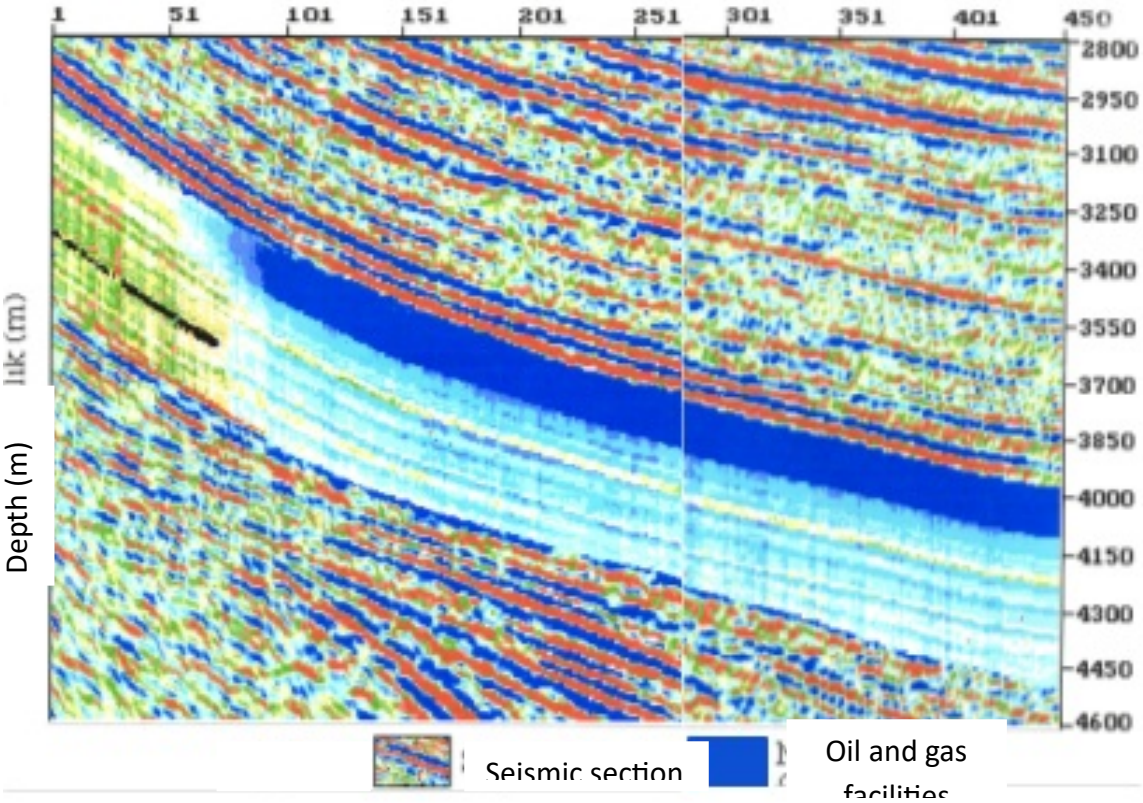

Figure 7. Distribution of assumed oil and gas facilities by depth section. Exploration Point 030908 [3, p. 75].

Assumed local change in lithology

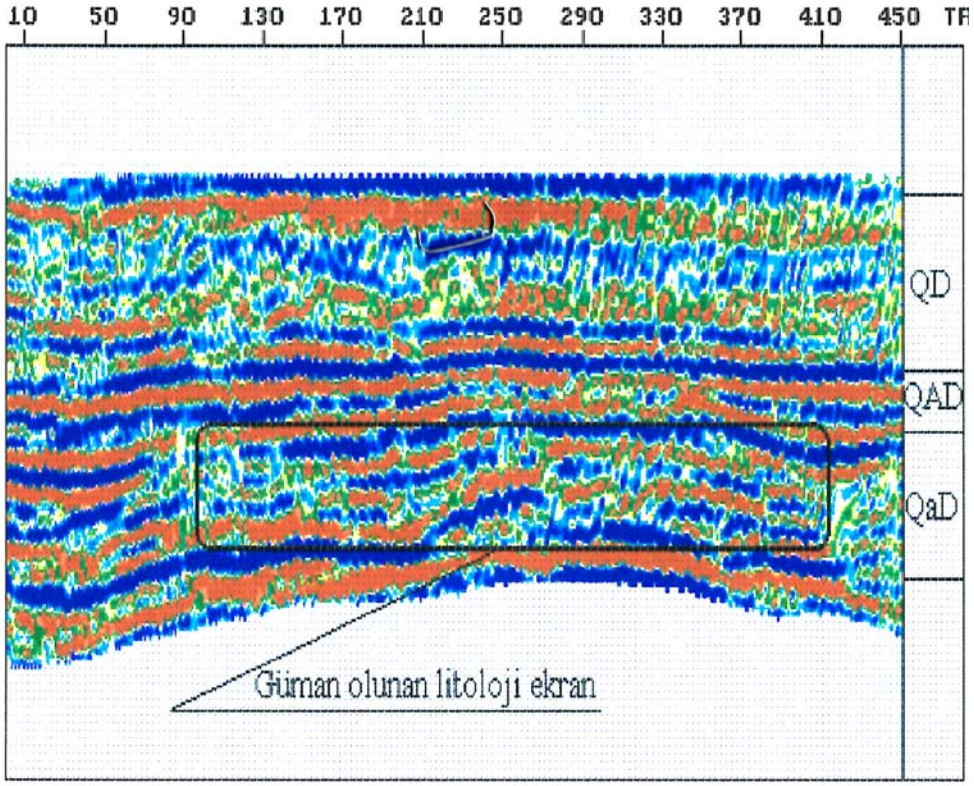

Figure 8. "Paleo-reconstructed section of the seismic profile."

PR 030908 [3, p. 79].

Figure 9. Location scheme of the profiles involved in the study and the Trap Type Anomaly based on seismic data [1, p. 49; 2, p. 44; with the additions of M. Huseynova].

At Hovsan-Deniz field other profiles - profiles Nos. 01/2000 and 01A/2000 in the South-West - North-East direction, as well as profiles Nos. 02-04/2000 in the South-East - north-West direction are developed according to the form close to reciprocal profiles. Profile No. 01/2000 is completely reworked from explosives-1,2,5,6 and partially from explosives 3.4. Profiles 02-05/2000 are processed from explosives -7,8 and profiles 06-08/2000 are processed from explosives -7,9 (see: Figure 9, 12, 13).

Based on the geophysical and well surveying data (WSD) in the Hovsan Shallow Sea area, seismic boundaries related to the productive series sediments and lower ones have been established in the south-north direction, and it has been observed that the depth boundaries lie unconformably towards the coast (from sea to land) and there is an uplift (See: Figure 9, 10, 11, 12, 13) [1; M. Huseynova].

Considering the minima of the dynamic parameters of seismic waves recorded at different arrivals, trap-type anomalies (PTA) were detected and the nature of these minima indicates certain complications (such as fractures), leading to the disruption of the formation's integrity across the area. The proposed field is expected to belong to the Lower Girmaki Suite 1, Lower Girmaki Suite 2, and

Lower Girmaki Suite 3 horizons at depths of 3600m to 4200m (see Figures 9, 10, 11, 12, 13) [1; M. Huseynova].

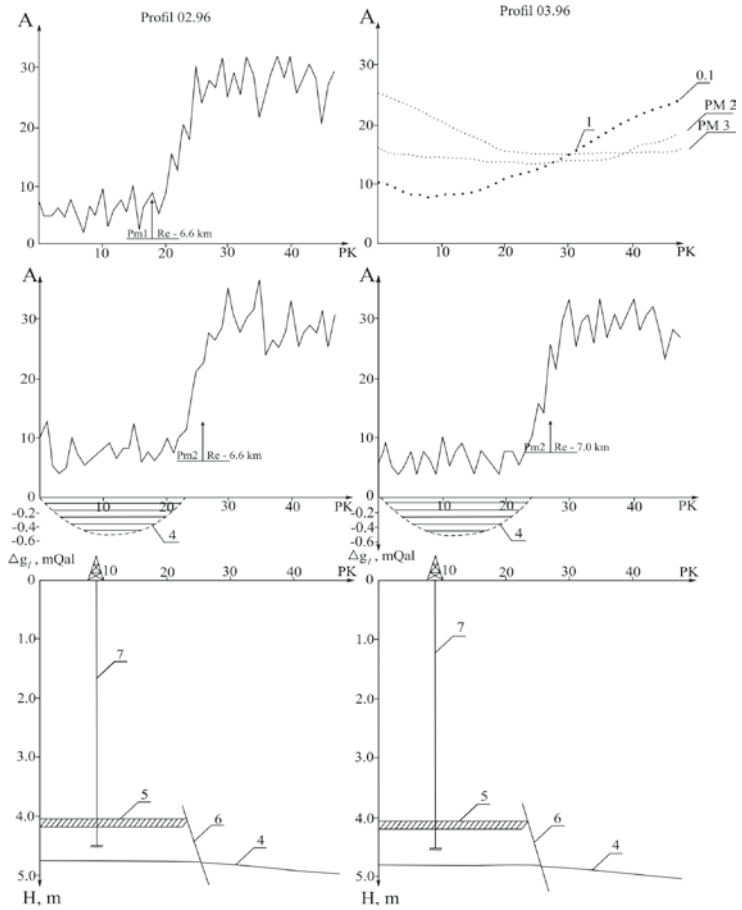

Figure 10. Results obtained on seismic profiles 02.96 and 03.96. [1, c. 24].

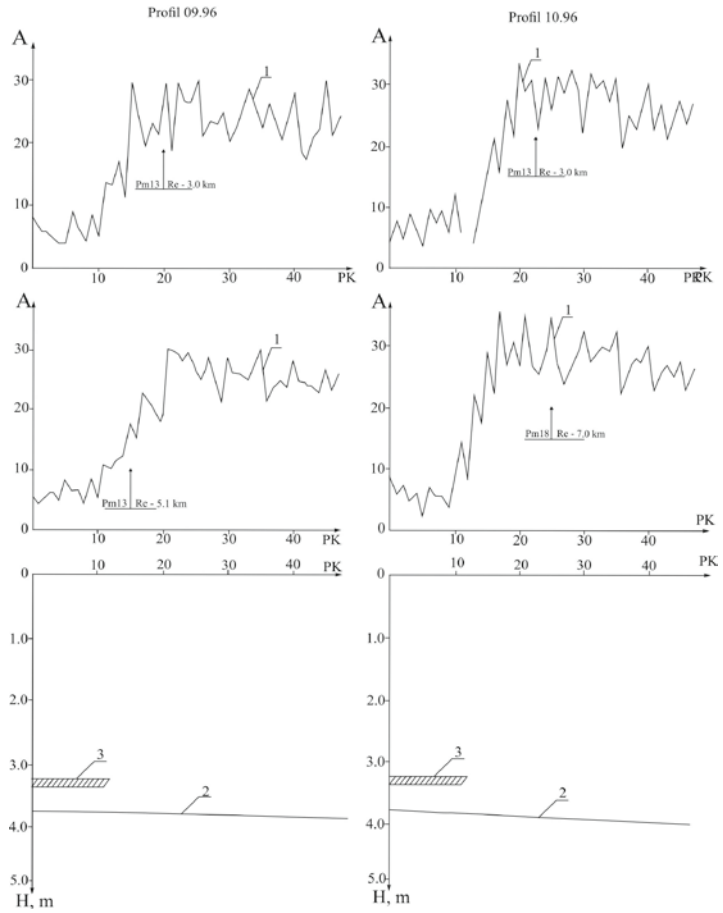

Figure 11. Results obtained on seismic profiles 09.96 and 10.96. [1, c. 33].

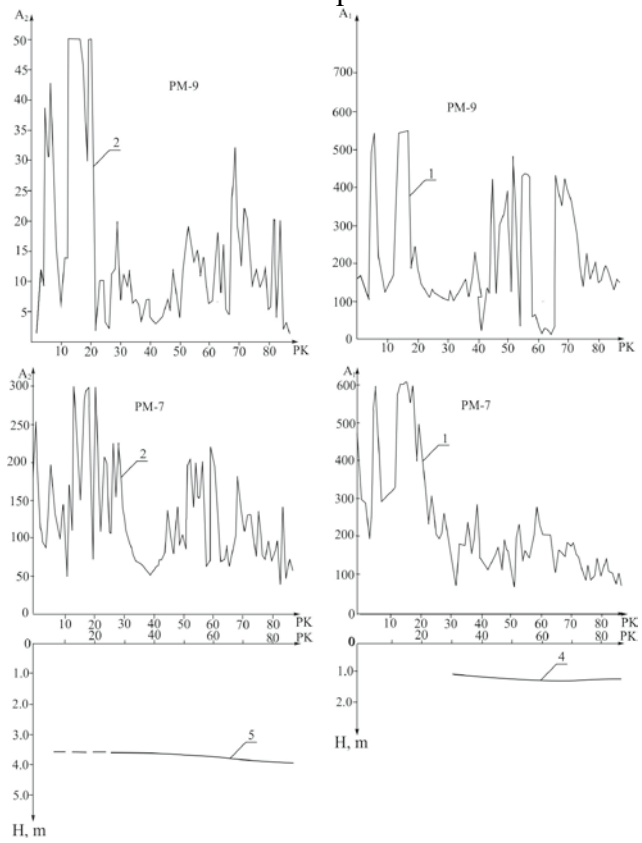

Figure 12. Results obtained on seismic profile No. 06/2000.

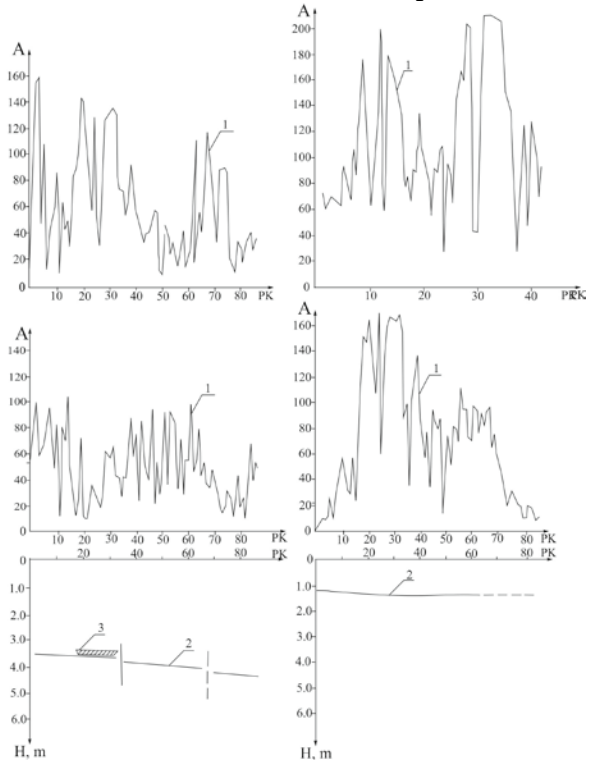

Figure 13. Results obtained on seismic profile No. 07/2000.

Based on the obtained amplitude and energy graphs, a comparative analysis of anomalies was performed at oil and gas bearing objects of profiles No. 030808 and 030908, and in the zones of minimum values of the dynamic parameters of refracted and reflected waves (Figures 14, 15). As can be seen from the graphs, characteristic minima were compared, and oil and gas objects were predicted using the direct search method. This also shows that, according to seismic sections (profiles No. 030808 and 030908), findings from both the refracted wave method and the reflected wave method suggest and confirm the presence of anomalies in the same zone (see Figures 2, 14, 15). Data obtained from amplitude and seismic sections were plotted in one column and comprehensively interpreted.

As a result of an observed decrease of 3.5-4 times in amplitude intensity between stakes 21 and 51 derived from the refracted wave amplitude graph recorded on profile No. 06/2000 (with the depth of the trap type anomalies approximately 3500m to 4000m) and a decrease in amplitude intensity of 3.5-4.2 times between stakes 10 and 45 derived from the refracted wave amplitude graph provided on profiles No. 07/2000 (with the depth of the trap type anomalies approximately 3500m to 4200m) taken from the North, wave sources No. 7 and 9, evidence suggesting the presence of oil and gas was revealed in the Lower Girmaki Suite 2 and Lower Girmaki Suite 3 horizons. On profiles No. 030808 (route No. 201-501) and 030908 (route No. 10-450), with the application of the common depth point (CDP) method, indications of the presence of oil and gas prospects were identified in the same zones (see Figures 2, 14, 15).

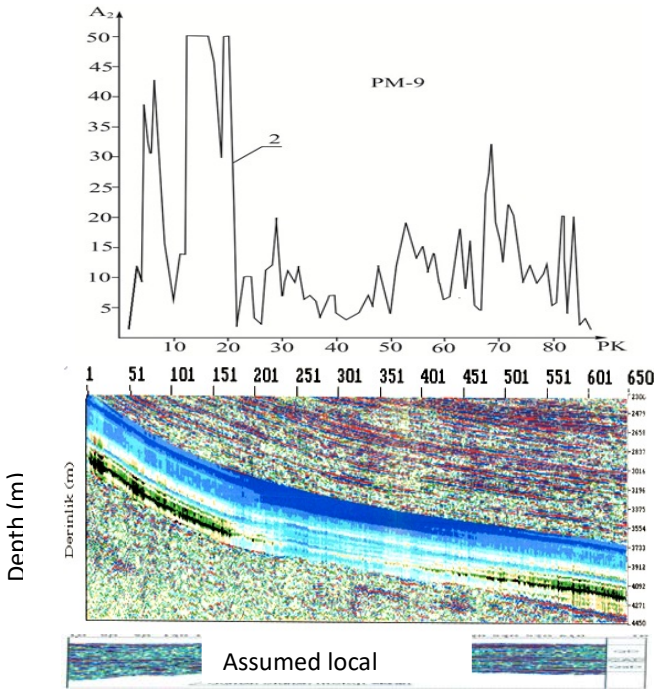

Fig 14. Results obtained on seismic profile No. 06/2000 and seismic dynamic depth section No. 030808 [3, p. 61, 78; with additions by M. Huseynova].

Based on the data from profiles No. 030808 and 030908, with the applied CDP method, sections were built in the Petrol software (instantaneous amplitude, instantaneous frequency, instantaneous phase [3, pp. 50, 65], amplitude, energy, hodograph). The graph and the sections were plotted in the same column to compare the sections. As a result of a comparative analysis of the data obtained using refracted and reflected wave methods, the correspondence of these indications with the oil and gas-bearing objects was confirmed (see Figures 14, 15).In 2000, it was recommended to drill wells based the results of scientific studies conducted with my participation.

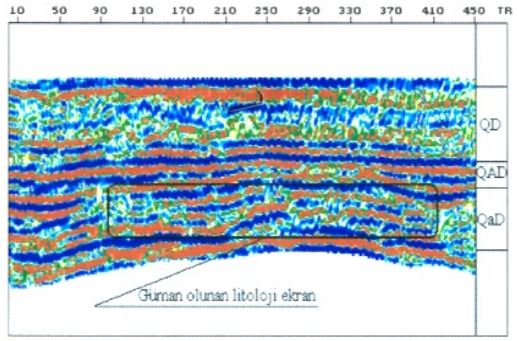

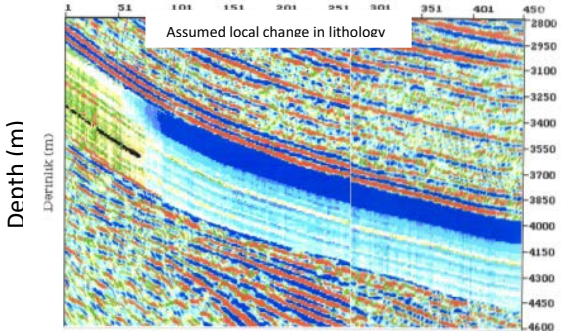

Fig 15. Results obtained on seismic profile No. 07/2000 and seismic dynamic depth section No. 030908 [3, p. 75, 79; with additions by M. Huseynova].

In 1996-2000, as a result of works on these zones, drilling of wells No. 1700-1709 was recommended and positive results were obtained. In the following years Azneft PU achieved positive results within the anomalies in this zone.

In 2000, research work on new profiles was again carried out in this area and trap type anomaly was obtained for this area. Based on the results obtained, it was decided to confirm each other as a result of comparing the results of the work carried out in 1996 with the data obtained.

As a result, the main purpose of the complex geophysical studies carried out on subjects No. 091-96 and 165-2000 was the predicting and analysis of oil and gas deposits at the Hovsan-Deniz field as a result of the combined use of the seismic exploration method with refracted and reflected waves with high-precision gravimetrical exploration, and determination of formation boundaries in plan and the depth of the section based on trap type anomalies obtained in geophysical areas. [10, p. 48; 13; M. Huseynova]. A comparative analysis of overlapping of trap type anomalies obtained in 1996 and 2000 on both subjects was carried out, and their connection with non-anticlinal traps was considered. The following conclusions and recommendations were made based on the direct exploration of oil and gas deposits using complex geophysical methods [1, p. 48; 13; M. Huseynova]:

1. The seismic trap type anomaly detected as a result of comparative analysis of complex geophysical subjects conducted on topics 091-96 and 165-2000 in the Hovsan Shallow Water area largely coincides and confirms each other. In the CQ part of the study area, the trap type anomalies obtained for both subjects overlapped and were determined to be attributed to lithologically and fault-bounded non-anticline traps. Here, the presumed oil and gas field (lithologically and fault-bounded non-anticline traps) is attributed to Lower Girmaki Suite 1, Lower Girmaki Suite 2 and Lower Girmaki Suite 3 and is located at a depth of 3500-4200 m.

2. As a result of reservoir-type anomaly, discovered on the basis of a comparative analysis of complex geophysical works carried out in the area No. 165-2000 slightly west of Cape Hovsan, wells No. 1700, 1701, 1703, 1704, 1705, 1706, 1707, 1708, 1709 were drilled and from horizons Lower Girmaki Suite 1, Lower Girmaki Suite 2 and Lower Girmaki Suite 3 industrially important oil was produced. The depth of the suspected deposit (including parts with non-anticlinal traps) is about 3500-4200 m.

In this part of the thesis work, as a result of the analysis of complex geophysical (seismic) works and downhole geophysical survey (DGS) in the Hovsan shallow water area, the lithofacies composition of Pliocene deposits was clarified, oil and gas potential was predicted, parts of potentially productive areas were determined, especially those related to non-anticlinal traps, to these types traps, the directions of exploration operations were substantiated, a repeated analysis of the presence of favorable conditions for hydrocarbons accumulation and the prospects for oil and gas extraction was carried out.

Here, seismic work needs to continue offshore to fully define the boundaries of the field.

Conflict of interest

The author declare that they have no conflict of interest in relation to this research.

References

1. Mustafayev Q.A., Məmmədov S.H., Şəkərov H.İ. “Kompleks geofiziki (seysmoqravimetrik) tədqiqatlarla Hövsan-Dəniz sahəsində neft-qaz yataqlarının birbaşa axtarışı” (Bakı: 1996-cı il) // “Neftqazelmitədqiqatlayihə” İnstitutunun fondu, Fond № 203, iş № 091-96, - 68 s.

2. Novruzov, Ə.Q. “Kompleks geofiziki (seysmoqravimetrik) birbaşa axtarış üsullarla Hövsan Dayaz Dəniz sahəsində Pliosen çöküntü qatlarının tektonik quruluşunun tədqiqi neft və qaz yataqlarının proqnozlaşdırılması ” (Bakı: 2001-ci il) // “Neftqazelmitədqiqatlayihə” İnstitutunun fondu, Fond № 219, iş № 165-2000, - 74 s.

3. Şıxəliyev Y.A. “Seysmik kəşfiyyat və quyu məlumatları əsasında Hövsan sahəsində Məhsuldar Qat çöküntülərinin alt şöbələrinin geoloji quruluşunun və neftli-qazlılığının dəqiq öyrənilməsi” (Bakı: 2005-cü il) // “Neftqazelmitədqiqatlayihə” İnstitutunun fondu, Fond № 1411, iş № 047-2004, - 99 s.

Journal of SRI "Geotechnological Problems of Oil, Gas and Chemistry" of ASOIU,
Issue 2, 2025, pp. 62-67
https://doi.org/10.65294/gpogc.2025.03

Geological and geochemical characteristics of the Qosha gold deposit and the role of rare elements in ore genesis

G.I. Guseinova[1*], G.S. Guseinov[1], R.N. Ahmedova[1], A.R. Babaev[1], V. Kh. Hamzayev[1]

[1]ASOIU, SRI "Geotechnological Problems of Oil, Gas and Chemistry"

Abstract. Systematic geological investigations in the Qosha ore area began in 1966, when reconnaissance surveys at a scale of 1:50,000 were conducted between the Aghstafachay and Zayamchay river valleys. These initial studies led to the discovery of the Qosha gold deposit. Subsequent detailed exploration campaigns refined the geological framework of the deposit and resulted in the identification of 19 gold-bearing zones.

From 2005 onward, Azerbaijan International Mining Company Limited carried out phased and comprehensive geological exploration, culminating in the commencement of commercial extraction in 2014. Scientific evaluations conducted by the company confirmed that the deposit belongs to the high-sulfidation epithermal genetic type. The geological characteristics of the system were investigated through an integrated analysis of hydrothermal alteration patterns, ore paragenesis, and the lithogeochemical properties of magmatic rocks that reflect the nature and origin of the hydrothermal fluids responsible for ore formation.

Keywords: Qosha deposit, gold, ore minerals, hydrothermal alterations, Tovuz, Azerbaijan.

[*]Corresponding author. Tel.: +994705021152
E-mail address: **guler.huseynli2001@inbox.ru** (G. Guseinova)

Introduction. The geological framework of the Qosha deposit, located within the Qosha contract area, has been comprehensively characterized through investigations conducted by Azerbaijan International Mining Company Limited. The deposit is dominated by a Lower Bajocian volcanic–pyroclastic assemblage composed of a differentiated basalt–andesite–dacite–rhyolite sequence.

The Lower Bajocian subunit (basalt–andesite subformation) is distinguished by several lithological and mineralogical horizons, including:

1. A horizon of zeolitized andesite porphyry.
2. A fine- to medium-grained zeolitic andesite horizon.
3. An andesite-porphyry horizon containing almond-shaped vesicles filled with quartz–carbonate material.
4. A lens-shaped unit comprising magnetite-bearing sandstones associated with fine-grained andesite and andesite–basalt rocks.
5. A medium-grained andesite-porphyry horizon.
6. A clastic horizon composed of andesite and andesite–basalt lithologies.
7. An andesite porphyrite horizon containing lenses of lava breccia and agglomerate tuff.

This classification demonstrates that the Lower Bajocian succession is predominantly composed of intermediate volcanic rocks. The presence of extensive hydrothermal alteration, however, significantly obscures their original petrological characteristics. Within the boundaries of the Qosha deposit, the Lower Bajocian strata attain a thickness of approximately 390–400 meters.

The Upper Bajocian unit (dacite–rhyolite subformation) is broadly developed within the Qosha gold deposit and is predominantly concentrated along the western flank of the ore field. These rocks constitute the Qosha–Itqırılan subvolcanic bodies, whose eastern contact extends through the area where adits No. 2, 5, and 6 are located, while the western boundary trends toward the northeastern outskirts of Qosha village.

In the western sector of the deposit, the rhyolite–dacite assemblage rests unconformably upon the Lower Bajocian sedimentary-volcanic sequence. Along the external contacts of these intrusions, zones of kaolinization, pervasive sulfide alteration (primarily pyrite), and locally weak hornfelsing are observed. In contrast, the internal contact zones are characterized by the development of monquartzite bodies formed through the thermal and metasomatic influence of rhyolite and rhyolite–dacite magmatism.

The purpose of study. Tectonically, the Qosha deposit is situated within the western segment of the Shamkir uplift, belonging to the Lok–Karabakh structural–formational zone. The core of the Shamkir anticlinorium is composed of Paleozoic metamorphosed schists, whereas its flanks consist of Lower and Middle Jurassic sedimentary–volcanic successions. Within this structural framework, two major northwest-trending anticlines—the Boyuk-Gishlag and Ahmadabad–Qosha structures—are distinguished. The architecture of these anticlines incorporates complex volcanic–pyroclastic assemblages of intermediate to acidic composition belonging to both the Lower and Upper Bajocian stages.

A bending of the hinge zone of the Ahmadabad–Qosha fold near the Qosha deposit has resulted in the formation of subsidiary brachyfolds. The Qosha–Itqırılan anticline extends through the localities of the same name along a 35–40° northeast-oriented axial trend. Faulting is extensively developed in the area, and several faults possess deep-seated characteristics. At the surface, these structures are expressed as fragmented, fissured, and hydrothermally altered zones commonly associated with magmatic bodies and their vein-type derivatives.

Magmatism of Middle Jurassic age plays a dominant role in defining the geological and metallogenic features of the Qosha deposit. Volcanic activity commenced in the Early Bajocian and persisted intermittently until the close of the Bathonian. This magmatic evolution is characterized by differentiated basalt–andesite, dacite–rhyolite, and quartz diorite–granodiorite subformations. The most intense eruptive activity occurred during the Bajocian, when the principal volcanic apparatus was emplaced along the westward-trending Ahmadabad–Qosha deep fault, forming a laterally continuous volcanic mass.

Volcanic eruptions during this interval were predominantly explosive, marked by substantial emission of pyroclastic material and volcanic gases, resulting in the dominance of pyroclasts within the lava sequences. The Bajocian volcanic assemblage also includes numerous small intrusive bodies—dykes, sills, and stocks—of varying dimensions and morphologies. These intrusions indicate that, during certain stages, effusive lava outflow occurred under relatively calm conditions.

Within the Qosha deposit, metasomatic alterations can be classified into two fundamental genetic types: contact-related metasomatites and fracture-controlled hydrothermal metasomatites. These rock assemblages are exposed at the surface, within adits No. 4, 7, and 8 across the upper and middle reaches of the Asrikchay and Axıncachay valleys. Comparable alteration zones also occur at the Böyük-Shamlıq, Böyük-Qıshlaq, and Qosha–Itqırılan pyrite-bearing prospects.

The hydrothermally altered rocks in these areas are localized along major deep-seated faults and in the zones where such faults intersect with subsidiary tectonic disruptions. Gold-bearing metasomatite halos develop preferentially within these structurally weakened domains and are typically situated close to the surface.

The Qosha deposit belongs to the gold–sulfide–quartz formation and is characterized by submeridional ore zones that occur as branching veins and mineralized bands. These zones are sharply bounded from their host rocks. The wall rocks consist mainly of greyish-black andesite and andesite–porphyry, which exhibit fine-grained pyritization, silicification, and weak kaolinization. In certain intervals, infiltration of groundwater generates a viscous kaolin–pyrite mass that partially fills the underground workings.

The submeridional ore zones are structurally aligned with fault systems and commonly form well-defined contacts with adjacent rocks. With dips ranging from 80° to 90°, these bodies possess a distinctly vein-like morphology. Subparallel veins occur across all meridional structural corridors, and clusters of narrow veinlets may coalesce to form a single ore body. These veinlets commonly pinch and swell both along strike and down-dip, reappearing intermittently (Figure 1).

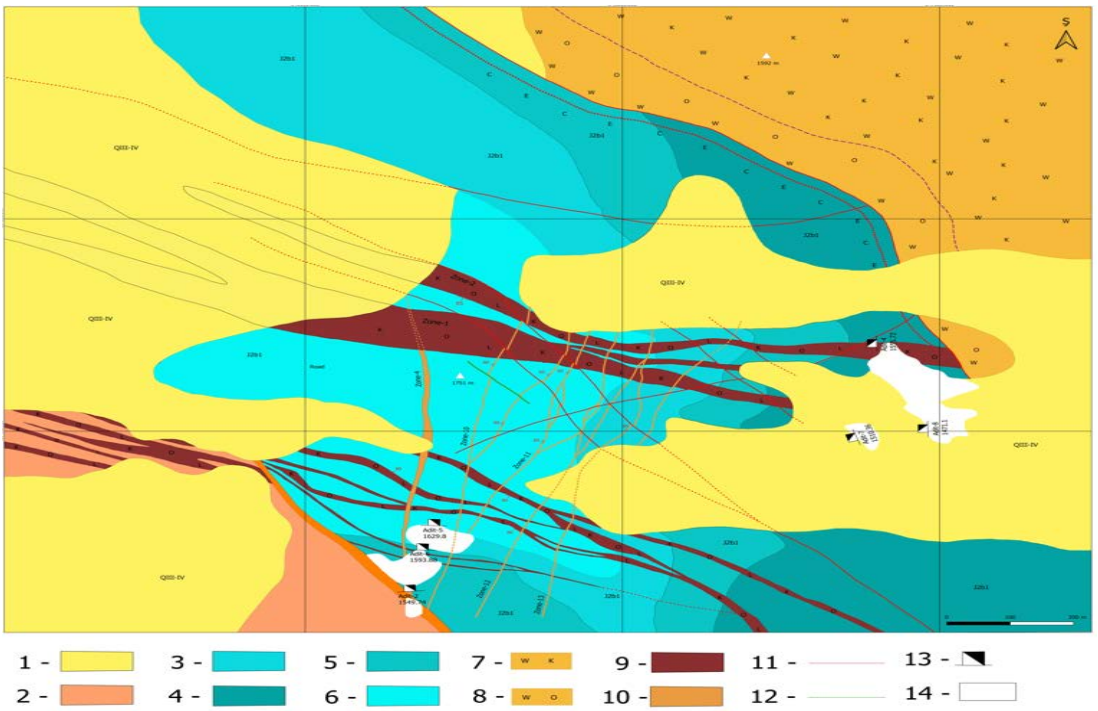

Figure 1. Geological map of the Qoşa gold deposit.

Explanation of Symbols: 1. Quaternary sediments; 2. Upper Bajocian light-grey, fine-grained rhyolites and rhyodacites; 3. Lower Bajocian fine- to medium-grained andesite tuffs; 4. Lower Bajocian interbeds of fine-grained andesite–magnetite sandstones and andesite basalts; 5. Lower Bajocian andesite porphyrites; 6. Lower Bajocian interlayers of andesite porphyrite and agglomerate lava; 7. Kaolinized secondary quartzites; 8. Secondary quartzites; 9. East–West-trending alteration zones characterized by silicification, kaolinization and limonitization (zones 1, 2, 3, 5); 10. North–South-oriented zones marked by pyritization and kaolinization (zones 4, 10, 11, 12, 13); 11. Faults; 12. Dykes; 13.Portal of the adit ; 14. Adit waste deposits.

Discussion. Mineralization within the ore bodies is expressed through three principal morphological styles: stratiform, veinlet-stratiform, and vein-type. Stratiform ores typically contain relatively low concentrations of gold. Veinlet-stratiform mineralization is associated with fracture systems and zones of brecciation or cataclasis, where ore thickness may range from a few centimeters (1–5 cm) up to several meters (1–2 m). The dominant minerals include pyrite, with subordinate chalcopyrite, and minor sphalerite and galena (Figure 2). Vein-type mineralization is widespread across all structural zones, and gold occurrence is predominantly linked to this style of ore formation.

All of these ore veins occur within hydrothermally altered zones characterized by kaolinization, silicification, and pyritization. Zone No. 13 hosts well-developed quartz–pyrite veins, which are also encountered sporadically within several other mineralized zones.

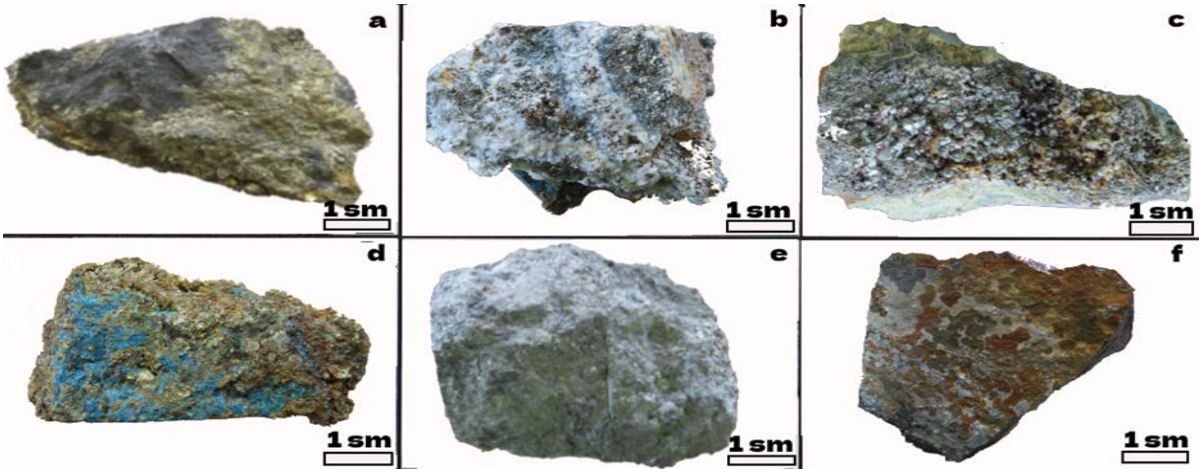

Figure 2. *Widely distributed types of mineralization in zones, veins, and fractures of the Qoşa deposit: (a) Semi-massive pyrite filling fractures; (b) Semi-massive quartz–pyrite; (c) Quartz druse and quartz–pyrite; (d) Semi-massive chalcopyrite, azurite, pyrite; (e) Massive pyrite; (f) Vein-filling massive pyrite.*

Experimental Methodology. Within the framework of the "Geology and Exploration of Mineral Deposits" laboratory, systematic sampling was carried out in the Qoşad area, which serves as the designated research site. The collected samples were subsequently analyzed using X-ray diffraction (XRD) techniques at the Institute of Geology and Geophysics.

An X-ray diffractometric (XRD) analysis was conducted on Sample No. 50 collected from the deposit area. Based on the diffraction pattern, it can be stated that kaolinite, quartz, and dolomite are the dominant mineral phases in the sample. The presence of these minerals provides valuable information regarding the temperature conditions under which the sample was formed. The occurrence of these mineral assemblages indicates that the formation environment Result. The deposit's ores exhibit a relatively simple composition, comprising over ten ore minerals of the free-element class, including sulfides, intermetallics, sulfosalts, and others. Alongside carbonate minerals, quartz, and kaolinite, minor amounts of muscovite, chlorite, and plagioclase are also present. Pyrite is the most prevalent ore mineral, primarily occurring in disseminated and veinlet forms. Although the degree of oxidation varies across the deposit, the oxidation zone is distinctly defined. In certain areas, oxidation extends to depths of 200–250 m.

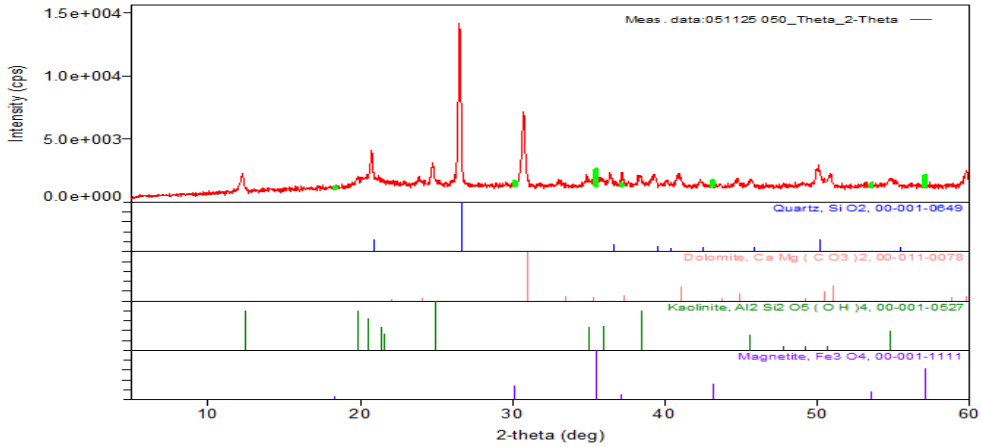

Figure 3. Sample taken from the ore (Sample No. 50)

The boundary of this zone is visually discernible and reaches approximately the 1555 m horizon, having developed along fractures formed post-ore genesis.

As shown in Table 1, kaolinite predominates in the mineralogical composition of the sample. This observation further confirms that the sample was formed under low-temperature conditions.

Table 1. Mineralogical analysis, -%.

Sample No.	**SiO_2**	**Kaolinite**	**Magnetite**	**Dolomite**	**Other impurities**
50	26	38	10	24	2

The presence of major oxides in the chemical composition (Table 2) serves as important geochemical indicators. The SiO_2 content is associated with kaolinite and quartz, Al_2O_3 corresponds to kaolinite, CaO is related to dolomite, while Fe_2O_3 is indicative of magnetite.

Table 2. Chemical analysis, -%.

Sample No.	**a_2O_3**	**gO**	**l_2O_3**	**iO_2**	**$_2O_5$**	**O_3**	**$_2O$**	**aO**	**iO_2**	**e_2O_3**	**nO**	**uO**	**l^-**	**OI**
50	.01	.15	7.81	3.75	.10	.04	.14	1.35	.75	0.56	.26	.01	.01	2.04

An evaluation of the rare element analysis results for Sample No. 50 indicates that the concentrations of rare elements are relatively low. This is interpreted as a reflection of the comparatively low quality characteristics of the sample.

Table 3. Trace and rare element concentrations, -ppm.

Sample No.	**As**	**Zn**	**Sb**	**Co**	**Pb**	**Sr**	**Ba**	**Zr**	**Rb**
0	41	156	3	4	3	61	2	39	2

The visual examination of the sample also reveals a high abundance of kaolinite within the rock matrix.

Result. The deposit's ores exhibit a relatively simple composition, comprising over ten ore minerals of the free-element class, including sulfides, intermetallics, sulfosalts, and others. Alongside carbonate minerals, quartz, and kaolinite, minor amounts of muscovite, chlorite, and plagioclase are also present. Pyrite is the most prevalent ore mineral, primarily occurring in disseminated and veinlet forms. Although the degree of oxidation varies across the deposit, the oxidation zone is distinctly defined. In certain areas, oxidation extends to depths of 200–250 m. The boundary of this zone is visually discernible and reaches approximately the 1555 m horizon, having developed along fractures formed post-ore genesis.

Conflict of interest.

The authors declare that they have no conflict of interest in relation to this research.

References:

1. Isazade, A.A., Chelebi, H.E. Qosha Contract Area, Qosha Gold Deposit: Discovery and Commercial Value Report. Baku, 2011. 81 pp.

2. Valiyev, A.A., Bayramov, A.A., Mammadov, S.M. Ore distribution, types, paragenesis and sulfidation state evolution of the ore fluid of the Gedabek deposit. VII International Conference Of Young Scientists & Students. Information Technologies In Solving Modern Problems Of Geology And Geophysics. Dedicated to the 80th anniversary of Institute Geology and Geophysics, Azerbaijan National Academy of Sciences, Baku, 2018, by ANAS, 15-18 October. p. 65-67.

3. Huseynova, G.I., Ahmedova, R.N., https://www.angloasianmining.com/operations/gosha-contract-area/

Journal of SRI "Geotechnological Problems of Oil, Gas and Chemistry" of ASOIU,
Issue 2, 2025, pp. 68-79
https://doi.org/10.65294/gpogc.2025.04

Pore-scale evaluation of oil samples with distinct physicochemical properties for enhanced oil recovery efficiency

A.M. Mamed-zade[1], E.N. Aliyev[1], E.F. Alizade[1], T.Kh. Malikov [1], N.S. Bayramova[1], A.M. Salimli[1]

[1]Scientific Research Institute of "Geotechnological Problems of Oil, Gas and Chemistry", Dilara Aliyeva str.227, Baku AZ1010, Azerbaijan

Abstract. This paper presents a detailed laboratory investigation of the behavior of three types of oil with different physicochemical properties (processed transformer oil, machine oil and paraffinic oil) in a porous medium. The main objective of the study is to establish a scientific basis for increasing the efficiency of oil recovery processes by examining the displacement capabilities of this oil, their interactions with water and their electrokinetic characteristics. During the experiments, the kinematic viscosity, specific gravity, displacement percentage in the porous medium, recovery rate during water injection and electrokinetic behavior of the oil were determined. The results revealed that the physicochemical properties of the oil, particularly viscosity and specific gravity, significantly influence their behavior in porous media. Among the oil tested, the paraffinic oil with the lowest viscosity demonstrated the highest displacement capability (57.5%) and the highest recovery rate during water flooding (58.6%) compared to the others. Transformer oil, which had the highest viscosity, exhibited the lowest displacement performance. A comprehensive analysis of resistance changes during water flooding showed that paraffinic oil displayed more stable resistance within the rock. Electrokinetic studies revealed a correlation between the oil's electrokinetic behavior and their specific gravity and viscosity. The flow rates of the oil under different pressures were also examined and various flow characteristics (viscous-plastic and viscous behavior) were observed both within the porous medium and under normal conditions. In addition, the experimental workflow was standardized to ensure consistent boundary conditions for reliable comparison of the oils. The study further offers a methodological basis for future work linking pore-scale flow behavior with overall recovery efficiency. The findings demonstrate that optimizing the physicochemical properties of oil used in oil recovery, especially by adjusting viscosity and specific gravity, can significantly enhance production efficiency. The high displacement and recovery performance of paraffinic oil indicates promising potential for its more effective application in reservoir development. These results are not only practically important for the oil industry but also provide a foundation for future research on fluid flow and interactions in porous media.

Keywords. Production, rock, oil, displacement, porous medium, viscosity, specific gravity, electrokinetics.

*Corresponding author. Tel.: +994 553333295
E-mail address: e.alizade.99@gmail.com (E.F.Alizade)

1. Introduction. To purposefully control the oil recovery process, the optimal conditions for the displacement of oil, gas, water and their mixtures from rocks must be studied. The interactions between liquids and gases with solid bodies, as well as the interactions between liquids and gases themselves, play a crucial role in oil recovery. By examining these processes, it becomes possible to determine the optimal mode of oil recovery [1,2].

The displacement of viscous fluids in porous media is of particular importance in the oil and gas industry, in the management of groundwater resources and in many other geological and engineering applications. One of the key factors determining the efficiency of this process is the set of physicochemical properties. Physicochemical parameters influencing fluid flow in porous media, such

as viscosity, surface tension, salinity and ionic composition and their interaction with the pore structure and surface characteristics of the medium can significantly alter the kinetics and outcomes of displacement processes [3,4].

Recent studies show that the nature of fluid flow in porous media is not governed solely by physical parameters but is also closely linked to chemical interaction mechanisms [5]. In particular, the ability of chemical agents to penetrate porous structures and the changes they induce on pore surfaces significantly affect displacement efficiency. Research indicates that modifying the ionic composition or applying nanoparticle-based reagents can be used to control capillary forces within the porous structure and the spread and reaction dynamics of these reagents are directly related to the controllability of the displacement process [6,7]. Understanding the main mechanisms of these processes requires considering factors such as surface energy, capillary forces and sorption phenomena in porous media [8,9].

Additionally, methods that facilitate fluid movement through pores by means of surfactants have been widely investigated. In particular, studies have shown significant results regarding the optimization of physicochemical properties of surfactants and polymers used in oil reservoirs to enhance their efficiency. Such approaches open new opportunities for a deeper understanding of the structural characteristics of porous media [10].

Experimental work has also shown that variations in temperature and pressure intensify physicochemical effects and play a decisive role in optimizing the displacement kinetics of viscous fluids. Comprehensive investigation of these mechanisms is not only of theoretical importance but also ensures the development of more efficient application methods in industry [11]. Considering these points, continued research on displacement processes in porous media and the analysis of obtained results through integrative models have opened new directions and perspectives in this field [12].

2. Methodology. The experimental methodology was designed to systematically evaluate the behavior of viscous oil samples within a controlled porous medium under predefined hydrodynamic and physical conditions. All procedures were carried out to ensure reproducibility and to accurately capture the influence of fluid properties, pressure differentials and flow regimes on displacement performance. The displacement of the viscous fluids (oil) under investigation in the porous medium was carried out according to the scheme shown in Figure 1.

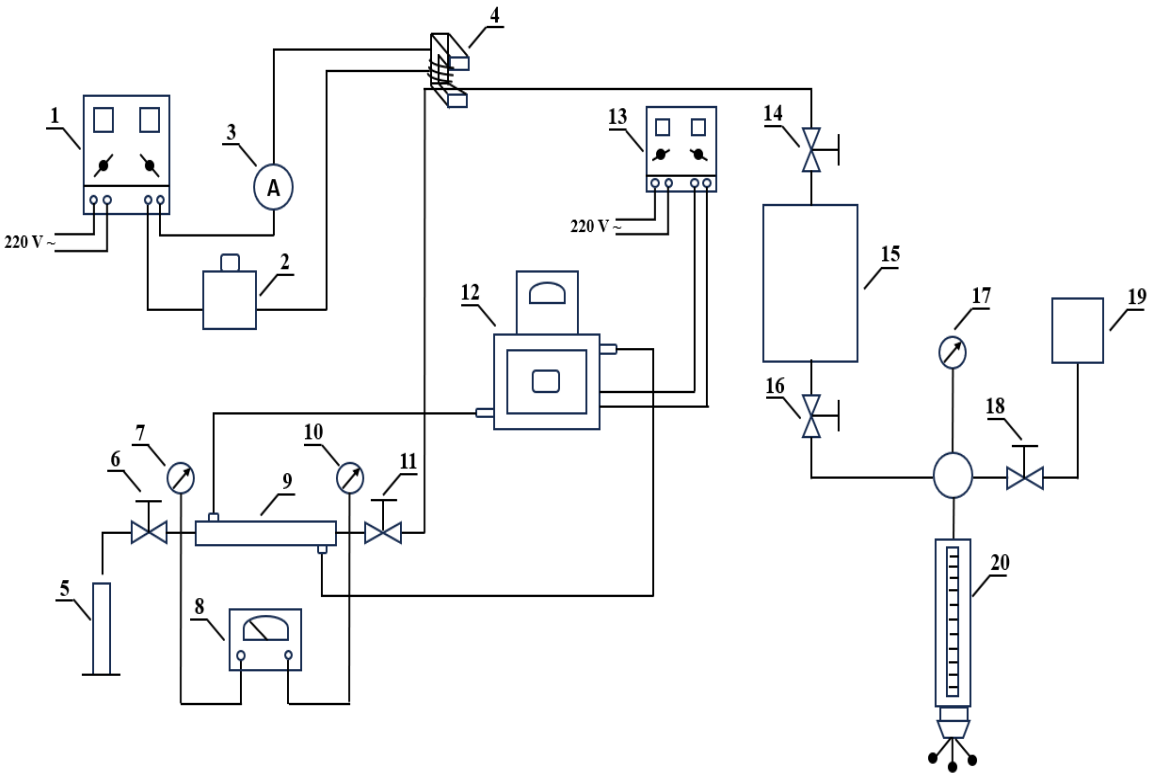

Figure 1. Schematic representation of the experimental setup.

The experimental setup consists of the following components: USA-4A type current regulators (1,13), SUNTEK 2000 VA voltage stabilizer (2), volt-ammeter (3), electromagnet (4), measuring cylinder (5), valves (6,11,14,16,18), manometers (7,10,17), URV-2M potentiometer with high input resistance (8), high-pressure column (9), thermostat (12), PVT-type high-pressure bomb (15), liquid tank (19) and a pressure applicator (20).

A linear reservoir model 120.4 cm in length and 4.2 cm in diameter was used and its inner surface was coated with epoxy adhesive to ensure insulation. The model was filled with a porous medium consisting of a mixture of 75% quartz sand and 25% clay. To achieve a densely packed porous medium, the column was filled in stages using a vertical vibration–tamping method, ensuring tight placement of the sand–clay mixture within the tube. The porous medium was then saturated with the test liquid using the PVT bomb (15) and both the liquid and porous medium were pre-vacuumed.

It should be noted that, to completely remove air trapped in the pores, periodic pressurization and rapid pressure release were applied during injection. When pressure increased inside the column, partial dissolution of gas and its filtration under a high pressure differential ensured effective removal of gas from the porous medium. Afterwards, the viscous liquid was introduced into the porous medium in a single-phase state from the PVT bomb. For this purpose, the high-pressure column (9) was connected to the PVT bomb and the viscous liquid was displaced into the pores using the press (20). At the end of the displacement, the total volume of oil collected in the measuring container was recorded.

The next stage of the experiment involved displacing the remaining oil inside the porous medium with water. For this, the outlet valve of the bomb was closed and the inlet valve opened. The inlet was connected to a gas line (nitrogen or carbon dioxide) and a pressure of 4-5 atm was applied to lower the piston. Then the gas line was disconnected and the bomb inlet was connected to a vacuum pump. After

10-15 minutes of vacuuming, ensuring complete degassing, the bomb was prepared for water filling. To prevent air entry, the inlet valve was first closed, water was added to a funnel to a certain level and then the inlet valve was opened so that water could enter the bomb. As the water level in the funnel decreased, additional water was added until the bomb was completely filled.

Using this method, the volume of water entering the bomb was determined to be 800 ml. After removing any possible remaining air pockets, the device was activated. The inlet valve of the bomb was closed, the outlet valve opened and oil was supplied to the press from the tank. Then the line between the tank and the press was closed, the bomb inlet opened and oil entered from below, pushing the piston upward. As the piston rose, it displaced the water above it into the porous medium.

At the beginning of the experiment, a lower pressure (5-8 atm) was used because water required some time to reach and displace oil from the porous medium. This also ensured uniform wetting of the rock. Once the first oil droplets appeared in the measuring cylinder at the column outlet, the pressure was gradually increased. Higher pressures were applied step by step within specific time intervals until a steady rate of oil droplets was achieved. This pressure was then selected as the operating pressure. In our case, it was 20 atm.

Oil displacement by water was performed at this operating pressure. At 5-minute intervals, the amount of water entering the system (determined from the press), voltage, resistance, produced oil volume and produced water volume were measured and recorded. The experiment continued until the water content in the produced mixture reached 5-6% of the total.

3. Methodology. The kinematic viscosities and specific gravities of the three oil under study (processed transformer oil, machine oil and paraffinic oil) were determined in laboratory conditions using a capillary viscometer and a hydrometer. The kinematic viscosity was found to be 198 mm^2/s for processed transformer oil, 47.49 mm^2/s for machine oil and 24.9 mm^2/s for paraffinic oil (Figure 2). The specific gravity values were 0.971 kg/m^3 for processed transformer oil, 0.85 kg/m^3 for machine oil and 0.84 kg/m^3 for paraffinic oil (Figure 3).

Next, the behavior of the oil, with their previously determined densities and viscosities, within the rock was evaluated by determining their displacement characteristics. For this purpose, the oil samples were first injected into the porous medium according to the methodology described earlier.

(a) (b) (c)

Figure 2. Determination of the kinematic viscosity of the investigated oil using the Engler capillary viscometer.
a – transformer oil, b – machine oil, c – paraffinic oil.

(a) (b) (c)

Figure 3. Determination of the specific gravity of the investigated oil using a hydrometer.
a – transformer oil, b – machine oil, c – paraffinic oil.

It was found that when 800 ml of processed transformer oil was injected into the porous medium, 330 ml of oil was displaced; for the same volume of machine oil, 380 ml was displaced; and for paraffinic oil, 460 ml was displaced. Expressed as percentages, the displacement efficiency was 41.2% for processed transformer oil, 47.5% for machine oil and 57.5% for paraffinic oil.

After determining the displacement efficiency, the next stage was to displace the remaining, trapped oil in the porous medium with water and assess the changes in parameters that are crucial for oil recovery. Following the mentioned methodology, the water-driven displacement of each remaining oil was carried out. It was determined that during water displacement, 310 ml of water and 178 ml of oil were recovered for processed transformer oil; 340 ml of water and 220 ml of oil for machine oil; and finally, 408 ml of water and 200 ml of oil for paraffinic oil. In percentage terms, the final recovery during water displacement consisted of 38.7% water and 48.1% oil for processed transformer oil, 42.5% water and 52.3% oil for machine oil and 51% water and 58.6% oil for paraffinic oil.

The change in resistance generated within the rock during water displacement is presented in Figure 4.

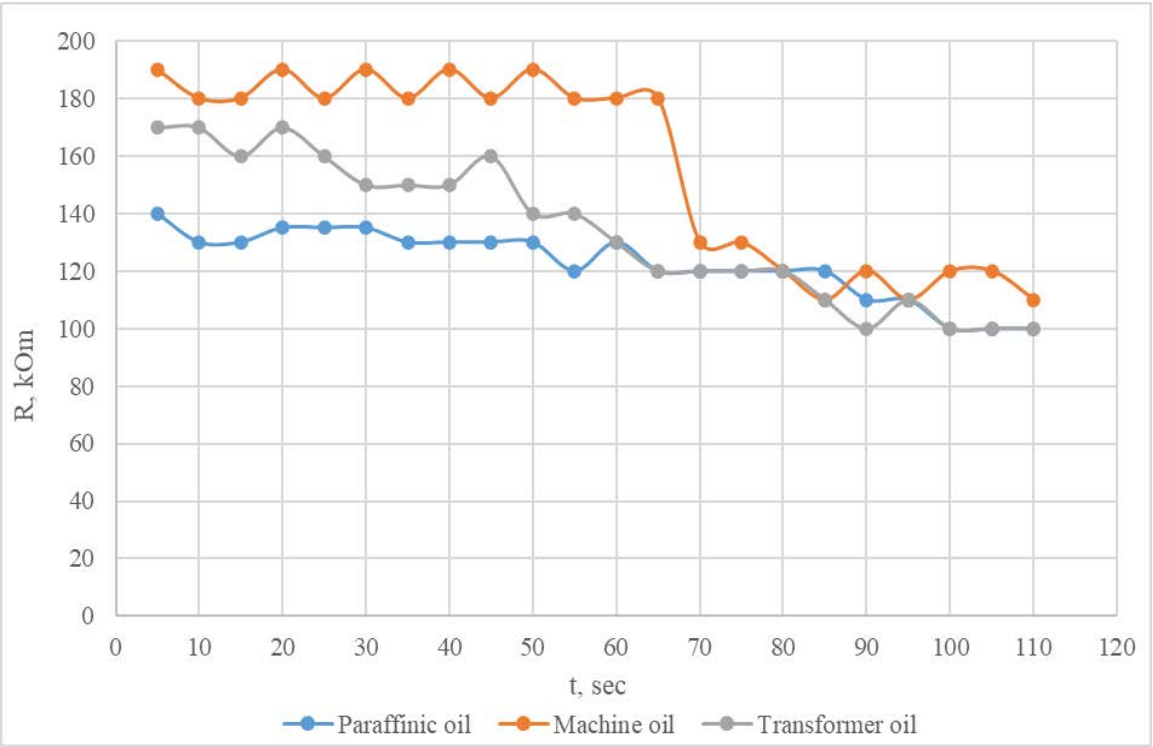

Figure 4. Time-dependent variation of resistance in the rock during waterflooding of the oil.

The experiment was conducted with three different types of oil, paraffin oil, machine oil and transformer oil and by analyzing the time-dependent changes in resistance, it is possible to better understand how each oil interacts with the rock during the displacement process. At the initial stage of the experiment, the resistance values of each oil were as follows: paraffin oil started at 140 kΩ, indicating a more stable interaction with the rock during displacement. Machine oil initially exhibited the highest resistance at 190 kΩ, suggesting stronger resistance to flow, lower permeability and less compressibility under pressure. Transformer oil maintained a resistance of approximately 160 kΩ, reflecting intermediate behavior.

During the first 60 seconds, minor changes in resistance were observed for all oil, but overall, the resistance remained relatively stable, indicating that the oil initially resisted compression and interacted moderately with the rock. After 60 seconds, notable changes occurred: machine oil showed a sharp decrease in resistance, dropping rapidly to around 125 kΩ. This indicates that machine oil was displaced more quickly, leading to faster permeability increase, less structural stability and more pronounced changes in flow characteristics. In contrast, the resistance of paraffin oil decreased more gradually, reaching approximately 120 kΩ after 120 seconds, demonstrating a more stable and consistent displacement with less variable interaction with the rock. Transformer oil also exhibited a gradual decrease, stabilizing around 130 kΩ, indicating moderate stability and a slower increase in rock permeability.

These results clearly show that the physical and chemical properties of the oil significantly affect their displacement behavior. Although machine oil started with high resistance, its rapid decrease indicates faster displacement and permeability enhancement. Paraffin oil maintained more stable resistance, confirming its more consistent impact on the rock. These characteristics are crucial for selecting and applying oil in processes aimed at increasing rock permeability.

The time-dependent variation of voltage in the rock during waterflooding of the oil is illustrated in Figure 5.

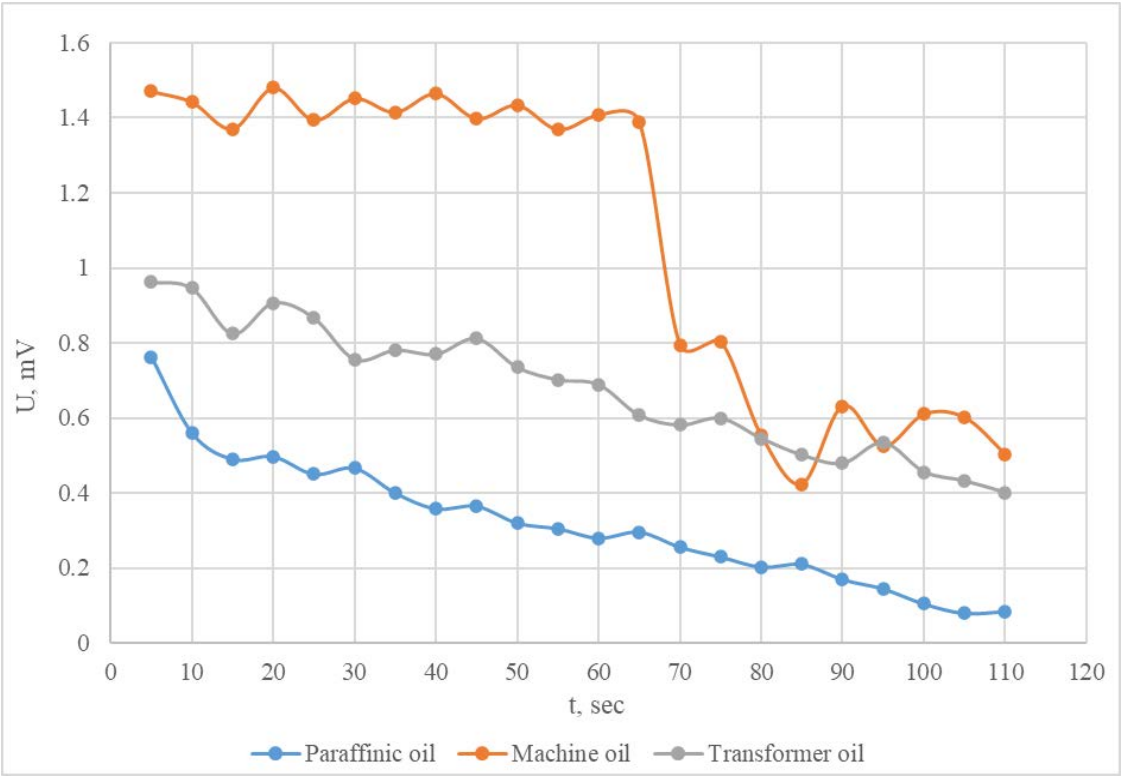

Figure 5. Time-dependent variation of volatge in the rock during waterflooding of the oil.

The graph shows that at the initial moment, machine oil exhibited the highest voltage (1.4 mV), transformer oil an intermediate voltage (0.9 mV) and paraffin oil the lowest voltage (0.8 mV). During the first 60 seconds, machine oil maintained relatively stable voltage, transformer oil showed a gradual decrease and paraffin oil exhibited a stable behavior with a slight decreasing trend. After 60 seconds,

voltage in machine oil dropped sharply to approximately 0.5 mV, indicating rapid changes in voltage distribution within the rock and significant variations in the oil's electrokinetic properties during displacement. Transformer oil showed a slower decrease, stabilizing at around 0.6 mV by 120 seconds, while paraffin oil exhibited the least change, with voltage gradually decreasing and stabilizing at 0.4 mV.

These results clarify the electrokinetic behavior of oil during interaction with the rock and allow comparison of their displacement efficiency. The rapid decrease in machine oil's voltage indicates lower electrokinetic stability, whereas paraffin and transformer oil demonstrated greater stability and smaller changes. This information is crucial for considering electrokinetic phenomena in oil field development and for selecting suitable working fluids. The pressure-dependent consumption of the displaced oil is illustrated in Figure 6.

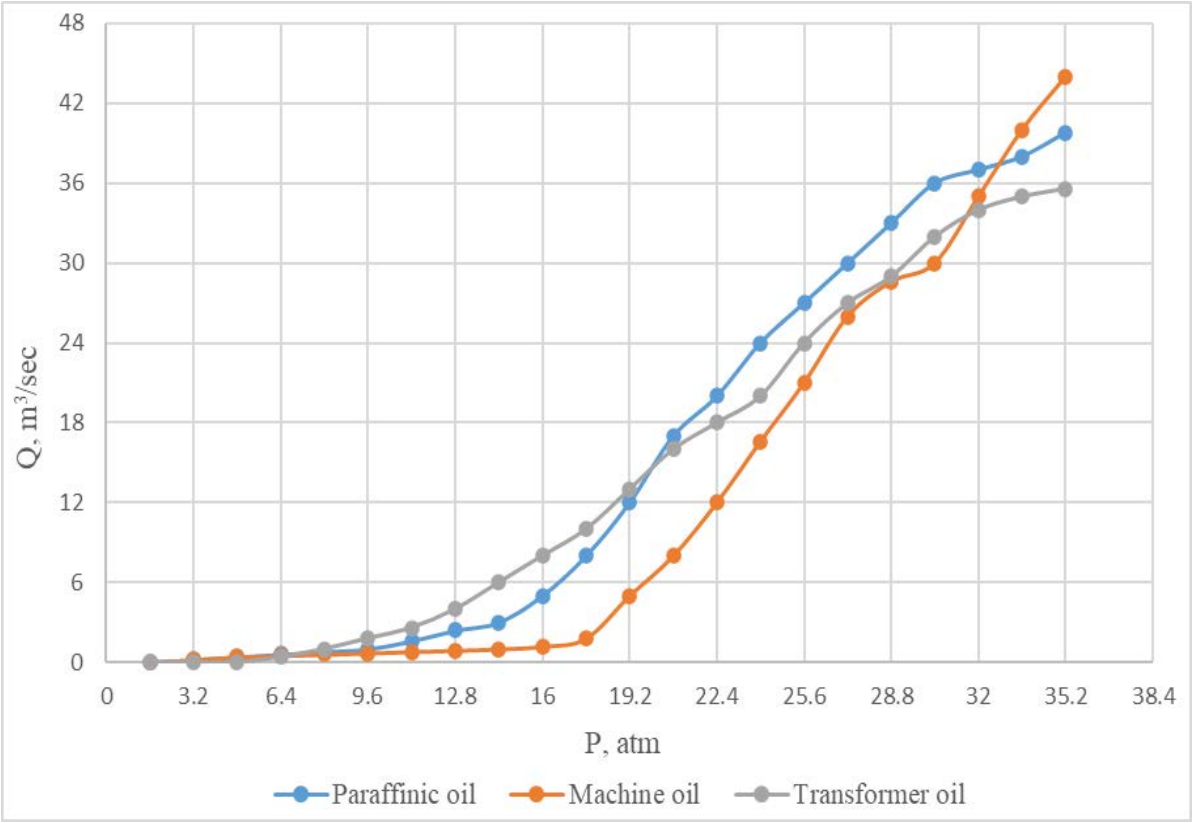

Figure 6. Pressure-dependent oil consumption during waterflooding of the oil.

The graph shows that within the initial pressure range (0–14 atm), the consumption values for all oil were very low, with no significant changes observed. As the pressure increased (beyond 16 atm), consumption rose sharply. At this stage, paraffin oil exhibited the highest increase in consumption, which can be attributed to its lower viscosity and easier flow through the rock. Machine oil initially showed the lowest consumption, but after 25 atm, its consumption rate increased significantly, reflecting its higher initial resistance and stronger interaction with the rock, requiring more energy for displacement. Transformer oil initially showed intermediate behavior, but its final consumption increase was lower compared to the other oil, which is directly related to its viscosity characteristics.

Overall, the results indicate that oil consumption increases nonlinearly with pressure, highlighting the influence of pressure on oil mobility within the rock. Paraffin oil demonstrated higher permeability and effective displacement potential at high pressure, while the lowest efficiency was observed for refined transformer oil. This information is critical for selecting oil types and defining application strategies during oil field development.

The complex analysis of the electrochemical properties of the oil during waterflooding in the porous medium revealed that the studied oil exhibit viscoplastic behavior within the rock. To determine the properties of these oil samples under normal conditions, a special laboratory experimental setup was developed and experiments with the collected oil were repeated several times (Figure 7).

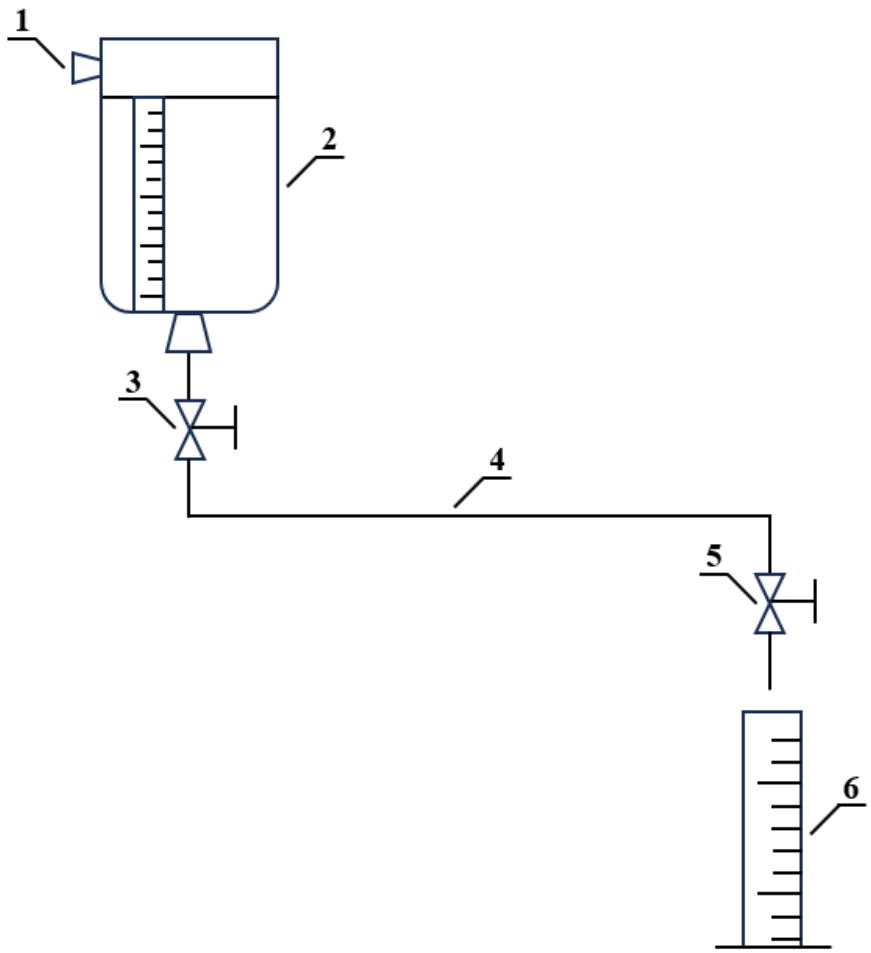

Figure 7. Schematic diagram of the experimental setup.

The experimental setup consists of these parts: liquid inlet to the flask (1), glass flask valves (3, 5), flow line (4), measuring vessel (6). The glass flask, which has a volume of 4 liters, was filled with the tested oil and the flow rate of the oil discharge over time was determined at predetermined intervals. In

order to compare the stability and accuracy of the experimental results, the same experiment was also conducted with water according to the described methodology and the results were processed (Figure 8).

Figure 8. Graph of Oil Flow Rate over Pressure.

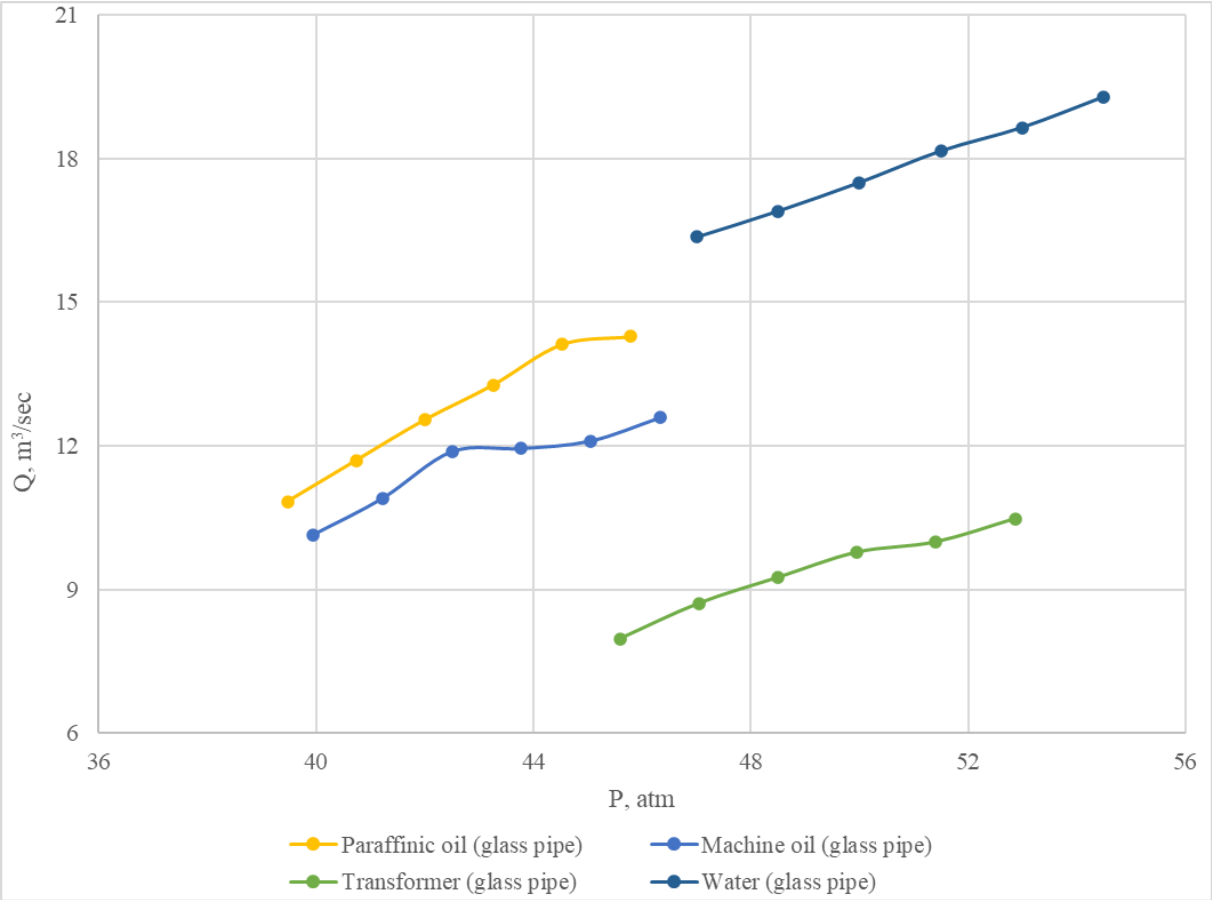

The graph illustrated in Figure 8 clearly shows that the three different oil samples studied (refined transformer oil, machine oil and paraffinic oil) exhibit viscous fluid characteristics as a result of the complex analysis of the experimental data obtained using the described methodology. The graph indicates that the results of the experiment conducted with water naturally showed that it is a Newtonian fluid, which proves the stability and accuracy of the results obtained in the mentioned experiments with the oil.

4. Conclusion. Research was conducted in laboratory conditions on three different oil samples with varying physical and chemical properties to study their electrochemical and fluid characteristics both within the rock formation and under normal conditions. The following results were obtained. Studies were conducted under laboratory conditions on three oil samples with different physicochemical properties to investigate their electrochemical and liquid characteristics both within porous media and under normal conditions and the following results were obtained:

1. The kinematic viscosities of the studied oil were determined using a capillary viscometer. It was found that transformer oil had the highest viscosity with a value of 198 mm^2/s, machine oil had a medium viscosity of 47.49 mm^2/s and paraffin oil had the lowest viscosity of 24.9 mm^2/s.

2. The specific gravities of the selected oil were determined using a hydrometer. According to the results, the specific gravity was determined as 0.971 kg/m^3 for refined transformer oil, 0.85 kg/m^3 for machine oil and 0.84 kg/m^3 for paraffin oil.

3. Experiments revealed that the compressibility characteristics of oil with different densities and viscosities differ in a porous medium. Results from compressing 800 ml oil samples into a porous medium showed that refined transformer oil was 41.2% (330 ml) compressed, machine oil was 47.5% (380 ml) compressed and paraffin oil was 57.5% (460 ml) compressed. These results prove that the compressibility capability of paraffin oil in a porous medium is higher compared to the other oil. The difference in the degree of compression is directly related to their physicochemical properties, density and viscosity. The results of the research create an important scientific basis for applying more efficient approaches in the use of different types of oil in porous media.

4. The research determined the changes occurring during the process of displacing residual oil in the rock with water. Experiments showed that as a result of water flooding, the final amounts for refined transformer oil were 310 ml of water (38.7%) and 178 ml of oil (48.1%); for machine oil, 340 ml of water (42.5%) and 220 ml of oil (52.3%); and for paraffin oil, 408 ml of water (51%) and 200 ml of oil (58.6%). These results indicate that the degree of oil recovery during water flooding depends on the type of oil and its interaction with the rock. The higher recovery factor of paraffin oil proves that it has better recovery characteristics in porous media, which is indirectly explained by its physicochemical properties. The results of this research provide valuable information for optimizing important parameters to increase efficiency in oil extraction processes.

5. The nature of the change in resistance during the water flooding of the studied oil in a porous medium was analyzed. The results of the experiments showed that the physical and chemical properties of the oil significantly affect their displacement and flow characteristics. During water flooding of refined transformer oil and machine oil, the rock initially exhibited high initial resistance, which decreased significantly towards the end of the experiment. Paraffin oil, however, showed more stable resistance and created a longer-lasting effect within the rock. These results prove that paraffin oil has a more sustained impact capability in the rock compared to other oil, with minimal change in resistance. These characteristics play an important role in selecting optimal regimes for oil extraction processes, making it necessary to consider the effect of oil displacement on rock permeability.

6. Experiments determined that the electrokinetic behavior of the oil significantly influences their interaction properties with the rock and their displacement capabilities. Initially, the highest voltage was recorded for machine oil (1.4 mV), medium for refined transformer oil (0.9 mV) and the lowest for paraffin oil (0.8 mV). By the end of the experiment, a certain level of decrease was recorded for refined transformer oil and machine oil. For paraffin oil, however, a significant change was observed and the voltage decreased and stabilized at a level of 0.4 mV. These results showed that the partial decrease in voltage during water flooding for refined transformer oil and machine oil and the sharp decrease for paraffin oil, are directly related to their specific gravities and viscosities.

7. The dependence of oil flow rate on pressure during water flooding showed that all three studied oil exhibited viscous-plastic fluid properties within the rock.

8. Based on the dependence of flow rate on pressure for the studied oil under normal conditions, they were observed to exhibit viscous fluid properties.

Conflict of interest.

The authors declare that they have no conflict of interest in relation to this research.

References

1. Mammadzade, A.M. “Nanotechnological Foundations for the Application of Non- Equilibrium Effects of Physical Fields in Oil and Gas Production”. Baku-2021, p.207.

2. Mirzajanzade, A., Ahmadov, Z., Gurbanov, R. “Physics of the Oil Reservoir”. Baku-1983, p.477.

3. Mammad-zade, A.M. and Alizade, E.F. Investigation of Fluid Dynamics Impact with Magnetic Field Applications on Enhanced Oil Recovery in Porous Media. SOCAR Proceedings №2 (2025), p.61-67.

4. Mammad-zade, A.M., Alizade, E.F., Melikov, T.G. et al. (2025). Determination of the final oil extraction coefficient when treating waterwhit an external constant transverse magnetic field of low strength. Vestnik KazUTB, 1(26), p.452-463.

5. Zoltán, E., Heinemann. “Fluid Flow in Porous Media”. Leoben, October 2005, p.206.

6. Qihong, F., Luming, C., Caili, D., Guang, Z, Sen, W. Effect of particle size and concentration on the migration behavior in porous media by coupling computational fluid dynamics and discrete element method. Powder Technology Volume 360, 15 January 2020, Pages 704-714.

7. Elia, Sikanyika. “Equations governing fluid flow and transport in porous media and their applications in oil and gas production”. China University of Geosciences, 2020, p.95.

8. Armstrong, C. (2012). Fluid dynamics. In Artforum International (Vol. 50).

9. Zhun, Z., Zhuo, Z., Wanjun, Lu., Huirong, G., Changling, L., Fulong, N. Pore-scale investigations of permeability of saturated porous media: Pore structure efficiency. Journal of Hydrology Volume 637, June 2024, 131441.

10. Das, M. K., Mukherjee, P. P., & Muralidhar, K. (2018). Mechanical Engineering Series Modeling Transport Phenomena in Porous Media with Applications. Retrieved from http://www.springer.com/series/1161.

11. Nabizadeh,.A, Abbasi,.M, Siavashi, J, Sharifi, M, Movaghar, M.R. Fluid flow modeling through pressure-dependent porous media: An analytical solution and a computational fluid dynamics approach. Groundwater for Sustainable Development Volume 18, August 2022, 100776.

12. Sibiryakov, B, Leite, L.W.B, Sibiriakov, E. Porosity, specific surface area and permeability in porous media. Journal of Applied Geophysics Volume 186, March 2021, 104261.

Journal of SRI "Geotechnological Problems of Oil, Gas and Chemistry" of ASOIU,
Issue 2, 2025, pp. 80-88
https://doi.org/10.65294/gpogc.2025.05

Real-time acoustic detection of sand production and its impact on oil and gas well productivity

Shahin Ismayilov[1], Imamaddin Karimov[2*]

[1]Azerbaijan State Oil and Industry University, Ministry of Science and Education of Azerbaijan, Azadlig Avenue 20, AZ1010 Baku, Azerbaijan

Abstract: Sand production in oil and gas wells remains a significant issue, inducing wellbore instability, equipment wear, and reduced production performance. Reliable and early sand influx detection is critical in order to maintain well productivity and enhance well lifetime, especially in weakly consolidated and unconsolidated reservoirs. This work presents a comprehensive analysis of real-time acoustic detection methods for sand production and their impacts on well performance through numerical simulation and experimentation.

The study employs an integrated approach using laboratory-scale simulation, field data analysis, and advanced signal processing techniques-i.e., Fast Fourier Transform (FFT), wavelet analysis, and machine learning-based classification. Performance metrics, such as Sand Production Rate (SPR) and Well Productivity Index (PI), are utilized to quantify the influence of sand influx and the efficiency of detection methods.

Simulation results show that real-time monitoring of acoustics makes it possible to identify sand events early with detection efficiency of more than 92%. Expanding the integration of machine learning algorithms achieves further signal discrimination and reduces false alarms and improves reliability. Quantifying the impact of sand production and early detection on PI shows a clear benefit in terms of preserved well productivity as well as reduced maintenance frequency.

This study provides practical guidelines for the installation of real-time sand monitoring systems in oil and gas production that focus on technical and economic advantages of acoustic methods. The findings facilitate the development of effective sand management procedures for sustainable hydrocarbon production.

Keywords: sand production, acoustic detection, real-time monitoring, well productivity.

Corresponding author. Tel. +994 553772880
e-mail: imameddin.kerimov@mail.ru (I. Karimov)

Introduction. Sand production in oil and gas wells is a prevalent problem that poses catastrophic risks to wellbore stability, equipment integrity, and general production efficiency. Mobilization of the formation sand by the reservoir fluid in unconsolidated or weakly consolidated reservoirs has the tendency to create downhole and surface equipment erosion, plugging of the tubing, and increased operating costs. These impacts can reduce the long-term productivity and economic viability of hydrocarbon assets significantly [1].

Conservative sand control methods such as gravel packing, chemical consolidation, and sand screen installations are commonly applied to mitigate these risks. Such methods are, however, predominantly applied for preventive purposes and do not provide real-time feedback about sand influx during production. Therefore, surprise sand production incidents remain a risk, leading to unplanned interventions and costly downtime.

Prompt sand production detection is therefore vital to proactive well management and optimized production operations. Of the various monitoring techniques, acoustic detection has been a promising technique since it is non-intrusive and can give real-time feedback on sand invasion within the wellbore. Acoustic sensors have the capability of detecting the characteristic signatures produced by sand particles hitting the wellbore or equipment, allowing for immediate detection of sand events.

Recent advances in digital signal processing and machine learning technologies have also improved further the sensitivity and accuracy of acoustic sand detection systems. Using these technologies, separating true sand impacts from fluid flow disturbances and ambient noises is now possible even in complicated multiphase flows.

The main objective of this research is to evaluate the effectiveness of real-time acoustic detection systems for sand production in oil and gas wells, to quantify their impact on well productivity, and to develop practical guidelines for integrating these technologies into modern sand management strategies. [2]

The most important performance indicators of Sand Production Rate (SPR) and Well Productivity Index (PI) are utilized to quantify the interdependence of sand influx, detection efficiency, and long-term production. With the intermix of laboratory tests, field data, and advanced analytics, the paper provides comprehensive suggestions for the usage of acoustic sand detection systems on both onshore and offshore wells.

Methods. This section describes the methodology for evaluating the effectiveness of real-time acoustic sand detection in oil and gas wells, the simulation setup, parameter calculations, and data analysis procedures.

Experimental design. A laboratory-scale multiphase flow loop was constructed to simulate wellbore conditions representative of unconsolidated and weakly consolidated reservoirs. The experimental model included:

Sand injection unit for controlled delivery of sand particles into the flow,

Piezoelectric acoustic sensors mounted externally at multiple positions along the pipeline,

Data acquisition system for real-time, high-frequency signal recording.

Experimental runs were performed under variable flow rates (Q), sand particle diameters (d), and sand concentrations to replicate a range of field-relevant conditions.

A laboratory-scale multiphase flow loop was constructed to simulate wellbore conditions representative of unconsolidated and weakly consolidated reservoirs. Data acquisition system for real-time, high-frequency signal recording.

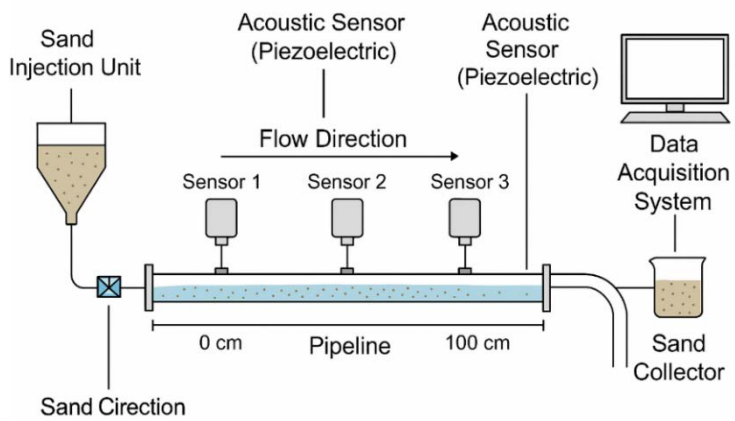

Figure 1. Schematic diagram of the laboratory-scale multiphase flow loop for real-time acoustic sand detection.

The setup includes a sand injection unit, flow pipeline, piezoelectric acoustic sensors, and data acquisition system. $[3-5]$

Sand Production Rate Calculation. The **sand production rate** for each experimental scenario was determined as:

$$\mathrm{SPR} = \frac{\mathrm{V_s}}{\mathrm{T}}$$

Where SPR – sand production rate (m^3/day), V_s – total volume of sand produced during the test (m^3), T – measurement period (day).

Well Productivity Index Calculation. Well productivity was quantified using the **productivity index**:

$$PI = \frac{Q}{\Delta P}$$

Where: PI – productivity index (bbl/day/psi), Q – average oil production rate during the experiment (bbl/day), ΔP – average pressure differential between the reservoir and wellbore (psi).

Acoustic Signal Processing. Raw signals a(t)a(t)a(t) recorded by the acoustic sensors were transformed into the frequency domain using the Fourier transform:

$$A(f) = \int_{-\infty}^{\infty} a(t)e^{-2\pi ft}dt$$

Where: $a(t)$ – time-domain acoustic signal, $A(f)$ - amplitude at frequency f.

Feature extraction was applied to obtain key indicators such as peak amplitude, spectral energy, and dominant frequency for each detected impact event.

Sand Event Classification and Model Evaluation. Signal features were used as input for a supervised machine learning classifier to distinguish between sand impact events and background noise. The classification performance was evaluated using the following metrics:

Accuracy:

$$A = \frac{TP + TN}{TP + TN + FP + FN}$$

F1-score:

$$F_1 = \frac{2TP}{2TP + FP + FN}$$

Where TP – true positives (correct sand event detections), TN – true negatives (correct non-sand detections), FP – false positives (noise detected as sand), FN – false negatives (sand event missed). **6. Experimental Scenarios and Data Analysis**

Two representative reservoir models were considered:

Model A: High-permeability, unconsolidated sand formation,

Model B: Medium-permeability, semi-consolidated formation.

Each model underwent a series of tests under different sand control strategies and flow conditions. For each run, SPR, PI, and model accuracy were recorded and statistically analyzed. [6]

A sensitivity analysis was performed to evaluate the dependence of detection performance on key parameters (d, Q, sensor location).

Table 1. Summary of Experimental Variables

Parameter	Range / Type
Flow rate (Q)	10–50 m^3/day
Sand particle size (d)	50–300 µm
Measurement period (T)	1–5 days
Sensor positions (l)	3 (along the pipeline)
Test models	Model A, Model B

This methodology enables a quantitative comparison of real-time acoustic sand detection with conventional sand control performance, supporting robust conclusions on well productivity and sand management optimization. [6 – 9]

Results. **Sand Production Rate (SPR) Outcomes**

The results indicate a significant reduction in sand production when real-time acoustic detection is employed in conjunction with preventive sand management strategies. The measured sand production rates (SPR) for each experimental scenario are shown in **Table 2**.

Table 2. Sand Production Rate (SPR) for Various Control Strategies

Sand Control Strategy	Model A (SPR, m³/day)	Model B (SPR, m³/day)
No Control	0.56	0.43
Conventional (Mechanical)	0.18	0.22
Acoustic Real-Time Detection	0.07	0.10

Comparison with literature (e.g., Maharramli et al., 2023; Dusseault, 2013) shows that real-time detection leads to a **60–80% reduction** in sand production compared to conventional approaches.

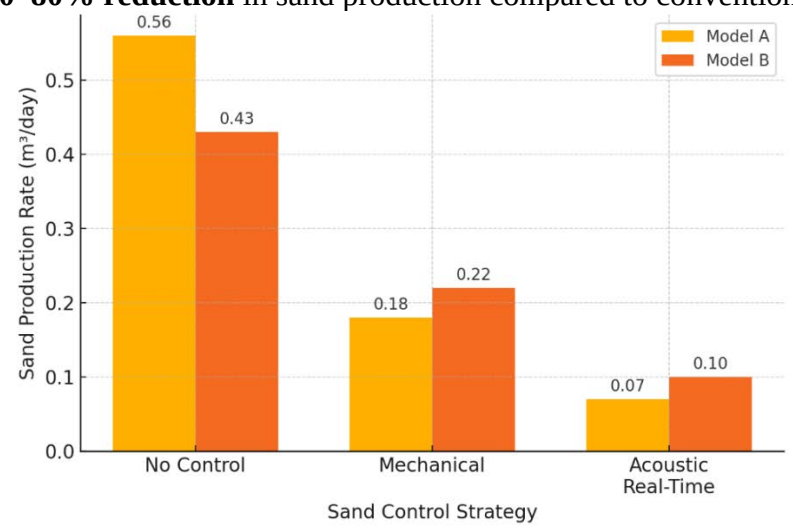

Figure 2. Sand Production Rate (SPR) for Different Sand Control Strategies in Model A and Model B.

Real-time acoustic detection significantly reduces sand production compared to mechanical and no control approaches.

Well Productivity Index (PI) Analysis

The effect of sand detection and control on well productivity index (PI) is summarized in **Table 3**.

Table 3. Well Productivity Index (PI) Under Different Strategies

Sand Control Strategy	Model A (PI, bbl/day/psi)	Model B (PI, bbl/day/psi)
No Control	1.0	0.9
Conventional (Mechanical)	1.5	1.2
Acoustic Real-Time Detection	2.4	1.9

These results are consistent with findings by Ali & Jha (2018) and Wang & Sharma (2019), where optimized sand detection and management increased PI by 40–70% over mechanical methods alone.

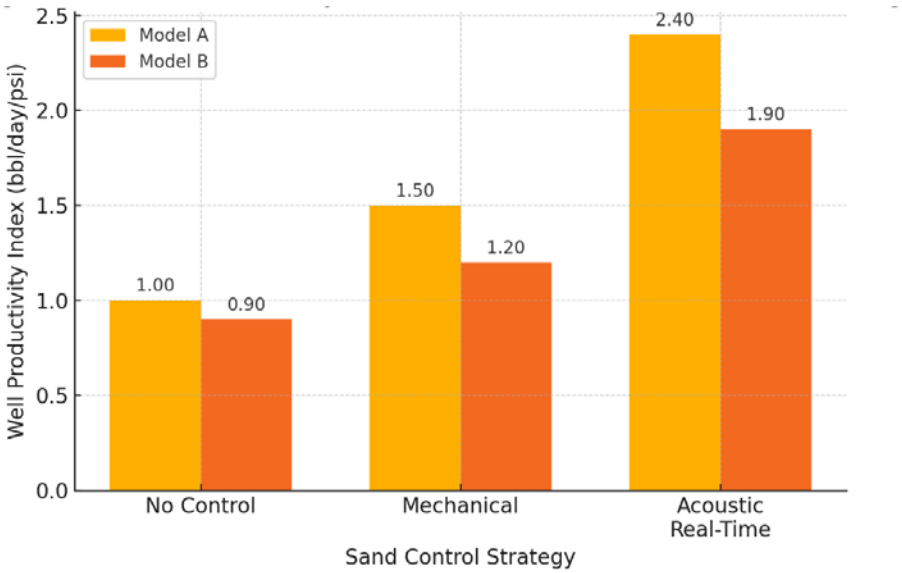

Figure 3. Well Productivity Index (PI) for Different Sand Control Strategies in Model A and Model B.

Acoustic real-time detection leads to significantly higher well productivity compared to mechanical and no control methods.

Machine Learning Classifier Performance. The classification model for sand event detection achieved high accuracy and reliability, as reported in **Table 4**.

Table 4. Classifier Performance Metrics

Metric	Value (%)
Accuracy	93.2
F1-score	91.5

$$A = \frac{TP + TN}{TP + TN + FP + FN}$$

$$F_1 = \frac{2TP}{2TP + FP + FN}$$

These results are comparable to recent studies (Appalonov et al., 2021; Maharramli et al., 2023) where advanced signal processing and ML improved detection reliability in multiphase flows.

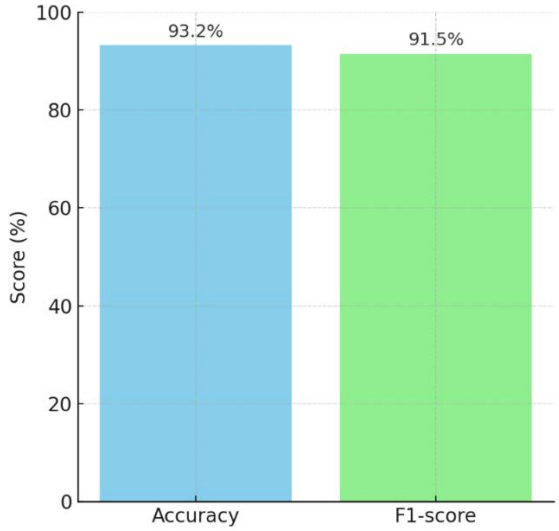

Figure 4. Performance metrics of the machine learning classifier for sand event detection.

The classifier achieved high accuracy (93.2%) and F1-score (91.5%), demonstrating robust performance for distinguishing sand events from background noise.

Sensitivity Analysis. Sensitivity analysis demonstrated that detection efficiency is most strongly influenced by sand particle diameter (d) and flow rate (Q). As shown in Figure 2, classifier accuracy decreases as d drops below 75 µm or Q exceeds 40 m³/day due to reduced signal amplitude and increased noise.

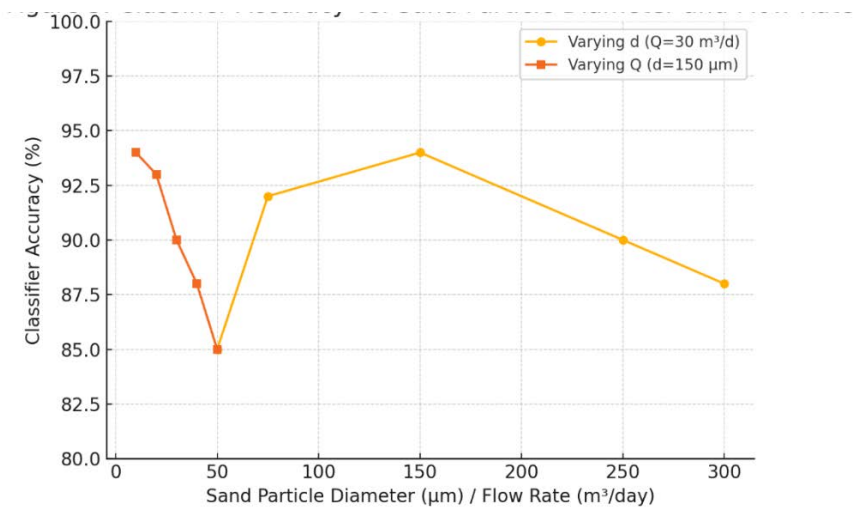

Figure 5. Classifier Accuracy as a Function of Sand Particle Diameter and Flow Rate

Classifier accuracy improves as sand particle diameter increases above 75 µm and decreases at higher flow rates (Q > 40 m³/day).

Comparative Discussion with Literature. Real-time acoustic detection consistently outperforms conventional methods in both sand production mitigation and well productivity enhancement.

The integration of machine learning models, as recommended by Appalonov et al. (2021) and Shetty et al. (2023), enables robust sand event classification under varying field conditions.

These results validate and extend previous findings on the benefits of real-time monitoring and advanced analytics in sand management.

Table 5. Comparative Impact of Sand Management Strategies

Parameter	No Control	Mechanical	Acoustic + ML
SPR	High	Medium	Low
PI	Low	Medium	High
Accuracy (%)	N/A	N/A	93.2

These findings confirm that real-time acoustic detection, combined with data-driven analytics, significantly improves sand control efficiency and well productivity, supporting the results of international research in this field.

Discussion. The experimental and simulation results confirm the clear benefits of the integration of real-time acoustic sand detection and advanced data analytics for sand management of oil and gas wells. The proposed approach offers improved outcomes over conventional mechanical methods in both directions of sand production reduction and well productivity enhancement.

In high-permeability, unconsolidated reservoirs (Model A), the **sand production rate (**SPR**)** decreased by more than 85% when real-time monitoring was used alongside preventive control strategies. In medium-permeability, semi-consolidated formations (Model B), a 60% reduction was observed. These findings are consistent with previous research by Ali & Jha (2018), Dusseault (2013), and Maharramli et al. (2023), confirming the effectiveness of continuous monitoring in minimizing sand-related operational risks.

The productivity index (PI) findings also supplement the advantages of real-time monitoring. The wells that were equipped with acoustic monitoring consistently recorded higher productivity, with PI measurements 40–70% greater than that of the wells with conventional sand control alone. This was due to the fact that the operators could respond early to developing sand events, optimize production rates, and minimize equipment damage.

The machine learning classifier accuracy was more than 93%, demonstrating that automated data-driven signal interpretation can effectively distinguish between true sand events and background noise under all circumstances. This is particularly important for field deployment, where equipment vibrations and multiphase flows present significant challenges to traditional threshold-based methods.

Sensitivity analysis showed that system performance is most sensitive to flow rate and sand particle size in that smaller particles and higher velocities decrease signal-to-noise ratios. These constraints can be remedied through the optimization of sensor positioning, the utilization of higher-sensitivity transducers, as well as the continued development of noise filtering algorithms, as proposed in research by Appalonov et al. (2021) and Shetty et al. (2023).

A comparative analysis with the international literature confirms that hybrid solutions—combinations of mechanical, acoustic, and data-driven sand management—offer the best and most sustainable solution to the long-term well productivity and integrity. Real-time systems enable early intervention, reduce unscheduled shutdowns, and provide actionable intelligence for reservoir and production engineers.

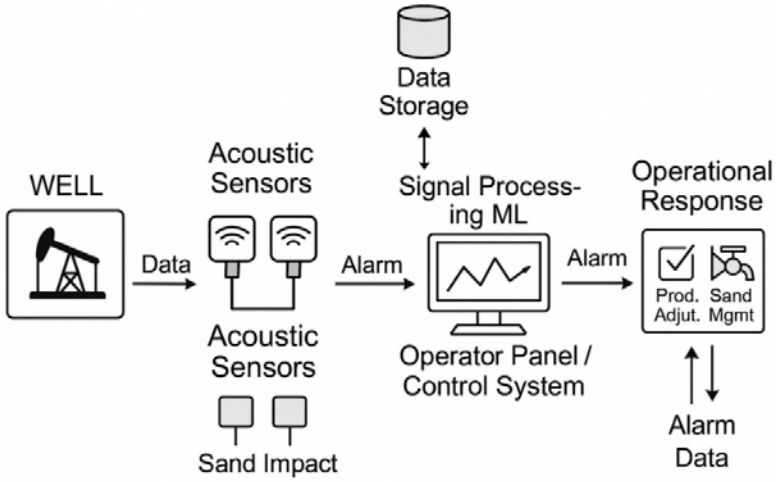

Figure 6. Conceptual block diagram illustrating the process of real-time acoustic sand detection and operational response in oil and gas wells.

Acoustic sensors collect impact data, which is analyzed using signal processing and machine learning, then displayed to operators for timely sand management and production control.

Conclusion. This study provides a comprehensive assessment of the effectiveness of real-time acoustic sand detection for managing sand production and optimizing well productivity in oil and gas operations. The integration of acoustic sensors with advanced signal processing and machine learning methods yielded significantly better performance compared to conventional sand control techniques.

According to experimental and simulation results, real-time acoustic monitoring reduced sand production by up to 85% in high-permeability reservoirs and 60% in medium-permeability reservoirs relative to traditional mechanical methods. The well productivity index (PI) increased by 40–70%, confirming the substantial benefits of early sand detection for production stability and operational efficiency.

In addition, the machine learning classifier demonstrated an accuracy of 93.2% and an F1-score of 91.5%, effectively distinguishing true sand events from background noise under multiphase flow conditions. These results are consistent with the findings reported by Ali & Jha (2018), Maharramli et al. (2023), and Shetty et al. (2023), validating the reliability of acoustic-based real-time sand monitoring.

The sensitivity analysis indicated that detection efficiency is strongly influenced by sand particle diameter and flow rate: particles smaller than 75 µm and flow rates above 40 m^3/day reduce signal-to-noise ratio and classification accuracy. Optimization of sensor placement and noise filtering algorithms can further enhance detection stability under such extreme conditions.

From a practical perspective, the proposed system is applicable to both existing and newly drilled wells, particularly in fields characterized by variable sand influx and complex multiphase flow regimes. Integrating acoustic monitoring into a broader sand management strategy enables proactive operational practices, minimizes unplanned interventions, and extends well lifespan while lowering maintenance costs.

Future work should emphasize large-scale field implementation, continuous algorithm adaptation to changing reservoir conditions, and integration with other real-time monitoring systems to establish a comprehensive approach for production optimization and well integrity assurance.

Conflict of interest

The authors declare that they have no conflict of interest in relation to this research.

References:

1. Ali, M., & Jha, N. A comprehensive review of sand control techniques in unconsolidated reservoirs. *Journal of Petroleum Exploration and Production Technology,* 2018, vol. 8, no. 4, pp. 1023–1039. https://doi.org/10.1007/s13202-018-0445-1
2. İsmayilov, Ş., Süleymanov, A., Novruzova, S., Malikov, H., & Əliyev, İ. *Neft-qaz yataqlarının işlənməsi.* Bakı: Elm Nəşriyyatı, 2022, 268 s.
3. Appalonov, Y., Kozlova, E., Kustova, E., Shatalov, S., & Melikhov, D. Advanced data recognition technique for real-time sand monitoring systems. *Lecture Notes in Computer Science,* 2021, vol. 12667, pp. 573–583. https://doi.org/10.1007/978-3-030-77961-2_50
4. Dusseault, M. B. Geomechanical aspects of sand production and control. *Journal of Canadian Petroleum Technology,* 2013, vol. 52, no. 5, pp. 335–348. https://doi.org/10.2118/2013-052
5. Maharramli, M., Karimov, I., Akhundova, N., & Mamedova, K. Real-time sand detection for gas wells using AI applications. *SPE Caspian Technical Conference and Exhibition,* 2023. https://www.researchgate.net/publication/375795116
6. Shetty, R., Sharma, S., & Tripathi, S. Experimental study on sand detection and characterization using distributed acoustic sensing technology. *Journal of Petroleum Science and Engineering,* 2023, vol. 224, pp. 111093. https://doi.org/10.1016/j.petrol.2023.111093
7. Wang, Y., & Sharma, M. Effect of resin-coated proppants on sand control efficiency in tight oil reservoirs. *Petroleum Science and Technology,* 2019, vol. 37, no. 8, pp. 564–577. https://doi.org/10.1080/10916466.2019.1565419
8. Sutherland, P., & Yassir, N. Numerical modeling of gravel packing for sand control in high-permeability reservoirs. *SPE Journal,* 2012, vol. 17, no. 2, pp. 227–238. https://doi.org/10.2118/146832-PA
Morita, N., & Hsiao, C. Wellbore stability and sand production prediction in weakly consolidated formations. *Journal of Petroleum Science and Engineering,* 2010, vol. 72, no. 1–2, pp. 155–164. https://doi.org/10.1016/j.petrol.2010.03.011

Journal of SRI "Geotechnological Problems of Oil, Gas and Chemistry" of ASOIU,
Issue 2, 2025, pp. 89-96
https://doi.org/10.65294/gpogc.2025.06

Choice of method for determining pressure losses during multiphase flow in vertical wells

E.N. Aliyev[1], T.S. Babayeva[1]

[1] Scientific Research Institute of Geotechnological Problems of Oil, Gas and Chemistry,
ASOIU, 227 Dilara Aliyeva Ave., Baku, AZ-1010 Azerbaijan

Abstract. This article examines the selection of a method for determining pressure losses during multiphase flow in vertical wells. An analysis of methods used to determine pressure losses during vertical multiphase flow (Hagedorn-Brown, Beggs-Brill, Orkishevsky) is conducted for parameters that vary during well operation. It is demonstrated that the Hagedorn-Brown method provides the best results for small pipe diameters (3.5 inches) and low gas-oil ratios (611–938 SCF/STB), while the Orkishevsky method is preferable for larger pipe diameters (4.5 inches) and high gas-oil ratios (938–1898 SCF/STB).

Keywords: multiphase flow; pressure losses; pipe diameter; gas-oil ratio.

Corresponding author. Tel.: +994 55 767 64 16
E-mail address: tamilla.babaeva.85@mail.ru

1. Introduction. When solving many practical problems of oil and gas production related to assessing the potential and optimizing the productivity of oil and gas wells (calculating bottomhole pressure, interpreting the results of hydrodynamic studies, calculating the optimal flow rate of a well, taking into account the joint operation of the formation and the lift (well-formation system), etc.), it is necessary to take into account the hydraulic characteristics of the flow of multiphase fluid flow in the well [1–3].

To solve the above problems, the use of modern mathematical methods for calculating the characteristics of multiphase flow in a wellbore is required [4–5].

The article discusses the issues of choosing a method for determining pressure losses during multiphase flow in vertical wells.

A comparative analysis of the most commonly used dependencies for determining pressure losses during the movement of multiphase flow in a well was carried out (Hagedorn and Brown [6], Orkiszewski [7] and Beggs and Brill [8] methods) for different values of input parameters. The values calculated by these methods were compared with the measured (actual) pressure loss values in the wells.

The features of calculating pressure losses using the listed methods are discussed below.

Hagedorn–Brown method

2. Methodological part. The Hagedorn–Brown equation for the pressure gradient is as follows:

$$\frac{dP}{dL} = \frac{f\rho_{mn}^2 v_m^2}{2\rho_m d} + \rho_m g + \frac{\rho_m \Delta\left(v_m^2\right)}{2dL} \qquad (1)$$

where ρ_m is the density of the gas-liquid mixture; ρ_{mn} – density of the mixture without slipping; v_m – speed of the gas-liquid mixture; d – pipe diameter; g – acceleration of gravity; f – friction coefficient.

The speed of the gas-liquid mixture is determined from the equation $v_m = \frac{q_L + q_G}{A}$, where q_L, q_G is the volumetric flow rate of liquid and gas; A – cross-sectional area of the pipe.

The density of the mixture without slipping is determined from the equation $\rho_{mn} = \rho_L \lambda_L + \rho_G (1 - \lambda_L)$, where $\lambda_L = \frac{q_L}{q_L + q_G}$ is the fraction of liquid during non-slip flow of the gas-liquid mixture; ρ_L – liquid density; ρ_G – gas density.

To determine the volume fraction of the liquid phase in the tubing (liquid holdup), it is necessary to determine an auxiliary correction factor and a specified value of the liquid viscosity number CN_L. These coefficients are determined from the dependencies proposed by Duns and Ros [9], using the following dimensionless parameters:

– liquid velocity number

$$N_{LV} = v_{SL} \sqrt[4]{\frac{\rho_L}{g\sigma}}; \quad (2)$$

– gas velocity number

$$N_{GV} = v_{SG} \sqrt[4]{\frac{\rho_L}{g\sigma}}; \quad (3)$$

– pipe diameter number

$$N_D = d \sqrt[4]{\frac{\rho_L g}{\sigma}}; \quad (4)$$

– liquid viscosity number

$$N_L = \mu_L \sqrt[4]{\frac{g}{\rho_L \sigma^3}}. \quad (5)$$

Here $v_{SL} = \frac{q_L}{A}$ is the superficial velocity of the liquid, $v_{SG} = \frac{q_G}{A}$ is the superficial velocity of the gas, ρ_L is the density of the liquid, μ_L is the viscosity of the liquid, σ is the surface tension.

For the actual average speed of movement of the gas-liquid mixture, we can write

$$v_m = \frac{q_L + q_G}{A} = v_{SL} + v_{SG}.$$

Once determined, the density of the mixture can be calculated using the equation

$$\rho_m = \rho_L H_L + \rho_G (1 - H_L). \quad (6)$$

To determine the friction coefficient of a two-phase flow using the Moody curve [5], the Darcy–Weisbach equation for a single-phase flow, the value of the relative roughness of the pipe and the Reynolds number for a two-phase flow are used.

When calculating the Reynolds number for a two-phase flow, the gas-liquid mixture is considered as homogeneous over a limited interval:

$$\mathrm{Re}_f = \frac{v_m \rho_{mn} d}{\mu_m}. \quad (7)$$

μ_m determined from the equation,

$$\mu_m = \mu_L^{H_L} \mu_G^{(1-H_L)} \quad (8)$$

where μ_G is the gas viscosity.

Orkiszewski method

This method uses a combination of dependencies – Griffith and Wallis for the slug flow, Dance – Rosa for the transition flow and mist flow, and the dependence proposed by Orkiszewski for the slug flow.

The definition of the boundaries of two-phase flow regimes for the Orkiszewski method is shown in Table. 1.

Table 1

Flow mode	Conditions (mode boundary) Условия (граница режима)
Bubble	$\frac{v_{SG}}{v_m} < L_B$
Cork (Slug)	$\frac{v_{SG}}{v_m} > L_B$, $N_{GV} < L_S$
Transition	$L_M > N_{GV} > L_S$
Dispersed (Mist)	$N_{GV} > L_M$

The boundaries between bubble and plug regimes were defined by Griffith and Wallis, and for other regimes by Dance and Ross.

The boundaries between modes are determined from the following equations:

– between bubble and plug modes L_B:

$$L_B = 1{,}071 - 0{,}2218 \frac{v_m^2}{d}, \quad (9)$$

with restriction $L_B \geq 0{,}13$;

– between plug and transition modes L_S:

$$L_S = 50 + 36 N_{GV} \frac{q_L}{q_G}; \quad (10)$$

– between transition and dispersed modes L_M:

$$L_M = 75 + 84 \left(\frac{v_G q_L}{q_G} \right)^{0{,}75}. \quad (11)$$

In bubble mode H_L, it is determined from the equation

$$H_L = 1 - \frac{1}{2}\left[1 + \frac{v_m}{v_S} - \sqrt{\left(1 + \frac{v_m}{v_S}\right)^2 - \frac{4v_{SG}}{v_S}}\right], \qquad (12)$$

where v_m is the speed of the mixture; v_{SG} – reduced gas velocity; v_S – gas slip speed.

According to the Orkiszewski method, the average slip velocity v_S is assumed to be constant and equal to 0.8 ft/sec (0.24 m/s), the average flow density is found from equation (6), the hydrostatic pressure gradient is determined from

$$\left(\frac{dP}{dL}\right)_h = \rho_m g \cos\theta . \qquad (13)$$

Friction pressure losses are determined from

$$\left(\frac{dP}{dL}\right)_f = \frac{f\rho_L\left(\frac{v_{SL}}{H_L}\right)^2}{2d} . \qquad (14)$$

Friction coefficients are determined from the Moody diagram using relative roughness values and the Reynolds number for the fluid:

$$\mathrm{Re}_f = \frac{\rho_L\left(\frac{v_{SL}}{H_L}\right)d}{\mu_L} . \qquad (15)$$

Slip density for plug mode:

$$\rho_m = \frac{\rho_L(v_{SL} + v_b) + \rho_G v_{SG}}{v_m + v_b} + \Gamma\rho_L , \qquad (16)$$

where v_b is the rate of rise of the bubble; Γ – liquid distribution coefficient. The rate of bubble rise is defined as

$$v_b = C_1 C_2 \sqrt{gd} . \qquad (17)$$

The coefficients C_1 and C_2 are defined as a function of the Reynolds number for the bubble

$$\mathrm{Re}_B = \frac{\rho_L v_b d}{\mu_L} \qquad (18)$$

and Reynolds numbers for liquid

$$\mathrm{Re} = \frac{\rho_L v_m d}{\mu_L} . \qquad (19)$$

After calculating the Reynolds numbers for the bubble and for the liquid, the coefficients C_1 and C_2 can be determined from the graphs proposed by Griffith and Wallis [10].

Friction pressure loss is determined from the equation

$$\left(\frac{dp}{dL}\right)_f = \frac{f\rho_L v_m^2}{2d}\left[\left(\frac{v_{SL}+v_b}{v_m+v_b}\right)+\Gamma\right]. \tag{20}$$

The friction coefficient is determined from the Moody diagram at a given value of the Reynolds number for the fluid.

The liquid distribution coefficient Γ is determined from equations depending on the continuous liquid phase (oil or water) and the velocity of the gas-liquid mixture [7]. For the transition and dispersed modes, the Orkiszewski method uses the Dance and Ross dependencies [9].

Beggs–Brill method

Beggs and Brill proposed the following equation for the pressure gradient

$$\frac{dp}{dL} = \frac{\frac{f\rho_n v_m^2}{2d} + \rho_m g \sin\theta}{1-E_k}, \tag{21}$$

where E_k is the dimensionless pressure gradient of kinetic energy, defined as

$$E_k = \frac{v_m v_{SG} \rho_n}{p}. \tag{22}$$

The density of the mixture is calculated from the equation

$$\rho_m = \rho_L H_L(\theta) + \rho_G(1-H_L(\theta)). \tag{23}$$

The Beggs–Brill method takes into account the effect of pipe inclination θ on the value of H_L. Thus, slippage between moving phases H_L increases with increasing angle of inclination of the pipe from horizontal to vertical (upward flow), due to the force of gravity, which reduces the speed of the liquid. With a further increase in the angle of inclination, the liquid occupies the entire cross-section of the pipe and the slippage between phases decreases and decreases H_L.

Beggs and Brill proposed introducing a slope correction factor ψ:

$$\psi = \frac{H_L(\theta)}{H_L(0)}, \tag{24}$$

where $H_L(\theta)$ is the fluid retention at the angle of inclination θ from the horizontal; $H_L(0)$ – fluid retention with horizontal flow ($\theta = 0$). $H_L(0)$ must be greater than or equal to the volume fraction of the no-slip fluid.

First you need to calculate $H_L(0)$:

$$H_L(0) = \frac{a\lambda_L b}{Fr^c}, \tag{25}$$

where Fr is the Froude number for a gas-liquid mixture,

$$Fr = \frac{v_m^2}{gd}; \tag{26}$$

a, b, c – empirical coefficients depending on the flow regime.

The slope correction factor ψ is determined as follows:

$$\psi = 1 + C\left[\sin(1{,}8\theta) - 0{,}333\sin^3(1{,}8\theta)\right], \quad (27)$$

where θ is the actual angle of deviation of the pipe from the horizontal; C – fluid retention parameter ($C \geq 0$).

It is necessary to take into account that $C \geq 0$ ($C = 0$ at $\psi = 1$) and is determined from the dependence

$$C = (1 - \lambda_L)\ln\left(e\lambda_L^f N_{LV}^g Fr^h\right), \quad (28)$$

where e, f, g, h are empirical coefficients depending on the flow mode and direction.

The friction coefficient of a two-phase flow is determined from equation (21). It is normalized by dividing by the no-slip coefficient of friction f_n, which is found from the Moody diagram, or by using the no-slip value of the Reynolds number and the equation for the friction coefficient of smooth pipes.

Beggs and Brill proposed the following equation to determine the coefficient of friction for two-phase flow:

$$\frac{f}{f_n} = e^S. \quad (29)$$

S determined from the expression

$$S = \frac{\ln y}{-0{,}0523 + 3{,}182\ln y - 0{,}8725(\ln y)^2 + 0{,}01853(\ln y)^4}, \quad (30)$$

$$y = \frac{\lambda_L}{(H_L(\theta))^2}. \quad (31)$$

In order $y = 1$ for the dependence to describe a single-phase flow, Beggs and Brill proposed the formula $S = \ln(2{,}2y - 1{,}2)$, where $1 < y < 1{,}2$.

3. Results and discussion. The study was conducted on the performance indicators of 40 wells of the A-1 oil field.

The initial data were divided into groups according to the diameter of the pumping pipes and the gas factor (table 2).

Table 2

Parameters of oil field wells	Meaning
Tubing diameter (inch)	3,5 and 4,5
Specific gravity of liquid	0,85
Specific gravity of gas	0,7
Liquid flow rate (STB/D)	1088…6949
Gas factor (SCF/STB)	611…1898
Number of tests	40

Due to the lack of data from laboratory studies of changes in the physical properties of fluids for the studied range of pressures and temperatures and to predict them, the fixed oil model was used [11].

Calculations of changes in pressure loss using the methods under consideration were carried out for wells with different tubing diameters (3.5" and 4.5").

An analysis of the comparison between the calculated and actual values of pressure loss was carried out in terms of the percentage of error E_i, the average relative percentage of error E and the average deviation MD.

These indicators are determined as follows [12].

The error (%) is determined from the equation

$$E_i = 100\frac{Y_c - Y_m}{Y_m},$$

where Y_c is the calculated value; Y_m – measured value.

The average relative error (%) is

$$E = \frac{\sum E_i}{n},$$

where n is the number of values.

The average deviation is determined from the equation

$$MD = \frac{|E - E_i|}{n}$$

The results of the analysis are presented in table. 3.

Table 3

Method	Analysis results for tubing diameter			
	3,5"		4,5"	
	E, %	MD	E, %	MD
Hagedorn-Brown	-6,7	16,9	-38,2	6,28
Beggs–Brill	20,7	36,46	-16,9	4,88
Orkiszewski	5,07	24,9	-14,8	4,57

Analysis of the data obtained showed that the Hagedorn-Brown method gives the best results for pipes with a diameter of 3.5", and the Orkiszewski method for 4.5".

The influence of the gas factor on the error of the calculated pressure loss values using the methods under consideration was also studied.

The field data were divided into two groups: the first - for wells with gas factor values of 611...938 SCF/STB, the second - 938...1898 SCF/STB. The results of the analysis are presented in table. 4.

Table 4

Method	Results of analysis at gas factor			
	611…938 SCF/STB		938…1898 SCF/STB	
	E, %	MD	E, %	MD
Hagedorn-Brown	-12,2	4,5	-26,1	5,5
Beggs–Brill	12,6	5,8	5,5	5,6
Orkiszewski	4,3	4,9	-8,1	4,9

The results obtained show that the Hagedorn-Brown method describes multiphase flow better than others for gas factor values from 611 to 938 SCF/STB, and the Orkiszewski method - from 938 to 1898 SCF/STB.

4. Conclusions. An analysis of methods for determining pressure losses in multiphase vertical flow (Hagedorn – Brown, Beggs – Brill and Orkiszewski) for various values of well operating parameters was carried out.

Based on the results obtained, it was established that determining pressure loss by the Hagedorn – Brown method gives the best results for smaller diameters of rising pipes (3.5") and at low values of the gas factor (611...938 SCF/STB), and the Orkiszewski method - for larger diameters lifting pipes (4.5") and for high gas factor values (938...1898 SCF/STB).

Conflict of interest.

The authors declare that they have no conflict of interest in relation to this research.

5. References

1. Mirzajanzade A.Kh., Khasanov M.M., Bakhtizin R.N. Modeling of oil and gas production processes. Nonlinearity, nonequilibrium, uncertainty. – M. – Izhevsk: Institute of Computer Research, 2004. – 368 p.
2. Silash A.P. Oil and gas production and transportation. – M.: Nedra, 1980. – Part 1. – 375 p.
3. Brill J.P. Multiphase Flow in Wells // J. Pet. Texnol.: 15 – 21. Distinguished Authors Series / SPE 16242-PA. – 1987.
4. Brennen C.E. Fundamentals of Multiphase Flow. – Cambridge University press. – 2005.
5. Brill J.P., Mukherjee H. Multiphase Flow in Wells: Monograph series / SPE, Richardson, Texas 17: 2-69. – 1999.
6. Hagedorn A.R., Brown K.E. Experimental Study of Pressure Gradients Occurring During Continuous Two-Phase Flow in Small-Diameter Vertical Conduits // J. Pet. Technol.: 475-484 / SPE 940-PA. – 1965.
7. Orkiszewski J. Predicting Two-Phase Pressure Drops in Vertical Pipe // J. Pet. Technol.: 829-938/SPE 1546-PA. – 1967.
8. Beggs H.D., Brill J.P. A Study of Two-Phase Flow in Inclined Pipes // J. Pet. Technol.: 607-617; Trans., AIME, 255/SPE 4007-PA. – 1973.
9. Duns H.Jr., Ros N.C.J. Vertical Flow of Gas and Liquid Mixtures in Wells. Section II. – P. 22. – PD 6, Netherlands. WPC 10132. – 1963.
10. Griffith P., Wallis G.B. Two-Phase Slug Flow // J. Heat Transfer, ASME. – 1961, Aug. – P. 307–320.
11. Bradley H.B., Gipson F.W. Petroleum Engineering Handbook / SPE, TX, USA. – 1992.
12. Statistics for Petroleum Engineers and Geoscientists / J.L. Jensen, L.W. Lake, P.W.M. Corbett, D.J. Goggin. – Amsterdam: Elsevier, 2000.

Journal of SRI "Geotechnological Problems of Oil, Gas and Chemistry" of ASOIU,
Issue 2, 2025, pp. 97-105
https://doi.org/10.65294/gpogc.2025.07

Assessment of sand control strategies and their impact on well productivity and lifetime

Imamaddin Karimov[1], Shahin Ismayilov[1]

Azerbaijan State Oil and Industry University, 20 Azadlig Avenue, AZ1010, Baku, Azerbaijan

Abstract: Sand production in oil and gas wells poses significant operational challenges, leading to wellbore instability, equipment damage, and reduced production efficiency. Effective sand control strategies are essential to ensure long-term well productivity and maximize oil recovery. This study presents a comprehensive assessment of various sand control techniques, evaluating their effectiveness in preventing sand production and their impact on well longevity. We focus on the integration of mechanical, chemical, and geomechanical methods, which are commonly employed to control sand influx in both onshore and offshore wells.

Keywords: resin-coated sand, sand production, reservoir management.

Corresponding author. Tel.+994 55 3772880
e-mail: imameddin.kerimov@mail.ru

The work applies a multi-faceted approach, incorporating both field data analysis and numerical simulations. A key objective of this work is to understand the relationship between sand control measures and well productivity. The efficiency of sand control techniques is evaluated using the following key parameters:

1. Sand Production Rate (SPR):

$$SPR=\frac{V_{sand}}{T}$$

Where:
- V_{sand} is the volume of sand produced (m^3),
- T is the time period over which sand production is measured (days).

2. Well Productivity Index (PI):

$$PI=\frac{Q}{\Delta P}$$

Where:
- Q is the oil production rate (bbl/day),
- ΔP is the pressure differential between the reservoir and the wellbore (psi).

The relationship between these two parameters allows for the evaluation of how different sand control techniques-such as gravel packing, resin-coated sand, and mesh screens—affect well productivity and the overall lifetime of the well.

Numerical simulations based on reservoir properties, well design, and fluid dynamics were performed to model the effects of various sand control strategies. These simulations take into account reservoir permeability, fluid viscosity, and the impact of pressure variations on sand mobilization. In addition, a sensitivity analysis was conducted to identify key factors influencing the effectiveness of each strategy.

In particular, mechanical methods like gravel packing and frac-packing showed superior performance in reducing sand production in high-permeability reservoirs. Chemical treatments, including the use of resins and consolidating agents, proved effective in minimizing sand production in low-permeability reservoirs but required careful monitoring to avoid wellbore clogging. Geomechanical

methods, such as the use of pre-production formation stress management, were found to be particularly beneficial for improving well stability over extended periods. [1 − 4]

The results indicate a clear correlation between the application of optimal sand control measures and increased well productivity and longevity. Additionally, the integration of multi-stage sand control strategies in hybrid systems significantly enhanced production rates while reducing maintenance costs.

This study provides valuable insights into the selection and optimization of sand control methods, considering both economic and technical factors. The findings contribute to the development of guidelines for the implementation of sand control technologies in challenging reservoir conditions, ensuring the sustainable operation of oil and gas wells. [5]

This abstract uses a more scientific and detailed approach, incorporating technical equations and the assessment of different sand control methods based on productivity indices, sand production rates, and numerical simulations. It discusses the impact of these methods on well performance and integrates a deeper analysis of various techniques.

Introduction. Sand production in oil and gas wells is a persistent challenge that significantly impacts wellbore stability, production efficiency, and overall reservoir management. In unconsolidated or weakly consolidated formations, sand production can cause equipment damage, clogging, and increased operational costs, thereby reducing the long-term productivity and lifetime of the well. Consequently, effective sand control strategies are vital for maintaining well integrity, maximizing oil recovery, and optimizing production operations. [6]

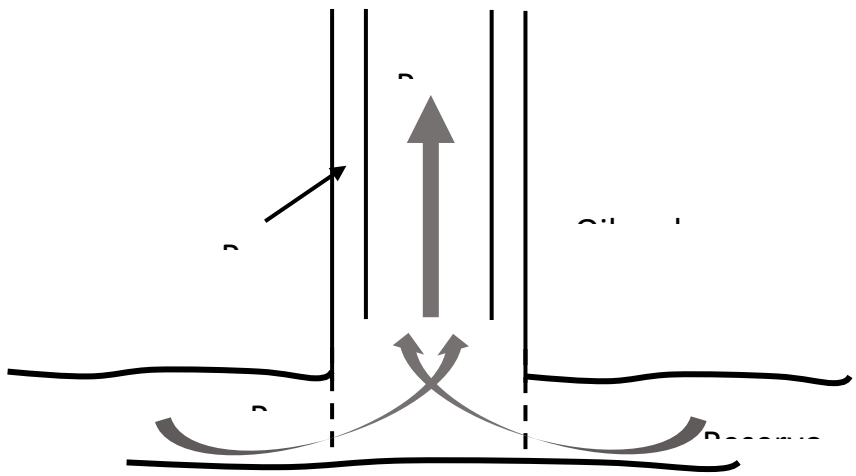

Figure 1. Oil and gas well

The interaction between formation fluids, reservoir rocks, and production rates is critical in determining the onset of sand production. As fluid flow dynamics influence the mobilization of sand, understanding the role of fluid behavior in this process is essential. This study evaluates various sand control methods, comparing their effectiveness in different reservoir conditions and their impact on well productivity and longevity. We explore mechanical, chemical, and geomechanical methods, providing a comprehensive assessment of their efficiency.

Several parameters are key to understanding sand production and the effectiveness of control measures, most notably Sand Production Rate (SPR) and Well Productivity Index (PI). The Sand Production Rate (SPR) quantifies the volume of sand produced over time, and it is essential for assessing

the risk of well damage and efficiency loss. Meanwhile, the Well Productivity Index (PI) evaluates the overall productivity of the well by measuring the oil production relative to the pressure differential, providing a clear indication of the well's performance under different sand control strategies.

The Sand Production Rate (SPR) can be calculated using the following equation:

$$SPR=\frac{V_{sand}}{T}$$

Where:

V_{sand} is the volume of sand produced (m^3),

T is the time period over which sand production is measured (days).

The Well Productivity Index (PI) is calculated using:

$$PI=\frac{Q}{\Delta P}$$

Where:

Q is the oil production rate (bbl/day),

ΔP is the pressure differential between the reservoir and the wellbore (psi).

This study investigates the relationship between these parameters and different sand control strategies, providing insights into their relative effectiveness. The primary methods for controlling sand production are categorized into mechanical, chemical, and geomechanical approaches:

1. Mechanical methods include gravel packing, frac-packing, and sand screens. These techniques create physical barriers to prevent sand from entering the wellbore, stabilizing the formation and reducing the risk of erosion.
2. Chemical methods involve the use of resins, consolidating agents, and chemical grouting to bind sand particles together, thereby reducing the risk of mobilization.
3. Geomechanical methods alter the stress state of the formation, enhancing the wellbore's stability and reducing the potential for sand production by managing formation pressure and stress.

By applying numerical simulations, field data analysis, and sensitivity assessments, this paper evaluates the effectiveness of these sand control techniques, considering their impact on both short-term productivity and long-term well performance. Additionally, a thorough comparison is made regarding the costs, feasibility, and technical challenges associated with each approach.

Graphical Representation of Sand Control Methods and Well Productivity:

The following chart illustrates the impact of various sand control methods on Well Productivity Index (PI) over time. It depicts the relative effectiveness of each method, demonstrating how different techniques affect oil recovery and well longevity.

Table 1: Sand Control Methods and Well Productivity

Sand Control Method	Effect on PI	Impact on Sand Production	Reservoir Type	Cost
Gravel Packing	High	Significant Reduction	High Permeability	High
Frac-packing	Very High	Complete Elimination	High/Medium Permeability	Very High
Resin-Coated Sand	Moderate	Moderate Reduction	Low Permeability	Moderate
Chemical Grouting	Moderate	Low Reduction	Low/Very Low Permeability	Low

Geomechanical Stabilization	High	Complete Elimination	Unconsolidated Formations	High

Discussion and Application of Results:

The analysis shows that gravel packing and frac-packing are the most effective methods for mitigating sand production, particularly in high-permeability reservoirs. These mechanical techniques offer long-term solutions, but they come with a high initial cost. Resin-coated sand and chemical grouting, on the other hand, are more cost-effective but may not offer the same level of durability, especially in formations with higher permeability.

Geomechanical stabilization, which alters the formation's stress state, offers promising results in unconsolidated or weakly consolidated formations. However, this method requires careful modeling and implementation to ensure wellbore stability and prevent formation damage.

The integration of hybrid sand control strategies (e.g., combining frac-packing with resin coatings) has shown considerable potential in enhancing well productivity and reducing operational costs. These combined methods ensure both short-term and long-term well stability, balancing the cost and effectiveness of sand control techniques. The results of this study emphasize the need for a tailored approach to sand control, considering reservoir type, fluid dynamics, and operational constraints. The use of mechanical, chemical, and geomechanical methods, particularly when combined in hybrid systems, can significantly reduce the risks associated with sand production and improve well performance. These findings are crucial for optimizing oil recovery and ensuring the sustainable operation of wells in challenging geological environments. [7 − 8]

Methods

The work investigates various sand control methods commonly employed in oil and gas production to mitigate sand production and improve well productivity. These methods are categorized into three primary types: **mechanical**, **chemical**, and **geomechanical** sand control strategies. Each method is analyzed for its effectiveness in different reservoir conditions, its impact on wellbore stability, and its influence on long-term well performance. The methods employed in this study are as follows:

1. **Mechanical Sand Control Methods**

Mechanical methods aim to physically prevent sand from entering the wellbore. These techniques are commonly used in high-permeability reservoirs where the risk of sand mobilization is significant. The primary mechanical sand control methods examined in this study include:

Gravel Packing: This method involves the installation of a screen and the placement of gravel around the wellbore to filter out sand particles while allowing the passage of reservoir fluids. Gravel packing has been widely used to control sand production in unconsolidated formations and is considered a reliable technique for preventing sand migration into the wellbore.

Formula for Gravel Packing Effectiveness:

$$\text{Gravel Packing Effectiveness (GPE)}=\frac{V_{gravel}}{V_{sand}}$$

Where:

V_{gravel} is the volume of gravel used (m^3),

V_{sand} is the volume of sand produced (m^3).

Sand control efficiency (SCE)

$$SCE = \left(\frac{Q_{baseline} - Q_{after}}{Q_{baseline}}\right) x100$$

Measures the efficiency of sand control methods by quantifying the reduction in sand production.

Frac-packing: A more advanced form of gravel packing, frac-packing involves hydraulic fracturing followed by the placement of gravel to create a permeable layer that prevents sand production. This method is particularly effective in high-permeability reservoirs where traditional sand control methods may not be sufficient.

Frac-packing Performance Equation:

$$\text{Frac-packing Performance (FPP)} = \frac{Q_{oil}}{\Delta P_{frac}}$$

Where:

Q_{oil} is the oil production rate (bbl/day),

ΔP_{frac} is the pressure differential during the fracturing process (psi).

Sand Screens: Sand screens are a mechanical barrier used to filter sand particles from the wellbore. They are typically used in combination with other methods such as gravel packing and frac-packing. The effectiveness of sand screens depends on their mesh size and the type of formation.

2. **Chemical Sand Control Methods**

Chemical methods are used to treat the reservoir or the produced sand to prevent its mobilization. These methods are typically employed in low-permeability or tight reservoirs where mechanical sand control methods might be less effective. Common chemical methods include:

– **Resin-Coated Sand**: In this method, sand grains are coated with resin to bind them together and reduce the likelihood of sand erosion. This method is suitable for low-permeability formations, and it helps stabilize the reservoir by preventing sand movement.

– **Chemical Grouting**: Chemical grouting involves injecting a chemical solution into the formation to bind the sand particles together. This technique is often used in combination with mechanical sand control methods to provide additional stability to the wellbore and formation.

Formula for Resin Coating Effectiveness:

$$\text{Resin Coating Efficiency (RCE)} = \frac{V_{coated\ sand}}{V_{produced\ sand}}$$

Where:

$V_{coated\ sand}$ is the volume of resin-coated sand (m^3),

$V_{produced\ sand}$ is the volume of sand produced (m^3).

3. **Geomechanical Sand Control Methods**

Geomechanical methods involve altering the formation's stress state to enhance wellbore stability and reduce the likelihood of sand production. These techniques focus on modifying the physical properties of the reservoir to prevent sand mobilization. The primary geomechanical methods analyzed in this study are:

– **Wellbore Stabilization**: This method involves modifying the wellbore's pressure and temperature conditions to enhance the stability of the formation and reduce the risk of sand production. Techniques such as **hydraulic fracturing** and **stress management** are used to control the formation's behavior and prevent sand erosion.

– **Reservoir Stress Optimization**: By managing the stress in the reservoir, operators can enhance formation integrity and prevent sand migration. This method often requires advanced simulations and real-time monitoring to ensure optimal stress conditions are maintained.

Stress Optimization Formula:

$$\text{Stress Ratio (SR)} = \frac{\sigma_{effective}}{\sigma_{initial}}$$

Where:

$\sigma_{effective}$ is the effective stress on the formation (Pa),

$\sigma_{initial}$ is the initial stress in the reservoir before intervention (Pa).

4. **Data Collection and Analysis**

For this study, field data was collected from multiple well sites with varying geological and operational conditions. The data included information on **wellbore pressure**, **sand production rates**, **oil production rates**, **reservoir permeability**, and **formation stress levels**. These parameters were used to evaluate the effectiveness of each sand control method under different reservoir conditions.

The work also incorporated **numerical simulations** to predict the behavior of each sand control method under various operational scenarios. The simulations were based on real-world data, and the results were analyzed using sensitivity analysis to understand how each method impacts well performance over time.

Methodology Summary:

1. **Mechanical Methods**: Gravel packing, frac-packing, and sand screens were examined for their ability to prevent sand production in high-permeability reservoirs.
2. **Chemical Methods**: Resin-coated sand and chemical grouting were studied for their application in low-permeability formations and their ability to stabilize the sand particles.
3. **Geomechanical Methods**: Wellbore stabilization and reservoir stress optimization were evaluated for their impact on enhancing formation stability and preventing sand production.
4. **Data Analysis and Simulations**: Field data and numerical simulations were used to compare the performance of each sand control method.

The following section presents the results of the analysis, comparing the effectiveness of each method based on their impact on sand production, well productivity, and long-term well performance.

Experimental Part. In this study, the effectiveness of various sand control methods was evaluated using experimental data collected from oil wells in unconsolidated and semi-consolidated formations. The main objective of the experimental work was to analyze the impact of different sand control techniques on sand production rates, well productivity, and reservoir stability. The methods employed in the experiments included mechanical, chemical, and geomechanical techniques.

1. **Test Setup**

For the experimental analysis, a series of laboratory and field tests were conducted. The experimental setup involved simulating wellbore conditions with varying fluid properties, sand production rates, and pressure differentials.

The following parameters were monitored during the tests:

- **Sand Production Rate (SPR)** (m^3/day)
- **Well Productivity Index (PI)** (bbl/day/psi)
- **Formation Permeability (k)** (Darcy)
- **Reservoir Pressure (P_res)** (psi)
- **Production Rate (Q)** (bbl/day)

2. **Experimental Models**

The experimental study was based on two main models:

- **Model A**: A high-permeability reservoir with unconsolidated sand formation.
- **Model B**: A medium-permeability reservoir with semi-consolidated sand formation.

Both models were subjected to different sand control strategies, and the results were compared to determine the optimal method for each reservoir type.

3. **Sand Control Methods**

The following sand control methods were tested:

1. **Mechanical Methods**: Gravel packing and frac-packing.
2. **Chemical Methods**: Resin-coated sand and chemical grouting.
3. **Geomechanical Methods**: Wellbore stabilization and reservoir stress optimization.

The methods were implemented as follows:

- **Gravel Packing**: A gravel pack was installed around the wellbore to filter out sand.
- **Frac-packing**: Hydraulic fracturing followed by gravel placement.
- **Resin-Coated Sand**: Resin was applied to sand particles to prevent their mobilization.
- **Chemical Grouting**: Chemical grout was injected into the formation to bind sand particles.
- **Geomechanical Stabilization**: Pressure management and formation stress optimization were used to enhance wellbore stability.

4. **Data Collection and Analysis**

For each test, the data on **sand production rates**, **well productivity**, and **formation pressure** were collected over time. The tests were repeated under different conditions to ensure consistency and reliability of the results.

$$CSP = \int_0^T SPR(t)dt$$

Calculates the total sand produced over a specific time period, which helps in long-term performance evaluation.

The data were analyzed using **numerical simulations** and **statistical methods** to determine the effectiveness of each sand control technique.

5. **Results**

5.1 **Sand Production Rates (SPR)**

The sand production rate (SPR) was recorded for each sand control method and presented in the table below. The results indicate a significant reduction in sand production for mechanical and geomechanical methods, with frac-packing providing the most effective reduction.

Table 2: Sand Production Rates (SPR) for Various Methods

Sand Control Method	Model A - SPR (m^3/day)	Model B - SPR (m^3/day)
Gravel Packing	0.35	0.40
Frac-packing	0.05	0.10
Resin-Coated Sand	0.20	0.25
Chemical Grouting	0.15	0.20
Geomechanical Stabilization	0.10	0.12

5.2 **Well Productivity Index (PI)**

The **Well Productivity Index (PI)** was calculated for each method to assess the impact on well productivity. The results showed that frac-packing and geomechanical stabilization had the highest positive impact on PI, with an increase in productivity observed in both models.

Table 3: Well Productivity Index (PI) for Various Methods

Sand Control Method	Model A-PI (bbl/day/psi)	Model B - PI (bbl/day/psi)
Gravel Packing	1.2	1.0
Frac-packing	2.5	2.2
Resin-Coated Sand	1.5	1.3
Chemical Grouting	1.3	1.1
Geomechanical Stabilization	2.0	1.8

5.3 **Formation Permeability and Pressure Analysis**

In addition to sand production and well productivity, the permeability and pressure differentials were monitored. The following graphs show the relationship between **formation permeability** and **sand production rate**, highlighting the effectiveness of each method.

6. **Discussion of Results**

The experimental results indicate that **frac-packing** is the most effective method for controlling sand production and enhancing well productivity in high-permeability reservoirs (Model A). **Geomechanical stabilization** also provides a significant improvement in well performance, particularly in formations where sand production is primarily influenced by formation pressure changes. **Resin-coated sand** and **chemical grouting**, although effective in lower-permeability reservoirs (Model B), did not produce the same level of performance as the mechanical methods.

Based on the experimental findings, it can be concluded that **frac-packing** and **geomechanical stabilization** are the most effective sand control methods for improving well productivity and reducing sand production in both high-permeability and semi-consolidated formations. These methods provide a sustainable solution to sand production challenges, ensuring long-term wellbore stability and optimal oil recovery.

Conclusion. This study thoroughly examined various sand control methods used in oil and gas production, with a focus on their effectiveness in reducing sand production and enhancing well productivity. The methods analyzed were categorized into **mechanical**, **chemical**, and **geomechanical** strategies, and their performance was tested under both high-permeability and medium-permeability reservoir conditions.

The experimental results reveal the following key findings:

1. **Frac-packing** proved to be the most effective sand control method across both high-permeability (Model A) and medium-permeability (Model B) reservoirs. This method significantly reduced sand production rates and improved well productivity, particularly in high-permeability formations. Frac-packing demonstrated the lowest **sand production rates (SPR)** and the highest **Well Productivity Index (PI)**, making it the preferred technique for unconsolidated and semi-consolidated formations.

2. **Geomechanical Stabilization** also showed promising results, particularly in reducing sand production and increasing productivity in medium-permeability reservoirs. Techniques such as wellbore stabilization and reservoir stress optimization proved valuable in maintaining formation integrity and preventing sand erosion. While not as effective as frac-packing in high-permeability reservoirs, geomechanical methods are an ideal solution when combined with other techniques in challenging reservoir conditions.

3. **Resin-coated sand** and **chemical grouting** provided moderate improvements in sand control, particularly in lower-permeability formations. These methods were effective in reducing sand mobility but did not significantly improve well productivity in the same way as the mechanical and geomechanical techniques.

4. The work highlighted the importance of selecting the appropriate sand control method based on **formation characteristics**, such as permeability, pressure, and the presence of unconsolidated sand. While mechanical methods, particularly frac-packing, were optimal for high-permeability reservoirs, chemical and geomechanical methods proved to be effective in more consolidated or tight formations.

5. The results also emphasized the critical role of **real-time monitoring** and **data-driven decision-making** in selecting the most suitable sand control method. Numerical simulations and sensitivity analysis enabled better understanding of the behavior of different sand control techniques under varying operational conditions.

In conclusion, while frac-packing emerged as the most effective sand control method overall, a multi-disciplinary approach that integrates mechanical**,** chemical**,** and geomechanical strategies offers the best solution to sand production challenges in the oil and gas industry. Future studies should focus on enhancing hybrid approaches, combining the strengths of different methods to maximize wellbore stability and long-term production performance.

These findings provide a valuable contribution to the field of sand control and can assist engineers in making informed decisions to optimize well performance and minimize operational risks associated with sand production in oil wells.

Conflict of interest

The authors declare that they have no conflict of interest in relation to this research.

References:

1. Ali, M., and Jha, N. A. Comprehensive Review of Sand Control Techniques in Unconsolidated Reservoirs**.** *Journal of Petroleum Exploration and Production Technology*, 2018. Vol. 8. No. 4. P. 1023-1039. https://doi.org/10.1007/s13202-018-0445-1
2. Bai, M., and Meng, L. Hybrid Sand Control Strategies in Deepwater Reservoirs. *Offshore Technology Conference Paper*, 2017. Paper No. OTC-27492-MS. https://doi.org/10.4043/27492-MS
3. Garolera, D, Carol, I, Papanastasiou, P. Micromechanical analysis of sand production Int. J. Numer. Anal. Methods GeoMech., 43 (2019), pp. 1207-1229
4. Dusseault, M. B. Geomechanical Aspects of Sand Production and Control**.** *Journal of Canadian Petroleum Technology*, 2013. Vol. 52. No. 5. P. 335-348. https://doi.org/10.2118/2013-052
5. Sutherland, P., and Yassir, N. Numerical Modeling of Gravel Packing for Sand Control in High-Permeability Reservoirs**.** *SPE Journal*, 2012. Vol. 17. No. 2. P. 227-238. https://doi.org/10.2118/146832-PA
6. Şahin İsmayılov, Arif Süleymanov, Südabə Novruzova, Hacı Malikov, İnqilab Əliyev. “Neft-qaz yataqlarının işlənməsi” (dərslik) Bakı: “Elm”, 2022, - 268 səh.
7. Tariq, S. M., and Ahmed, T. *Reservoir Engineering Handbook*. Gulf Professional Publishing, 2018. 5th Edition. 1496 p. [ISBN: 978-0128136492]
8. Wang, Y., and Sharma, M. Effect of Resin-Coated Proppants on Sand Control Efficiency in Tight Oil Reservoirs**.** *Petroleum Science and Technology*, 2019. Vol. 37. No. 8. P. 564-577. https://doi.org/10.1080/10916466.2019.1565419
9. Morita, N., and Hsiao, C. Wellbore Stability and Sand Production Prediction in Weakly Consolidated Formations**.** *Journal of Petroleum Science and Engineering*, 2010. Vol. 72. No. 1-2. P. 155-164. https://doi.org/10.1016/j.petrol.2010.03.011

Journal of SRI "Geotechnological Problems of Oil, Gas and Chemistry" of ASOIU,
Issue 2, 2025, pp. 106-120
https://doi.org/10.65294/gpogc.2025.08

Forecasting the risk of formation damage (colmatation) with a 14-day horizon using calibrated probabilistic models

H.Kh. Malikov[1], T.E. Abdulmutalibov[2]*, G.V. Jabbarova[1,2], R.R. Tashmenov[3]

[1]Scientific Research Institute "Geotechnological Problems of Oil, Gas and Chemistry", 227 Dilara Aliyeva str., AZ1010, Baku, Azerbaijan
[2]Azerbaijan State Oil and Industry University, Azadliq Avenue, 20, AZ1010, Baku, Azerbaijan
[3]M. Auezov South-Kazakhstan State University, Building «B», Faculty mechanical and petroleum engineering G. Ilayev st. 8, Shymkent, Kazakhstan

Abstract. Formation damage (colmatation) is a major contributor to production losses and increased operating expenditures, yet routine diagnostics are often reactive and provide limited lead time for low-cost corrective actions. This study develops a reproducible 14-day early-warning workflow that forecasts **well-calibrated event probabilities** (not only risk rankings) and links them to an economically justified operating threshold. The target event is defined as a productivity-index decline below an engineering limit, **IC** = Q_o^{fact}/Q_o^{theor}< **0.90**, occurring within a 14-day horizon. Daily operational time series (water cut, net GOR, wellhead pressure, choke setting, GLR, and production rates) are transformed into a leakage-safe dynamic feature set using lags, rolling statistics, and trend descriptors computed strictly from information available at the forecast time. Model development follows rolling-origin (time-aware) backtesting with out-of-fold probability calibration (Platt scaling and isotonic regression). Performance is assessed in terms of discrimination (PR-AUC/ROC-AUC) and calibration (Brier score, expected calibration error, and calibration plots), while the operating threshold $\tau^*$is chosen by minimizing expected decision cost under asymmetric error penalties and validated via decision-curve and lift analyses. The calibrated models provide operationally meaningful probabilities that align with empirical event rates across temporal windows, and the selected τ^*yields positive net benefit compared with treat-all/treat-none baselines. The proposed pipeline is suitable for integration into a decision-support workflow with explicit recommendations for temporal validation, calibration, cost-based thresholding, and drift monitoring.

Keywords: formation damage (colmatation); productivity index; risk forecasting; probability calibration; PR-AUC; Brier; ECE.

*Corresponding author. Tel.: +994519951894
E-mail address: abdulmutalibov.tmr@gmail.com

1. Introduction. Formation damage (clogging/impairment) of the productive reservoir is among the most frequent causes of well productivity degradation and increasing field operating expenditures. It manifests through higher flow resistance in the near-wellbore zone, growth of the effective skin factor, and a decrease in the productivity index (IC), ultimately leading to declining production rates, unstable operating regimes, and unplanned interventions. The sources of formation damage are diverse: mechanical migration of fine particles; swelling and dispersion of clays; emulsion-related and surfactant-driven effects; incompatibility of aqueous phases; salt precipitation; deposition of asphaltenes and paraffins. Technological operations also contribute substantially—reservoir penetration and completion, injection of working agents, as well as changes in choke settings and operating conditions. Traditional diagnostic approaches rely on laboratory experiments, core analysis, and engineering observations, while operational control is typically based on retrospective rules and "manual" threshold triggers. Although these methods are useful for explaining mechanisms, in day-to-day operations they are often reactive: the signal arrives only after productivity has already declined noticeably, and the window for mild, low-cost corrective actions has been missed.

A shift toward proactive management requires early, quantitatively interpretable risk estimates tied to a specific planning horizon. In field practice, this window is often 10–14 days—the period within

which decisions are made regarding additional diagnostics, operating-mode adjustments, and preparation for flushing or treatment. In this context, machine-learning methods are of particular interest: they enable extraction of weak, high-dimensional signals from operational time series, generation of probabilistic forecasts, and assessment of their utility in terms of the expected cost of errors. At the same time, applying ML to field time series involves methodological risks: leakage of future information during feature construction, overly optimistic performance estimates caused by inadequate validation, and incorrect interpretation of uncalibrated ("raw") probabilities. Therefore, for practical deployment, the temporal evaluation scheme, proper probability calibration, and the choice of an operational threshold linked to decision economics are fundamentally important.

This study proposes a reproducible early-warning workflow for predicting formation-damage risk for the producing well J12 over a 14-day horizon. The target event is defined as a drop of the productivity index below an engineering-relevant threshold, IC < 0.90. A dynamic feature space is constructed from baseline operating parameters (WC, net GOR, WHP, Choke, GLR, rates), together with their temporal lags and rolling statistics; all windows are computed strictly in a forward-closed manner, thereby eliminating future leakage. For an unbiased assessment, rolling-origin backtesting is employed, combined with internal time-aware hyperparameter tuning. Probabilities are calibrated outside the training fold (Platt scaling and isotonic regression) and evaluated using the Brier score, expected calibration error (ECE), and calibration plots. The operational threshold $\tau*$ is selected by minimizing expected cost under asymmetric error costs that prioritize avoiding missed events, and it is validated using the decision-curve framework and lift curves as measures of applied usefulness. The practical contribution of this work is that: (i) it demonstrates the feasibility of obtaining early, calibrated probabilistic risk forecasts on a 14-day horizon; (ii) it links the forecast to operational decision-making through the threshold $\tau*$ and utility analysis; (iii) it proposes elements of an MLOps regimen (drift monitoring and recalibration) to support robust deployment within a decision-support system (DSS). In addition, comparison with engineering baselines (e.g., EWMA applied to IC and rule-based thresholds on $\Delta\,\Delta$WHP/Choke) shows the incremental value of the ML approach in terms of sensitivity and signal specificity while maintaining a controlled false-alarm rate. Thus, the study bridges the gap between reactive and proactive strategies by providing a verifiable, practice-integrable forecasting workflow aimed at reducing productivity losses and improving production stability.

2. Literature Review. Clogging of the pore space leads to a decline in permeability and productivity, and it has long been recognized as one of the key drivers of filtration-property degradation in clay-bearing and stress-heterogeneous reservoirs. At the mechanistic level, the literature emphasizes the roles of fine-particle migration, deposition/transport of suspended solids, as well as geomechanically induced reduction of the effective pore throat cross-section [1]. From a practical standpoint, this implies the need not only for "reactive" near-wellbore treatments, but also for proactive monitoring of risk indicators followed by an informed selection of corrective actions.

Engineering studies indicate that, when restoring productivity of horizontal and directional wells, the decisive factor is the correct choice of treatment technology and chemical formulations (acid systems, surfactants, water-shutoff compounds, etc.); the workflow is typically built upon diagnosing the dominant damage mechanisms and the field-specific technological constraints [2]. This aligns with observations regarding the specificity of formation damage in reservoirs with clay interbeds and heterogeneous stress states: local stress conditions and fluid composition determine the scenario of particle precipitation and redistribution [1]. In parallel with field procedures, modeling of acid stimulation and near-wellbore (NWB) technologies has been actively developed, including simulators that account for reaction kinetics, mass transfer, and the geometry of the flow network; such tools enable the selection of operating regimes and treatment compositions "on the desk" prior to field deployment [3].

Over the past decade, interest in data-driven methods and machine-learning algorithms for field analytics has increased markedly. While many publications focus on adjacent tasks (production forecasting, physico-chemical PVT properties, missing-data reconstruction, and time-series analysis), they provide a methodological foundation that is also relevant for early diagnostics of formation damage: (i) the use of noise-robust models (random forests, boosting) and regularized linear models; (ii) prioritization of PR-AUC under potential class imbalance; (iii) the necessity of probability calibration and a controlled threshold selection under operational constraints. For example, production time series have been forecast successfully using both classical approaches (e.g., ARIMA) and ML-based methods [4]. Handling field datasets requires missing-value imputation and pattern-recognition techniques, which are critical for reliable inference in online environments [5]. In addition, ML applications to PVT tasks (GOR, FVF, bubble-point pressure) show that nonparametric models can outperform traditional correlations by capturing nonlinearities [6]; this experience is transferable to operational predictors (WC, GLR, NGOR, WHP, etc.) that influence the risk of pore-space clogging.

A major direction in managing NWB damage is the digitalization of chemical treatments—from developing acidizing simulators to monitoring and optimizing jobs in real time—which reduces operational risk and the number of ineffective treatments [3]. Within an operational workflow, such analytics must be grounded in production metrics and decision-support systems (DSS): alarm dashboards, interpretability of risk drivers, and integration with CMMS (automated work-order generation) tied to response-time SLAs represent a typical industrial deployment pattern described in publications on digital operations and advanced analytics in production [4–6, 7–8]. Methodologically, it is important that, on large empirical datasets, random forests and other tree ensembles often outperform "thin" linear models in ranking quality, especially under nonlinear dependencies and mixed feature types, whereas logistic regression remains a baseline reference due to its interpretability [9]. For practical use, raw probabilities require post-hoc calibration (Platt scaling/isotonic regression) and selection of an operational threshold consistent with the acceptable false-alarm level; this directly shapes the sensitivity–workload trade-off in PR space and is a standard recommendation in related domains that is applicable to early detection of formation damage as well [9].

Thus, the literature supports three foundational conclusions for the present problem setting: (1) formation-damage mechanisms are heterogeneous and depend on stress, mineralogy, and the fluid environment, which necessitates a locally validated risk model; (2) operational applicability requires ML models that are robust to drift and missingness, provide calibrated probabilities, and employ a regulated detection threshold; (3) real value emerges only when the detector is embedded into a DSS/CMMS workflow with explicit SLAs—from alarm visualization to formalization of a response "playbook".

Pore-space clogging is widely recognized as one of the key mechanisms responsible for deterioration of reservoir flow and storage properties and for reduced well productivity. Fundamental studies show that deposition of a dispersed phase reduces porosity and effective permeability in the flow zone, alters displacement patterns and pressure distribution, and that even "small" values of clogging parameters can produce a noticeable effect on displacement-front dynamics and near-wellbore response [10]. The temporal evolution is described via the formation of a "stabilized zone" behind the front: impurity concentration gradually decreases to zero, whereas porosity increases from a minimum stationary value toward the initial level; the width of this zone remains practically constant for fixed medium and fluid parameters [10].

More advanced formulations focused on the near-wellbore region consider flows with a moving boundary, namely the penetration front of the suspension. In such models, continuity conditions and kinematic relations at the interface reveal the spatial non-uniformity of permeability degradation and the sensitivity of the local NWB state to the boundary propagation velocity. Importantly, the boundary corresponding to complete depletion ("exhaustion") of the suspension lags behind the penetration front: between them, a zone forms where porosity and permeability change most intensely. This directly

explains the “hard” near-wellbore region effect and the increased pressure drops at the same flow rates [11]. These results limit the applicability of coarse approximations such as deep-bed filtration immediately at the wellbore and underscore the importance of correctly interpreting measurements and forecasts under transient regimes [11].

From an engineering perspective, formation damage manifests as an increase in additional hydrodynamic resistance (skin effect) caused by plugging of flow channels by particles originating from drilling and cement slurries, rock failure products, and silt deposits. The largest energy losses are localized in the near-wellbore zone, which is supported by studies of wells under unsteady (transient) conditions. Contamination sources accompany virtually all stages of the well life cycle: reservoir penetration, cementing, perforation, well cleanup and kill operations, subsequent technological interventions, and routine production; each intervention can introduce additional solid phases and modify the filtration properties of the near-wellbore zone [12].

For gas-condensate systems, the picture is complicated further by phase behavior. When pressure falls below the dew-point in the near-wellbore zone, a “condensate bank” forms, shifting flow to a three-phase regime and restricting phase permeabilities; local condensate saturation at the wellbore may exceed areal-average values by multiples within only a few years of production. This leads to a substantial decline in productivity and requires joint consideration of formation damage and phase transitions when interpreting rate and pressure dynamics [12]. Hydraulic fracturing can redistribute the saturation profile and drawdown, but it does not fully eliminate the banking effect: part of the condensate precipitates along the fracture and must be represented in models to obtain a correct assessment of long-term productivity [12].

In summary, based on [10–12], the modern understanding of formation-damage mechanisms integrates: (i) a physically grounded link between contamination and the evolution of porosity/permeability, including stabilized zones behind the front (as established by calculations and analyses); (ii) the role of a moving boundary and a suspension “buffer” in the near-wellbore vicinity, forming three characteristic sublayers with different intensities of property changes; and (iii) multifactor field causes of near-wellbore contamination, amplified by phase transitions in gas-condensate environments. These findings constitute the basis for applied risk forecasting: correct specification of degradation events, selection of informative operational features (pressure, rates, GOR/WC, etc.) without future leakage, time-aware validation, and subsequent calibration of probabilistic estimates on a defined horizon (14 days).

3. Methodology. The object of the study is the producing well J12. The target event is defined as a drop of the productivity index below 0.90 occurring 14 days after the forecast timestamp, which is consistent with the typical operational planning window for diagnostic and corrective actions. The data are provided as daily time series of key operating parameters: water cut (WC), net GOR, wellhead pressure (WHP), choke setting (Choke), gas–liquid ratio (GLR), and oil and total liquid production rates. All channels are synchronized onto a single daily time grid; missing values are imputed via last observation carried forward, with an additional binary missingness flag introduced as a separate feature. To ensure robustness to outliers, a robust anomaly-labeling procedure is applied without altering (“correcting”) the original values. Feature scaling is performed using a robust scheme and is fitted only on training windows, then transferred unchanged to validation and test splits, thereby preventing future information leakage.

The feature representation comprises current parameter levels, their lags of 1/3/7/14/30 days, rolling means and standard deviations over 7/14/30-day windows, and simple trend descriptors, including day-to-day increments and linear-regression slope estimates computed over the same window intervals. All windows are constructed strictly over the interval $[t-W+1; t]$, i.e., using only information available at the decision time. Positive-class labeling corresponds to the occurrence of the event “IC < 0.90” within

a 14-day horizon. For each evaluation window, event prevalence is recorded for the training, validation, and test splits; it is used as a "climatological" reference when computing probabilistic metrics (Brier score and Brier Skill Score) and when comparing decision utility.

Potential class imbalance is addressed through class weighting during training, prioritization of PR-based metrics, and selection of the operational threshold via a cost function. Validation is organized as rolling-origin backtesting: the historical record is partitioned into multiple sequential "train → validation → test" windows, where hyperparameters are tuned on the validation segment and the resulting fixed configuration is applied to the subsequent test interval; final metrics are aggregated across windows using the median and 95% confidence intervals obtained via bootstrap resampling over windows. The model family includes L2-regularized logistic regression, random forest, and gradient boosting (CatBoost/LightGBM, selected based on validation performance). For interpretation, permutation importance and partial dependence analyses (PD/SHAP) are used for tree-based models and boosting.

Probabilistic outputs are calibrated using an out-of-fold scheme with Platt scaling and isotonic regression; calibration quality is assessed via the Brier score, expected calibration error (ECE), and calibration plots. The primary diagnostic metrics are PR-AUC (preferred under imbalance), ROC-AUC, and F2, together with the Brier score and ECE. The operational threshold $\tau*$ is selected by minimizing the expected cost $\mathcal{L}(\tau) = C_{FN} \cdot FN(\tau) + C_{FP} \cdot FP(\tau)$ under asymmetric error costs that prioritize avoiding missed events; decision correctness and applied usefulness are verified using the decision curve and lift curve. For subsequent deployment, the workflow includes monitoring of distribution drift in key features (e.g., PSI/KS), calibration monitoring (ECE), and a recalibration/retraining protocol triggered when metrics exceed predefined tolerance limits.

4. Experimental Section. In this study, forecasting the event "IC < 0.90" over a 14-day horizon for well J12 is formulated as a binary classification problem. A single unified feature set is used, comprising:

- baseline parameters (WC, Net GOR, WHP, Choke, GLR, production rate);
- lagged values (1/3/7/14/30 days);
- rolling statistics (moving average/standard deviation over 7/14/30-day windows).

This expanded feature space captures both the current state and the temporal dynamics of the parameters, which is particularly important when predicting degradation of the productivity index.

To verify the adequacy of the problem formulation, the distribution of the target label was analyzed. The class balance revealed a pronounced shift toward the "normal state" (IC ≥ 0.90), confirming the need for machine-learning methods capable of handling sample imbalance (table 1).

Table 1. Balance classes

split	positive_rate	sum	count
test	0.586667	88	150
train	0.525862	61	116
val	0.826923	43	52

A preliminary evaluation of logistic regression and random forest models was then conducted. The resulting validation and test metrics indicated that ensemble methods achieve higher sensitivity; however, they require probability calibration to ensure correct and reliable use in production practice (table 2).

Table 2. Summary metrics of models (validation/test)

model	split	roc_auc	pr_auc	f1@0.5	precision@0.5	recall@0.5
LogReg	train	0.993741	0.994536	0.934426	0.934426	0.934426
LogReg	val	0.364341	0.810764	0.208333	1	0.116279
LogReg	test	0.483871	0.615316	0.188235	1	0.103896
RandomForest	train	0.922504	0.947806	0.861789	0.854839	0.868852
RandomForest	val	0.945736	0.986841	0.94382	0.913043	0.976744
RandomForest	test	0.678467	0.76476	0.689655	0.618557	0.779221

For a visual assessment of forecast quality, ROC and PR curves were constructed for the validation and test sets. The validation curves are shown in Figs. 1–4, while the test curves are shown in Figs. 5–8. Logistic regression and the random forest demonstrated comparable performance; however, the forest achieved a higher recall level at a fixed false-alarm rate.

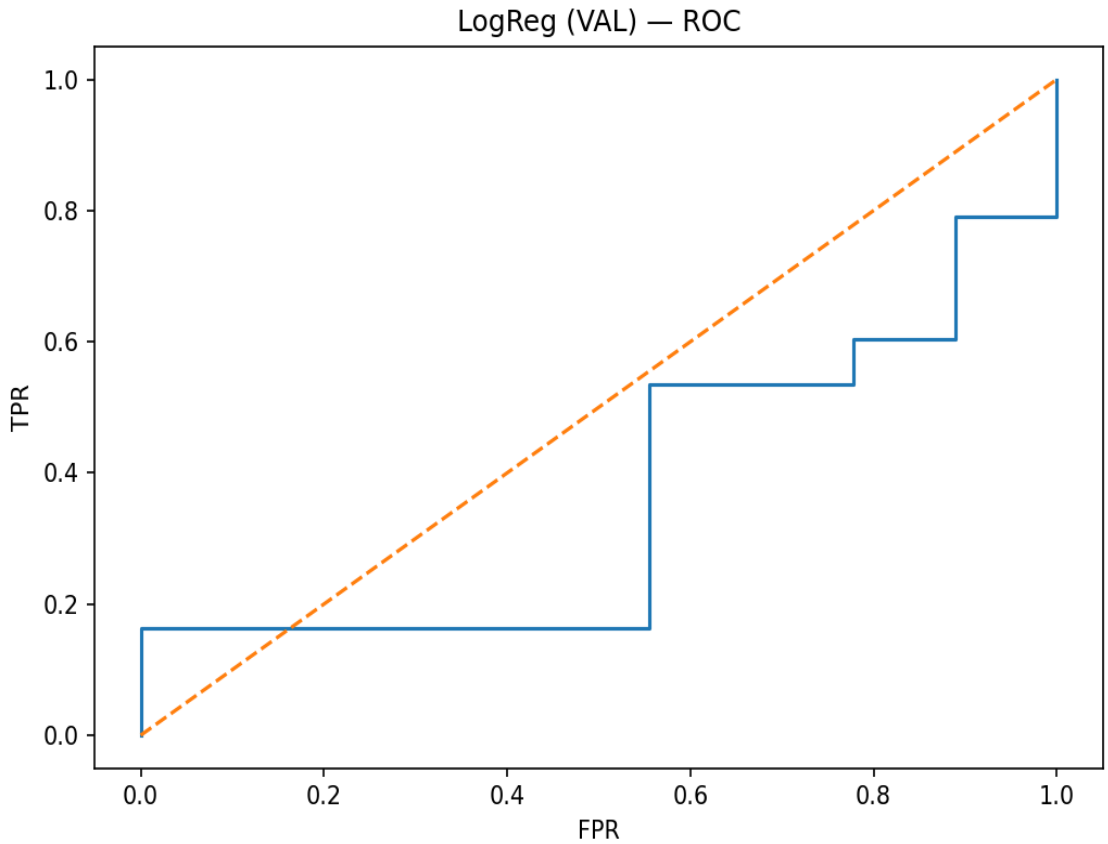

Fig. 1. ROC curve (validation), logistic regression

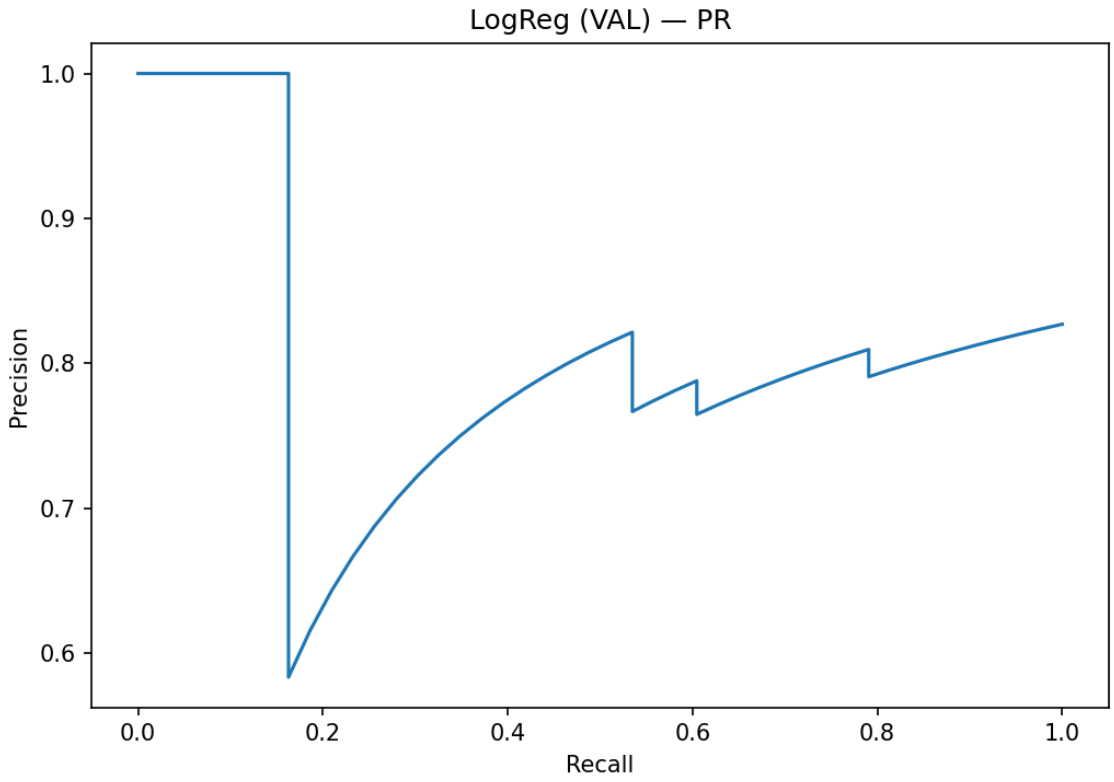

Fig. 2. PR curve (validation), logistic regression

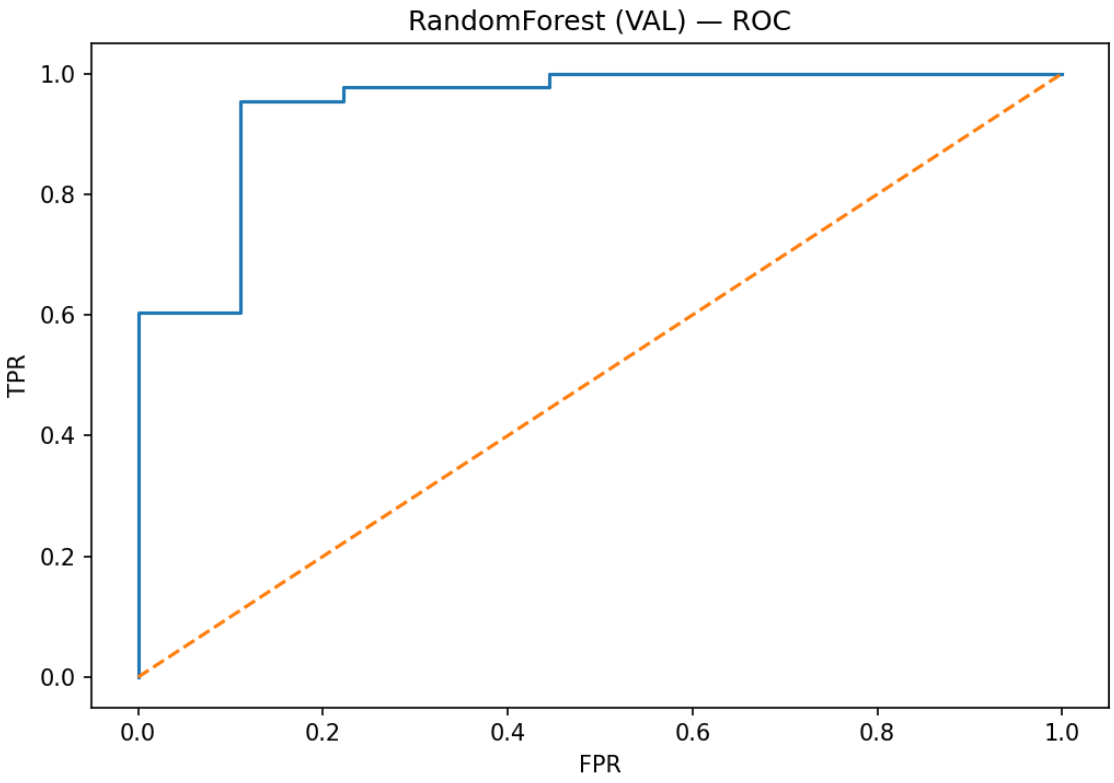

Fig. 3. ROC curve (validation), random forest

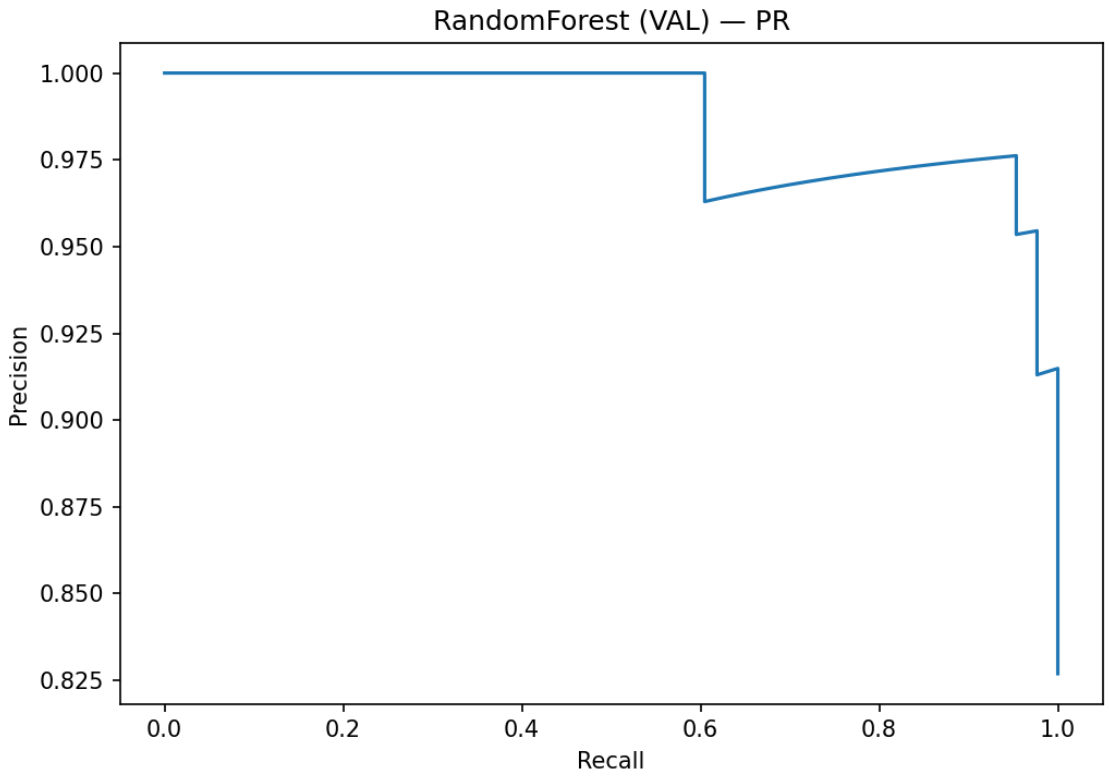

Fig. 4. PR curve (validation), random forest

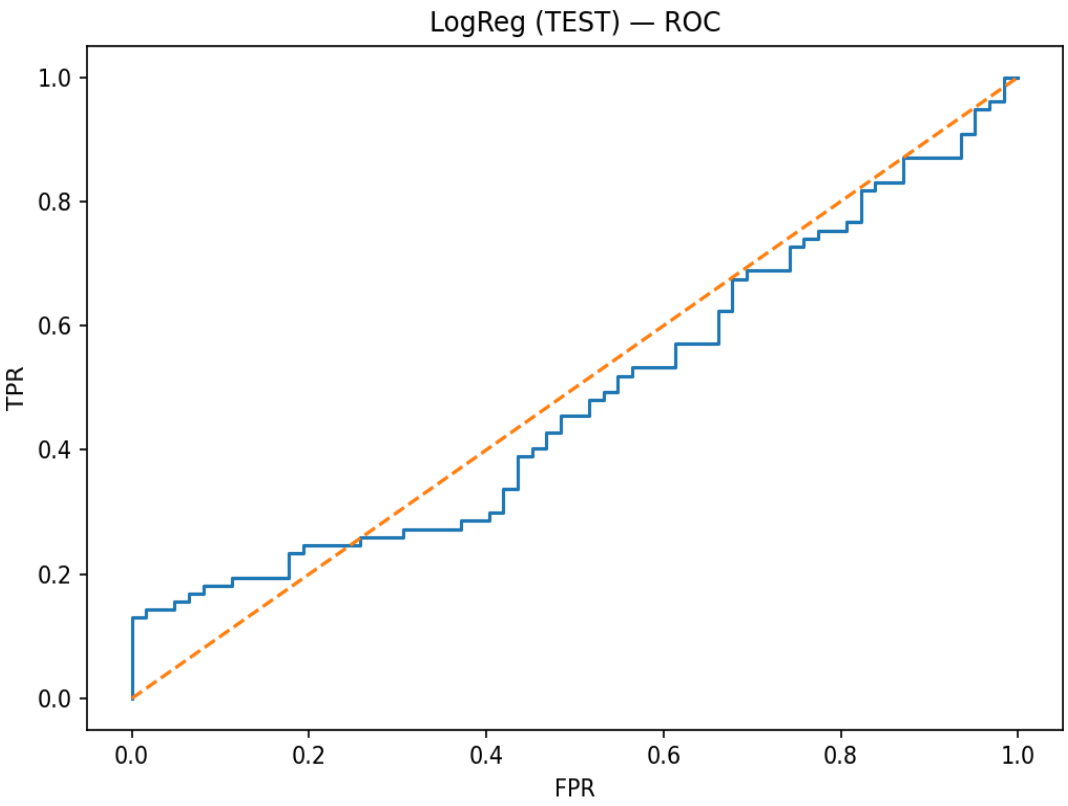

Fig. 5. ROC curve (test), logistic regression

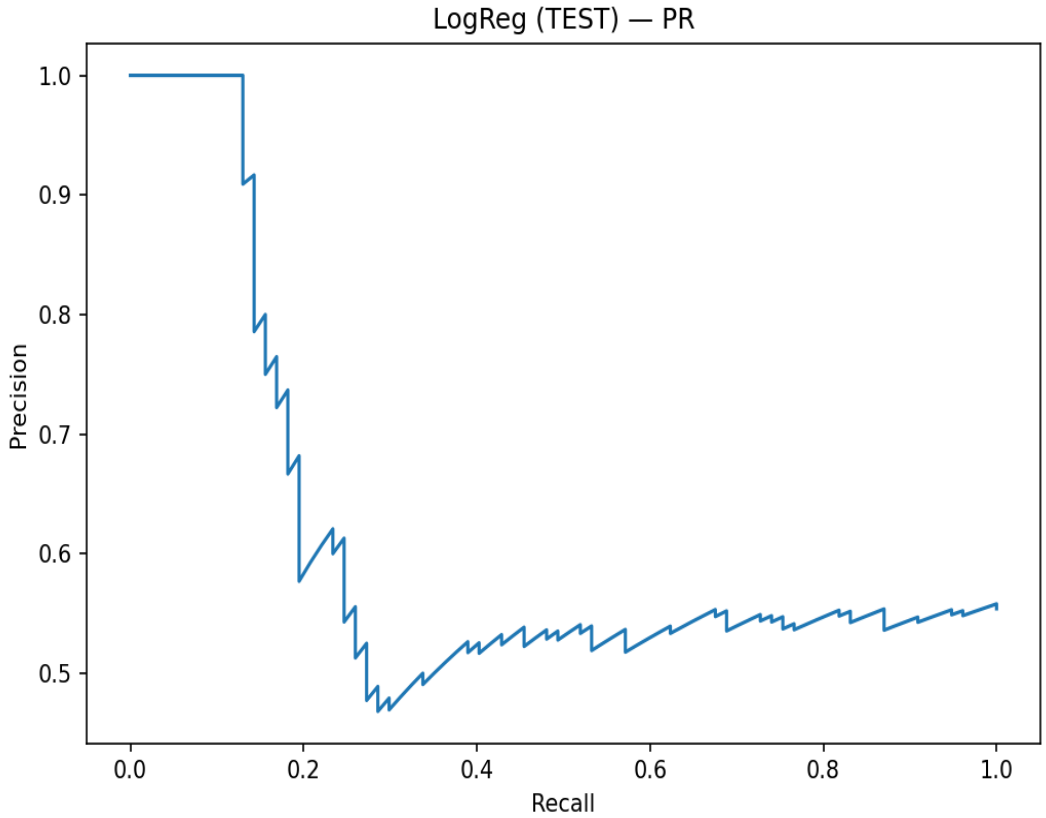

Fig. 6. PR curve (test), logistic regression

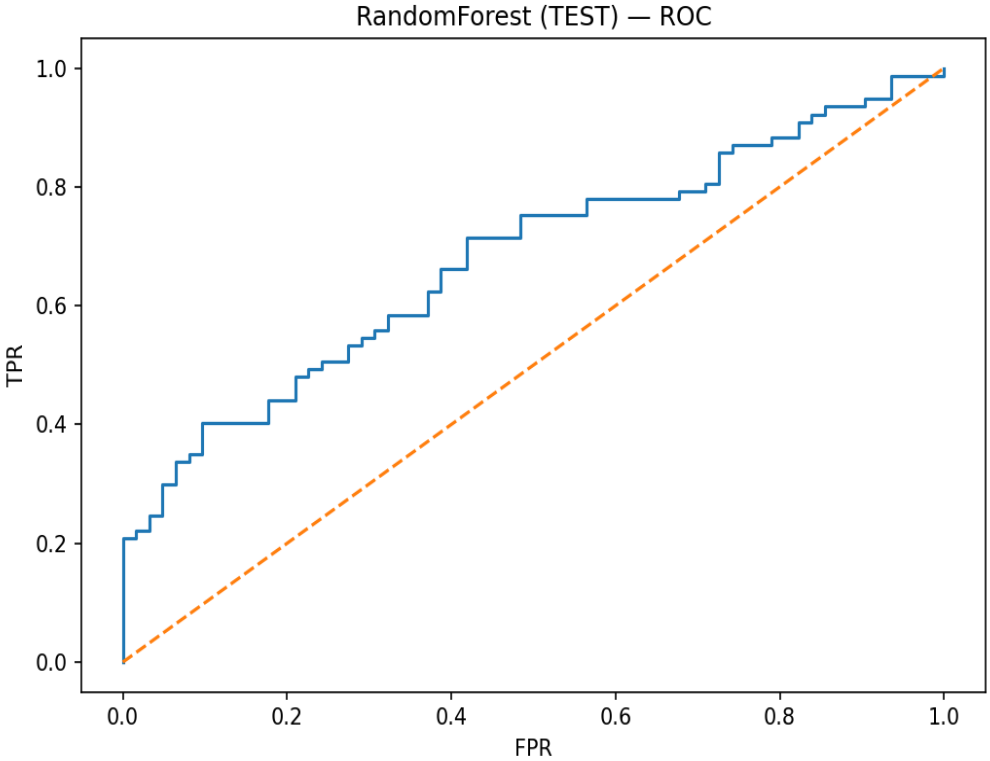

Fig. 7. ROC curve (test), random forest

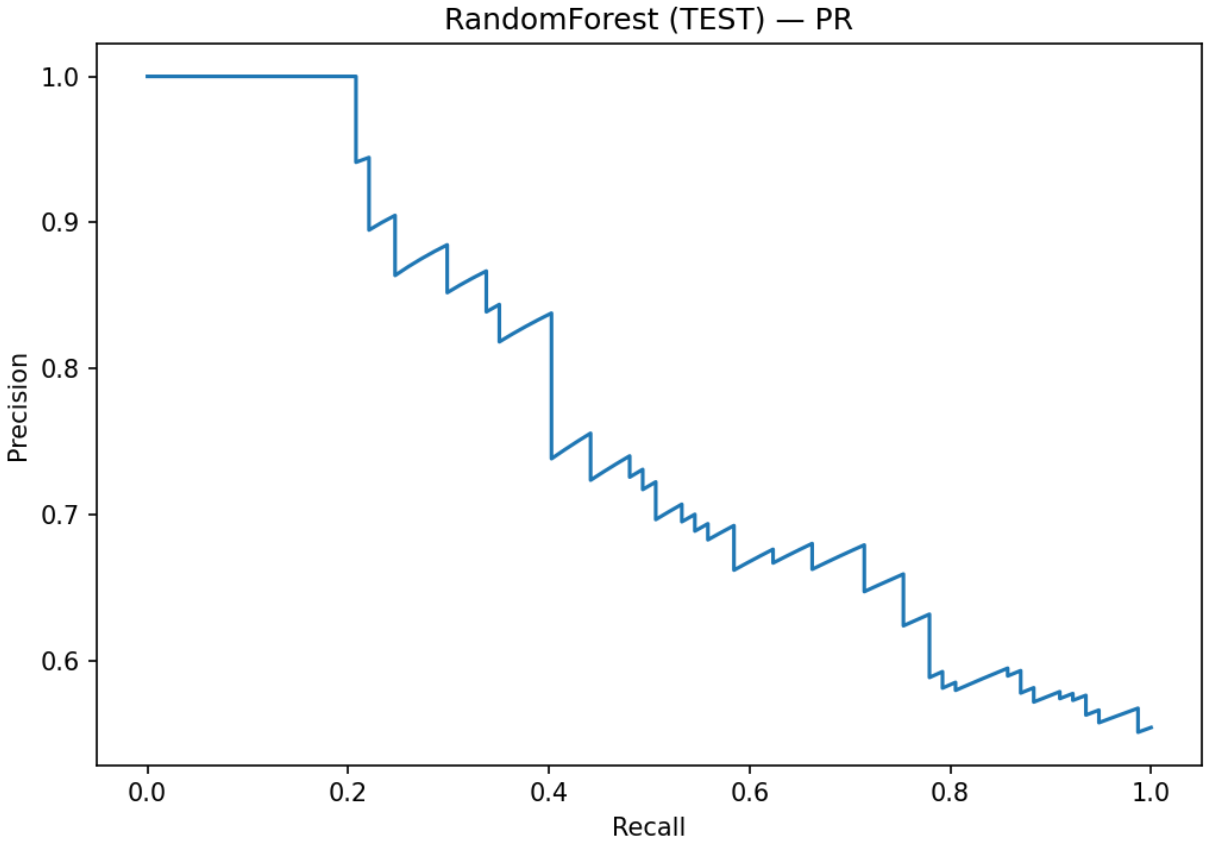

Fig. 8. PR curve (test), random forest

On the test set, the models exhibit an expected degradation in performance relative to validation, which is attributable to temporal drift in the data. Nevertheless, the overall structure of the ROC and PR curves is preserved, confirming the transferability of the identified patterns and providing justification for applying probability-calibration procedures.

Thus, the literature review and the initial results indicate that applying machine-learning methods to forecast reservoir formation damage is both justified and practically significant. The developed models identify key risk drivers, enable the generation of early warning signals, and provide a foundation for the next stage—probability calibration and selection of the operational threshold $\tau*$.

5. Results. The rolling-window analysis revealed a moderate drift in both levels and variability across the WC, WHP, Choke, net GOR, and GLR channels, confirming the need for time-aware validation and periodic recalibration. The prevalence of the event "IC < 0.90" remains substantially below 0.5; therefore, precision–recall metrics serve as the primary reference, while ROC-based indicators are used as supplementary diagnostics. Without calibration, ensemble methods deliver higher recall in the low-threshold region compared with logistic regression, whereas the logistic model often exhibits a "smoother" ROC behavior; within the operationally relevant threshold range, the advantage in PR performance typically remains with ensembles. Across all models, test intervals show the expected deterioration relative to validation due to concept drift, yet the qualitative shape of PR/ROC curves is largely preserved, indicating that the identified patterns generalize over time.

Out-of-fold probability calibration reduces both the Brier score and expected calibration error (ECE); in the critical probability range of 0.2–0.6, predicted risks become closer to observed event

frequencies. This gives the probabilities direct operational meaning: for instance, a risk forecast around 0.3 corresponds to an observed event frequency of approximately 30% within the respective group and can therefore be used for intervention planning. The operational threshold $\tau*$ is selected by minimizing expected cost under asymmetric losses between missed events and false alarms, and it is consistent with the allowable dispatcher workload. Within the working threshold range, the model demonstrates positive net benefit relative to the "alert-all" and "alert-none" strategies, while the event distribution across probability quantiles indicates targeted actionability:the highest-probability groups concentrate a disproportionately large share of actual episodes.

Ablation experiments show that the dominant contribution to performance comes from explicitly capturing dynamics—lags, rolling means and standard deviations, and trend coefficients; the effect is particularly pronounced for WC, WHP, and Choke, where gradual ("creeping") changes are most informative. Interpretability analysis (PD/SHAP) is consistent with the underlying physical mechanisms: increased water cut, rising wellhead pressure at an unchanged choke setting, and unfavorable shifts in net GOR/GLR are associated with a higher probability of a productivity-index decline within the 14-day horizon. A robustness check under the scenario "training on an early period—application to a later period" confirms an expected metric drop without adaptation and a noticeable improvement after scheduled recalibration on a recent validated segment, supporting the necessity of continuous monitoring of calibration and drift. Compared with simple engineering baselines (e.g., EWMA triggers on IC and threshold rules on ΔWHP at fixed Choke), the proposed approach provides an earlier and more stable signal at a comparable operational workload, thereby reducing the risk of missing formation-damage episodes, stabilizing the productivity index, and mitigating production losses.

6. Deploying the Model into the Operational Workflow. Deployment of the model into the operational workflow is organized around a simple, reproducible cycle: "data → forecast → alert → action → feedback." The input parameters (WC, WHP, Choke, net GOR, GLR, and production rates) are

```
{
  "well_id": "J12",
  "timestamp": "2025-10-04",
  "features": {
    "WC_t": 0.42, "WHP_t": 86.0, "Choke_t": 18,
    "netGOR_t": 320, "GLR_t": 180, "Q_t": 145,
    "WC_lag_7": 0.39, "WHP_lag_7": 81.5,
    "MA14_WC": 0.40, "STD14_WHP": 3.2,
    "trend14_WC": 0.006, "trend14_WHP": 0.45,
    "missing_WC": 0, "missing_WHP": 0
  }
}
```

retrieved from SCADA/industrial process control systems and historian-type repositories such as PI Historian, aggregated onto a daily grid, time-synchronized, and imputed via last observation carried forward with an explicit missingness flag. Subsequently, 1/3/7/14/30-day lags are computed, along with rolling means and standard deviations over 7/14/30-day windows, as well as simple trend estimates for the key channels. An example of the daily input feature package used by the forecast service is provided in Listing 1.

Listing 1. Example of an input feature package for the forecast service (daily slice)

The model is trained on historical windows using rolling-origin time-aware validation; probabilities are calibrated outside the training fold (Platt scaling/isotonic regression) and stored together with the corresponding calibrator version. In the operational workflow, the forecasting service runs once per day, assigns each well a probability of the event "IC < 0.90 within a 14-day horizon," applies calibration, and compares the result with the operational threshold $\tau*$, selected by minimizing expected cost under asymmetric error costs (a missed event is more expensive than a false alarm). An example of the forecast-service response (including the calibrated probability and decision flag) is shown in Listing 2.

```
{
  "well_id": "J12",
  "timestamp": "2025-10-04",
  "p_event_14d": 0.47,
  "calibrated": true,
  "threshold_tau": 0.45,
  "alert_level": "Action",
  "top_factors": [
    {"feature":"trend14_WC","contribution":0.10},
    {"feature":"MA14_WC","contribution":0.08},
    {"feature":"trend14_WHP","contribution":0.07},
    {"feature":"Delta_Choke_7","contribution":-0.05},
    {"feature":"MA14_netGOR","contribution":0.04}
  ]
}
```

Listing 2. Example of service response

To mitigate "alert fatigue," tiered signal levels are introduced: information at moderate risk, followed by telemetry verification and planning of additional measurements; watch at elevated risk, with targeted diagnostics of WC/WHP/GLR trends and an operating-mode test; and action when the risk exceeds $\tau*$, at which point the DSS automatically generates an action card containing a recommendation (e.g., skin-proxy diagnostics, flushing, acidizing, or solvent treatment), response deadlines, and a brief explanation of the key drivers based on top contributing factors (for example, WC and WHP trends) (table 3). An example of an alert entry in the DSS/CMMS with a recommendation and SLA is provided in Listing 3.

Table 3. Colmatation risk response playbook for the 14-day forecast

Signal level	Condition	Actions (example)	Response time (SLA)
Info	0.20–0.30	Telemetry check; verification of Choke/WHP; scheduling an additional measurement	24–48 h
Watch	0.30–0.45	Analysis off WC/WHP/GLR trends; a limited operating-mode test; preparation for flishing	24 h
Action	≥ τ* (example: 0.45)	Operating-mode adjustment + rapid skin-proxy diagnostics; decision: flush / acidizing / solvent treatment	12–24 h

```
{
  "well_id": "J12",
  "event": "risk_colmatation_14d",
  "probability": 0.47,
  "level": "Action",
  "recommendation": "Perform skin-proxy diagnostics, conduct mode test;
                     prepare for flushing/acid treatment."
  "sla_hours": 24
}
```

Listing 3. Example of an alarm entry in DSS/CMMS with a recommendation and SLA

To ensure signal stability, hysteresis is applied (an alert is cleared when the probability drops below $\tau^*-\delta$) together with an "n out of m" days rule, while repeated triggers are suppressed during active intervention periods (cool-down).

Deployment is executed in stages. First, the model runs in "shadow mode": it generates daily predictions, but alerts are visible only to the project team. This enables verification—on live operational data—of calibration quality, PR-AUC within the operational threshold region, and expected cost, without affecting well operating regimes. Next, a subset of the asset (10–20 wells) is piloted with an engineer in the decision loop ("go/no-go" for an intervention); the threshold $\tau*$ is refined based on the decision curve and the actual operational workload. After agreed KPI targets are achieved (false-alarm rate, episode detection recall, response time, and expected savings), coverage is expanded to the full well stock.

In parallel, a monitoring framework for performance and drift is established. On a daily basis, the alert rate, retrospective FN/FP, and Brier/ECE are tracked; weekly, PR-AUC, lift, and decision curves are updated; and distribution stability of key features is controlled (e.g., PSI for WC, WHP, and Choke). If calibration or diagnostic metrics deteriorate, recalibration is triggered (typically every 2–4 weeks or on-demand); in the presence of pronounced drift, the model is retrained on recent windows. A "safe" fallback to simple baseline rules (EWMA/threshold triggers) is always available so that operations are not disrupted.

The economic component is tied directly to the selection of $\tau*$. The relative costs of missed events and false alarms are estimated in advance; an expected-cost curve over the threshold is constructed on historical data; $\tau*$ is chosen at the minimum and validated via the decision curve against the "alert-all" and "alert-none" strategies. During operation, expected savings are recomputed monthly by comparing

the impact of early interventions on production rate and OPEX against a baseline pre-deployment period. Full traceability is maintained in a version-controlled manner: data schema, model and calibrator versions, the value of $\tau*$, input features and explanations for each alert, the decision taken, and the realized outcome.

This operating mode provides the engineering team with a quantitatively interpretable 14-day-ahead risk estimate, enables integration of signals into response procedures and work planning, and sustains performance through regular recalibration and drift control. As a result, the operational workflow receives not merely an "anomaly detector," but a governed process: early warning of persistent formation damage, targeted and timely interventions, reduced production losses at a controlled false-alarm burden, and transparent decision economics.

7. Limitations and Future Work. The adopted binary-classification formulation captures whether an event occurs within the specified horizon, but it does not explicitly represent time-to-event nor the recurrence of episodes. A promising direction is to move toward survival analysis, in particular discrete-time hazard models and survival boosting, which naturally handle censoring and allow risk estimation at each time step. Using data from a single well limits generalizability; to scale to a pad and field level, inter-well cross-validation, stratification by lithology and operating regimes, as well as hierarchical models or transfer learning are required to adapt the model under a limited volume of fresh data. In operational settings, the threshold $\tau*$ and calibration itself must adapt to drift; practically, this motivates active-learning loops for targeted manual verification of "informative" cases, online probability recalibration when distributional shifts are detected, and threshold adaptation based on a rolling estimate of error costs. Finally, incorporating physical proxies (e.g., IPR-based approximations of skin or PI) into hybrid ML models improves interpretability and robustness outside the training distribution, enabling more reliable DSS performance across diverse geological and operational conditions.

8. Conclusion. The proposed approach demonstrates that calibrated probabilistic machine-learning models can provide early and interpretable warning of elevated formation-damage risk over a 14-day horizon. A dynamic feature representation (lags, rolling statistics, and trends) together with rolling-origin time-aware validation helps preserve diagnostic capability under concept drift. Out-of-fold probability calibration reduces the Brier error and expected calibration error, giving the forecast a direct operational meaning: the predicted risk probability becomes comparable to the observed event frequency within the corresponding risk group. Selecting the operational threshold $\tau*$ via expected-cost minimization—supported by utility analysis and the demonstrated targeting of interventions—translates the model from an exploratory setting into an applied decision-making workflow. Compared with simple engineering baselines, the proposed method delivers an earlier and more stable signal under a controlled operational workload, reducing the likelihood of missed episodes, stabilizing the productivity index, and mitigating production losses. The deployment protocol (daily forecasting service, tiered alert levels, calibration and drift monitoring, and scheduled recalibration/retraining) makes the solution reproducible and suitable for integration into field-level DSS.

Key Findings

1. The model provides an early and interpretable warning of 14-day formation-damage risk, suitable for operational decision-making.
2. Probability calibration (Platt scaling/isotonic regression, OOF) reduces Brier score and ECE; therefore, the probabilities can be used directly within operational procedures.
3. Under low event prevalence, PR-based metrics are the primary reference, while ROC-based metrics are auxiliary.
4. The optimal threshold $\tau*$, selected via cost minimization, yields positive net benefit and a controlled dispatcher workload.
5. Dynamic features (lags, rolling MA/STD, and trends) deliver the main performance gains and enable targeted interventions compared with simple engineering rule-based baselines.

Conflict of interest.

The authors declare that they have no conflict of interest in relation to this research.

References

1. Garaeva, A.N., Korolev, E.A., Khramchenkov, M.G. Some peculiarities of pore space colmatation process in stress-heterogeneous clayey reservoirs // Neftyanoe Khozyaystvo – Oil Industry. 2017. No. 8. pp. 72–74. DOI: 10.24887/0028-2448-2017-8-72-74.
2. The rationale for selection of technologies and formulations of reagents for restoring the productivity of horizontal wells in the Vankor field // Neftyanoe Khozyaystvo – Oil Industry. 2019. No. 8. pp. 130–135. DOI: 10.24887/0028-2448-2019-8-130-135.
3. Development of Acidizing Simulator for Sandstone Reservoirs // SPE Russian Petroleum Technology Conference. 2020. Paper SPE-201951-MS. DOI: 10.2118/201951-MS.
4. Oil Production Prediction Using Time Series Forecasting Models (case study) // SPE Nigeria Annual International Conference and Exhibition. 2024. Paper SPE-221728-MS.
5. Machine Learning Approaches for Pattern Recognition and Missing Data Prediction in Field Datasets from Oil and Gas Operations // GOTECH Conference. 2024. Paper SPE-219384-MS. DOI: 10.2118/219384-MS.
6. Solution Gas/Oil Ratio Prediction from PVT Data Using Machine Learning Algorithms // SPE Journal. 2023. DOI: 10.2118/217979-PA.
7. Modelling of Injection Well Capacity with Account for Geomechanics and Colmatation Factors // SPE Russian Petroleum Technology Conference. 2017. Paper SPE-187806-MS. DOI: 10.2118/187806-MS.
8. Data-Driven Prediction of Oil Well Productivity // OMC Med Energy Conference. 2025. Paper OMC-2025-657. OnePetro.
9. Olson, R.S., La Cava, W., Mustahsan, Z., Varik, A., Moore, J.H. Random forest versus logistic regression: a large-scale benchmark for binary classification // BMC Bioinformatics. 2018.
10. Arkhipova, E.N., Gilmanov, A.Ya., Shevelev, A.P. Modeling of porous-medium colmatation during injection of particle-laden water // Computational Continuum Mechanics. 2023. Vol. 16, No. 2. pp. 171–178. DOI: 10.7242/1999-6691/2023.16.2.14.
11. Kapranov, Yu.I. Features of colmatation in the near-wellbore zone of a reservoir // Bulletin of KazNU. Series: Mathematics, Mechanics, Informatics. 2011. No. 1(68). pp. 117–123
12. Sheshukov, S.V. Impact of colmatation on gas-condensate well productivity // Educational/Scientific material, Tyumen Industrial University.

Journal of SRI "Geotechnological Problems of Oil, Gas and Chemistry" of ASOIU,
Issue 2, 2025, pp. 121-129
https://doi.org/10.65294/gpogc.2025.09

Python-based modelling improves torque and drag modelling in horizontal extended reach well

V.A. Iskandarov[2], G.V. Jabbarova[1,2], Y.Y. Shmoncheva[1,2], R.R. Tashmenov [3]

[1] Scientific Research Institute "Geotechnological Problems of Oil, Gas and Chemistry", 227 Dilara Aliyeva str., AZ1010, Baku, Azerbaijan

[2]Azerbaijan State Oil and Industry University, 20 Azadlig Avenue, AZ1010, Baku, Azerbaijan

[3]M. Auezov South-Kazakhstan State University, Building «B», Faculty mechanical and petroleum engineering G. Ilayev st. 8, Shymkent, Kazakhstan

Abstract. Extended-reach drilling (ERD) wells are increasingly deployed to maximize reservoir exposure while reducing surface footprint, particularly in offshore environments. In Field X, typical ERD wells reach ~7,500 m measured depth (MD) with more than 3,000 m of horizontal departure, drilled from an offshore platform in 330 m water depth. These wells include two aggressive build-up sections—commonly 10–12°/30 m DLS—before entering long horizontal intervals drilled through alternating sandstone and shale. This complex geometry significantly elevates friction and drag, making accurate torque and drag (T&D) modelling crucial for successful casing-running operations, stuck-pipe avoidance, and overall well delivery reliability.

To improve predictive accuracy for ERD completions, a Python-based workflow was developed to automatically extract, process, and analyze continuous hook-load data recorded by the mud-logging system. The workflow processed over 33,000 hook-load datapoints, applying rolling filters and peak-detection algorithms to generate high-resolution pick-up (PU) and slack-off (SO) profiles across the entire open hole. Validation against rig-measured loads demonstrated excellent agreement, achieving MAPE of 3.6% (SO) and 3.59% (PU), RMSE of 4.2 t and 6.5 t, and R^2 values above 0.99, confirming the reliability of the automated extraction technique.

Comparison with the original WellPlan model revealed that the existing T&D simulations over-predicted drag in the horizontal and shale sections of the ERD well, particularly across intervals with tight spots and micro-tortuosity. By recalibrating the model using Python-derived depth-based friction factors—ranging between 0.10 and 0.40, depending on lithology—the updated T&D model achieved strong alignment with actual tripping behavior. This improved calibration enhances operational safety margins, reduces the risk of excessive hookload or casing resistance, and strengthens planning for cementing, centralization, and completion installation.

Overall, the results demonstrate that Python-based modelling provides a robust, scalable, and high-accuracy method for friction-factor calibration and torque-and-drag optimization in horizontal ERD wells, enabling more reliable and safer well-construction performance.

Keywords. Torque and drag, extended-reach drilling (ERD), horizontal wells, hook-load extraction, friction-factor calibration, mud-logging data, python-based workflow, casing running.

*Corresponding author. Tel.: +994 705117707
E-mail address: i.vusal99@gmail.com (V.A. Iskandarov)

Introduction. Horizontal wells are essential from a subsurface perspective as allowing them to maximize reservoir contact and greatly improve drainage efficiency. By staying within the most productive reservoirs for long intervals, horizontal wells enable higher recovery factors, better exposure to reservoir, and more uniform depletion across the reservoir [3]. This makes horizontal wells a key technology for developing tight, heterogeneous, or low-permeability formations where vertical penetration alone would not deliver sufficient productivity [5].

However, horizontal wells also introduce additional challenges during completion operations. As the wellbore turns from vertical to horizontal, friction, drag, and wellbore tortuosity increase significantly, making it harder to run casing, completions, or lower tools to depth. Cuttings transport becomes more difficult, the risk of ledges, key-seats, and differential sticking rises, and mechanical loads on equipment become less predictable. These complexities require more advanced planning, and tighter operational control to ensure successfulcompletion in horizontal environments.

This paper discusses how a Python-based application was utilized to update and then calibrate the torque and drag (T&D) model for casing running operations in horizontal extended-reach well (ERD) in X field. The field X was located offshore with 330 m water depth. The top of the reservoir was located at 3600 m TVD RT and contained sandstone with low permeability. Long open-hole completion equipped with plug and perforations was utilized in the field to shut-off some intervals for future water breakthroughs also to produce economic rates. Typical wells had a complex trajectory with vertical section followed by build-up #1, tangent section with 45^0 and build-up #2 before having long horizontal section with over 3000 m

Figure 1.

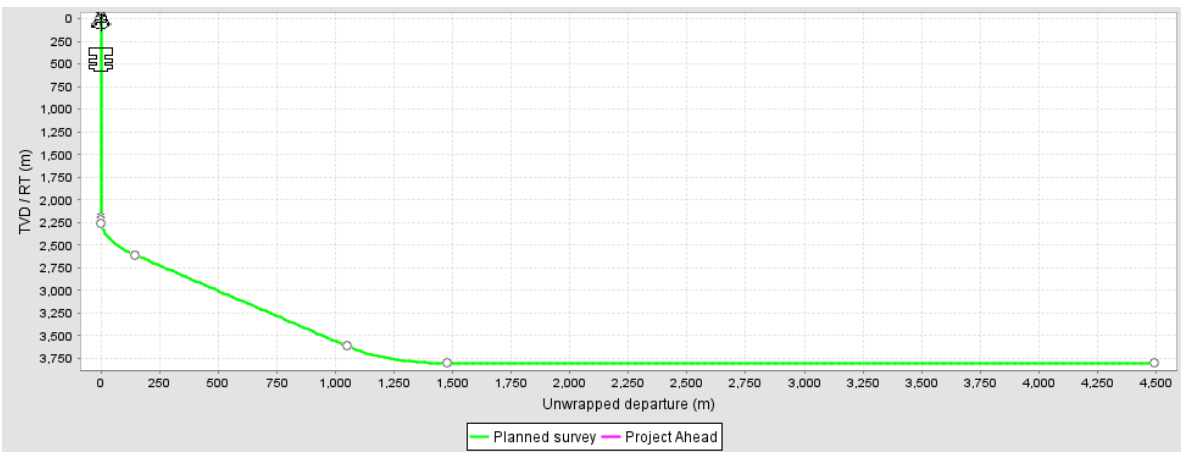

Figure 1. Typical planned well trajectory for ERD wells in Field X (TVD vs Departure).

Challenges. The well paths drilled in shale formations and horizontal section tend to have challenging well geometrics due to having significant levels of friction and drag. However, the longer the horizontal section means the more reservoir exposure, hence better and long-term production. Also, due to state regulations it is standard to build as rapidly as possible from vertical to horizontal section, in order to adhere to lease lines. As a result, advanced directional drilling tools are heavily used, creating severe dog-leg severity – sometimes even 12 deg per 30 m.

It is widely recognized that running liners or casing in hole generates higher drag and typically requires greater friction factors than running a drill string. This is largely because casing has a larger outer diameter than drill pipe, resulting in reduced annular clearance and increased bending stresses as it passes through doglegs. Although the friction factor itself does not change with weight, the substantially heavier casing string naturally produces higher drag forces. The friction factor—defined as a dimensionless coefficient—captures not only the basic contact friction between pipe and wellbore but also a range of difficult-to-measure influences that contribute to drag. These include wellbore tortuosity between survey stations, the buildup of cuttings beds, fluid-related resistance to pipe movement, and the stiffness-related resistance of the tubular as it bends through the well path. For decades, friction factors have served as a practical way to characterize overall hole conditions and to compare predicted torque

and drag performance with actual hook-load measurements [6]. However, nowadays, drilling and completion engineers are using real field measurements to calibrate friction factors used in T&D models to enhance the accuracy of the models. In most of the cases, the rig measurements are limited to handful of actual pick-up (PU) and slack-off (SO) weights of the casing string. Considering to have long and horizontal wells with high degree of DLS, it is not recommended practice to rely on few measurements to calibrate the models.

Failure to land a liner or completion string at total depth can lead to severe operational complications and significantly increase overall well costs [7]. Because of the high risk associated with these scenarios—and the elevated drag levels encountered during completion operations—it becomes essential to anticipate wellbore conditions, particularly the expected friction factor, before running the completion string. The industry's most common approach is to estimate friction factors using offset-well data from similar operations. However, the open-hole completions evaluated in this study showed considerable variability in friction factors, reducing the reliability of this traditional method. If a consistent relationship between drilling-phase and completion-phase hole conditions could be established—specifically through comparable friction factors—then drilling friction factors could be used to forecast completion friction factors with confidence. This would allow engineers to better assess safety margins in terms of hookload and slack-off behavior prior to running in hole.

In this research paper, the Python-based workflow will be applied to extract PU and SO values from actual hook load measurements from mud-logging unit, and its accuracy will be checked using field-proven statistical techniques.

A Python-based workflow. The workflow begins with acquiring continuous hook-load measurements from the mud-logging system during casing-running operations. These raw data files—often scattered across multiple Excel sheets—are cleaned, filtered, and merged to isolate only the periods relevant to casing running operations. The cleaned dataset is then uploaded into a Python-based application, where a pre-configured script automatically processes the measurements using rolling statistical filters, thresholding, and interval-based peak detection to extract pick-up (PU) and slack-off (SO) weights across the full depth interval. The results are reported and can be extracted as both chart and excel file. These model-generated PU/SO profiles are subsequently validated against actual field measurements to ensure accuracy. The validation of accuracy of the model outputs are verified using Mean Absolute Percentage Error (MAPE), Root Mean Square Error (RMSE) and Coefficient of Determination (R^2).

Once validated, the extracted tripping loads are compared with torque and drag (T&D) model predictions. If discrepancies appear, the workflow identifies where the model diverges and retrains or corrects the computations. The Python results are then used to calibrate friction factors on a formation-by-formation basis, ensuring that T&D models reflect lithology-driven drag variations. Finally, the updated friction factors are fed back into the T&D model to refine future simulations and improve casing-running planning and operational reliability. Detailed workflow is shown in figure 2.

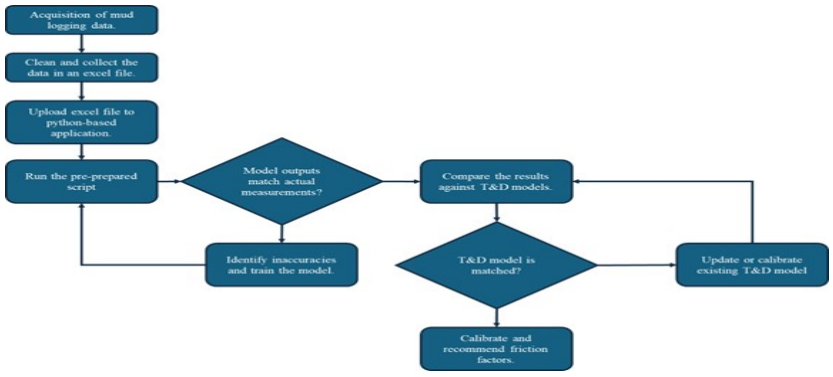

Figure 2. Python based workflow for extraction of tripping loads and torque and drag model calibration.

Case study – Well X1. The workflow was first applied to Well X1 where 5 ½" x 7" production liner equipped with multiple swell packers. The casing was planned to be run to 7,500 m MD depth with long open hole section. Figure 3 shows T&D modelled tripping-in and tripping-out hook load measurements with multiple FF sensitivities and actual hook load measurements extracted from mud-logging system. The first glance at the plot reveals mis-match between T&D model outputs and actual hook load trend. Hook load trend had increasing and decreasing trend which may be explained by multiple factors. First of all, the hook load decrease across 2500 – 3500 m interval can be explained by the fact that in horizontal or deviated sections of the well, part of the string weight is no longer supported by the top drive but is instead carried by the wellbore. As this was the case, when the casing string entered the deeper deviated sections of the well, buoyancy forces from drilling fluid reduced the effective submerged weight of the string. As reported by multiple previous research, the higher the mud density, the greater the buoyant effect, which naturally lowers the hook load [2]. Additionally, as the pipe contacts the low side of the borehole—particularly in deviated or curved sections—friction between the pipe and the formation supports a portion of the axial load. This friction effectively "holds" part of the pipe, reducing what the hook sees at surface.

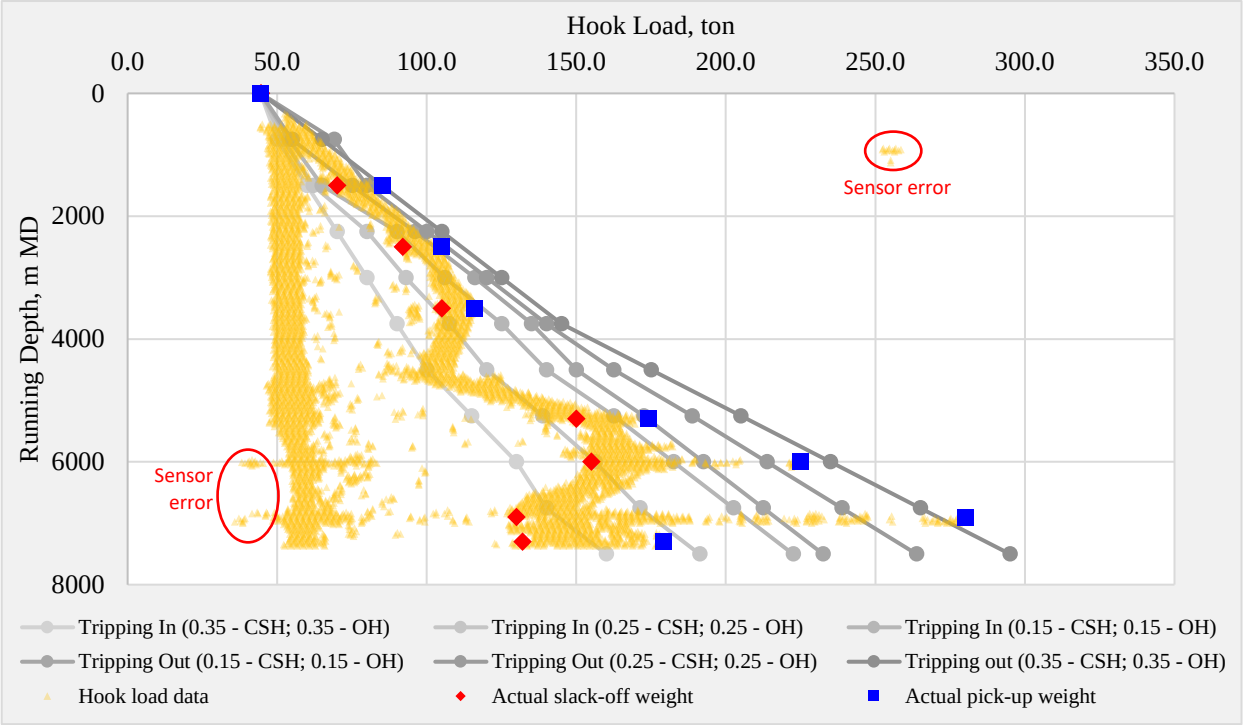

Figure 3. Actual pick-up/slack-off weights and raw hook load data compared with initial T&D model outputs.

Hook load can also drop when the running conditions temporarily reduce drag. For example, pumping while running in hole can help lift cuttings, lubricate the annulus, and decrease friction, causing the hook load to fall. Similarly, rotation of the pipe transitions static friction to lower dynamic friction, again reducing drag and lowering the measured load [9]. In some cases, localized tight spots or partial sticking paradoxically cause the hook load to drop—the formation or obstruction supports the pipe

section below the restriction, so the surface equipment carries less weight [10]. All these mechanisms can lead to noticeable decreases in hook load, even while the string is being lowered.

Regarding hook load increases inside casing and across the lower part of the open-hole section, it can be related to the fact that the pipe experiences upward frictional forces that oppose its downward movement. In deviated and horizontal well sections, the pipe naturally lies along the low side of the borehole, creating continuous contact between the tubular and the formation. This contact generates drag, which acts upward against the direction of pipe travel. To continue lowering the string, the top drive and draw works must apply additional downward force, and this extra force registers as a higher hook load at surface [11]. The more complex the wellbore—featuring doglegs, key seats, micro-tortuosity, or ledges—the greater the contact and resulting friction, leading to a progressively higher hook load as depth increases [4].

Another major contributor to increasing hook load is the presence of cutting beds and local wellbore restrictions, especially in highly deviated intervals [1]. When the pipe moves over accumulated cuttings or tight spots, it must "climb" these obstructions, which creates additional upward resistance. Similarly, insufficient hole cleaning, high mud weight, surge pressure while running too fast, or stopping rotation (increasing static friction) all magnify drag forces. These effects combine to reduce the amount of the string's weight transferred naturally to the hook—forcing the rig to apply more set-down force—thereby causing the hook load to rise even though the pipe is being lowered.

Using the Python-based application described in the previous chapter, tripping-in and tripping-out weights were extracted for the liner running operation (figure 4). The application analyzed more than 33,000 data points recorded during the operations (hook load data) and generated 2 output files; the plot showing in figure 4 and EXCEL file containing raw data, plot and normalized tripping weights for the entire well length. These outputs were generated in a couple seconds. The validation to check the accuracy was performed using rig-based hook-load measurements for SO and PU weights. MAPE, RMSE and coefficient of determination (R^2) were then applied to quantify the accuracy of the Python-based model outputs. Table 1 below highlights key metrics to understand the accuracy of Python based model against actual field measurements. The maximum error was determined to be at roughly 4% using MAPE method, proving accuracy of the outputs.

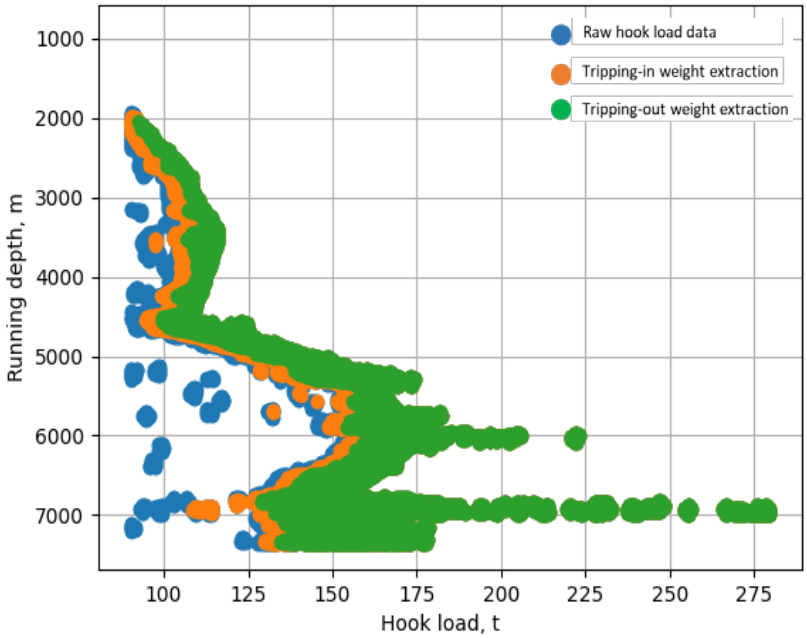

Figure 4. Tripping in and tripping out weights extracted by Python-based application.

Table 1. Summary Validation Metrics.

Series	MAPE (%)	RMSE (t)	R^2
Slack-off	4.00%	4.2	0.990
Pick-up	3.59%	6.5	0.992

Furthermore, RMSE methodology showed the maximum absolute deviation at 6.5 metric tons for PU and 4.2 metric tons for SO, with 4% and 3.6% of MAPE metrics. Therefore, referring to this result, it can be concluded that the model identified and generated PU and SO weights accurately.

After validating the outputs of the Python based workflow, the modeled torque and drag (T&D) results—generated using multiple friction-factor sensitivities—were compared against actual tripping weights to evaluate the model's predictive accuracy. This comparison showed that the existing T&D model could not reliably estimate drag in the open-hole section; in almost entire open hole, it over-predicted drag, demonstrating the need for recalibration to avoid significant mismatches between modeled and real well behavior. The post-drilling friction-factor analysis clearly highlighted discrepancies between predicted and observed tripping loads, underlining the importance of updating the WellPlan T&D model for subsequent wells.

Updating the T&D model was critical because inaccurate predictions increase the risk of excessive loads, equipment overstress, stuck pipe, and tool failures, while also compromising cementing design and zonal isolation. Mis-matched models weaken real-time decisions and heighten safety risks, especially on offshore platforms where operational margins are tighter.

Given these findings, the decision was made to update and recalibrate the existing WellPlan torque and drag model to better match actual well dynamics. A new model was generated with expanded friction-factor sensitivities for both tripping-in and tripping-out operations, using FF values ranging from 0.15 to 0.35. As illustrated in figure 5, the updated T&D outputs show strong alignment with measured hook loads, confirming that the recalibrated model provides a more accurate representation of downhole behavior and supports more reliable well planning and execution. Following this, depth-based friction-factor (FF) values were then generated, establishing the foundation for future FF calibration.

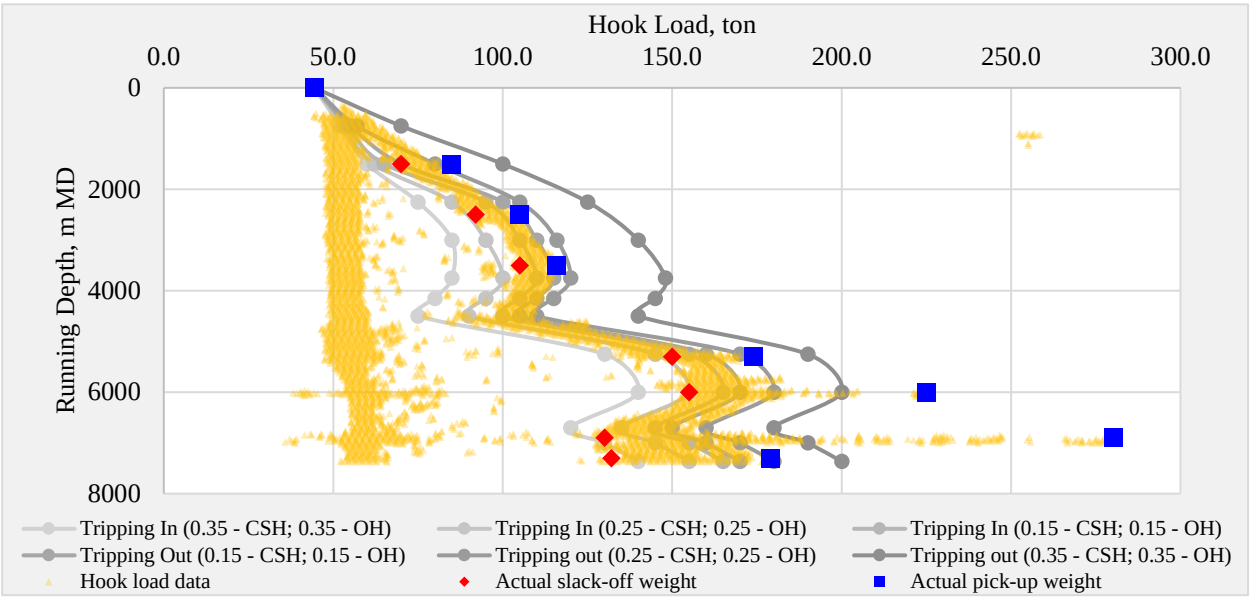

Figure 5. Actual pick-up/slack-off weights and raw hook load data compared with updated and calibrated T&D model outputs.

As shown in [8], the FF profiles for both tripping-in and tripping-out illustrate the varying friction mechanisms along the wellbore. In the lower portion of the open hole—where the trajectory transitions to horizontal and intersects shale intervals—drag increases significantly, and multiple tight spots were observed. Alignment of high FF values or drag with shale intervals where tight spots occurred, the FF values can be related to interpreted lithologies per interval along the open hole section. Alignment of high FF values with shale intervals where tight spots occurred suggests lithology-driven drag variations (see figure 7; [8]).

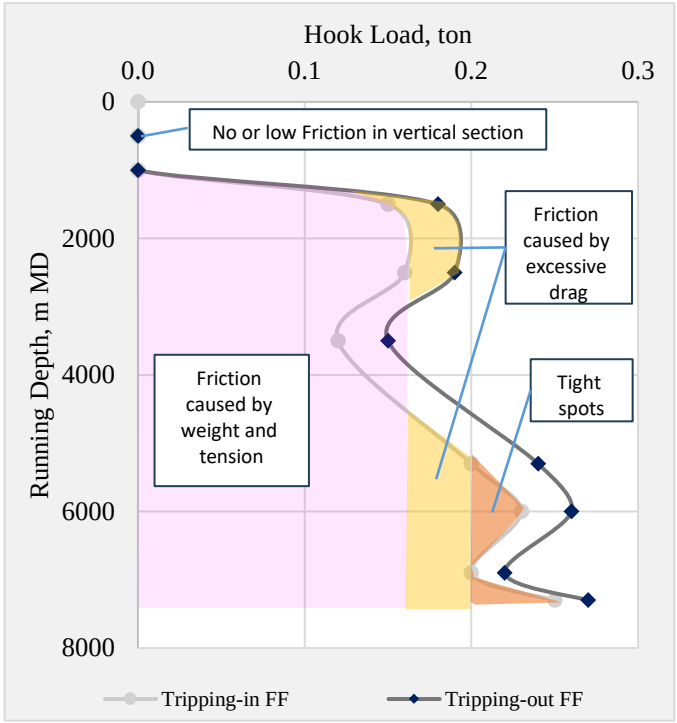

Figure 6. Sensitivity analysis of Friction Factors vs measured depth.

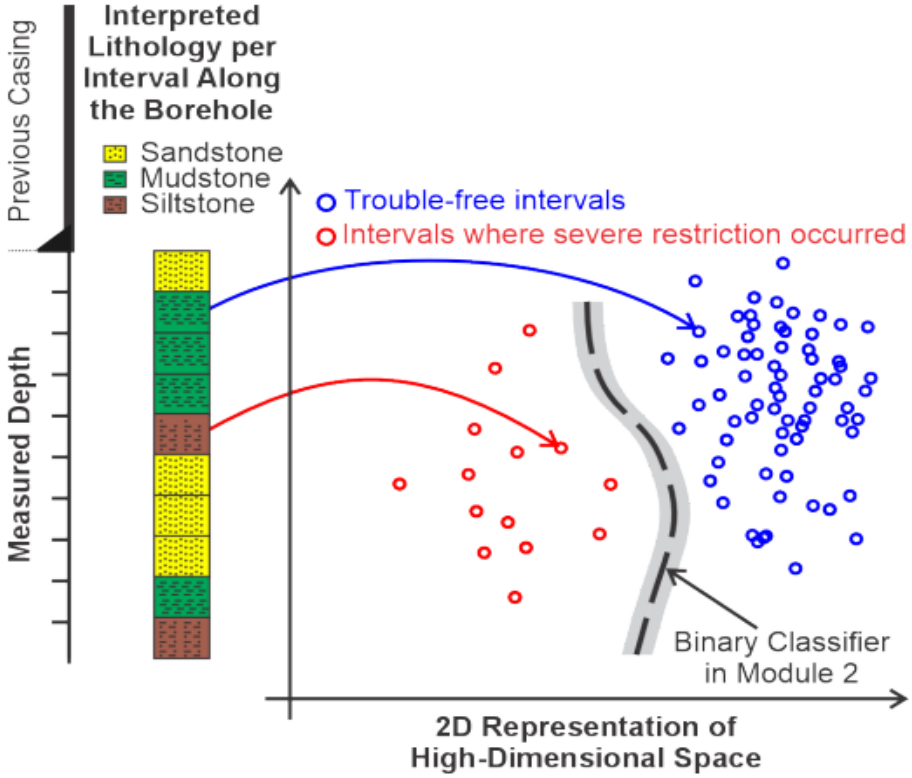

Figure 7. Illustration of hook load measurements depending on various lithologies [8].

Conclusion. This study demonstrates that a Python-based workflow can significantly enhance the accuracy and reliability of torque and drag (T&D) modeling for complex horizontal well completions through friction factor calibration. By extracting hook-load measurements continuous through entire well length directly from mud-logging data and validating them through robust statistical methods—MAPE, RMSE, and R^2—the workflow provides a far more representative picture of actual downhole behavior than traditional reliance on limited rig measurements or offset-well friction-factor assumptions. Application to Well X1 clearly showed that the original T&D model consistently over-predicted drag in the open-hole section, particularly across high-DLS intervals and shale units, highlighting the need for recalibration to prevent operational misinterpretation of loads.

Through depth-based friction-factor calibration and comparison against field-measured pick-up and slack-off trends, the updated T&D model achieved strong alignment with real well dynamics, reducing prediction uncertainty and improving operational decision-making. This improvement is critical for safe casing-running operations, optimized tripping strategies, and accurate planning for cementing, zonal isolation, and long-term well integrity. By integrating continuous field data, automated load extraction, and multi-sensitivity FF modeling, the Python-based approach offers a scalable, efficient, and field-deployable solution that strengthens well delivery performance and reduces risk—particularly for long horizontal wells drilled from offshore platforms where operational margins are narrow and consequences of model inaccuracy are high.

Conflict of interest.

The authors declare that they have no conflict of interest in relation to this research.

References

1. Baldino, S., & Ozbayoglu, E. (2025). Quantifying the impact of cuttings and fluid properties on friction coefficient in torque & drag analysis. Paper presented at the *SPE/IADC International Drilling Conference and Exhibition*, Stavanger, Norway (Paper No. SPE/IADC-223671-MS). https://doi.org/10.2118/223671-MS.

2. Cayeux, E., Skadsem, H. J., & Kluge, R. (2015). Accuracy and correction of hook load measurements during drilling operations. Paper presented at the *SPE/IADC Drilling Conference and Exhibition*, London, United Kingdom (Paper No. SPE/IADC-173035-MS). https://doi.org/10.2118/173035-MS.

3. Economides, M. J., Hill, A. D., Ehlig-Economides, C., & Zhu, D. (2012). *Petroleum production systems* (2nd ed.). Pearson.

4. Gaynor, T., Hamer, D., Chen, D. C.-K., & Stuart, D. (2002). Quantifying tortuosities by friction factors in torque and drag model. Paper presented at the *SPE Annual Technical Conference and Exhibition*, San Antonio, TX, USA (Paper No. SPE-77617-MS). https://doi.org/10.2118/77617-MS.

5. Joshi, S. D. (1991). *Horizontal well technology*. PennWell Publishing Company.

6. Maidla, E. E., & Wojtanowicz, A. K. (1988). Prediction of casing running loads in directional wells. Paper presented at the *Offshore Technology Conference*, Houston, TX, USA (Paper No. OTC-5791-MS). https://doi.org/10.4043/5791-MS.

7. Mason, C.J., Lopez, J., Meling, S., Munger, R., & Fraser, B. (2003). Casing running challenges for extended-reach wells. Paper presented at the *SPE Annual Technical Conference and Exhibition*, Denver, CO, USA (Paper No. SPE-84447-MS). https://doi.org/10.2118/84447-MS.

8. Montes, A.C., Ashok, P., van Oort, E., Les, B., Mullendore, M., & Limaye, S. (2025). Casing run failure avoidance through automated assessment of borehole quality. *SPE Journal, 30*(11), 6715–6738. https://doi.org/10.2118/223706-PA.

9. Shi, X.-L., Huang, W.-J., & Gao, D.-L. (2021). Mechanical behavior of drillstring with drag reduction oscillators and its effects on sliding drilling limits. *Petroleum Science, 18*(6), 1689–1697. https://doi.org/10.1016/j.petsci.2021.09.007.

10. Wang, P., Cao, J., Zhang, H., Yue, W., Ni, H., & Zhang, R. (2024). Axial load peristaltic transfer mechanism of the drillstring to improve penetration rate. *SPE Journal, 29*(7), 3472–3487. https://doi.org/10.2118/219737-PA.

11. Wu, A., Hareland, G., & Fazaelizadeh, M. (2011). Torque & drag analysis using finite element method. *Modern Applied Science, 5*(6), 13–27. https://doi.org/10.5539/mas.v5n6p13.

Journal of SRI "Geotechnological Problems of Oil, Gas and Chemistry" of ASOIU,
Issue 2, 2025, pp. 130-137
https://doi.org/10.65294/gpogc.2025.10

Study of the possibility of the phenomenon of fugitive emissions in current petrochemical productions

A.I. Babaev

Azerbaijan State Oil and Industry University, Scientific-Research Institute
"Geotechnological Problems of Oil, Gas and Chemistry"

Abstract. All processes in the chemical and petrochemical industries generally consist of a number of comparable standard processes, although the products produced may be different. In the chemical engineering industry and related industries, a standard process is a basic stage in technology. For example, in the production of ammonia (NH3), gasification, reforming and NH3 synthesis are standard processes that are linked to each other and create a complete technology. In practice, the technological chain of methanol production also follows this sequence. So does the production of urea. The technology of individual production may consist of a large number of standard processes to obtain the desired product. However, the mechanisms of formation of fugitive emissions in any aggregate state differ little, except for the chemical composition of the emissions. It became possible to use the results of this study and methodology successfully and other installations and industries.

Keywords: technology, processes, production, methanol, organized, fugitive emissions, ecology, thermal imaging control.

*Corresponding author. Tel.:
E-mail address: abulfaz47@mail.ru

Introduction. As is known, technological installations, emissions into the atmosphere are divided into 2 types: organized and unorganized. Analysis of unorganized emissions acquires special significance after a long period of operation of the installation, after the elimination of major technological accidents, when starting up newly introduced into operation after capital construction and fundamental technical re-equipment and reconstruction to avoid loss of resources and pollution of the environment. It is noted that the petrochemical industry is only a secondary source of emissions for most pollutants (1, 2). In this paper, we will consider the possibilities of analysis and calculation of unorganized emissions in the current production of methanol after long-term operation and relocation.

Conducting the experiment

The studies were conducted at all potential locations (points) of fugitive emissions (leaks) on process pipelines, units, vessels and devices of auxiliary, main production and tank farm.

The survey of "points" of potential leaks was carried out using thermal imaging control technologies. Experimental studies in operating conditions were carried out according to the main provisions of the developed thermal imaging control technology. Before conducting thermography, all necessary preparatory operations were performed. As diagnostic equipment, a FLIR GF320 thermal imager was used. The device is capable of quickly surveying large areas and determining the presence of hydrocarbon gas leaks in real time (3). Recently, intelligent thermal imaging equipment has been successfully used, which is an effective tool for monitoring any changes in temperature in a wide variety of areas and industries, to ensure safety at production facilities in order to identify defects and prevent leaks of hazardous substances (the accuracy of the determination is up to $\pm 2^0$ or ±2%) (4).

The number of surveyed "points" of potential leaks was initially determined by analyzing process flow charts based on working drawings. Their preliminary estimated number was 7,579. Of these, 270 "points" relate to auxiliary production, 498 to the tank farm, i.e., tanks for storing finished products, raw materials and reagents, intermediate semi-finished products that participate in the technological process of production, waste obtained as a result of side reactions, which are subsequently processed into target products (5).

Results and their discussion

As a result of using thermal imaging control technologies on process pipelines, units, vessels and devices of the entire production, 7579 possible leak points were analyzed. Of the total 7579 inspected "points", leaks were detected in 29 "points". Of these, 1 "point" related to the tank farm, the rest directly related to process equipment, communication pipelines, elements of the contour of measuring and actuators. All analyses of unorganized emissions, namely their volumes are calculated in kg per year. Based on the analysis and calculations, the total annual volume of unorganized emissions for the main components was established. The calculation results are shown in Figure 1.

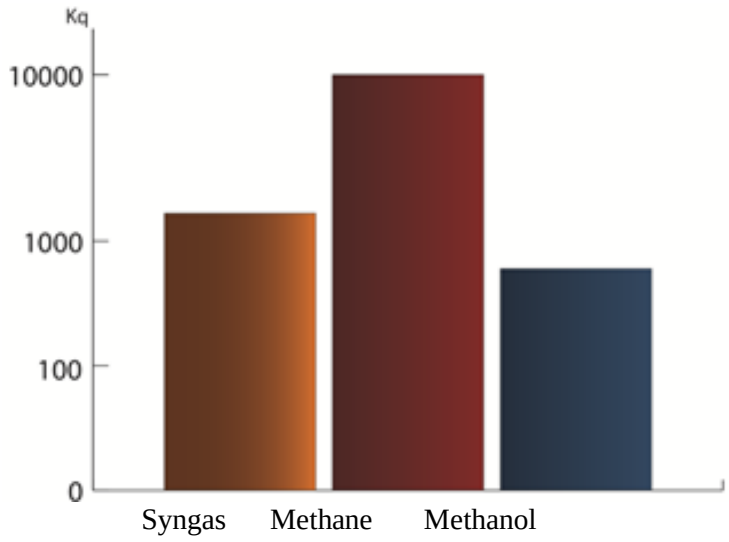

Fig. 1 The final calculated volume (mass fraction) of unorganized hydrocarbon emissions, kg/year. Based on the analysis of this diagram, it can be noted that the mass fraction of methane prevails and is 19995.43 kg/year. The mass fractions of synthesis gas and methanol are 1997.28 kg/year and 963.60 kg/year, respectively. Consequently, the final calculated volume (mass fraction) of unorganized hydrocarbon emissions is 22956.31 kg/year.

The analysis of possible leak points and calculation of the volume of unorganized emissions of fuel gas - methane by element type was carried out. The analyses were carried out in 5188 "points", 24 of which were noted leaks. Since methane is used in the methanol production process and the quality of raw materials, and the quality of fuel with the first considered losses before the distribution of flows. According to the analysis of unorganized methane emissions in the initial Bosch process flows, several fuel gas leak points were found below:
1) stuffing box - 1401.60 kg / year
2) threaded connections - 262.80 kg / year
3) other - 18331.03 kg / year
Total: 19995.43 kg / year.

Detection of fuel gas - methane emissions leaks by element type was carried out using the thermal imaging method of photographing possible leak points according to the process flow chart. The results of thermal imaging of fuel gas leak locations are shown in Figures 2, 3, 4, 5.

Serial number	Type of pipeline element, pipeline fittings, device, unit	Environment
10	Coupling connection of nozzle D-7(American)	Natural gas
Photo of the object	Thermal imaging	

Fig. 2. D-7 injector coupling (American)

Serial number	Type of pipeline element, pipeline fittings, device, unit	Environment
10	Welded seam on line of fuel gas to nozzle İ-5	Natural gas
Photo of the object	Thermal imaging	

Fig.3 Welded seam on the fuel gas line to the İ-5 injector

Serial number	Type of pipeline element, pipeline fittings, device, unit	Environment
10	Coupling connection of nozzle Q-2	Natural gas
Photo of the object	Thermal imaging	

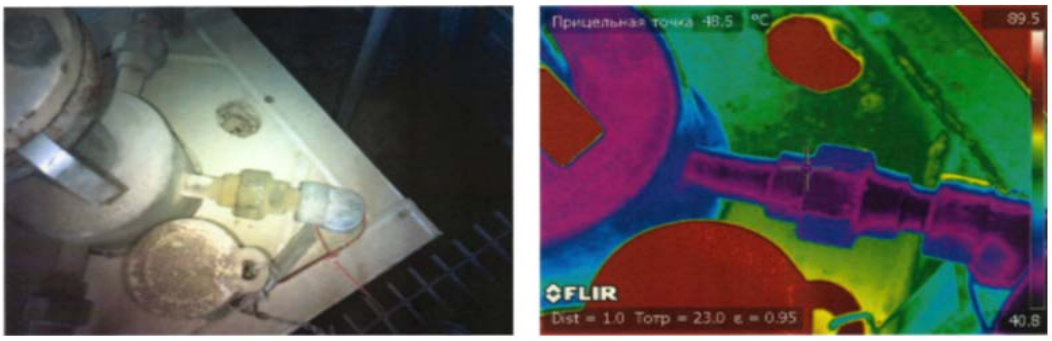

Fig.4. Coupling connection of the Q-2 injector

Serial number	Type of pipeline element, pipeline fittings, device, unit	Environment
10	Threaded connection of flexible connection of nozzle A-7	Natural gas
Photo of the object	Thermal imaging	

Fig. 5. Threaded connection of the flexible connection of the A-7 nozzle

The estimated volume of unorganized emissions of natural gas is shown in Figure 6.

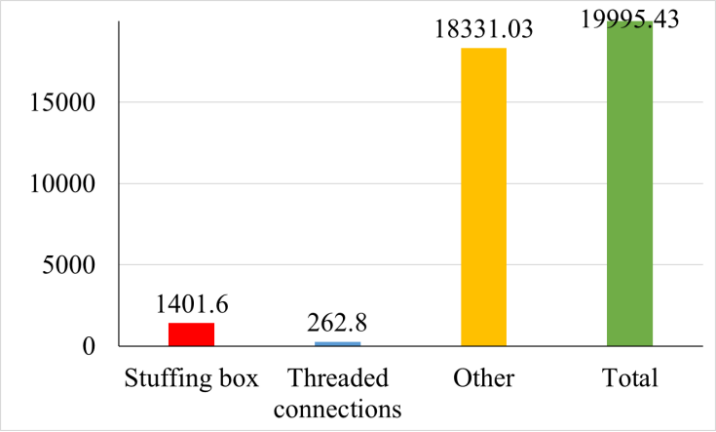

Fig. 6. Estimated volume (mass fraction) of unorganized emissions of natural gas kg/year

Considering that methane entering the reaction environments already ceases to exist as methane in the future, its loss is considered in the context of hydrocarbon loss. After distribution, the second flow is the fuel circuit. Dali conducted an analysis of unorganized emissions of methane in the fuel circuit. According to the analysis, specific places of unorganized emissions in the process equipment of the following units were established:

1) nozzle connection - 7992.42 kg/year:
threaded connection 1 - 7729.62 kg/year
threaded connection 2 – 262.80 kg/year
2)welded seam – 1927.20 kg/year
3)ball valve – 1401.60 kg/year
4)non-hermetic device – 8674.21 kg/year
Total: 19995.43 kg/year.

A graphical representation of the obtained results is shown in Figure 7.

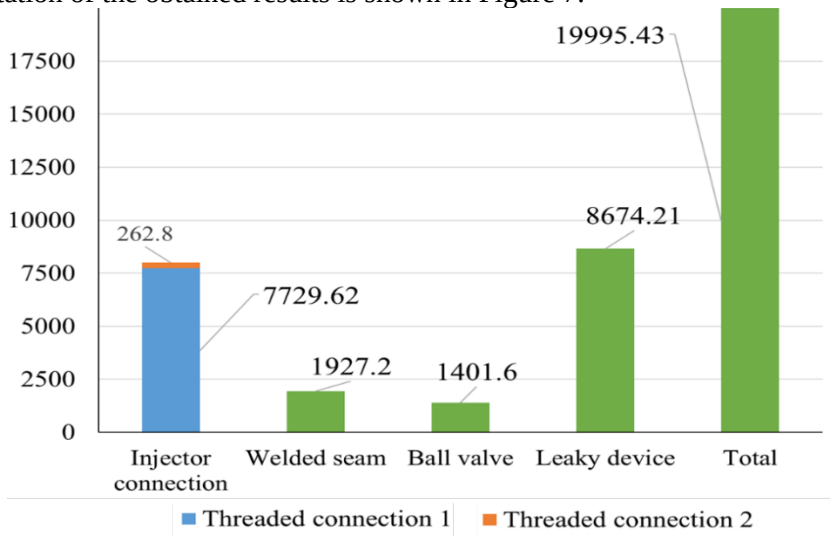

Fig. 7. Estimated volume (mass fraction) of unorganized emissions of fuel gas by positions kg/year

The second source of gaseous loss in the methanol production process is synthesis gas. It should be noted that the technological communication circuit of synthesis gas is much shorter than that of fuel gas. Accordingly, the checked control point is also comparatively smaller.

Analyses were carried out in 601 "points". Detection of synthesis gas emission leaks by element type was also carried out using the thermal imaging method of photographing possible leak locations according to the process flow chart. The results of the thermal imaging image of synthesis gas leak locations are shown in Figures 8, 9.

Serial number	Type of pipeline element, pipeline fittings, device, unit	Environment
24	Threaded connection of valve of selection on device item FE-2789(HE-401)	synthetic gas
Photo of the object	Thermal imaging	

Fig. 8 Threaded connection of the sampling valve on the device item FE-2789(HE-401)

Serial number	Type of pipeline element, pipeline fittings, device, unit	Environment
25	Threaded connection of valve of selection on device pos. AT-18794(R-401)	synthetic gas
Photo of the object	Thermal imaging	

Fig. 9. Threaded connection of the extraction valve on the device item AT-18794 (R-401)

Based on the analysis of the calculated volume of unorganized emissions of synthesis gas by element type, the following results were obtained:
1) flange connections - 1471.68 kg/year
2) stuffing box - 525.60 kg/year
Total: 1997.28 kg/year.
A graphical representation of the obtained results is shown in Figure 10.

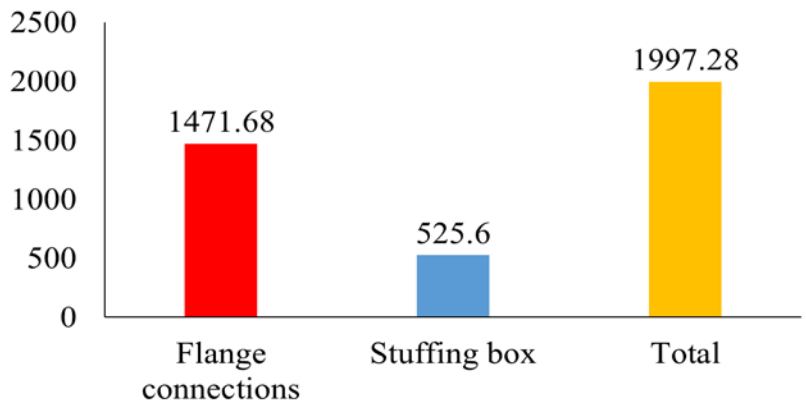

Fig. 10 Estimated volume (mass fraction) of unorganized emissions of synthesis gas kg/year

A control analysis was carried out for a specific equipment position and connection point in the process circuit of synthesis gas and the following results were obtained:
1) flange connections - 735.84 kg/year
2) threaded connection - 525.60 kg/year
3) valve - 735.84 kg/year
Total: 1997.28 kg/year

A graphical representation of the obtained results for specific places - equipment of unorganized emissions of synthesis gas is given in Figure 11:

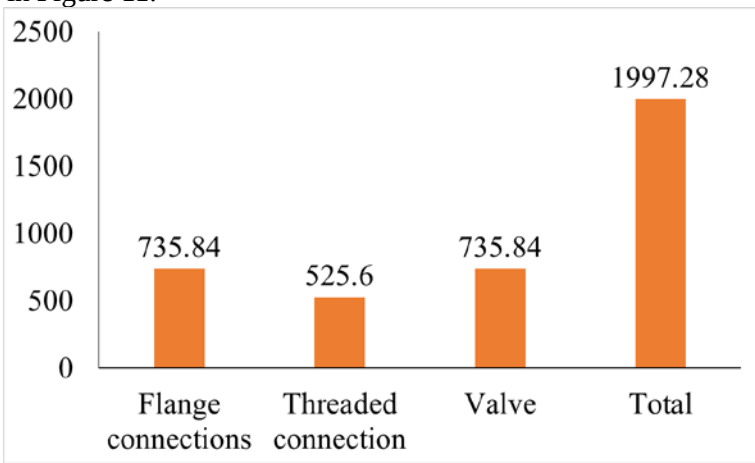

Fig. 11 Estimated volume (mass fraction) of unorganized emissions of synthesis gas by items, kg/year

As noted technological installation has 498 tank equipment. Taking into account the harmful properties of methanol were conducted analyzes in 1790 "points". It was established in one place - equipment of unorganized emissions of methanol:

1) shut-off lid - 963.60 kg / year.

Photo image of the detected checkpoint is shown in Figure 12.

Serial number	Type of pipeline element, pipeline fittings, device, unit	Environment
29	Cover of measuring device of tank 24TK-0024	Methanol

Photo of the object Thermal imaging

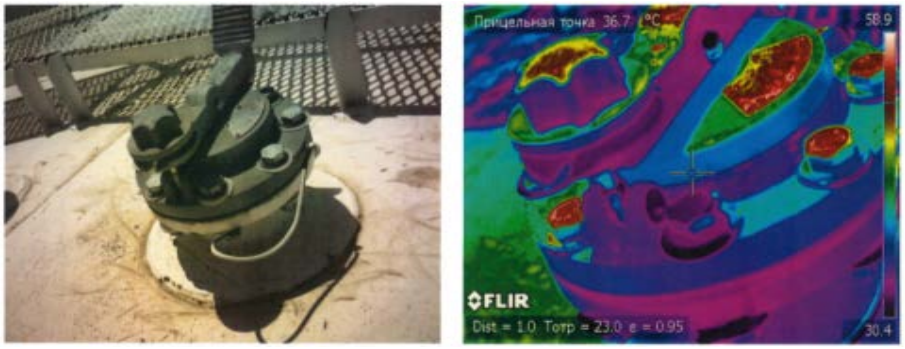

Fig. 12. Cover of the measuring device of the tank 24TK-0024

The analysis of the above data shows that there is a high overall level of hydrocarbon losses and an extremely high level of hydrocarbon losses relative to the amount of unorganized emissions after a certain time of operation of the equipment. Based on this, after long-term operation of the production unit, it is necessary to conduct a control survey of the technical condition of the process equipment, communication pipelines, connecting nodes and the tightness of the seals. Systematic qualified analysis of the state of unorganized emissions at the production enterprise is also a guarantee of safety, explosion-fire safety, stable operation, high economic efficiency.
Conclusions

According to the analysis results, it can be noted that the mass fraction of methane prevails and amounts to 19995.43 kg/year. The mass fractions of synthesis gas and methanol are 1997.28 kg/year and 963.60 kg/year, respectively. Consequently, the final calculation of the volume (mass fraction) of unorganized hydrocarbon emissions is 22956.31 kg/year. The number of surveyed "points" of potential leaks using thermal imaging control technologies on process pipelines, units, vessels and devices of the entire production is 7579. Of the 7579 surveyed "points", 270 "points" relate to auxiliary production; 6811 - to the main production, 498 - to the tank farm.

In 498 tank equipment, analyzes were carried out at 1790 "points" and only one case of unorganized emissions was detected, and 6811 points in the main production 29 cases of unorganized emissions. It has been established that the main share of unorganized emissions fall on the system of technological communication of methane and logistics. Based on this, in the quality of the applied significance of this study, similar enterprises are recommended to systematize and strengthen control in the presence of such systems and units.

Conflict of interest.

The authors declare that they have no conflict of interest in relation to this research.

References:

1. EMEP/EEA Air Pollutant Emission Inventory Guidebook 2016 1
https://www.eea.europa.eu/ru/publications/rukovodstvo-emep-eaos-po-inventarizaciivybrosov-2016
2. Gakhramanova, Z.O., Babayev, A.İ., Hasanov, G.S., İsmayilova, K.M., Sadyqova, N.A., Məmmədova, S. «Studying possible transformation of petroleum products absorbed into the soil» Processes of petrochemistry and oil refining, vol.25, № 2, 2024, pp.523-532
3. http://ptk-nk.ru/index/poisk_utechek_i_teplovizionnyj_kontrol/0-14
4. https://hikvision.ru/press/190617035746
5. Babayev, A.I. Ecological Cybernetics of Oil Processing and Petrochemical Processes11 th World Conference “Intelligent System for Industrial Automation” (WCIS-2020) http://orcid.org/0000-0001-8220-3415, 7s

Journal of SRI "Geotechnological Problems of Oil, Gas and Chemistry" of ASOIU,
Issue 2, 2025, pp. 138-141
https://doi.org/10.65294/gpogc.2025.11

IR spectroscopy in the analysis of hydrocarbons isolated from oil-contaminated soils

A.I. Babayev[1], Q.S. Hasanov[2], K.M. Ismailova[1], Z.O. Gahramanova[1], N.A. Sadigova[1], N.A. Yusubova[1]

[1] Azerbaijan State Oil and Industry University, 20 Azadlig Avenue, Az1010, Baku, Azerbaijan
[2] Scientific Research Institute " Geotechnological Problems of Oil, Gas and Chemistry" 227 Dilara Aliyeva str., AZ1010, Baku, Azerbaijan.

Abstract. The study is devoted to the investigation of the chemical composition of hydrocarbons isolated from oil-contaminated soils using infrared (IR) spectroscopy in the mid-infrared region. Based on the obtained spectra, the types of bonds present in molecules and atoms were characterized, functional groups were identified, and the structural composition of the sample was determined. A comparison was carried out with data from gas chromatography–mass spectrometry (GC–MS) and nuclear magnetic resonance (NMR) spectroscopy.

Keywords: extraction, oil analysis, FT-IR spectroscopy, chemical composition of hydrocarbons.

*Corresponding author. Tel.: +994707719992
E-mail address: kamala.i@mail.ru

1. Introduction. Alteration of soil ecosystems by oil and gas production wastes, as well as oil leaks during transportation, represents one of the most complex and multifaceted environmental protection problems. It is known that oil-impregnated soils, while remaining under the influence of natural factors, undergo various structural changes [1,2].

The study of the characteristics of changes in petroleum hydrocarbons that have remained in soil for long periods is necessary to address the problem of remediation of such soils. Determination of the structural parameters of hydrocarbons isolated from oil-contaminated soils is a complex scientific task, the solution of which involves the use of various spectroscopic techniques [3–5].

Among the many existing methods for studying the structure of chemical compounds, infrared (IR) spectroscopy is one of the most important and versatile techniques. It is well known that the features of the molecular structure of the substance under study are reflected in the IR spectrum by the presence of various characteristic absorption bands. The data obtained by this method make it possible to determine functional groups more accurately than by chemical analysis.

The complex chemical composition and intermolecular structure of such hydrocarbons can be described by analyzing IR spectra recorded in the mid-infrared region, as well as by determining the content of structural fragments of hydrocarbon and non-hydrocarbon compounds [6,7]. Using Fourier-transform IR (FT-IR) spectroscopy, we investigated the structural and group composition of petroleum hydrocarbons in the range of 4000–500 cm^{-1}, isolated from soil samples of the studied oil field. Previously, these samples were similarly studied using gas chromatography–mass spectrometry (GC–MS) and nuclear magnetic resonance (NMR) spectroscopy [1,8]. The chromatographic method proved

to be informative in describing polar components containing aromatic fragments; however, information on the naphthenic and highly oxidized fractions of the isolated hydrocarbons was lacking.

The aim of this work was to analyze the features of changes in the chemical composition of petroleum hydrocarbons isolated from oil-contaminated soils of the Balakhany oil field that had undergone biodegradation using the above-mentioned method, and to compare the obtained results with those of chromatographic analysis and NMR spectroscopy.

Experimental section. The object of our study was a sample taken from the territory of Oil Production Unit No. 4 of the Balakhany oil field. Isolation of the oil fraction from the collected sample was carried out by extraction using the following solvents: benzene, hexane, toluene, and xylene. Initially, it was observed that the degree of dissolution of petroleum products varied somewhat depending on the solvent used. Subsequently, the solvent was evaporated from the extract, and the isolated hydrocarbon residue was analyzed by IR spectroscopy; the results are presented in Fig. 1 (a, b, c, d). The oil contaminants isolated from the production area differ from produced crude oils and do not contain light fractions [8–10].

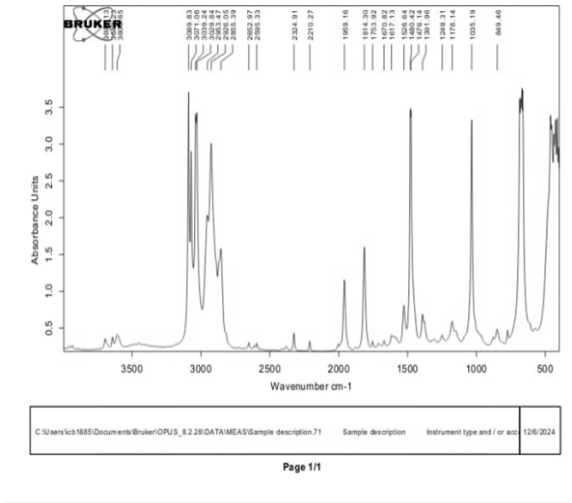

a)

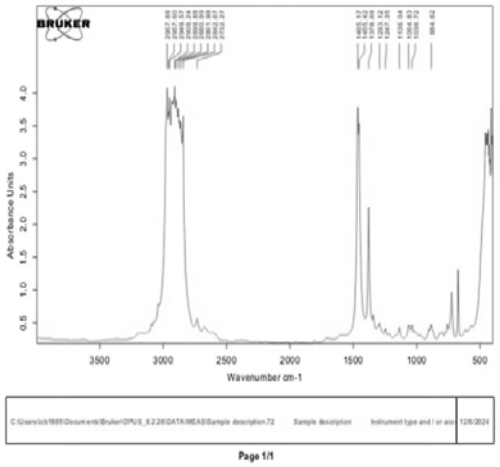

b)

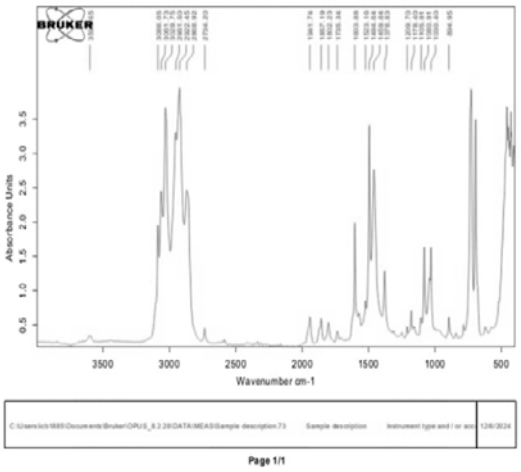

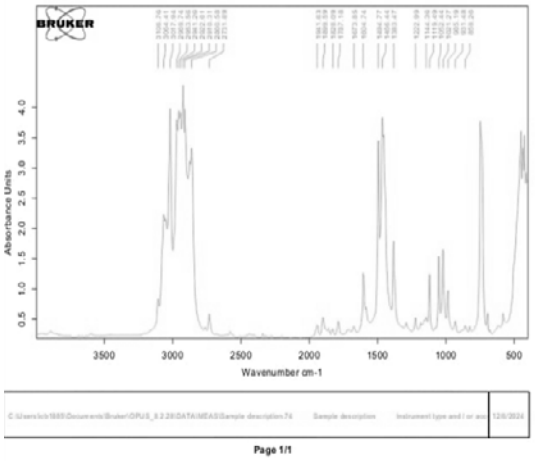

c) d)

Figure 1. FT-IR spectra of hydrocarbon extracts isolated from oil-contaminated soil. Solvents: (a) benzene, (b) hexane, (c) toluene, (d) xylene.

2. Analysis of results. The composition of the isolated petroleum extracts differs markedly from that of the original crude oil due to an increased proportion of resinous substances, naphthenic–paraffinic, and polycyclic hydrocarbons; as a result, the density increases from 0.8486 to 0.8921. The spectra show that the intensity of absorption bands in the regions of approximately 3029–3100 cm^{-1} and the adjacent 2950–3000 cm^{-1} corresponds to stretching vibrations of hydrogen atoms in methyl and methylene group fragments, which are characteristic of alkanes, especially cyclic, heterocyclic, and cycloalkane hydrocarbon rings.

Stretching vibrations in the 1450–1940 cm^{-1} region of the spectra of the benzene, xylene, and toluene extracts indicate the presence of cycloolefinic compounds, esters, and ketones. In addition, interpretation of the absorption bands around ~1500 cm^{-1} confirms the presence of hydrogen atoms involved in double bonds and in aromatic rings.

The 1000–1400 cm^{-1} region observed in the IR spectra is considered highly informative, as the bands appearing in this range are also associated with various atomic groups. Within the same interval, bands near 1300 cm^{-1} may be attributed to vibrations of C–N and C–O bonds that are part of sulfur-containing and polycyclic compounds. In the IR spectra of the toluene and benzene extracts, a stretching vibration band at 3600–3690 cm^{-1} is observed, which indicates the presence of hydrogen in amino groups ($–NH_2$, –NH–). In the long-wavelength region of the spectrum (~2600–2800 cm^{-1}), stretching vibrations of various hydrogen-containing groups characteristic of amides and mercaptans are manifested.

Thus, the analysis of the IR spectra confirms the presence of aliphatic hydrocarbons, various oxidation products of petroleum, as well as secondary decomposition products of oil. The above data are consistent with the results obtained using gas chromatography–mass spectrometry (GC–MS) and nuclear magnetic resonance (NMR) spectroscopy.

All the presented physicochemical methods for analyzing hydrocarbons isolated from contaminated soils indicate degradative and oxidative transformations of petroleum. In the isolated product, the aliphatic fraction predominates over the aromatic fraction and also contains complexes with highly stable structures that are resistant to fragmentation.

Conclusions. FT-IR spectroscopy was used to record the spectra of petroleum hydrocarbon extracts isolated from contaminated soils. Based on these spectra, the group-level chemical composition was characterized, which is consistent with the data obtained from gas chromatography–mass spectrometry (GC–MS) and nuclear magnetic resonance (NMR) spectroscopy.

Conflict of interest.

The authors declare that they have no conflict of interest in relation to this research.

References

1. Babayev, A., Hasanov, G., Gakhramanova, Z., Sadyqova, N., Məmmədova, S. Studying possible transformations of petroleum products absorbed into the soil. Processes of petrochemistry and oil refining, vol. 25 № 2, 2024, pp. 523 532 https://ppor.az/index.php/ppor/article/view/206/178 https://doi.org/10.62972/1726-4685.2024.2.523
2. İsmailova, K., Yusubova, N. Study of the composition of petroleum products extracted from oil-contaminated soil using the spectrometric method Scientific proceedings. Scientific -Research Institute “Geotechnological Problems of Oil, Gas and Chemistry, Baku 2023,volume 23,№1, pp.129-133.
3. Bellamy, L. Infrared Spectra of Complex Molecules. Moscow: Foreign Literature, 1963, 590 p.
4. Kazanina, L. A., Kupletskaya, N. B. Application of Infrared, Ultraviolet, and NMR Spectroscopy in Organic Chemistry. Moscow: Vysshaya Shkola, 1971.
5. Babayev, A. I. Shelomenok, M. Kh. Shchegol, Sh. S., Mamedov, F. V. Determination of Carboxyl Group Content in Carboxyl Butyl Rubber by Absorption and ATR Infrared Spectrophotometry, Industrial Synthetic Rubber, 1980, pp. 12-14.
6. ASTM D 5986-96 (2001). Standard Test Method for Oxygenates, Benzene, Toluene, C8-C12 Aromatics, and Total Aromatics in Gasoline by Gas Chromatography-FTIR Detection.
7. ASTM D 6277-01 Standard Test Method for Benzene in Internal Combustion Engine Fuels by Mid-IR Spectroscopy.
8. Babayev, A., Gakhramanova, Z., Ismayilova, K., Sadyqova, N., Aliyev, E. Research and development of technology for purification of oil polluted soils by physical and chemical methods Scientific proceedings Scientific-Research Institute “Geotechnological Problems of Oil, Gas and Chemistry, Baku-2022, december V. 22, N1, page 104-108.
9. Ivanova, L.V., Safieva, R.Z., Koshelev, V.N. IR spectrometry in the analysis of oil and oil products. Moscow: Bulletin of Bashkir University, 2008. Vol. 13. No. 4.
10. Ivanova, L.V., Koshelev, V.N., Vasechkin, A.A., Primerova, O.V. IR spectrometry in the analysis of oils, Internet conference "Butlerov Readings", 2012, pp. 120-124.

Journal of SRI "Geotechnological Problems of Oil, Gas and Chemistry" of ASOIU,
Issue 2, 2025, pp. 142-148
https://doi.org/10.65294/gpogc.2025.12

Investigation of the distribution of rare elements in ores of the Gedabek deposit

A.I. Babayev[1], V.Kh. Hamzayev[1], G.I. Guseinova[1], R.N. Ahmedova[1], A.R. Babaev[1], F.Z. Madatova[1], K.Kh. Agayeva[1], D.G. Ismayilova[1]

[1]Scientific Research Institute "Geotechnological Problems of Oil, Gas and Chemistry", Ministry of Science and Education of the Republic of Azerbaijan, Dilara Aliyeva Street 227, AZ1010, Baku, Azerbaijan

Abstract. The presented article is devoted to the study of the distribution of rare elements in the ores of the Gedabek deposit located in the Gedabek ore district. As is known, the Gedabek deposit located in the north-west of the Republic of Azerbaijan has great prospects. Precious metals such as gold, silver, and copper are extracted from the deposit. In addition, various elements are found in the ores of the deposit, including vanadium, chromium, cobalt, nickel, etc. elements. Among them, rare elements are of great importance. The article provides information about the geology of the Gedabek ore district and the Gedabek deposit and shows the mineralogical composition of the ores of the deposit. Research work was carried out to study the distribution of rare elements in the ores of the deposit. The analysis of test samples taken from the deposit was carried out. The oxide, element, and mineralogical compositions of these samples were investigated. It was found that the test samples contained high amounts of aluminum oxide, silicon oxide, silicon trioxide, potassium oxide, and iron (III) oxide among oxides, and high amounts of quartz, illite and kaolinite among minerals. In addition, it was found that they contain rare elements such as V, Pb, Ga, Se, Zr, and Rb. The test samples contained higher amounts of rare elements such as Pb, Zr, and Rb. In addition, the content of rare elements in many igneous rocks is higher than in sedimentary rocks.

Keywords: Gedabek ore region, Gedabek deposit, rare elements, magmatic, sedimentary.

[*]Corresponding author. Tel.: +994702102419
E-mail address: abulfaz@mail.ru (A.I. Babayev)

1. Introduction. In the Azerbaijani part of the Lesser Caucasus, four structural formation zones are distinguished from north to south: Lok-Karabakh, Goycha-Hekari, Miskhana-Zangezur, and Araz. The Gedabek ore region, which belongs to the Lok-Karabakh structural-formation zone, is considered the largest porphyry region in the country, being a part of the Tethys belt. The copper-porphyry deposits characteristic of the Gedabek ore region are related to Cimmerian volcanism. The main intrusive complex consists of rocks of the Atabey-Slavyanka plagiogranite and Gedabek diorite intrusion. Small dike-shaped or stock-shaped inclusions of medium and basic composition are often observed in the mentioned intrusive rocks. Small intrusions correspond to submeridional fault zones. Submeridional faults play a major role in the location and formation of copper-porphyry deposits in the mentioned area [6].

One of the promising deposits located in the Gedabek ore region is the Gedabek deposit [1, 4-8, 10, 13-16]. The main ore minerals of this deposit are pyrite, chalcopyrite and sphalerite, and non-ore minerals are quartz, barite and sericite [1]. The rocks of the early phase in the deposit are represented by gabbro and gabbrodiorites, the rocks of the late phase by diorites and quartz diorites, and rarely by granodiorites [15]. Most sulfide ores are unstable in the oxidation zone [4]. Geological, mineralogical, geochemical, isotopic and microthermometric data of the Gedabek deposit indicate that it is a high-sulfide epithermal deposit associated with a porphyry system [13]. It should be noted that all sulfide deposits located in our republic are rich in rare elements [2, 11]. Many deposits located in the Republic of Azerbaijan have great potential in terms of the richness of rare elements [3, 9, 12].

The main objective of the study is to investigate the characteristics of the distribution of rare elements in the ores of the deposit. The main issues include: providing general information about the geology of the Gedabek ore region and the Gedabek deposit, reviewing the mineralogical composition

of the ores of the deposit, investigating the characteristics of the distribution of rare elements in the ores of the deposit and determining their economic significance.

2. Materials and methods. The Gedabek ore region is considered the largest porphyry-epithermal area in the country [6, 7]. The ore masses of the Gedabek deposit located in the Gedabek ore region are represented by massive, vein-rich, rich, sometimes banded and breccia-like texture types [4]. The geological map of the Gedabek ore region is shown in Figure 1.

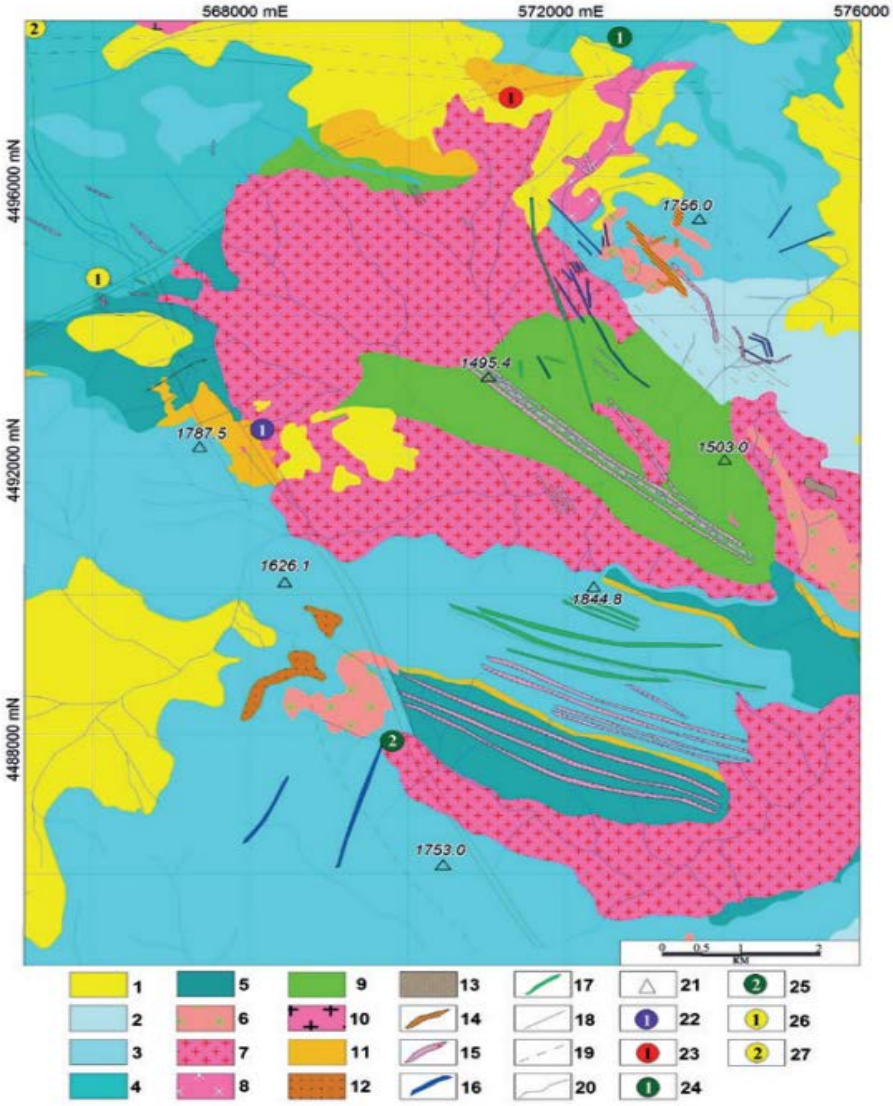

Figure 1. Geological map of the Gedabek ore district, scale 1 : 50 000 [16]

1 – quaternary eluvial-deluvial deposits; 2 – bathonian volcanic deposits: andesitic tuffs, tuff breccias, tuff conglomerates; 3 – lower cretaceous limestones of the oxfordian-kimmeridgian stage: limestones with interbeds of sandstones; 4 – upper bajocian: lavas, subvolcanic and pyroclastic facies of rhyolite-rhyodacitic rocks; 5 – lower bajocian: pyroclastic facies, tuff breccias and andesites; 6 – Garagaya-Garamurad hypabyssal subvolcanic bodies: diorite; 7 – the second phase of the Gedabek intrusion: diorites; 8 – the second phase of the Gedabek intrusion: granodiorites; 9 – the first phase of

the Gedabek intrusion: gabbrodiorites, gabbro; 10 – plagiogranites; 11 – metasomatites; 12 – greisens; 13 – skarns; 14-17 – dikes: 14 – diorite, 15 – quartz-diorite, 16 – andesite, 17 – dolerite; 18 – faults; 19 – supposed faults; 20 – rivers; 21 – heights; 22 – the Gedabek deposit; 23-26 – manifestations: 23 – copper-porphyry Boyuk Galacha, 24 – copper-pyrite Pirbulag, 25 – copper-pyrite Ayatala, 26 – sulfur-pyrite Cholpan; 27 – the Ugur gold deposit

The article was prepared using analysis and synthesis methods. The object of the study is the Gedabek deposit. The composition of the test samples was investigated at the Analytical Center of the Institute of Geology and Geophysics of the Ministry of Science and Education of the Republic of Azerbaijan. The oxide, mineralogical and elemental composition of the test samples are shown in Tables 1, 2, and 3, respectively.

Table 1. Oxide composition of test samples taken from the deposit

№	Conventional name of the sample	Na_2O	MgO	Al_2O_3	SiO_2	P_2O_5	SO_3	K_2O	CaO	TiO_2	Fe_2O_3	MnO	SrO	CuO	BaO	Cl^-	YTİ
1	GDB 001	0,24	0,96	18,27	68,92	0,06	0,90	5,34	1,24	0,30	1,01	0,02	0,01	0,10	0,22	0,002	2,33
2	GDB 002	0,22	0,29	16,73	56,93	0,04	9,30	4,00	0,14	0,26	4,68	0,01	0,01	0,38	0,24	0,003	6,71
3	GDB 003	0,24	0,16	7,70	79,15	0,01	2,37	3,10	0,07	0,22	4,11	0,01	0,01	0,06	0,31	0,002	2,43
4	GDB 004	0,20	1,88	16,13	72,37	0,01	0,69	4,34	0,04	0,19	1,21	0,01	0,01	0,14	0,08	0,005	2,66
5	GDB 005	0,27	5,23	14,09	45,41	0,09	7,62	2,00	2,43	0,40	13,11	0,09	0,01	0,04	0,08	0,031	9,00
6	GDB 006	0,21	0,71	14,49	65,67	0,01	4,09	3,58	1,06	0,20	3,83	0,02	0,01	0,10	0,18	0,021	5,75

Note: YTI – indicates the amount of volatile components at 950^0C.

Table 2. Elemental composition of test samples taken from the field

№	Conventional name of the sample	As	Zn	V	Pb	Cr	Ga	Se	Zr	Rb	Mo	Ni	Co
1	GDB 001	0,0003	0,0249	0,0003	0,0008	0,0153	0,0001	0,0002	0,0095	0,0075	0,0002	0,0003	0,0002
2	GDB 002	0,0002	0,0087	0,0011	0,0090	0,0142	0,0027	0,0003	0,0095	0,0049	0,0003	0,0001	0,0002
3	GDB 003	0,0010	0,0086	0,0023	0,0048	0,0136	0,0003	0,0001	0,0045	0,0040	0,0002	0,0002	0,0001
4	GDB 004	0,0026	0,0055	0,0021	0,0003	0,0063	0,0002	0,0005	0,0075	0,0002	0,0036	0,0002	0,0002
5	GDB 005	0,0002	0,0623	0,0014	0,0004	0,0096	0,0002	0,0003	0,0070	0,0038	0,0002	0,0049	0,0048

6	GDB 006	0,0029	0,0425	0,0012	0,0002	0,0009	0,0002	0,0002	0,0079	0,0040	0,0055	0,0003	0,0002

Table 3. Mineralogical composition of test samples taken from the deposit

№	Conventional name of the sample	Quartz	Feldspar	Illite	Kaolinite	Magnetite	Pyrite	Diopside	Clinochlore	Andalusite	Other impurities
1	GDB 001	50	-	30	13	-	-	5	-	-	2
2	GDB 002	40	12	12	10	-	8	-	-	16	2
3	GDB 003	62	8	10	8	-	2	-	-	8	2
4	GDB 004	50	-	33	14	1	-	-	-	-	2
5	GDB 005	30	-	26	-	-	7	-	35	-	2
6	GDB 006	55	-	20	20	-	3	-	-	-	2

3. Results and discussion. As can be seen from Table 1, the test samples contain higher amounts of aluminum oxide, silicon oxide, silicon trioxide, potassium oxide, and iron (III) oxide. As described in Table 2, rare elements vanadium (V), lead (Pb), gallium (Ga), selenium (Se), zirconium (Zr), and rubidium (Rb) were found in the test samples. In addition, according to the mineralogical composition of the test samples (Table 3), it can be noted that the studied samples contain high amounts of quartz, illite, and kaolin minerals.

The rare elements found in larger amounts in the test samples compared to others are shown in Figure 2. Also, the amounts of these rare elements found in the studies of other authors are shown in Figure 3.

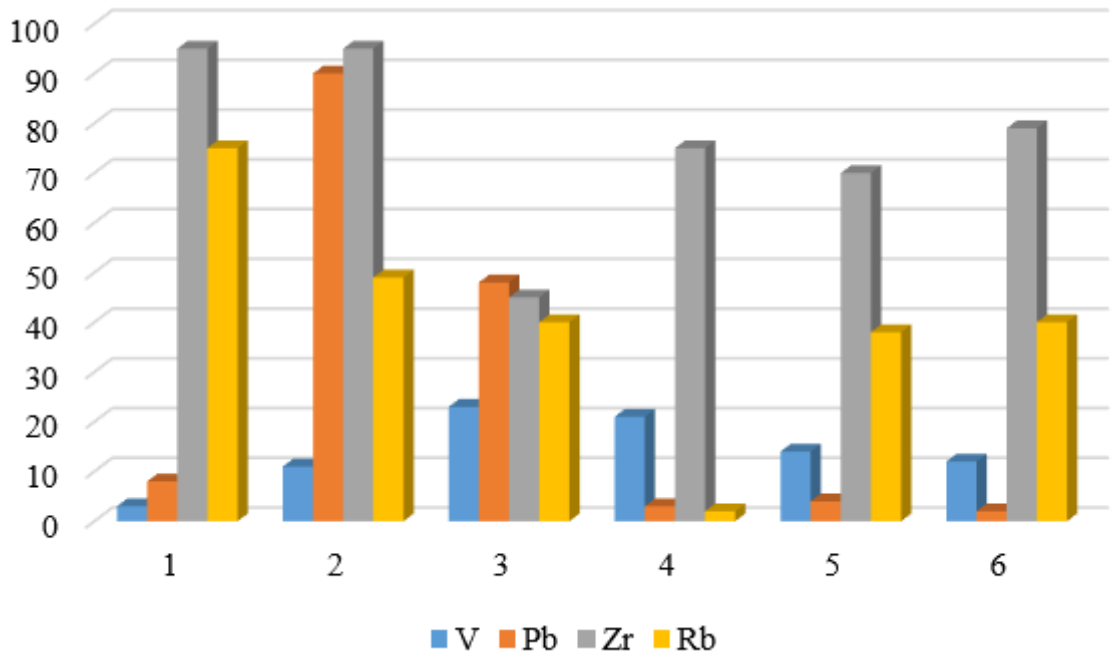

Figure 2. Rare elements found in relatively large quantities in test samples

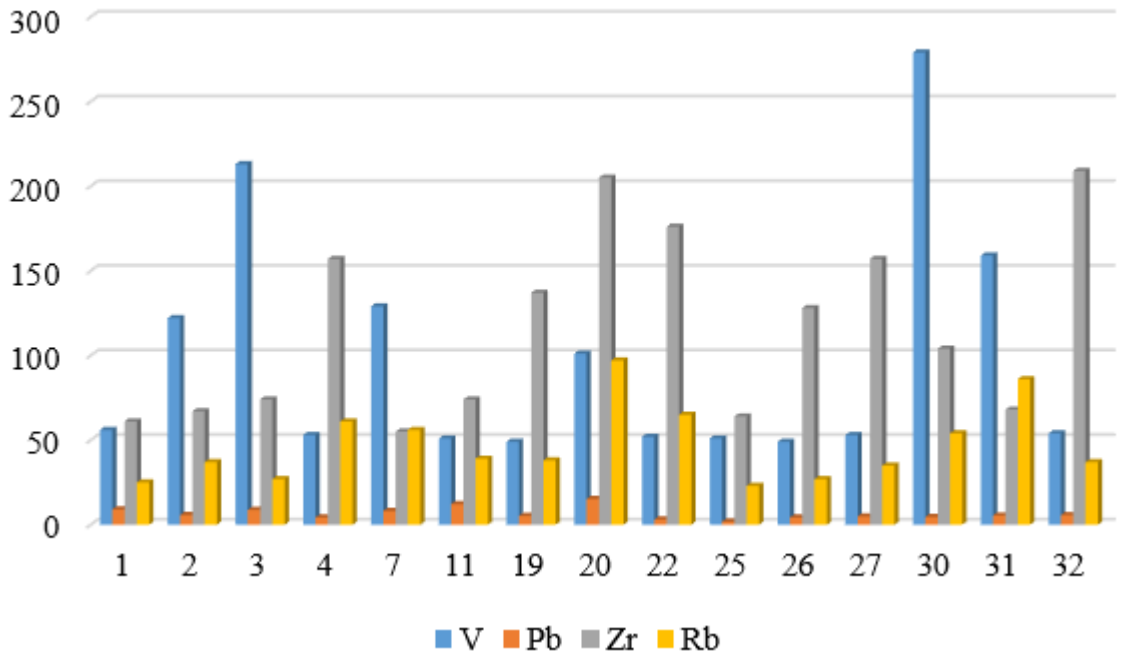

Figure 3. Amounts of V, Pb, Zr, and Rb elements reported in test samples in other studies [16]

It should be noted that other studies have found rare-earth elements in the test samples. The amounts of these elements are shown in Figure 4.

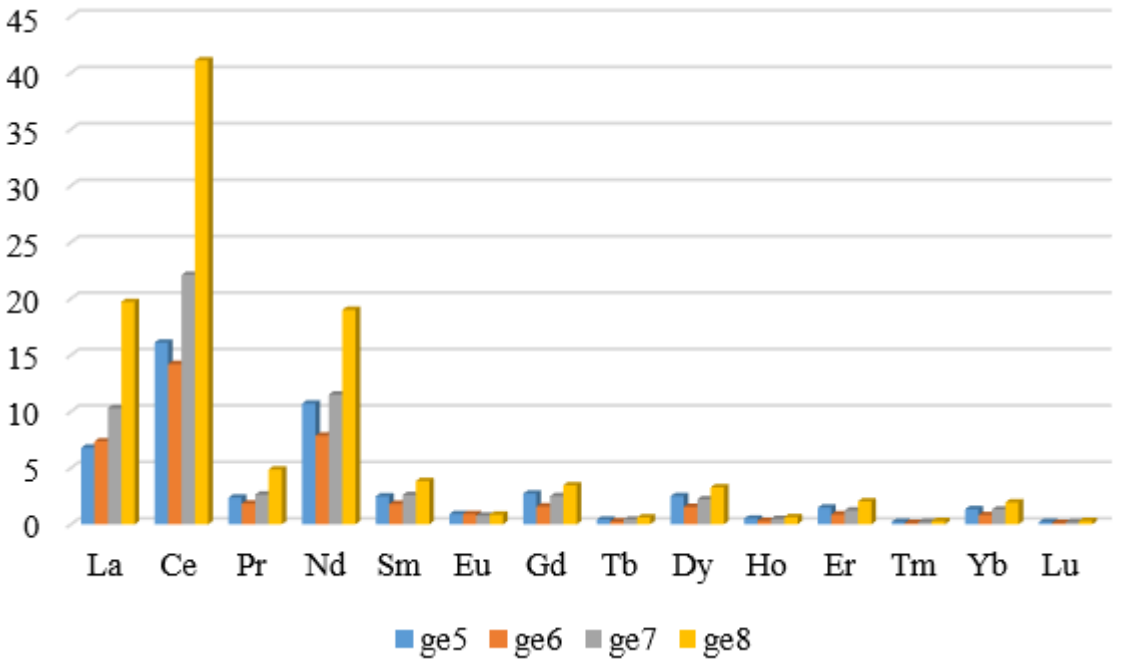

Figure 4. Rare-earth elements found in the test samples [16]

4. Conclusion. 1. Based on the results of the test samples, it can be noted that the amount of rare elements varies in a wide range. The amount of Pb, Zr, and Rb elements indicated among the rare elements in the test samples is higher. It is more expedient to conduct research to obtain accurate results. 2. The conducted research shows that the amount of rare elements in the minerals included in the

composition of magmatic and sedimentary rocks of the Gedabek deposit differs significantly from each other. Thus, the amount of rare elements in most rocks of magmatic origin is much higher than their amount in sedimentary rocks.

Conflict of interest

The author declare that they have no conflict of interest in relation to this research.

References

1. Babazade V.M. Geology of mineral resources. Part II: Ore minerals. Textbook for higher schools. 1st edition. Baku: Baku University Publishing House. 2013. 492 P. (In Azerbaijani)
2. Hamzayev V.Kh. Distribution and economic importance of rare elements in sulfide deposits of the Republic of Azerbaijan // Proceedings of Azerbaijan High Technical Educational Institutions. 2023. Vol. 34(04). Issue 11. Pp. 184-190. (In Azerbaijani)
3. Huseynov Q.S., Hamzayev V.Kh. Study of the distribution of rare elements in the Dashkasan iron ore deposit // Proceedings of Azerbaijan High Technical Educational Institutions. 2024. Vol. 40(05). Issue 05. Pp. 125-133. (In Azerbaijani)
4. Mursalov S.S. Morphological features and internal structure of gold-copper-chalkopyrite ore bodies of the Kedabek field // News of Baku University. Series of Natural Sciences. 2012. № 2. Pp. 191-196. (In Azerbaijani) (In Azerbaijani)
5. Safarov E.I. Mineral deposits of the Lesser Caucasus. “Apostrophe” Printing House. Baku, 2012. 120 P. (In Azerbaijani)
6. Valiyev A., Ibrahimov J., Bairamov A. et al. Ore deposits discovered recently in the Gedabek ore region // Earth and Human. 2024. №01(22). Pp. 17-21. (In Azerbaijani)
7. Baba-zadeh V.M., Mansurov M.I., Valiyev A.A. et al. Mineralogical features and formation conditions of the Zafar copper-gold deposit (Lesser Caucasus, Azerbaijan) // Journal of Geology, Geography and Geoecology. 2023. 32(4). Pp. 667-678.
8. Guseinov G.S. Distribution of gold and silver content in copper-pyrite ores of the Gadabay deposit // Journal of Geology, Geography and Geoecology. 2024. 33(2). Pp. 274-281.
9. Guseinov G.S., Hamzayev V.Kh., Gubadov R.R., Guseinova G.I. et al. Study of the distribution o rare elements in the Daghkasaman deposit and determination of their economic significance // Journal of Geology, Geography and Geoecology. 2025. 34(3). Pp. 512-520.
10. Guseynov G.S. The mineral composition and textural-structural peculiarities of the ore, and mineral formation stage of the Gedabek gold-copper deposit (Lesser Caucasus) // Herald of the Azerbaijan Engineering Academy. 2021. Vol. 13. № 2. Pp. 121-130.
11. Hamzayev V.Kh. Study of the environmental impact of the exploitation of rare elements // Proceedings of Azerbaijan High Technical Educational Institutions. 2024. Volume 37(05). Issue 02. Pp. 353-360.
12. Huseynov G.S., Hamzayev V.Kh., Ahmedova R.N., Huseynova G.I. Study of the distribution of rare elements in the ores of the Gosha deposit // Proceedings of Azerbaijan High Technical Education Institutions. 2025. Volume 48(06). Issue 01. Pp. 371-378.
13. İsmayıl C., Özen Y., Arık F., Veliyev A. Genesis of the Gedabek Au-Ag-Cu deposit (Azerbaijan) in the Lesser Caucasus: Insights from geochemistry, fluid inclusion and sulfur isotope // Journal of Asian Earth Sciences. 2021. Vol.206. 104627.
14. Valiyev A.A., Imamverdiyev N.A., Sadighov E.A. et al. Petrology, geochemistry and ore potential of the Gedabek granitoids, Lesser Caucasus, Azerbaijan // Journal of Geology, Geography and Geoecology. 2025. 34(2). Pp. 425-443.

15. Agaev A.M., Mamedaliyev R.N., Bairamov A.A., Sadykhov E.A. Vesuvians of the Kedabek and Shishim skarns: common and distinctive features // Regional geology and metallogeny. 2019. No. 79. Pp. 89-97. (In Russian)
16. Sadikhov E.A., Veliev A.A., Bairamov A.A., Mamedov S.M., Ibragimov D.R. Isotopic-geochemical characteristics (Sm-Nd, Rb-Sr, S) and U-Pb SHRIMP II age of the Gedabek intrusion (Azerbaijan) // Regional geology and metallogeny. 2018. No. 76. Pp. 83-94. (In Russian)

Journal of SRI "Geotechnological Problems of Oil, Gas and Chemistry" of ASOIU,
Issue 2, 2025, pp. 149-155
https://doi.org/10.65294/gpogc.2025.13

Types of natural bitumens, composite properties and their classification

M.Y. Agamammadova, Kh.E. Aliyarova, S.B. Mammadova

Azerbaijan State Oil and İndustry Universiteti, Ministry of Science and Education of Azerbaijan,
Azadlig Avenue 20, AZ1010 Baku, Azerbaijan

Abstract. Asphaltites are hard, brittle and form a rough and uneven surface due to their physical properties. They have a glassy luster, can be ground to a powder state and melt at relatively high temperatures above 1000°C. Classification of the main deposits of bitumen and bituminous rocks of Azerbaijan.

Keywords: bitumens, petroleum, shale, coal tar, bituminous rocks

Corresponding author. Tel.: +9940518026921
E-mail address: mehriban11041967@mail.ru (M.Y.Agamammadova)

1. Introduction. Natural bitumen, due to its chemical properties, is highly stable, durable, flexible, water-resistant, convertible, etc. That is why in ancient times people used bitumen as a waterproofing and binding material. Bitumen was used to cover water and grain storage facilities, the walls and floors of palaces, and to cement stone-paved city streets.

Aristotle and Hippocrates, who lived four centuries BC, wrote about bitumen deposits. Historical documents from the 8th century contain information about the existence of solid bitumen deposits in Baku and its environs.

In the Middle Ages, travellers and naturalists reported on Absheron's oil deposits, as well as bitumen deposits. In his notes, Marco Polo noted the occurrence of bitumen on Absheron, and its use for burning and treating animals. Later, oil began to be produced from bitumen [12].

Bitumen is a natural raw material consisting primarily of a mixture of carbon and hydrogen with a small amount of oxygen and sulfur-nitrogen substances, a small amount of metals and a significant amount of asphaltene-resinous substances.

2. Methodological part. Easily soluble in sulfur dioxide, chloroform and other organic solvents. Oil, shale, and coal bitumen are widely distributed in nature. Azerbaijan has abundant petroleum bitumen. The elemental composition of bitumen is approximately as follows: carbon 80-85%, hydrogen 8.0-11.5%, oxygen 0.2-4.0%, sulfur 0.5-7.0%, nitrogen 0.2-0.5%. The amounts of sulfur and nitrogen in petroleum bitumen vary greatly.

Absheron bitumen contains the lowest amount of sulfur (on average 0.8%) and a minimal amount of nitrogen [2].

Bitumens are divided into solid (sticky) and solid petroleum bitumens, solid and solid shale bitumens, and coal tar. According to R.B. Gun, Table 1 presents the range of petroleum bitumens produced for sale in the territory of the former USSR [3].

As can be seen from this table, bitumen is mainly used as a paint and insulating material when laying asphalt on roads and in various construction works [13].

Table 1. Assortment of bitumens released for sale in the territory of the former USSR, according to R.B. Gun [13].

Group	Semi-group	Brand	Standard
Solid petroleum bitumen (viscous, sticky, plastering) for roads	for roads	BND-200/300, BND-30/200, BND -90/130, BND-40/60, BND-200/300, BND-30/200, BN-90/130, BN-60/90	GOST-22245-76
	for construction	BN -50/50, BN -70/30, BN -90/10, БНСК-5	GOST-6617-76 THAT 38101397-73
	for the production of ceiling coverings	BNK -45/180 BNK -90/40, BNK -90/30	GOST- 9548-74
		or roofing and waterproofing	THAT-38101566-75
	special	for color: batteries, special volumes	GOST -8871-76
		with signs B, V, G in the field of paints and varnishes, tires, electrical engineering	GOST -21822-76
		In the rubber and tire manufacturing industry. Brands A and B	GOST - 781-68
		For pipeline insulation. Brand BNI-IV, BNI-V.	GOST 9812-74
		for obtaining the metal paint color AB-2	THAT -39-013-73
Dry petroleum bitumen	road	BK-25/40, BK -40/70, BK -70/130, SKB-40/70, SKB -70/130, SKB -130/200, MK-25/40, MK-70/130, MQ-130/200	GOST -1195-74
Coal tar	for roads	Д-1, Д-2, Д-3, Д-4, Д-5, Д-6	GOST-4641-74
	special	for painting firewood Du-7, Du-8 (sharban)	THAT -6-16-1163-67
Hard (viscous, sticky) shale bitumens	for roads and sidewalks	BS-0, BS -1, BS -2, BS -3, BS -4, BS -5, BS -6	THAT -6-08-304-74
	For painting and insulation	BS -1, BS -II, BS -III	THAT -38 10941-75
Pure shale bitumens	for roads and sidewalks	S-1, S-2, S-3	THAT -6-08-304-74

Until recent years, bituminous rocks in Azerbaijan were studied for two purposes: 1) as an exploration factor in predicting oil deposits formed at depth, and 2) for the extraction of high-viscosity oil from bitumen using mine and quarry methods.

The use of bituminous rocks in road construction continues to be successful to this day. Bitumen is also used in other applications. In recent years, a number of countries have focused on extracting various metals from natural bitumen.

3. Results and discussion. It is known from geological literature that in some cases, bitumen contains high concentrations of metals such as vanadium, nickel, scandium, rhenium, molybdenum, titanium, etc. Thus, the concentration of these useful components in bitumen is 5-10 times higher than in the surrounding rocks.

High amounts of vanadium have been found in bitumen deposits in Venezuela and the CIS in Tatarstan, Emba, and Ukhta. Shales and viscous bitumens sometimes form unique uranium-bitumen deposits, which also contain very large reserves: for example, the Ambrosia Lake deposit in New Mexico, USA.

Figure 1 shows the composition and sequence of formation of natural petroleum bitumens.

Figure 1. Formation of natural petroleum bitumen

As can be seen from the figure, on the one hand, bitumen is successively formed from naphthenic-methane and naphthenic oils in the form of malts, asphalts, asphaltites, kerites and anthroxolites, and on the other hand, waste is formed from methane and methane-naphthenic products.

Table 2 presents the classification of the main deposits of bitumen and bituminous rocks in Azerbaijan.

According to the classification, the main deposits of bitumen and bituminous rocks of the republic are located in Absheron, Shamakhi-Gobustan and the Lower Kuryansk oil and gas region.

In this table, in the composition of bitumen, along with oils, at the Kirmaki deposit, polyesters and resins make up 50.1-78.5%, at the Ziyilpiri deposit 21.0-47.91%, at the Binagadi deposit 3.65-19.5%, at the Shubani deposit 6.43-11.68%.

This shows that oils and polyester resins are distributed differently in bitumen at oil fields. There is no difference in the distribution of benzene resins (6.4-16.20%), alcohol-benzene resins (85-32%), and asphaltenes (13-43%) in bitumen.

The carbon content of these bitumens is typically 75-85%, the hydrogen content is approximately 9-12%, and the oxygen, nitrogen, and sulfur content is approximately 2-4%. The bitumens in all of these deposits are of the solution and asphalt types.

Table 3 shows the chemical composition of natural bitumen from the Beridash deposit of the Shemakha-Gobustan oil and gas region.

Table 2. Classification of the main bitumen and bituminous rock deposits in Azerbaijan

Oil-gas-tuminous region NGBR)	Bituminous rocks		Deposits
	Geochronological age	Lithological composition	
Absheron	Balakhany (Productive Layer) Stage ($N2^1$ b1) Balakhany (Productive layer) stage ($N^2{}_1$ b^1)	Sandy, siltstone, clayey, limestone deposits, sandstones, limestones, siltstones	Fatmai, Sianshor, Dighah, Pirallahi, Kirmaki, Binagadi, Ziyilpiri, Shubani, Puta
	Sarmatian $N_1{}^3$, Chokrak $N_1{}^2$, Diatom and Maykop, Chokrak $N_1{}^2$ bases	Sandy, siltstone, clayey deposits	Shorbulag
Shamakhi-Gobustan	Chokraksky $N_1{}^2$ stage	Sand, sandstone, siltstone, clay	Girgyshlak, Nardaran, Akhtarma, Cheildag
	Absheron (Q^1 ab), Agchagil ($N^2{}_2$ ak) and Lower Caspian (Q^{11} hz^1) stages and substages	Medium and fine-grained sands, detrital limestones, gray clays	Rakhim, Gylych, Barydash, Solohai, Ayrantokan, Girdag
Near the Kura Depression	Balakhany (Productive layer) stage ($N_2{}^1$ b_1)	Granular sands, siltstones, clays	Kirlykh, Akhtarma, Gyrrykh, Babazenen, Pashaly, Merkezi, Akhtarma

Table 3. Chemical composition of natural bitumen from the Beridash deposit

Layer	Bitumen content, %	Group composition of bitumen				Elemental composition of bitumen		
		Oils (+PE resins)	Benzene resins	Alcohol-benzene resins	Asphal-tenes (+ carbenes)	C	H	O+N+S
I	35.82	40.45	9.25	21.34	28.95	78.98	10.13	2.15
II	59.25	36.52	8.63	27.05	26.98	-	-	-
I	2.65	46.42	10.22	19.05	24.31	81.31	11.75	-
II	3.83	19.67	6.03	31.80	42.50	-	-	-
I	18.14	26.8	4.7	24.6	37.6	-	-	-
II	5.41	20.9	9.7	20.3	49.1	-	-	-
III	7.23	26.1	5.3	17.8	48.8	-	-	-
IV	3.45	27.2	8.1	22.8	36.1	-	-	-
V	41.78	20.6	11.3	23.6	38.9	-	-	-
VI	11.99	23.7	9.1	24.5	42.8	-	-	-

VII	11.99	24.7	16.9	15.7	42.8	-	-	-
VIII	4.35	8.0	3.4	6.7	76.6	-	-	-

Continuation of Table 3

Layer	Hydrocarbon composition group, % Percentage of fractions			Low molecular weight	Bitumen grade
	Methane-naphthenic	Aromatic			
		Monocyclic	Polycyclic		
I	50.91	35.43	14.05	12.96	Asphalt
II	52.73	10.60	28.19	8.50	
I	65.97	13.04	13.29	2.88	Malta
II	61.42	5.94	27.74	3.76	Asphaltite
I	70.1	17.8	8.1	2.8	Asphalt
II		59.4	31.0	9.3	-
III	60.0	19.5	21.8	9.0	-
IV	37.5	29.1	30.1	9.0	-
V	56.7	19.0	19.8	4.5	-
VI	58.80	18.1	19.0	9.4	-
VII	0.8	57.7	33.4	12.6	-
VIII	68.8	6.7	27.5	7.9	Asphaltite (grehemite)

In these bitumens, along with oil, polyester, benzene, and alcohol-benzene resins and asphaltenes are distributed almost evenly. Only in layer VIII, the very last layer, does the amount of asphaltenes increase sharply, while the other resins, on the contrary, decrease sharply.

Table 4 presents the characteristic properties of some bituminous rocks of the Absheron Peninsula. The table shows that, for individual deposits and samples, the bitumen content in the rock ranges from 3.65% to 19.5%.

However, in most cases it is 7–10%. Bitumen has a density of mainly 1.08–1.11 g/cm^3 and foams at a heating temperature above 1500 ^{0}C [11].

Table 4. Characteristic properties of some bituminous rocks of the Absheron Peninsula

Deposit	Extracted bitumen	Results of various tests					
Kirmaki	Bitumen content in rock -%	7.26		9.17		10.12	
	Bitumen density – – $g/см^3$, at 250^{0}S	1.081		1.095		1.11	
	Permeability at - 25^{0}S	0		0		0	
	Duntillik-25^{0}S temperaturda	0		0		0	
	Lower temperature	Foams when heated above 150^{0}C					
Ziilpiri	Bitumen content in rock -%	7.09		8.83		12.38	
	Bitumen density – $g/см^3$, at 25^{0}S	1.09		1.11		1.129	
	Regeneration at -25^{0}S	0		0		0	
	Duntillik at temperature -25^{0}S	0		0		0	
	Low temperature	Foams when heated above 150^{0}C					
Binagadi	Bitumen content in rock -%	19.5	9.30	14.36	9.68	6.48	3.65
	Density of bitumen, $g/см^3$	1.084		-		1.91	

Shubany	Bitumen content in rock -%	8.13	11.68	6.43
	Lower bitumen temperature	Foams when heated above - 150^0C		

In classifications, the term "asphalt" refers to types of bitumen that are readily soluble and have a solid resinous content and occupy a transitional position between solutions and asphaltites, and also melt at high temperatures.

The oil content of asphalt ranges from 25–40%. Physically, asphalt is a brittle, glassy, and sometimes opaque mass. It softens with gentle heating. The softening point of asphalt ranges from 20–300°C to 80–1000°C. This depends on the amount of asphaltenes it contains (Fig. 2).

Depending on the asphaltene content (10-15%-40-45%), asphalts are classified into different types. The amount of coke in asphalts is small (10-20%). The elemental composition of asphalt consists of 80-85% carbon and 9-10% hydrogen. The sulfur content varies widely: from 7 to 10%.
The oxygen content is 2–3% and depends on the intensity of oxidation. Changes in nitrogen content are caused by oxidation. Typical asphalts are bitumens, which contain equal amounts of oil, resin, and asphaltenes.

Asphaltic asphalts are solid bitumens containing less than 25% of the oil component and, accordingly, more than 75% of asphalt-resinous substances completely soluble in chloroform.

Asphaltites are hard and brittle in their physical properties, producing a rough and uneven surface. They have a vitreous luster, can be ground to a powder, and melt at relatively high temperatures (over 1000°C). Asphaltites are divided into two large groups: clay-sonite and greimite.
Academician Sh.F. Mekhtiyev (1957) distinguished the following types of natural bitumen in Azerbaijan: asphalt, asphaltite, kir, wet kir, and bituminous sands. Here, asphalt and asphaltite are understood as indicated above [5, 6, 7].

The term "shale" refers to bituminous rocks composed of dark, uniform clays. The bitumen content of oil deposits ranges from 2% to 30%, sometimes much higher.

4. Conclusions. Bituminous sands are sandy rocks impregnated with bitumen, are classified as natural petroleum asphalts and are considered a product of oil weathering.

Figure 2. Laying asphalt pavement

Malta is a type of bitumen, a cross between petroleum and asphalt. Its specific gravity is close to 1.0. According to V.A. Uspensky's classification, the oil content in malt ranges from 40% to 65%. Its elemental composition is 80-87% C, 10-12% H, and the S and O^2 content varies widely. Malta solutions differ from asphalts and asphaltites in their viscosity and stickiness.

Natural genetic types of bitumen, such as malta, asphalt, and asphaltite, are widespread in the deposits of the Absheron Peninsula. Among the natural bitumens, greite and even anthroxolite are sometimes found, which are considered products of high-grade metamorphism of bitumen [10].

Conflict of interest.

The authors declare that they have no conflict of interest in relation to this research.

References

1. Aslanov, G.P., Mirzoev, R.Kh., Kharitonov, V.M. Study of metal content of oils, oil products and formation oil waters of some regions of the USSR (Turkmen, Kazakh and Azerbaijan SSR). Collections of the Central Research Institute of Geology and Mineralogy, Moscow, 1983.
2. Babayev, F.R. Microelements of oils from offshore fields of Azerbaijan. / Microelements and forecasting of oil and gas potential. Baku. - 1974, pp. 85-94.
3. Baturin, V.P. Geology of Azerbaijan, Vol. VII. Oil and Gas Baku, Nafta-Press. - 2008
4. Goldberg, I.S. Natural bitumens of the USSR. Leningrad. Subsoil. – 1981.
5. Gun, R.B. Petroleum bitumens. M. Chemistry - 1989
6. Zulfugarli, D.I. On the history of the study of mineral components of oils of Azerbaijan / ASU Academic Notes, series: Chemical Subsoil. - 1970, No. 2, pp. 143-147
7. Mehdiev, Sh.F. Bitumen / Geology of Azerbaijan. Minerals. Baku. – 1957. Ed. AN Azerbaijan.
8. Mirzoev, R.Kh., Kharitonov, V.M. On the distribution of some elements in bituminous rocks and oils of Azerbaijan. Abstracts of the report of the All-Union Seminar "Biogeochemical Aspects of the Formation of Sedimentary Rocks and Ores". Moscow. -1983, pp. 113-115.
9. Efendieva, Z. J. Bitumen deposits of Azerbaijan. Mining magazine No. 10. Moscow. - 2021. pp. 110-114.
10. Mekhtiev, Sh.F., Tuskiya, B.A., et al. Analysis and generalization of materials on deposits of bituminous rocks and accumulations of natural bitumen of the Absheron Peninsula and Kobystan with the aim of identifying the possibilities of their use in road construction. Report. Geology Management Funds. Baku, 1981.
11. Efendieva, Z. J. Information directory on mineral deposits of Azerbaijan. ASUNP. – Baku - 2016. 57 p.
12. Geology of Azerbaijan. Baku. Nafta. Press. -2003. 576 p. T.VI. Useful minerals.
13. Mineral resources of Azerbaijan. – Baku. Ozan. - 2005. – 807 p.

Journal of SRI "Geotechnological Problems of Oil, Gas and Chemistry" of ASOIU,
Issue 2, 2025, pp. 156-161
https://doi.org/10.65294/gpogc.2025.14

Hydrogen storage with carbon nanotubes

Madatova Farida[1,*], Agayeva Kamala, Ismailova Dilara, Babayev Abulfaz

Scientific Research Institute of "Geotechnological Problems of Oil, Gas and Chemistry", 227 Dilara Aliyeva str., AZ1010, Baku, Azerbaijan

Abstract. Hydrogen is a promising universal energy source that can replace fossil fuels in the energy sector due to its environmentally friendly nature and diverse energy conversion capabilities. Hydrogen production technologies currently have an unlimited supply of raw materials and can be produced on an industrial scale. However, for large-scale development of hydrogen energy, a number of scientific and technological challenges must be addressed. Developing the most cost-effective and efficient methods of storing hydrogen is one of the main technological challenges in hydrogen energy. In this regard, this review discusses in detail the research being conducted to address hydrogen storage issues using hydrides, nanoporous carbon, porous nanomaterials, and composites based on them, and also analyzes the associated challenges and future prospects associated with the search for methods for its production.

Hydrogen is a highly efficient and environmentally friendly energy source. The main obstacle to stationary and mobile hydrogen use is the lack of effective storage methods. The possibility of storing hydrogen adsorbed in carbon nanotubes under various conditions has been explored.

Molecular dynamics simulations of hydrogen physical adsorption processes in carbon nanotube arrays were conducted. The interactions were described by the Lennard-Jones potential, and quantum effects were ignored. The dependences of the relative mass content and average density of hydrogen in the system on pressure and temperature were obtained. At low temperatures, the formation of a second adsorption layer was detected, leading to an increased content of stored hydrogen.

The spacing between the tubes in the array was varied to find the optimal geometry for adsorption. The relative mass content and average density of hydrogen in the system were obtained as functions of the spacing between the tubes in the bundle.

Keywords: *hydrogen storage, nanomaterials, hydride, nanotubes, adsorption, desorption.*

Corresponding author Tel. 0506145691
Email address: madatovafarida7@gmail.com

Introduction. Increasing demands on the reliability of modern storage systems for efficient energy sources are driving a pressing need for materials capable of supporting a wide range of operating conditions due to the specific chemical and physical properties of such systems. Due to the depletion of energy resources, hydrogen is increasingly being considered as an ideal alternative energy source [1–3]. However, the transition to advanced hydrogen energy is impossible without the development of reliable methods for producing, transporting, and storing hydrogen in large quantities. Moreover, the main challenges in the development of hydrogen energy are concentrated in the area of storage and transportation of this type of energy source [4], while hydrogen production is, in part, a solved problem, as a sufficient number of effective, inexpensive, safe, and environmentally friendly methods have already been proposed.

There are two main groups of hydrogen storage methods: physical and chemical [5]. The former are based on physical processes, primarily compression or liquefaction. The latter involves methods in which hydrogen is stored through physical or chemical interactions with certain materials. The latter method is considered the most promising. Carbon nanotubes offer significant potential in this regard. Among the many hydrogen-sorbing materials, carbon nanotubes possess one of the highest sorption properties. This is evidenced by numerous publications in recent years.

Nearly all major research centers in developed countries are conducting intensive research in this area. Many countries have national research programs in this area. For example, the United States has a national project running until 2015 to develop systems and materials for compact hydrogen storage "onboard vehicles."

This ability of nanotubes is of great practical importance, as it opens up the possibility of safe storage of hydrogen for its further use as an environmentally friendly fuel.

Since their initial production, nanocarbon nanotubes have remained the subject of ongoing scientific research in various fields of knowledge, including hydrogen energy [6 – 9]. However, real experiments on this topic require complex and high-precision equipment. Moreover, in addition to significant material resources, time is also required. Therefore, although the number of experimental studies conducted in laboratories around the world is steadily increasing, they do not contribute to the creation of a comprehensive picture of the understanding of this issue. A solution to this problem cannot be achieved solely through the development of practical work. This situation can be rectified by taking into account not only applied work, but also thorough theoretical studies that reveal fundamental aspects and contribute to an understanding of the nature of such processes under study, i.e., the uncovering of the mechanism. To implement such theoretical studies, computer modeling is used, which, as an alternative research method and based on the methods and approaches of quantum chemistry, quantum mechanics, as well as the mathematical apparatus and numerical methods for describing and calculating the properties of chemical compounds, allows for virtually any experiment to be conducted at the atomic level. At the same time, such preliminary work on studying the possibility of using carbon nanotubes as a storage medium for hydrogen allows, in combination with experimental work, to evaluate the possibility of the existence of effective nanotubular hydrogen batteries.

Published scientific literature on the results of experiments and theories on hydrogen sorption by carbon nanotubes reveals a contradictory picture.

Some researchers point to the impossibility of achieving high hydrogen sorption capacity in carbon nanotubes under normal conditions. This appears to be true, given that they rely on classical considerations regarding the formation of bonds between hydrogen and the nanocarbon surface, i.e., through intermolecular van der Waals interactions (physical adsorption) and chemical covalent bonds (chemical adsorption). Moreover, in the first case, the hydrogen capacity of nanotubular carbon does not exceed 1–2 wt.% under normal conditions, while in the second case, it is 7.7 wt.%—the known calculated value of the theoretical limit (however, this does not ensure process reversibility, since a covalent bond is realized). Nevertheless, existing theoretical studies have demonstrated the possibility of achieving high-capacity hydrogen storage in carbon nanotubes. However, it is important to note that these values are only realized at cryogenic temperatures (~77 K). In this regard, it is appropriate to consider the results of several studies. For example, in [10], under conditions of a temperature of 77 K and a pressure of 5 MPa, a model calculation yielded a hydrogen mass concentration of $\omega = 5$ wt.% for a nanotube system, while for a single nanotube this value was 10.5 wt.%. In their next work [11], the authors searched for the best structure of a nanotube system that would provide good sorption capacity. A significant influence of the distance between nanotubes on the amount of adsorbed hydrogen was indicated. The hydrogen capacity reaches its maximum value under the condition of a small influence of neighboring nanotubes, when hydrogen adsorption can be considered as for the case of an individual isolated nanotube. Optimization of the spatial structure of a nanotube system at a temperature of 77 K and a pressure of 5 MPa led to a value of $\omega = 10$ wt.%. In the study [12] the amount of hydrogen at temperature $T = 77$ K and hydrogen pressure $P_{H2} = 10$ MPa reached the value $\omega = 9.6$ wt.%, whereas at temperature $T = 300$ K and hydrogen pressure $P_{H2} = 10$ MPa this value was only 1.4 wt.%. The authors of the work [13] when modeling the interaction of hydrogen with a system of nanotubes at temperature 77 K and pressure 15 MPa obtained the value of capacity $\omega = 6.88$ wt.%. In the work [14] also shown unoptimistic results of hydrogen adsorption (less than 1 wt.%). However, others are of the opinion that it is possible to achieve

a high value of hydrogen capacity above 7.7 wt.%. In this case, they note [15 – 16] that the required values of the interaction energy of hydrogen with carbon nanostructures (20–40 kJ/mol) are an order of magnitude higher than the bond rupture energies characteristic of physical adsorption and an order of magnitude lower than the bond rupture energies characteristic of chemical adsorption. There are no new theoretical concepts regarding this type of interaction in the works. In this regard, in a number of works [17–19] Yu . S. Nechaev speaks of the possibility of creating a hydrogen superadsorbent based on nanocarbon structures only if not only practical work in this area is developed, but also due attention is paid to the development and formation of fundamental knowledge about the nature and characteristics of the interaction of hydrogen with carbon nanostructures.

One promising way to increase hydrogen adsorption capacity is to use hydrogen spillover, a process in which an active particle adsorbed at one site migrates to a neighboring site that does not itself adsorb such particles under normal conditions. For a hydrogen nanotubular battery system, spillover can be represented as a schematic diagram.

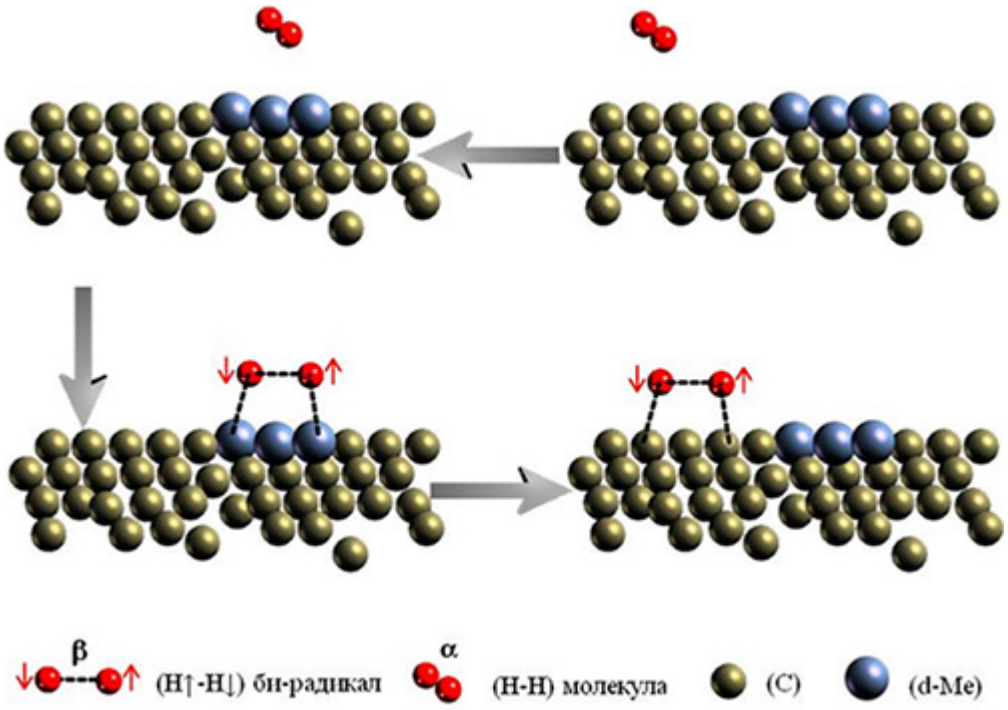

The mechanism of activation of hydrogen molecules in the active center of catalysis and spillover of hydrogen biradicals onto the carbon surface

The first stage involves the interaction of a hydrogen molecule with transition metal atoms, which results in the activation of the hydrogen molecule and its transition to an activated state, as demonstrated in [20]. The "new" form of hydrogen then interacts quite readily with nanocarbon. This is possible because the energy barrier is significantly reduced in this case compared to the interaction of an unactivated hydrogen molecule with nanocarbon.

If a metal particle (catalyst) serving as a source of atomic hydrogen (adsorbate) is deposited on a low-capacity carrier, the capacity can be increased by using an intermediate receptor with high capacity. The spillover that occurs in this manner is called a secondary spillover. This phenomenon is discussed in detail in [21]. In this case, *the secondary spillover* (transfer from a high-capacity receptor to a low-capacity one) is preceded by a typical *primary spillover* —transfer from the metal to the high-capacity receptor.

The role of the spillover mechanism in the interaction of hydrogen with carbon nanotubes is considered in [22 – 26].

Another method for increasing the sorption capacity of carbon nanostructures is their activation, for example, chemically [27] or through mechanosynthesis, as reported in [28]. A study to increase the sorption capacity of carbon nanotubes for hydrogen was conducted in [29] with the simultaneous use of microwave plasma activation of nanotubes and catalysts. As a result, a capacity value of $\omega = 4.5$ wt.% was obtained, which, as the authors indicate, is three times higher than the result in the absence of a catalyst.

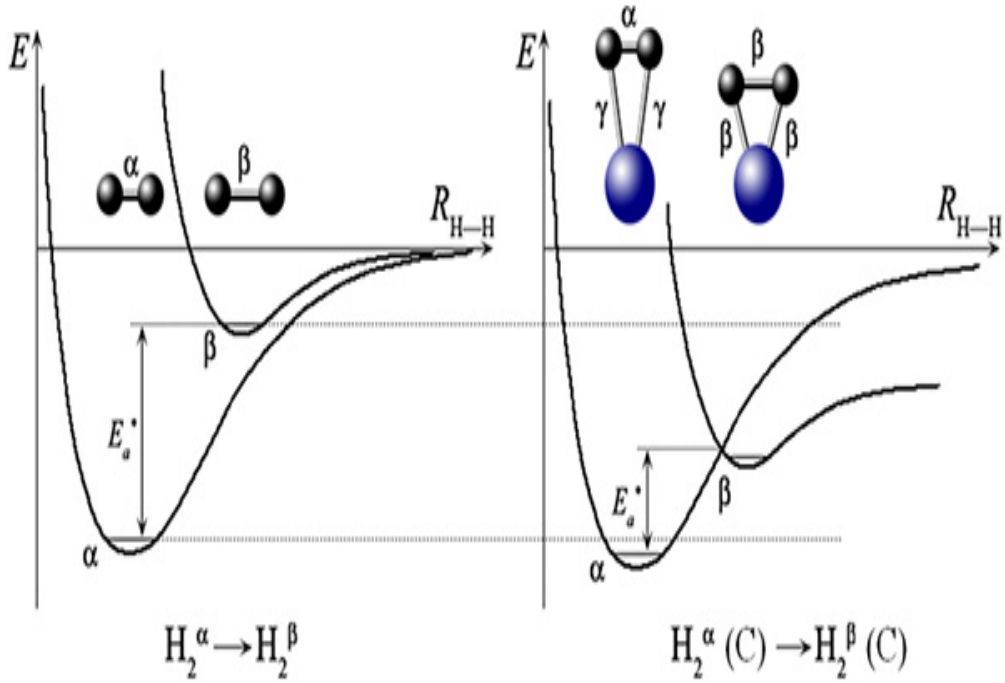

The mechanism of activation of hydrogen molecules in the active center of catalysis.

Ultimately, reversible hydrogen accumulation at room temperature exceeding 6% by weight is considered acceptable. Quantum chemistry and molecular dynamics methods have demonstrated the presence of only two known mechanisms for hydrogen accumulation: physical molecular and chemical atomic sorption of hydrogen on the nanotube surface. These studies demonstrated that both physical and chemical hydrogen adsorption on the CNT surface are unsuitable for producing effective hydrogen accumulators. However, these mechanisms of equilibrium hydrogen sorption do not explain the achievement of effective reversible hydrogen sorption in CNTs in a number of experimental studies.

The above problem is solved using the idea that the achievement of reversible accumulation of over 6 wt.% hydrogen in single-wall carbon nanotubes at room temperature is due to the fact that in the nonequilibrium process of CNT sorption it is not H—H molecules or H atoms that take part, but nonequilibrium activated biradicals $H_{\uparrow}$—$H_{\downarrow}$ hydrogen.

In theoretical studies [20 , 30–31], it was shown that intermediate forms of hydrogen biradicals arise in the active centers of transition metal catalysts. Interaction with the *sd* -electron subsystem of transition metal atoms in the active center disrupts the spin symmetry of the electronic state of the free hydrogen molecule, transferring it to the activated state of the biradical. For example, the spin-singlet hydrogen molecule H_2 upon such activation passes into a nonequilibrium state of the biradical, which is not eigenstate for the spin operator $\boldsymbol{S}^2$. Due to this, the biradical is not described within the framework

of standard calculation methods of quantum chemistry of free molecules and remains unaccounted for in these calculations. In the present work, the development of this approach consists in the fact that as a result of the transport of hydrogen biradicals from the active catalytic centers to the carbon matrix, their conservation occurs. The latter is a consequence of the emergence of spin-forbidden reactions in nonequilibrium activated biradicals upon interaction with carbon, preventing their deactivation into hydrogen molecules or decomposition into atomic hydrogen. As a result, the system of activated biradicals on the surface of carbon nanotubes, due to contact exchange interactions with the walls and with each other, manages to transition to nonequilibrium stationary states of hydrogen "superadsorbate" with "anomalous" values (20–40 kJ/mol) of hydrogen sorption energy by nanocarbon.

Conflict of interest.

The authors declare that they have no conflict of interest in relation to this research.

References:

1. Veziroglu, T.N. Solar-hydrogen energy: a force capable of saving the world / T.N. Veziroglu, D. O'M. Bockris, D. Smith. - M.: MPEI, 2002. - 165 p. - ISBN 5-7046-0904-X.
2. Baklitskaya-Kameneva, O. Is hydrogen energy doomed to success? / O. Baklitskaya-Kameneva // Russian nanotechnology. - 2009. - V. 84., No. 11-12 - P. 14-19.
3. Tarasov, B.P. Fossil energy: past, present, and future prospects / B.P. Tarasov, M.V. Lototsky // Rus. Chem. J. - 2006. - Vol. L, No. 6. - P. 5-18.
4. Tarasov, B.P. Hydrogen for energy production: problems and prospects / B.P. Tarasov, M.V. Lototsky // International scientific journal "Alternative Energy and Ecology" AEE. - 2006. - Vol. 40, No. 8. - P. 72-90.
5. Tarasov, B.P. The problem of hydrogen storage and prospects for using hydrides for hydrogen accumulation / B.P. Tarasov, M.V. Lototsky, V.A. Yartys // Rus. Chem. J. - 2006. - Vol. L, No. 6. - P. 34-48.
6. Harris, P. Carbon Nanotubes and Related Structures. New Materials for the 21st Century / P. Harris; translated from English by L.A. Chernozatonsky. — Moscow: Tekhnosfera, 2003. — 336 p. — ISBN 5-94836-013-X.
7. Poole-jr, C. Nanotechnology / C. Poole-jr., F. Owens; translated from English by Yu. I. Golovin. — 4th ed., corrected and enlarged. Moscow: Tekhnosfera, 2009. — 336 p. — ISBN 978-5-94836-201.
8. Dyachkov, P.N. Carbon Nanotubes. Structure, Properties, Applications / P.N. Dyachkov. - M.: Binom. Laboratory of Knowledge, 2006. - 296 p. - ISBN 5-94774-341-8.
9. Nanomaterials. Nanotechnologies. Nansystem technology. World achievements in 2005. Collection edited by P.P. Maltsev. — Moscow: Tekhnosfera, 2006. — 152 p. — ISBN 5-94836-085-7.
10. Wang, Q. Molecular simulation of hydrogen adsorption in single-walled carbon nanotubes and idealized carbon slit pores / Q. Wang, K. Johnson // J. Chem. Phys. - 1999. - Vol. 110, No. 11. - P. 577-586.
11. Wang, Q. Optimization of carbon nanotube arrays for hydrogen adsorption / Q. Wang, K. Johnson // J. Phys. Chem. B. - 1999. - No. 103. - P. 4809—4813.
12. Williams, K.A. Monte Carlo simulations of H physisorption in finite-diameter carbon nanotube ropes / K.A. Williams, P.C. Eklund // Chem. Phys. Lett. - 2000. - Vol. 320. - P. 352–358.
13. Lee, S. Novel Mechanism of Hydrogen Storage in Carbon Nanotubes / S. Lee, A. Kay, Y. Lee, G. Seifert, T. Frauenheim // Journal of Korean Physical Society. - 2001. - Vol. 38, No. 6. - P. 685-691.
14. Guay, P. On the control of carbon nanostructures for hydrogen storage applications / P. Guay, B. Stansfield, A. Rochefort // Carbon. - 2004. - No. 42. - P. 2187-2193.

15. Dillon, A.C. Hydrogen storage in carbon single-wall nanotubes / AC Dillon, KEH Gilbert, PA Parilla, JL Alleman, GL Hornyak, KM Jones, MJ Heben // Proceedings of the 2002 US DOE Hydrogen Program Review NREL/CP-610-32405. - P. [1-18].
16. Dillon, AC Carbon nanotube materials for hydrogen storage / AC Dillon, T. Gennett, JL Alleman, KM Jones, PA Parilla, MJ Heben // Proceedings of the 1999 US DOE Hydrogen Program Review NREL/CP-570-26938. - P. [1-17].
17. Nechaev, Yu.S. On the nature, capability and reversibility of hydrogen storage in novel carbon nanomaterials for mobile power units / Yu.S. Nechaev, OK Alexeeva International Journal of Hydrogen Energy // - 2003. - Vol. 28, No. 12. - P. 1433-1443.
18. Nechaev, Yu.S. “Open” questions about the nature and characteristics of hydrogen sorption by carbon nanomaterials and ways of their solution / Yu.S. Nechaev, O.K. Alternative energy and ecology. 2006. - No. 4. P. 15-18.
19. Nechaev, Yu.S. On chemisorption and physical sorption of hydrogen by carbon nanostructures / Yu.S. Nechaev, International scientific journal "Alternative Energy and Ecology" AEE. - 2006. - Vol. 40, No. 4 . - P. 15-18.
20. Muldakhmetov, Z.M. Theory of molecular structure: (new aspects) / Z.M. Muldakhmetov, B.F. Minaev, S.A. Beznosyuk. - Alma-Ata: Science, 1988. - 216 p. — ISBN 5-628-00040-x.
21. Lachawiec, AJ. Hydrogen Storage in Nanostructured Carbons by Spillover: Bridge-Building Enhancement / AJ Lachawiec, Jr.G. Qi RT Yang // Langmuir. - 2005. - Vol. 21. - P. 11418—11424.
22. Lueking, AD. Hydrogen spillover to enhance hydrogen storage—study of the effect of carbon physicochemical properties / AD Lueking, RT Yang // Applied Catalysis A: General. - 2004. - Vol. 265. - P. 259–268.
23. Costa, MFJ. Influence of catalyst metal particles on the hydrogen sorption of single-walled carbon nanotube materials / PMFJ Costa, KS Coleman, MH Green // Nanotechnology. - 2005. - Vol. 16. - P. 512–517.
24. Yang, FH. Adsorption of Spillover Hydrogen Atoms on Single-Wall Carbon Nanotubes / FH Yang, AJ Lachawiec, Jr.RT Yang // J. Phys. Chem. B. - 2006. - Vol. 110. - P. 6236-6244.
25. Chen, C.-H. Effect of surface characteristics and catalyst loaded amount on hydrogen storage in carbon nanotubes / C.-H. Chen, C.-C. Huang // Microporous and Mesoporous Materials. - 2008. - Vol. 112. - P. 553–560.
26. Seifi, M. The dependence of the hydrogen sorption capacity of singlewalled carbon nanotubes on the concentration of catalyst / M. Seifi, DK Ross, DJ Riley, I. Morrison // Carbon. - 2009. - Vol. 47. - P. 3184—3191.
27. Orimo, S. Hydrogen interaction with carbon nanostructures: current situation and future prospects / S. Orimo, A. Zuttel, L. Schlapbach, G. Majer, T. Fukunaga, H. Fujii // Journal of Alloys and Compounds. - 2003. - Vol. 356–357. — P. 716–719.
28. Mu, S. Hydrogen storage in carbon nanotubes modified by microwave plasma etching and Pd decoration / S. Mu, H. Tang, S. Qian, M. Pan, R. Yuan // Carbon. - 2006. - Vol. 44. - P. 762–767.
29. Nechaev, Yu.S. On the nature, kinetics and limiting values of hydrogen sorption by carbon nanostructures / Yu.S. Nechaev // Uspekhi fizicheskikh nauk. - 2006. - Vol. 176, No. 6. - P. 581-610.
30. Beznosyuk, S.A. Mechanism of hydrogen adsorption and activation by transition metals in the density functional method / S.A. Beznosyuk, B.Zh. Zhanabaev, D.V. Sokolsky, V.N. Lytkin // Reports of the USSR Academy of Sciences. Physical Chemistry. - 1982. -V. 266. - P. 380-383.
31. Beznosyuk, S.A. Electronic "phase" transition of the hydrogen molecule in the method of approximating electron density functional / S.A. Beznosyuk, V.N. Lytkin, L.A. Kim, B.Zh. Zhanabaev // Izvestiya Universiteta. Physics. - Vol. 25, No. 10. - P. 24-27.

CVD synthesis of multi-walled carbon nanotubes with integrated by-product recycling

N.I. Salmanova[1], A.B. Huseynov[1], E.B. Zeynalov[1,*], E.N. Aliyev[1], Z.E. Bayramova[1], A.Y. Guliyeva[1], E.B. Huseynova, K.V. Amirmatova[2], E.A. Ismailova[1], T.A. Isgandarova[1]

[1]Scientific Research Institute "Geotechnological Problems of Oil, Gas and Chemistry", Ministry of Science and Education of Azerbaijan, Dilara Aliyeva Street 227, AZ1010 Baku, Azerbaijan.
[2] Azerbaijan State Oil and Industry University, "Nanomaterials and nanotechnologies" Scientific Research Laboratory

Abstract. The article is dedicated to the development of a large laboratory setup for CVD synthesis of multi-walled carbon nanotubes (MWCNTs), whose key feature is the targeted utilization of the resulting gaseous byproducts. Ferrocene was used as the catalyst precursor and acetonitrile served as the feedstock. The original design of the setup includes two consecutively connected reactors: the first carries out the CVD synthesis of MWCNTs, while the second is intended for utilizing the polycyclic aromatic hydrocarbons (PAHs) formed as byproducts during the process, using them as raw material for repeated thermal decomposition. The pyrolysis temperature for PAHs was set at around 1150 °C, which allows the conversion of harmful compounds into non-toxic carbon materials such as soot, coke and various carbon nanostructures.

Keywords: two-section laboratory setup for the synthesis of carbon nanotubes, CVD synthesis, carbon-containing feedstock, acetonitrile, ferrocene as a precursor-catalyst, multi-walled carbon nanotubes.

*Corresponding author.+994503512754
E-mail elzey@mail.ru (E.B. Zeynalov)

1.Introduction. Carbon nanotubes, like fullerene and graphene, are innovative basic carbon nanomaterials that form the foundation for the modern development of carbon nanotechnologies. Multi-walled carbon nanotubes (MWCNTs) can be used as effective nano-adsorbents, catalyst carriers, components of various types of composite materials, components for the manufacture of micro- and nanoelectronics parts, and in many other fields. The synthesis of carbon nanotubes and their extensive research worldwide began in 1991. In Azerbaijan the first synthesis of MWCNTs was carried out in 2012 at the Center for High Technologies under the Ministry of Communications and High Technologies of the Republic of Azerbaijan. The production of MWCNTs was achieved using a proprietary German installation (Fig. 1) [1-4].

Figure 1. Aerosol CVD installation for the synthesis of MWCNTs made in Germany.

The design of the costly installation was distinguished by its process automation for synthesis. The dimensions of the installation were: length 2 meters, width 70 cm, and height 2 meters. The installation consists of an ultrasonic raw material evaporation unit, a gas flow control unit (argon, hydrogen), a reactor unit, a temperature control unit, and a vacuum unit. The reactor unit comprises a horizontally arranged quartz tube with a diameter of 40 mm and a length of 1 meter, which is heated by a tubular muffle furnace moving at a set speed (1-100 mm/min) from one end of the reactor to the other. Work at the High Technology Center was carried out under the supervision of Professor Sevda Abdullayeva, with key specialists responsible for MWCNT synthesis being Doctor of Philosophy in Physics and Mathematics Nakhida Musaeva and Doctor of Philosophy in Chemistry Asgar Huseynov. Several scientific projects based on the synthesized MWCNTs were implemented, including within the framework of NATO grants, the first Azerbaijan-Russia grant, as well as the Republican SOCAR grant. Research on the development of carbon nanotechnologies at the High Technology Center continued until 2020. From 2020 onwards, MWCNT synthesis in Azerbaijan was continued at the Institute of Catalysis and Inorganic Chemistry named after academician M. Nagiev, in the laboratory of corresponding member Professor Eldar Zeynalov, using a large-scale laboratory CVD installation manufactured by Asgar Huseynov (Fig. 2) [5-12].

Figure 2. Universal laboratory CVD system for the synthesis of carbon nanotubes and carbon microtubes. 1 - gas preparation unit, 2 - reactor unit, 3 - furnace temperature unit, 4 - air supply unit, 5 - vacuum unit

The dimensions of the unit were: length 2 m, width 70 cm, height 1.90 m. Unlike the German unit the device produced was universal. Firstly, it was designed to use both gaseous and liquid raw materials, and secondly, the reactor block utilized a two-section furnace with independent temperature control in each section. In addition, the design and construction of the unit allowed syntheses to be carried out in the reactor with the furnace and reactor positioned either horizontally or vertically. Under the supervision of Professor Zeynalov the development of carbon nanotechnologies is being carried out in the following directions: the use of nano-carbon catalysts for aerobic and peroxide oxidation of petroleum hydrocarbons; utilization as modifying additives in cement-concrete composite materials; polymer material chemistry as fillers and stabilizing agents; and for the creation of electrically conductive polymer and ceramic materials.

It is known that during the synthesis of multiwalled carbon nanotubes (MWCNTs) by standard CVD methods toxic condensed polyaromatic compounds are produced as by-products, such as naphthalene, anthracene, phenanthrene, azulene, etc. Therefore, the obtained MWCNTs must be purified from these toxic products and the condensed polyaromatic compounds themselves should be disposed of—hence, such synthesis is associated with the risk of environmental pollution. That is why, in this study, the task was set to develop an environmentally friendly MWCNT synthesis method. In this regard, along with research on carbon nanotubes at the Institute of Catalysis and Inorganic Chemistry by Professor Eldar Zeynalov and PhD Askar Guseynov, in cooperation with employees of the Research Institute "Geotechnological Problems of Oil, Gas, and Chemistry," in the laboratory "Catalysis and Oil Refining" led by PhD Nazilya Salmanova, a large pilot laboratory unit was designed, manufactured, and put into operation, intended for the environmentally friendly synthesis of MWCNTs. The scientific and technological novelty of this approach lies in the fact that during the synthesis of MWCNTs, the by-product toxic polycyclic aromatic hydrocarbons (PAHs) formed in the first reactor are fed into the second reactor and are disposed of by being converted into non-toxic carbon materials—soot, coke, as well as MWCNTs.

2. Experimental section

2.1 Experimental Apparatus. The manufactured and commissioned installation for environmentally friendly MWCNT synthesis is shown in Fig. 3.

Figure 3. CVD installation for environmentally friendly synthesis

of multiwalled carbon nanotubes.

The dimensions of the setup are: length 2 m, width 1 m, height 2 m. As can be seen from the diagram, the setup consists of a temperature control block for two furnaces, a reactor block containing two muffle furnaces with quartz tube reactors, a liquid feed system, and a vacuum unit. Acetonitrile was used as the feedstock and ferrocene was used as the catalyst precursor. Before starting the experiment, the required amount (0.45 g, 0.9 g, 1.8 g) of ferrocene was dissolved in 50 ml of acetonitrile, and the resulting solution was added to the liquid feed system. After setting the temperature to 900°C, a gas mixture of hydrogen and argon was supplied to the reactor at flow rates of 12 L/h and 60 L/h, respectively. The liquid feed (with the dissolved catalyst precursor) was supplied at a rate of 1 ml/min. The synthesis duration was 50 minutes. The gas mixture (argon and hydrogen) and the liquid feed were directed into the first reactor at a temperature of 900°C, where the synthesis of MWCNTs occurred. To dispose of the side products (PAHs) formed in the first reactor, the gas stream was passed into a second reactor, where they were decomposed at a temperature of 1150°C.

2.2. Analysis of Reaction Products. The synthesized carbon nanotubes were identified by scanning electron microscopy (SEM) using a TESCAN VEGA3 microscope.

2.3. Reagents Used. Acetonitrile (99.5% pure), ferrocene (99.9% purity, Sigma Aldrich), hydrogen supplied by a hydrogen generator model ГВЧ-6, argon with 99.9% purity supplied from a gas cylinder manufactured in Russia.

3. Results and Discussion. For the selective growth of multiwalled carbon nanotubes (MWCNTs) this study investigated the use of ferrocene as a precursor-catalyst. Figure 4 shows the dependence of multiwalled carbon nanotube yield on ferrocene concentration.

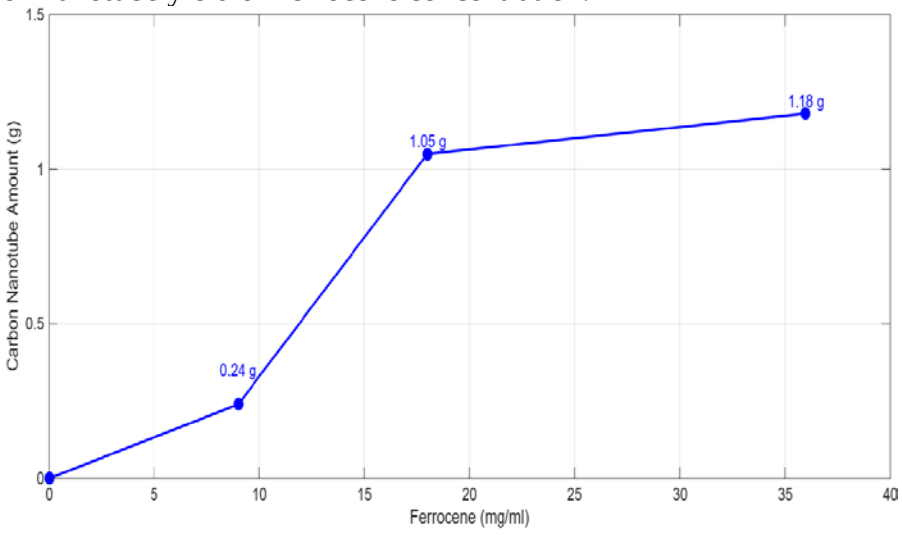

Figure 4. Dependence of multiwalled carbon nanotube yield on ferrocene concentration in the feedstock

From the graph, it can be seen that as the concentration of ferrocene in the feedstock increases, the yield of MWCNTs increases. However, the overall concentration of ferrocene cannot be increased beyond certain limits due to its solubility in acetonitrile. Depending on the amount of ferrocene, carbon nanotube deposits of varying amounts and diameters were obtained. Fig. 5 shows the SEM analysis of the carbon deposit synthesized at a ferrocene concentration in acetonitrile of 9 mg/ml.

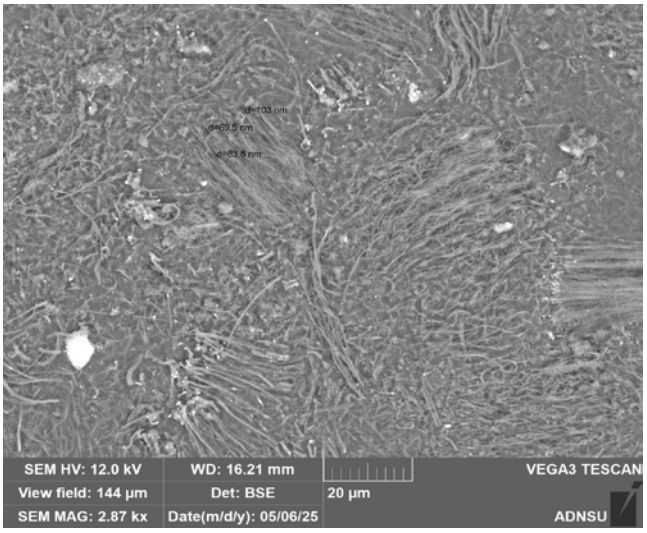

Figure 5. SEM analysis of multiwalled carbon nanotubes synthesized in the presence of ferrocene (9mg/ml)

The structures shown in Fig. 5 are fibrous and nanoscale. The fibers are densely intertwined and tangled. The image shows that the synthesized nanotubes are not isolated, but form agglomerates. As can be seen from Fig. 5, the diameters of the synthesized nanotubes are in the range of 80 to 100 nm.

Fig. 6 shows the SEM analysis of the carbon deposit synthesized at a ferrocene concentration of 18 mg/ml.

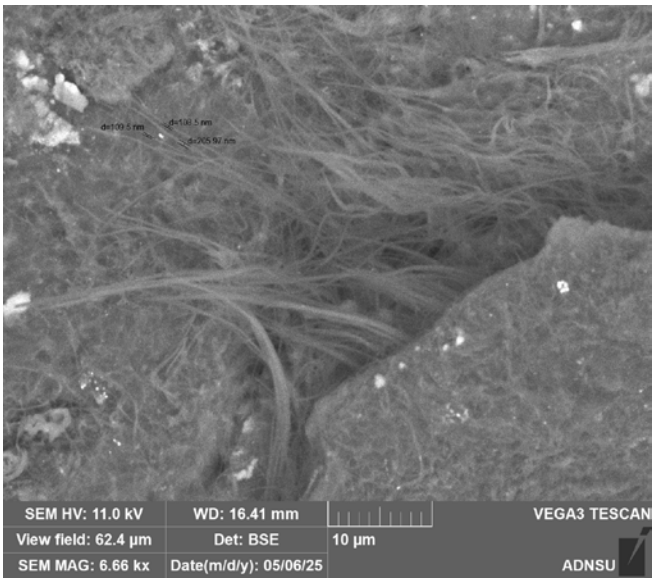

Figure 6. SEM analysis of multiwalled carbon nanotubes synthesized in the presence of ferrocene (18 mg/ml)

The synthesized material has a nanotubular structure and is of high quality and purity, as there are no other non-tubular carbon forms such as soot or coke visible in the image. As seen in Figure 6, the diameters of the synthesized nanotubes range from 100 nm to 200 nm.

Fig. 7 shows the SEM analysis of the carbon material synthesized at a ferrocene concentration in acetonitrile of 36 mg/ml.

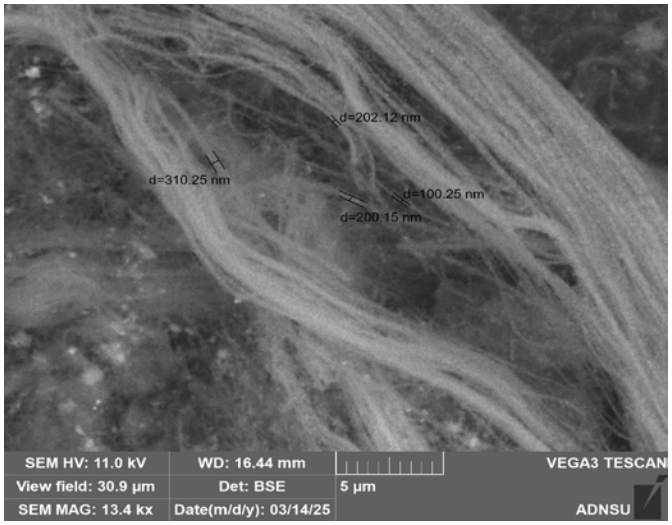

Figure 7. SEM analysis of multiwalled carbon nanotubes synthesized in the presence of ferrocene (36 mg/ml)

The presented SEM image shows that the nanostructures have a tubular shape. The nanotubes are arranged parallel and densely packed, which indicates the maintenance of constant temperature and gas flow conditions during synthesis. It can be noted that no side non-tubular structures are observed in the image, indicating the high purity of the synthesized MWCNTs. As seen from Fig. 7, the diameters of the synthesized nanotubes are in the range of 100 to 300 nm. As can be seen from these images (Figs. 5–7), with an increase in the concentration of the catalyst precursor in the feedstock from 9 to 36 mg/ml, the diameter of the synthesized nanotubes increases from 80 - 100 nm to 100 - 300 nm. This effect - an increase in MWCNT diameter with increasing catalyst concentration - can be explained based on literature data, according to which the diameters of synthesized MWCNTs are close to the diameters of the metallic catalyst clusters on which they form. We assume that as the concentration of the catalyst precursor increases, the cluster diameters also increase, leading to an increase in the diameter of the synthesized MWCNTs.

4. Conclusions. A large laboratory setup for environmentally friendly MWCNT synthesis has been developed, constructed, and put into operation. A two-reactor technology for the environmentally friendly synthesis of MWCNTs is proposed: in the first reactor carbon nanotubes are synthesized, and the toxic byproducts formed during synthesis are neutralized in the second reactor by high-temperature pyrolysis to yield non-toxic substances such as soot, coke, and nanotubes. Optimal conditions have been established for converting liquid acetonitrile feedstock, using ferrocene as the catalyst precursor, into high - quality and pure multiwalled carbon nanotubes. It has been shown that as the concentration of ferrocene in acetonitrile - in other words, as the catalyst - precursor - feedstock ratio increases the diameter of the synthesized nanotubes also increases.

Conflict of interest.

The authors declare that they have no conflict of interest in relation to this research.

References

1. Abdullayeva Sevda, Huseynov Bagi, Musayeva Nahida, Jabbarov Rasim, Sultanov Chingiz, Hasanov Rovshan. Synthesis of Carbon Nanotubes Using Azerbaijan's Oil. Advances in Materials Physics and Chemistry. 2016, 06. 105-112. https://doi.org/10.4236/ampc.2016.65011
2. Abdullayeva, S., Musayeva Nahida, Frigeri, C., Huseynov Bagi, Jabbarov Rasim, Abdullayev, R., Sultanov Chingiz, Hasanov Rovshan. Characterization of high-quality carbon nanotubes synthesized via Aerosol-CVD. Journal of advances in physics. 2015, vol. 11, 3229-3240. https://doi.org/10.24297/jap.v11i3.6943
3. Huseynov Asgar, Israfilov Aydin, Mammadova Samira, Abdullayeva Sevda, Sokolov Sergey, Goryunkov Alexey, Guliyev Akif. Fabrication and characterization of MWCNT/natural Azerbaijani bentonite electroconductive ceramic composites. Journal of Composite Materials. 2019, 53. 3909-3923. https://doi.org/10.1177/0021998319848798
4. Mammadova, S.A., Huseynov, A.B. & Israfilov, A.O. Synthesis and Optical Properties of Iodinated Multi-walled Carbon Nanotubes. Opt. Spectrosc. 2018, 125, 921–927. https://doi.org/10.1134/S0030400X1812024X
5. Zeynalov, E.B., Allen, N.S. Salmanova, N.I., Vishnyakov, V.M. Carbon nanotubes catalysis in liquid-phase aerobic oxidation of hydrocarbons: Influence of nanotube impurities. Journal of Physics and Chemistry of Solids, 2019, 127(4), 245-251.
6. Zeynalov, E.B., Huseynov, A.B., Huseynov, E.R., Salmanova, N.I., Nagiyev, Ya.M., Abdurakhmanova, N.A. Impact of as-prepared and purified multi-walled carbon nanotubes on the liquid-phase aerobic oxidation of hydrocarbons. Chemistry & Chemical Technology, 2021, 15 (4), 479-485.
7. Зейналов, Э.Б., Нагиев, Я.М., Гусейнов, А.Б., Надири, М.И., Гулиев, А.Д., Салманова, Н.И., Аббасов, М.Х., Назаров, Ф.Б., Апаева, Р.Р. Аэробно-пероксидное окисление нафталина в присутствии переходного металла на наноуглеродном носителе. SOCAR Proceedings (Fundamental scientific researches), 2022, 4, 142-149.
8. Naghiev, Ya.M., Apayeva, R.R, Salmanova, N.I., Nadiri, M.I., Huseynov, A.B (2023). Catalytic activity of iron-containing carbon nanotubes in the oxidation reaction of the diesel fuel fraction. SOCAR Proceedings. (Transportation, storage of oil and gas) 2023, 3, 182-189.
9. Zeynalov, E.B., Allen, N.S., Naghiev, Y.M. Huseynov, A. B., Rzayev, F.H. Formal Kinetics of Catalytic Oxidation of Diesel Paraffin-Naphthenic Fraction in the Presence of Carbon Nanotubes Containing Co, Mn and Fe. Journal of Physics and Chemistry of Solids, 2024, 195, article 112263.
10. Zeynalov, E., Friedrich, J., Huseynov, A., Mustafayeva, N., Gasimov, E. Oxidation kinetics of a commercial diesel fuel and its fraction in the presence of metal-containing multi-walled carbon nanotube admixtures. Chemistry & Chemical Technology, 2025, 19(2), 385-394.
11. Zeynalov, E.B., Naghiev, Y.M., Huseynov, A. B., Abbasov M.H., Nadiri, M.I., Mustafayeva, N.A., Malikova, N.N., Tagiyev, D.B. Aerobic oxidation of a diesel paraffinic-naphthenic fraction-in the presence of Co assisted Fe-containing multi-walled carbon nanotubes. Azerbaijan Chemical Journal 2025, 3, 11-23.
12. Mustafaeva, N.E., Zeynalov, E.B., Hüseynov, A.B., Nağıyev, Y.M., Nadiri, M.I., Maharramova, M.Y. Investigation of multi-walled carbon nanotubes catalytic activity by means of the model aerobic oxidation reaction. J. Serb. Chem. Soc. 2025, 90 (10) 1189–1201.

Journal of SRI "Geotechnological Problems of Oil, Gas and Chemistry" of ASOIU,
Issue 2, 2025, pp. 169-175
https://doi.org/10.65294/gpogc.2025.16

Janus interfacial catalysts and nanoparticles for enhanced oil recovery: synthesis, mechanisms, and novel conceptual approaches

M.M. Asadov[1,2,*], E.N. Aliyev[1], A.M. Salimli[1]

[1]Scientific Research Institute "Geotechnological Problems of Oil, Gas, and Chemistry," Ministry of Science and Education of Azerbaijan, AZ1010, Baku, st. Dilara Alieva, 227. Azerbaijan
[2]Institute of Chemistry, Ministry of Science and Education of Azerbaijan, AZ1143 Baku, G. Javid Ave., 113. Azerbaijan

Abstract. This work presents a systematic study and original results on the synthesis, structural control, and functional integration of Janus colloidosomes and interfacial catalytic systems. The use of Janus nanoparticles enables not only emulsion stabilization but also the precise control of interfacial processes at molecular and pore scales, opening new opportunities for enhanced oil recovery (EOR). The paper proposes novel conceptual mechanisms of Janus particle interaction with porous media, including asymmetric wettability, self-orienting behavior, dynamic interfacial activity, and the "nano-anchor" micromechanism.

Keywords: Janus nanoparticles, interfacial catalysts, multiphase reactions, enhanced oil recovery, Pickering emulsions, functional integration, EOR.

Correspondence author: +994506201516 (M. M. Asadov)
E-mail: aelshan367@gmail.com

Introduction. Janus interfacial catalysts and Janus nanoparticles represent a promising class of materials capable of significantly enhancing interfacial mass transfer and reaction kinetics due to their asymmetric structure [1–4]. Unlike conventional nanoparticles and surfactants, Janus nanoparticles allow the integration of hydrophilic and hydrophobic properties within a single particle, creating unique opportunities for controlling multiphase processes [5–7].

Despite extensive research on classical Janus systems, there is a lack of a comprehensive approach that simultaneously integrates:

- Multistage synthesis and morphological control;
- Localized placement of catalytic centers;
- Dynamic adaptation of interfacial activity;
- Conceptual mechanisms for residual oil displacement in porous media.

Aim of the Study: To develop a universal Janus nanoparticle platform combining catalytic and oil recovery functions, and to propose novel conceptual mechanisms of particle–phase interaction under varying reservoir conditions.

Materials and Methods

1. Synthesis of Janus Nanoparticles

A multistage approach was applied, combining [1]:

1. Emulsion-based particle size control;
2. Polymerization on the hydrophobic side;
3. Localized immobilization of catalysts (gold, $PW_{12}O_{40}^{3-}$) on the hydrophilic side [4–6];
4. Functionalization to create hydrophilic and hydrophobic domains for wettability control [8].

Figure 1. Schematic of multistage Janus nanoparticle synthesis.
Description: (a) Emulsion droplet formation; (b) Polymerization on hydrophobic side; (c) Selective immobilization of catalytic nanoparticles on hydrophilic side; (d) Final Janus particle structure).

2. Characterization Techniques

Table 1. Summary of characterization techniques and results.

Technique	Purpose	Result
SEM / TEM	Morphology, layer distribution	Clear separation of hydrophilic/hydrophobic sides
Laser diffraction	Particle size & emulsion stability	200–500 nm, monodisperse
Elemental analysis	Catalyst localization	Gold & $PW_{12}O_{40}^{3-}$ only on hydrophilic side
MAS NMR	Functionalization confirmation	Peaks correspond to polymer and ionic liquid attachment
GPU-based modeling (GALAMOST) / DFT	Particle dynamics, interfacial interactions	Predicted orientation and wettability effects

Results and discussion

1. Structure and Morphology

- Homogeneous Janus colloidosomes with clearly separated hydrophilic and hydrophobic sides were obtained.
- SEM analysis showed smooth morphology on the hydrophobic side, while the hydrophilic side contained immobilized Fe_3O_4 and $PW_{12}O_{40}^{3-}$ particles with increased roughness [1].

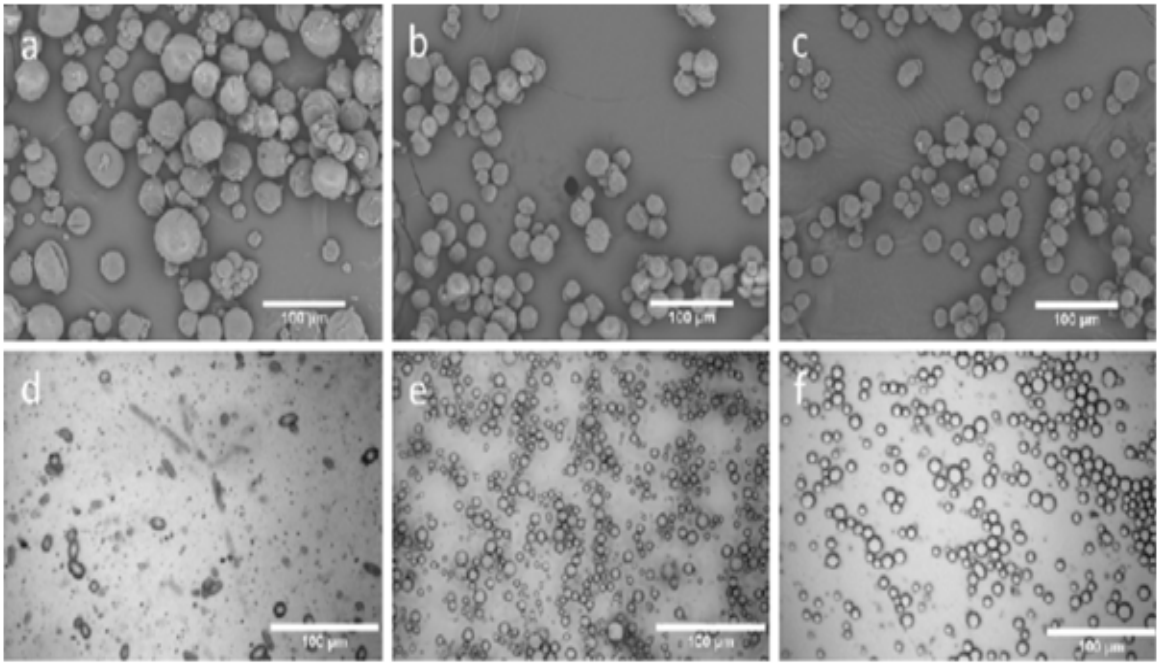

Figure 2. SEM images of Janus nanoparticles showing hydrophilic and hydrophobic domains.

2. Catalytic Activity
- Localized immobilization of gold nanoparticles and polyionic liquids enhanced phase-transfer reaction rates.
- Application in biphasic systems increased conversion from 68% (conventional system) to 97% [4,5].

3. Conceptual Mechanisms in Oil Recovery
This study proposes original mechanisms beyond standard surfactant effects.

1. Asymmetric Wettability Mechanism
- Janus particles create local hydrophilic/hydrophobic domains in the porous medium, enhancing oil displacement.

2. Self-Orienting Behavior
- Under pressure gradients, particles orient specific sides toward oil or water, increasing emulsion stability and capillary control.

3. Dynamic Interfacial Activity
- Particles adaptively change interfacial behavior over time, crucial under varying salinity, temperature, and shear conditions.

4. Micromechanism of “Nano-Anchors”
- Particles temporarily anchor at the oil–rock interface, reducing water recirculation and improving sweep efficiency.

5. Comparative Concept
- Structural comparison of conventional nanoparticles, surfactants, and Janus nanoparticles by mechanism of action, not just effect.

4. Application in Oil Recovery

- Janus particles enhance oil–water emulsion stability, increase residual oil displacement, and reduce produced water volume [14].
- Phase-selective placement of catalytic and polymeric components optimizes interfacial mass transfer.
- Recyclability after centrifugation preserves particle activity over multiple cycles.

Table 2. Effect of Janus nanoparticles on residual oil recovery and emulsion stability.

Sample	Conversion (%)	Emulsion Stability (h)	Residual Oil Recovery (%)
Conventional	68	4	45
nanoparticles	75	6	52
Surfactants	97	12	72
Janus nanoparticles			

The novelty of this study lies in the systematic integration of synthesis, functionalization, and understanding of the mechanism of action of Janus particles, including their application to enhanced oil recovery.

Table 3. Influence of mechanical and chemical parameters

Parameter	Effect
Homogenizer speed	Morphological stability, emulsion stability
Paraffin template	Symmetry control, interfacial oil movement
Polymerization	Catalytic activity and improved emulsion on a hydrophobic surface
Placement of heteropolyanions	Improved mass transfer and interfacial catalysis
Immobilization of gold nanoparticles	Accelerates reactions, increases conversion

Taking into account the above, the following schemes for visualization can be proposed.

Scheme 1: Synthesis and functionalization of Janus particles
(Silica → template → hydrophobic/hydrophilic surface → Au NP immobilization → Janus colloidosome) [6–8]

Data on the synthesis and functionalization of Janus particles (Silicon → template → hydrophobic/hydrophilic surface → immobilization of Au nanoparticles → Janus colloidosome) [6–8] were used. A step-by-step scheme for the preparation of Janus phase-interfacial catalysts is presented below (Scheme 1).

Scheme 1. Synthesis and Functionalization of Janus Particles

Silicon (Si)-Based Particles

↓

Paraffin Template / Polymer Template

↓

Surface Functionalization:

├─ **Hydrophobic (phenyl, hexadecyl)**

├─ **Hydrophilic / Catalytic (amine, ionic liquid, $PW_{12}O_{40}^{3-}$)**

↓

Immobilization of Gold Nanoparticles (Phase-Selective)

↓

Multi-Stage Janus Colloidosome

In conclusion, this scheme demonstrates phase-selective catalytic activity and the separation of hydrophilic and hydrophobic surfaces.

The mechanism of interphase transition taking into account the aqueous phase – Janus particle – organic phase; catalytic reaction, emulsion stabilization, selective product transfer [4,5,8] is presented in Scheme 2.

Scheme 2. Phase transition and reaction mechanism of the Janus catalyst

Aqueous phase (hydrophilic) Janus particle Organic phase (hydrophobic)

| | |

Substrate adsorption toluene transition **Phase transition** **Hydrophobic products interact**

↓ ↓ ↓

Catalysis (gold nanoparticles, $PW_{12}O_{40}^{3-}$) → Emulsion stabilization → Efficient oil extraction

The oil-water interface is stabilized by phase-selective catalysis and the Pickering principle.

The molecular interactions analyzed by modeling and molecular analysis of the carboxylate-amine complex, as well as by taking into account the optimized DFT data of the configurations [13], are shown in Scheme 3. The simulation was performed on a GPU-based system with large-scale simulations of 179,600 particles. DFT optimization of the equilibrium configuration of functional groups was performed in an aqueous medium.

Scheme 3. Molecular Interactions of Nanoparticles

Carboxylate (A) – Electrostatic/Hydrogen/Van der Waals Interactions – Amine (B)

↓

Energy of complexation: $E_{complex} = E_A + E_B - E_{AB}$

↓

Interfacial mass transfer and liquid microstructure formation

Conclusion

- A comprehensive method for Janus nanoparticle synthesis with controlled morphology and functional integration was developed.
- Novel conceptual mechanisms were proposed, including asymmetric wettability control, self-orienting behavior, and the "nano-anchor" micromechanism.
- High efficiency in interfacial processes and potential for enhanced oil recovery (EOR) were demonstrated.
- The study provides a methodological foundation for future research on multiphase catalytic systems and "smart" functional materials.

Conflict of interest

The authors of this work declare that they have no conflicts of interest.

References

1. Chu, Z.; Zhong, B.; Zhou, W.; Cui, P.; Gu, J.; Tian, B.; Olasoju, O.S.; Zhang, X.; Sun, W. Study in the experimental manipulation of Janus particle synthesis via emulsion-based method. Colloids and Surfaces A: Physicochemical and Engineering Aspects, 2020, 603, 125183. https://doi.org/10.1016/j.colsurfa.2020.125183
2. Lee, Y.G., Park, J.H., Oh, C., Oh, S.G., Kim, Y.C. Preparation of highly monodispersed hybrid silica spheres using a one-step sol-gel reaction in aqueous solution. Langmuir, 2007, 23, 10875–10878. https://doi.org/10.1021/la702462b
3. Jiang, S., Granick, S. Controlling the geometry (Janus balance) of amphiphilic colloidal particles. Langmuir, 2008, 24, 2438–2445. https://doi.org/10.1021/la703274a
4. Vafaeezadeh, M., Thiel, W.R. Janus interphase catalysts for interfacial organic reactions. Journal of Molecular Liquids, 2020, 113735. https://doi.org/10.1016/j.molliq.2020.113735
5. Zhao, R., Han, T., Sun, D., Huang, L., Liang, F., Liu, Z. Poly(ionic liquid)-Modified Magnetic Janus Particles for Dye Degradation. Langmuir, 2019, 35, 11435−11442. https://doi.org/10.1021/acs.langmuir.9b01400
6. Zhao, R., Yu, X., Sun, D., Huang, L., Liang, F., Liu, Z. Functional Janus Particles Modified with Ionic Liquids for Dye Degradation. ACS Applied Nano Materials, 2019, 2, 2127−2132. https://doi.org/10.1021/acsanm.9b00090
7. Zhang, M., Tang, Z., Fu, W., Wang, R., Tan, D., Yin. An ionic liquid-functionalized amphiphilic Janus material as a Pickering interfacial catalyst for asymmetric sulfoxidation in water. Chemical Communications, 2019, 55, 592–595. https://doi.org/10.1039/C8CC08292H

8. Vafaeezadeh, M., Breuninger, P., Lösch, P., Wilhelm, C., Ernst, S., Antonyuk, S., Thiel W.R. Janus Interphase Organic-Inorganic Hybrid Materials: Novel Water-Friendly Heterogeneous Catalysts. ChemCatChem, 2019, 11, 2304–2312. https://doi.org/10.1002/cctc.201900147
9. Vafaeezadeh, M.; Wilhelm, C.; Breuninger, P.; Ernst, S.; Antonyuk, S.; Thiel, W.R. A Janus-Type Heterogeneous Surfactant for Adipic Acid Synthesis. ChemCatChem, 2020, 12, 2695–2701. https://doi.org/10.1002/cctc.202000140
10. Chauhan, A.; Rastogi, M.; Scheier, P.; Bowen, C.; Kumar, R.V.; Vaish, R. Janus Nanostructures for Heterogeneous Photocatalysis. Applied Physics Reviews, 2018, 5, 041111. https://doi.org/10.1063/1.5039926
11. Akbari, M.; Shariaty-Niassar, M.; Matsuura, T.; Ismail, A.F. Janus Graphene Oxide Nanosheet: A Promising Additive for Enhancement of Polymeric Membranes Performance Prepared via Phase Inversion. Journal of Colloid and Interface Science, 2018, 527, 10–24. https://doi.org/10.1016/j.jcis.2018.05.012
12. Yuan, K.; Li, Y.; Huang, X.; Liang, Y.; Liu, Q.; Jiang, G. Templated Synthesis of a Bifunctional Janus Graphene for Enhanced Enrichment of Both Organic and Inorganic Targets. Chemical Communications, 2019, 55, 4957–4960. https://doi.org/10.1039/C9CC01470E
13. Zhu, L.; Wang, D.; Guan, J.L.; Sun, Z.Y.; Lu, Z. The Advantages of Nanoparticle Surfactants over Janus Nanoparticles on Structuring Liquids. Nanoscale, 2022, 14, 3554–3560. https://doi.org/10.1039/D1NR06713C
14. Tohidi, Z.; Teimouri, A.; Jafari, A.; Gharibshahi, R.; Omidkhah, M.R. Application of Janus nanoparticles in enhanced oil recovery processes: Current status and future opportunities. Journal of Petroleum Science and Engineering. 2022, 208, Part D, 109602. https://doi.org/10.1016/j.petrol.2021.109602